

Behavior of Magnetic Microswimmers

Simulations for Natural Swimmers

and Synthetic Propellers

Dissertation
zur Erlangung des akademischen Grades
doctor rerum naturalium
(Dr. rer. nat.)
im Fach Physik

by

Agnese Codutti



**Max Planck Institute
of Colloids and Interfaces**



**Max Planck Institut für Kolloid und Grenzflächenforschung,
Biomaterialien**
eingereicht an der
Universität Potsdam, Institut für Physik, Biologische Physik

Supervisor(s):
Stefan Klumpp
Damien Faivre

This work is licensed under a Creative Commons License:
Attribution 4.0 International
To view a copy of this license visit
<https://creativecommons.org/licenses/by/4.0/>

Potsdam, January 10, 2019

Published online at the
Institutional Repository of the University of Potsdam:
<https://nbn-resolving.org/urn:nbn:de:kobv:517-opus4-422976>
<https://doi.org/10.25932/publishup-42297>

Codutti, Agnese

agnese.codutti@mpikg.mpg.de

Behavior of Magnetic Microswimmers

Dissertation

Max Planck Institut für Kolloid und Grenzflächenforschung

eingereicht an der Universität Potsdam, January 2019

"Basically, this research asks the question: Why is the universe not boring?" cit.

I am not very good with the 'thank you', so do not expect too much! First of all, I would like to thank my supervisors Stefan and Damien for the support during these three years and for helping me to become a better scientist. I would like to thank the International Max Planck Research School on Multi-scale Biosystems for funding my PhD. Then I would like to thank all the amazing people that helped me with my project: Klaas, for making the bacteria experiments I was not able to do; Felix, for the propellers experiments I was not able to do; Mohammed and Elisa, for other bacteria experiments I was not able to do; Paul Zaslansky, for helping me with the microCT experiments; Sarah, for the help with my program; Sara and Bahareh, for useful discussions, as well as all the other group members for support and for not falling asleep during my talks; thanks to Andreas for the help with German and Dan for the help with English. Thanks to the IT, in particular to Rene', for saving my computer from myself. Thanks to all my new dear friends, without you all I could not have gone through this PhD: in random order Patricia, Eddie, Lorena, Andreas, Elisa, Melis, Batu, Delphine, Ana, Rikhia, Erika, Anna, Sandy, Alberto, Alessandro, Emilia, Chuang, Paolino, Valentino, Jose', Sadra, Weronika, Wei, Julia, Ines and many more. Thanks to my old friends back at home or in another part of this world, for supporting me from a distance: Giacomo, Enrico S., Isabella, Giorgia, Enrico M., Nicola and mr. Feng. Thanks to my dear family (Antonella Andrea and Alice), it is a cliché, but without you I couldn't be here writing these poorly written lines: I could never be grateful enough for you believing in me and supporting me to become a scientist. Last but not least, thanks to Michele: without you I wouldn't have made it till here, without you pushing me I would be still in a bank: thank you from the deep of my heart.

Selbständigkeitserklärung

Hiermit erkläre ich, daß ich die vorliegende Arbeit selbständig angefertigt, nicht anderweitig zu Prüfungszwecken vorgelegt und keine anderen als die angegebenen Hilfsmittel verwendet habe. Sämtliche wissentlich verwendeten Textausschnitte, Zitate oder Inhalte anderer Verfasser wurden ausdrücklich als solche gekennzeichnet.

Potsdam, January 10, 2019

Agnese Codutti

Abstract

Die Forschung an Mikroschwimmern oder genauer gesagt an aktiv schwimmenden Mikroorganismen oder Objekten mit niedrigen Reynolds Zahlen, hat in den letzten Jahren wegen ihrer vielfältigen Anwendungen in der Medizin und Bioremediation stark an Bedeutung gewonnen. Besonders vielversprechend ist die Arbeit mit magnetischen Mikroschwimmern, da deren biokompatibler Magnetismus genutzt werden kann um die Schwimmer gezielt zu steuern. In dieser Arbeit werden zwei Beispiele von magnetischen Mikroschwimmern aus physikalischer Sicht untersucht. Das erste Modellsystem hierfür sind magnetische Zellen. Diese können entweder magnetische Biohybride (eine schwimm-Zelle gekoppelt mit einer synthetischen magnetischen Komponente) oder magnetotaktische Bakterien (natürlich vorkommende Bakterien die eine intrazelluläre Kette von magnetischen Kristallen produzieren) sein. Die passive Wechselwirkung der magnetischen Zelle mit einem externen Magnetfeld kann zu deren Steuerung genutzt werden. Das Ziel dieser Arbeit ist es zu verstehen wie magnetische Zellen die magnetische Wechselwirkung mit ihre Schwimmstrategie verknüpfen, oder genauer gesagt, wie sie sie zur Chemotaxis (die Fähigkeit externe chemische Gradienten wahrzunehmen und die Fortbewegungsrichtung daran anzupassen) zu nutzen. Es ist immer noch nicht restlos geklärt worin in der natürlichen Umgebung der magnetischen Bakterien, wie beispielsweise in porösem Sediment, der Vorteil der Wechselwirkung mit dem externen magnetischen Feld liegt. In dieser Arbeit wurde ein modifiziertes „Active Brownian Particle model“ verwendet um mittels Computersimulationen experimentelle Ergebnisse an Bakterien zu reproduzieren, die sich frei, in einer Glaskapillare, oder in anders begrenzten Geometrien bewegen. Ich werde zeigen, dass abhängig von der Schwimmstrategie („run-and-tumble“ oder „run-and-reverse“), aerotaktische Strategie (axial oder polar), und der Feldintensität und Orientierung, das magnetische Feld Chemotaxis beschleunigen kann. Abhängig von dem gewählten Modellsystem kann es jedoch auch zu einer Behinderung der Chemotaxis kommen. Das zweite Beispiel für magnetische Mikroschwimmer sind starre (z.B. Helices) oder zufällig geformte magnetische Propeller. Sie werden durch ein externes magnetisches Feld angetrieben und gelenkt. Hierbei stellt sich die Frage wie die Form der Propeller deren Verhalten beeinflusst und wie sie für eine bestimmte Anwendung optimiert werden können. Daher ist es das Ziel dieser Arbeit Simulationen vorzuschlagen um das experimentell beobachtete Verhalten zu reproduzieren und die magnetischen Eigenschaften der Propeller zu beschreiben. Hierfür wird die Mobilitätsmatrix verwendet um die hydrodynamischen Simulationen zu realisieren. Ein Hauptresultat meiner Arbeit ist eine neue Methode, welche die Simulationen in Einklang mit den experimentellen Resultaten bringt. Hierbei zeigt sich, dass nicht nur die Form sondern insbesondere auch die magnetischen Eigenschaften die Schwimmcharakteristik der Propeller entscheidend beeinflussen.

Abstract

Microswimmers, *i.e.* swimmers of micron size experiencing low Reynolds numbers, have received a great deal of attention in the last years, since many applications are envisioned in medicine and bioremediation. A promising field is the one of magnetic swimmers, since magnetism is biocompatible and could be used to direct or actuate the swimmers. This thesis studies two examples of magnetic microswimmers from a physics point of view.

The first system to be studied are magnetic cells, which can be magnetic biohybrids (a swimming cell coupled with a magnetic synthetic component) or magnetotactic bacteria (naturally occurring bacteria that produce an intracellular chain of magnetic crystals). A magnetic cell can passively interact with external magnetic fields, which can be used for direction. The aim of the thesis is to understand how magnetic cells couple this magnetic interaction to their swimming strategies, mainly how they combine it with chemotaxis (the ability to sense external gradient of chemical species and to bias their walk on these gradients). In particular, one open question addresses the advantage given by these magnetic interactions for the magnetotactic bacteria in a natural environment, such as porous sediments. In the thesis, a modified Active Brownian Particle model is used to perform simulations and to reproduce experimental data for different systems such as bacteria swimming in the bulk, in a capillary or in confined geometries. I will show that magnetic fields speed up chemotaxis under special conditions, depending on parameters such as their swimming strategy (run-and-tumble or run-and-reverse), aerotactic strategy (axial or polar), and magnetic fields (intensities and orientations), but it can also hinder bacterial chemotaxis depending on the system.

The second example of magnetic microswimmer are rigid magnetic propellers such as helices or random-shaped propellers. These propellers are actuated and directed by an external rotating magnetic field. One open question is how shape and magnetic properties influence the propeller behavior; the goal of this research field is to design the best propeller for a given situation. The aim of the thesis is to propose a simulation method to reproduce the behavior of experimentally-realized propellers and to determine their magnetic properties. The hydrodynamic simulations are based on the use of the mobility matrix. As main result, I propose a method to match the experimental data, while showing that not only shape but also the magnetic properties influence the propellers swimming characteristics.

Contents

1	Introduction	1
1.1	Aim of the Thesis	2
1.2	Thesis Outline	2
2	Background Information	3
2.1	Microswimmers	3
2.1.1	Low Reynolds Numbers and Scallop Theorem	3
2.1.2	The Mobility Matrix	4
2.1.3	Brownian Motion Equation and Active Brownian Particles	4
2.1.3.1	The Langevin Equation	5
2.1.3.2	Mean Squared Displacement and Diffusion	6
2.1.3.3	Method of Integration for the Langevin Equation	7
2.1.4	Magnetism for Microswimmers	8
2.1.4.1	Applications for Magnetic Microswimmers	9
2.2	Natural Swimmers	10
2.2.1	Runs and Changes of Direction	10
2.2.2	Taxis	10
2.2.2.1	Chemotaxis of <i>E. coli</i>	11
2.2.2.2	Aerotaxis and Capillary Experiments	11
2.2.3	Magnetotactic Bacteria	12
2.2.4	Sediments	14
2.3	Synthetic Swimmers	15
2.3.1	Helices	15
2.3.2	Non-helical Propellers and Random Shaped propellers	16
2.3.3	Theoretical Description	17
2.3.4	Bead Simulation	19
3	Materials and Methods: Bacterial Swimming	21
3.1	The Theoretical Model	21
3.2	Chemotaxis and Aerotactic Models	22
3.2.1	Axial	22
3.2.2	Polar	22
3.3	Oxygen Integration	23
3.4	Capillary Simulation	23
3.5	Wall Interaction	23
3.5.1	Induced Reverse	24
3.5.2	Weeks-Chandler-Anderson Potential	24

3.6	Sand Sample	25
3.7	MicroCT of Sand	26
3.8	2D Sand Analysis	26
3.9	3D Sand Analysis	26
3.10	Sphere Generation	27
4	Results for Free Swimming Bacteria	28
4.1	Bacterial Motion	28
4.1.1	Tumble	28
4.1.2	Reverse	29
4.1.3	Flick	30
4.2	The Magnetic Torque	31
4.2.1	Alignment Time	31
4.2.2	Alignment Angle	33
4.3	Chemotaxis in Constant Gradients	36
4.3.1	Attractant	36
4.3.1.1	Forces	36
4.3.1.2	Magnetic Torque	37
4.3.2	Preferred Concentration	40
5	Capillary Simulations	42
5.1	Tuning	42
5.1.1	Constant Gradient	42
5.1.2	Dynamic Gradient with 1D Integration	44
5.1.3	Dynamic Gradient with 3D Integration	46
5.2	Axial	47
5.3	Polar	54
5.3.1	Change of Parameters and Comparison Polar and Axial	59
5.4	Alternative Aerotactic Models	61
6	Bacteria In Confinement	63
6.1	Circular Traps	63
6.1.1	Simulations	63
6.2	Bacteria in Sediments	65
6.2.1	2D Experimental Characterization	66
6.2.2	2D Simulation	67
6.2.3	3D Experimental Characterization	71
6.2.4	3D Simulation	73
7	Discussion: Bacterial Swimming Behavior	74
7.1	Tumble vs. Reverse: the Change of Direction	74
7.2	The Aerotactic Models	75
7.3	Advantages in the Use of Magnetic Fields in the Bulk	77
7.4	Confined and Porous Environments	79

8	Materials and Methods: The Synthetic Propellers	81
8.1	The Theoretical Model	81
8.2	The Simulation Algorithm	83
8.3	Approximations	83
8.4	Discretization with Beads	84
8.4.1	Helices	84
8.4.2	Generated Random Propellers	84
8.4.3	Experimental Random Propellers	84
8.5	Inferring the Magnetic Moment from Experimental Data	85
8.5.1	The Cylindrical Approximation	85
8.5.2	Inferring from the Comparison with Simulations	85
8.6	Determining the Step-out Frequency	85
8.7	Reproduce Branching in Simulations	86
9	Synthetic Propellers	87
9.1	Three-beads Propeller	87
9.2	Systematic Study of the Parameters Influence on Helices	89
9.2.1	Helix Regimes for a Perpendicular Magnetization	89
9.2.2	Effect of the Mobility Matrix Approximations	90
9.2.3	Bead Size and Number of Beads per Turn	91
9.2.4	Magnetic Moment Orientation	92
9.2.5	Asynchronous Behavior	95
9.3	Random Propellers	97
9.3.1	Generated by a Growth Algorithm	97
9.3.2	Experimentally Realized Propeller - 1	98
9.3.3	Experimentally Realized Propeller - 2	101
10	Discussion: Magnetic Propellers	104
10.1	Validation of the Model	104
10.2	Features of the Propellers Behavior	105
10.3	Challenges for the Study and Production of Experimental Propellers	106
11	Conclusions and Outlook	107
	List of Figures	109
	List of Tables	112
	Bibliography	115
A	Appendix: Simulation Parameters for Free Bacteria	126
B	Appendix: Mean Squared Displacement for Free Bacteria	127
C	Appendix: Simulation Parameters for Capillaries	130

D	Appendix: Simulation Parameters for Bacteria in Confinement	131
E	Appendix: High Density of Bacteria	132
F	Appendix: Focus Depth for 2D Tracking	133
G	Appendix: Passage Times for 2D simulations	134
H	Appendix: Comparison between Simulated and Experimental Data for MTB in a 2D Porous Environment	136
I	Appendix: Calculating the Mobility Matrix in the Center of Hydrodynamic Mobility	138
J	Appendix: Simulation Parameters for the Helices	140
K	Appendix: Random shaped propellers: the Center of Hydrodynamic Mobility	141
K.1	Propeller 1, 49 beads	141
K.2	Propeller 1, 501 beads	141
K.3	Propeller 2, 55 beads	142
K.4	Propeller 2, 518 beads	142
K.5	Propeller 2, 4276 beads	142

1 Introduction

Swimming is an everyday experience at all the scales of life, from microbes to whales. However, the physics that such diverse swimmers experience is inherently different. Microswimmers, *i. e.* any system (natural or synthetic) capable of swimming in the bulk without the help of any surface at the micron scale, face highly viscous environments. Macroscopic swimmers adopt reciprocal cyclic motions; *e.g.*, a scallop swims opening slowly its valves and closing them fast in a time-invariant reciprocal motion. This kind of strategy doesn't work for microswimmers according to the "scallop theorem" [1]. High viscosity is not the only challenge for microswimmers: they experience thermal noise, which reorients them and makes them lose their intended direction [2].

In recent years, research on microswimmers received a big boost, with many groups studying their biological, physical and applicative properties, for natural swimmers such as bacteria or eukaryotic cells, as well as for man-made synthetic swimmers or for biohybrids featuring a synthetic and biological component [3, 4, 5, 6, 7, 8, 9, 10, 11, 12]. These studies included experimental, theoretical and computational approaches, in which hydrodynamics is usually involved. Why such a great deal of attention for these 'challenging' systems? First of all, natural microswimmers such as pathogenic bacteria impact society; the more is understood on their behavior, the better we can defend ourselves. Secondly, many applications are envisioned for natural, synthetic and biohybrid microswimmers: from biomedical applications such as drug delivery, biofilm or cancer targeting, fertilization, biopsies and others [6, 7, 11, 12], to bioremediation techniques, *i. e.* the possibility of cleaning contaminated soil and waters [13, 14, 15]. For all these applications, the hydrodynamic properties and the general behavior of the microswimmers have to be well understood.

One promising field is the one of magnetic microswimmers. External magnetic fields can be used to guide, activate and image the microswimmers, without being harmful for the body [12]. I thus concentrate on two types of such magnetic microswimmers: magnetotactic bacteria (MTB) and rigid random-shaped synthetic propellers. MTB are a group of bacteria that produce intracellular magnetic crystals usually arranged in a chain, which they use to passively align to the Earth magnetic field in their quest for finding the best place to live [16]. The general idea is that magnetic fields help them in their search, allowing them to perform faster aerotaxis, a special kind of chemotaxis, *i.e.* the ability to sense external gradients of chemical species (in this case, oxygen) and to bias their motion to reach their favored concentration. The coupling between magnetic interaction and chemotaxis becomes particularly important for some envisioned biomedical applications: *e.g.*, magnetotactic bacteria have been recently used as magnetically-guided drug-carriers *in vivo* for the first time [17], managing to target solid tumors in mice. Other magnetic biohybrids could be employed for drug-delivery: for example, recently a magnetic bead was coupled to *E coli*, one of the most studied bacteria, without hindering its motion and chemotaxis [18]. Still, there are many open questions: how does the aerotaxis of magnetotactic bacteria work? How does it couple to the magnetic interaction? Are all the biohybrids performing chemotaxis correctly when interacting with magnetic fields? These questions leads to the necessity of studying such systems from the theoretical, computational and experimental point of view, to fully predict their behavior.

The other system on which I concentrate is a special kind of synthetic microswimmer: random-shaped rigid clusters of magnetic material are produced in the lab, and they can propel if a rotating magnetic field is applied [19, 20, 21]. These rigid clusters are not the first ever magnetic propellers actuated by rotating magnetic fields: rigid helices have also been thoroughly studied in literature [5, 22, 6, 23, 12]. For future applications, new propellers shapes can be designed, outperforming the helices; the use of the random-propellers can help in the search for the best shape that fulfills the required qualities for a certain system (*e.g.*, a particularly fast swimmer, or a swimmer that is activated only at certain frequencies, etc.). For such envisioned designs, it is needed to fully understand the propellers behavior in relation to the shape and the magnetic properties. Theoretical approaches cannot provide a full description for most complicated cases, thus simulations can come in hand.

1.1 Aim of the Thesis

The general aim of the thesis is to model and simulate magnetic microswimmers, both natural and synthetic, and to compare the simulated results to the experimental ones, to test the validity of my assumptions and to provide a predictive frame for future experiments. I am interested in modeling the swimming behavior of magnetic bacteria, including both the magnetic biohybrids based on *E. coli* and natural-occurring magnetotactic bacteria. I aim to understand how their chemotaxis/aerotaxis works and to provide an effective model; moreover, I want to quantify what benefits these swimmers receive from the interaction with magnetic fields, both in lab conditions (as for studies in the bulk or capillary experiments), as well as natural conditions (crowded porous environments as sediments). As for the synthetic swimmers, the aim is to propose a simple method to simulate and reproduce experimentally-realized, random-shaped magnetic-propellers. Specifically, the aim is to understand to what extent the shape, the magnetic moment and the used discretization method influence the swimming capabilities of the propeller, and to investigate scarcely-studied properties such as the change of the sign of velocity, branching, and instabilities after the step-out frequency, underlying the challenges for future custom-designs of magnetic propellers.

1.2 Thesis Outline

The thesis will be divided in the following sections: at first, the background information for both natural and synthetic swimmers will be given (Chapter 2). The thesis is then divided in two main parts: natural and synthetic magnetic microswimmers. For natural microswimmers, the theoretical model, as well as details on the simulation and the analysis process, are given in the Materials and Methods (Chapter 3). The results for magnetic natural swimmers are given in Chapter 4, where I dealt with free swimming bacteria undergoing magnetic interactions and chemotaxis; in Chapter 5, where I reproduced the capillary experiments for magnetotactic bacteria (axial and polar); and in Chapter 6, where magnetotactic bacteria in confinement (in circular traps or in the sand) are considered. A general discussion of the results on the natural magnetic bacteria is drawn in Chapter 7. In the second part of the thesis, I concentrate on synthetic rigid micro-propellers. The theoretical model, as well as details on the simulation procedure are given in Chapter 8. The results are presented in Chapter 9 and are discussed in Chapter 10. Finally, general conclusions on natural and synthetic swimmers are drawn in Chapter 11.

2 Background Information

In this chapter, the background information useful to understand the thesis content will be provided. The state-of-the-art information is given; open questions are highlighted in the view of future discussion (see Chapter 7 and 10). The chapter is divided in general information about microswimmers, followed by a focus first on natural and then on synthetic swimmers.

2.1 Microswimmers

Microswimmers can be defined as 'objects' moving at the microscale, being natural entities like bacteria, algae and eukaryotic cells, as well as synthetic, man-made entities, or even biohybrids featuring a synthetic and a natural component. A swimmer moves in the bulk without the help of walls (no rolling on surface, twitching or glitching is considered in this thesis). Another term used in this thesis is 'propeller': a propeller moves in the bulk, but without shape-deformation, while for a swimmer a certain shape-deformation could happen (for example, the beating of cilia or flagella [24]). A microswimmer experiences different physics laws than a macroscopic swimming object. The main differences are the high viscosity (see 'Low Reynolds Number' Section 2.1.1), and the thermal rotational diffusion (see 'Brownian Motion' Section 2.1.3).

2.1.1 Low Reynolds Numbers and Scallop Theorem

To describe a swimmer, the Reynolds number is used [25, 1]. This number provides the ratio between inertial and viscous forces: $Re = F_{\text{inertial}}/F_{\text{viscous}}$. The viscous force felt by a swimmer is proportional to its dimension a , to its velocity v and to the dynamic viscosity of the fluid η : $F_{\text{viscous}} \propto a\eta v$, while the inertial (apparent) force is given by $F_{\text{inertial}} \propto \rho a^2 v^2$, where ρ is the mass volume density. The Reynolds number becomes:

$$Re = \rho a v / \eta.$$

A low Reynolds number (<1) indicates that the viscosity prevails over the inertia: as a consequence, when a swimmer ceases to actively propel, the drift immediately stops [2] (while it can still undergo thermal Brownian motion, see Section 2.1.3). For a bacterium of typical size $a \sim 1 \mu\text{m}$, velocity of $10 \mu\text{s}^{-1}$, density 1 g cm^{-3} , moving in water ($\eta \sim 0.01 \text{ Pas}$), the Reynolds number becomes $\sim 10^{-5}$ [2]. In general, the microswimmers live at low Reynolds number. Using low Reynolds numbers, thus neglecting the inertia term, the Navier-Stokes equations become the Stokes Equation [2, 26, 1, 27, 12]:

$$\eta \nabla^2 \mathbf{u} + \mathbf{f} = \nabla p, \quad \nabla \cdot \mathbf{u} = 0, \quad (2.1)$$

with \mathbf{u} being the fluid velocity vector field and p the fluid pressure, and \mathbf{f} being an external force density. $\nabla \cdot \mathbf{u} = 0$ comes from the fluid incompressibility condition applied to the fluid continuity

equation. The Stokes equation does not depend on time and is linear. The fluid undergoes only laminar flow; moreover, time reversals do not change the equation. This means that a swimmer cannot propel through a reciprocal motion, *i.e.* a motion that presents an identical pattern if the time is reversed: this is the so-called Scallop theorem [1]. To move, a pattern that is not reciprocal in time must be adopted. For natural swimmers, the beating of a cilium or the rotation of a helical flagellum satisfies this requirement [1]; for synthetic helical swimmers, a screw-like motion also satisfies this theorem [1].

2.1.2 The Mobility Matrix

Since the Stokes equation is linear, linear relationships can be written between externally applied forces \mathbf{F} and torques \mathbf{T} , and the swimmer's velocity \mathbf{v} and frequency $\boldsymbol{\omega}$ [1, 26, 27, 28, 12]. The matrix responsible for this linear relationship is the mobility matrix \mathbf{M}_{CM} :

$$\begin{pmatrix} \mathbf{v} \\ \boldsymbol{\omega} \end{pmatrix} = \mathbf{M}_{\text{CM}} \begin{pmatrix} \mathbf{F} \\ \mathbf{T} \end{pmatrix}. \quad (2.2)$$

It can be divided in four sub-matrices:

$$\mathbf{M}_{\text{CM}} = \begin{pmatrix} \mathbf{M}^{\text{tt}} & \mathbf{M}^{\text{tr}} \\ \mathbf{M}^{\text{rt}} & \mathbf{M}^{\text{rr}} \end{pmatrix}, \quad (2.3)$$

where the upper index t stands for translational and r for rotational. The matrix is symmetrical, with $\mathbf{M}^{\text{tr}} = (\mathbf{M}^{\text{rt}})^T$. To have a net translation $v \neq 0$ caused only by the torque \mathbf{T} (thus only by the rotation of the swimmer), the \mathbf{M}^{tr} should be non-zero. A screw propels thanks to a non-zero rotational-translation term. The flagellum of the bacteria presents a screw-like shape when rotating [1]; many synthetic swimmers base their motion on screws [12]. In general, to have motion, a certain degree of asymmetry should be present in the swimmer [29, 30]. Often, the asymmetry is given by a certain achirality of the object, as it happens for a screw. However, also symmetrical-achiral-shaped propellers move under certain conditions [29, 31, 30]. I will discuss this point further in the Synthetic propeller Section 2.3, as well as in the Result Chapter 9. The mobility matrix can be easily derived for spheres, as it is discussed in the Background Section 2.3.4 and in the Method Section 8. The terms of the matrix will depend on the translational and rotational mobility coefficients of a sphere μ^t , μ^r , given by the inverse of the translational and rotational friction coefficients of a sphere [2]:

$$\gamma_t = 6\pi\eta a = (\mu^t)^{-1}; \gamma_r = 8\pi\eta a^3 = (\mu^r)^{-1}, \quad (2.4)$$

where η is the dynamic water viscosity and a the radius of the sphere.

2.1.3 Brownian Motion Equation and Active Brownian Particles

Another important feature in the microswimmers world is the thermal brownian noise. Microswimmers can be considered as colloidal particles immerse in a fluid. The dimension of the particle is much bigger than the dimension of the fluid particles, therefore we can consider the fluid as a continuum; this is what allowed us to use the equations in Section 2.1.2. Still, the size of

the microswimmers is not big enough to completely ignore the influence of the fluid particles collisions that takes place due to the thermal agitation. Due to these collisions, the colloid/swimmer feels a thermal noise and experiences a noise-induced translational and rotational motion. While for a microswimmer (such as a bacterium) the translational motion due to noise can be irrelevant [2, 12], the rotational motion is of major importance. A bacterium that wants to swim straight would lose its orientation after few seconds: the characteristic reorientation time is [32]:

$$\tau_{\text{rot.diffusion}} = \frac{\gamma_r}{k_B T} \quad (2.5)$$

where γ_r is the rotational friction coefficient, T is the temperature and k_B is the Boltzmann constant. This characteristic time emerges from the Langevin equation and from the diffusion constant.

2.1.3.1 The Langevin Equation

The Langevin equation describes the motion of a single colloid that feels thermal motion. Here, I show how to derive the equation for 1D and for the translational motion [33]. The rotational motion derivation is completely equivalent. To go to three dimensions, 3 degrees of freedom should be considered when writing the energy of the system (equipartition theorem), but the rest of the derivation remains unchanged. To start, we should consider a particle that does not feel thermal noise. Its equation of motion is obtained considering the friction force:

$$m\dot{v} + \gamma_t v = 0, \quad (2.6)$$

where v is the velocity, \dot{v} is the acceleration, t is the time, and γ_t is the translational friction coefficient; the solution of the equation is $v(t) = v(0)e^{-t\gamma_t/m}$. If now the colloid feels thermal noise, we know from the equipartition law that the mean energy is $\frac{1}{2}m\langle v^2 \rangle = \frac{1}{2}k_B T$. To obtain this correct energy, an additional fluctuating noise force F_f should be added to the equation of motion, which then becomes

$$\dot{v} + (\gamma_t/m)v = F_f/m. \quad (2.7)$$

When we average this equation on an ensemble, the mean velocity should follow the equation 2.6 for a particle without noise. Thus the fluctuating force should have the following property:

$$\langle F_f \rangle = 0. \quad (2.8)$$

Moreover, we could make the assumption that the fluctuating forces (given by the collisions) calculated at different times are uncorrelated, if the times differ more than the average collision time τ_0 : $\langle F_f(t)F_f(t') \rangle = 0$, $|t - t'| > \tau_0$; this is true since the collisions are in good approximation independent between each others. Taking this collision time to be zero, we obtain:

$$\langle F_f(t)F_f(t') \rangle = q\delta(t - t'). \quad (2.9)$$

The final step is to determine the proportionality constant q . It can be proven by substitution that a formal solution of the Langevin equation 2.7 is:

$$v = v(0)e^{-\frac{\gamma_t}{m}t} + \int_0^t e^{-\frac{\gamma_t}{m}(t-t')} \frac{F_f(t')}{m} dt'. \quad (2.10)$$

From this, it can be derived that, at large times, $\langle v^2(t) \rangle = \frac{q}{2m\gamma_t}$. Using this expression, and equating the average kinetic energy of the particle to the thermal energy, we obtain:

$$\langle E \rangle = \frac{1}{2}k_B T = \frac{1}{2}m \frac{q}{2m\gamma_t} \quad (2.11)$$

from which we finally determine q :

$$q = 2\gamma_t k_B T. \quad (2.12)$$

In n dimensions, the formula becomes $q = 2n\gamma_t k_B T$. For our microswimmers, the inertia is negligible $m \sim 0$, so Equation 2.7 becomes $\gamma_t v(t) = F_t$. If the colloid is actively swimming, it is defined as Active Brownian Particle (ABP), and a term for self propulsion should be included; considering a constant velocity v_{self} , the equation becomes $\gamma_t \frac{dx}{dt} = \gamma_t v_{\text{self}} + F_t$. If external forces are acting on the colloid, then equating all the forces gives the equation $\gamma_t \frac{dx}{dt} = \gamma_t v_{\text{self}} + F_{\text{ext}} + F_t$. Writing the equation in three dimensions, we obtain the final formula that I will use throughout thesis to describe natural swimmers (see Chapter 3):

$$\gamma_t \frac{d\mathbf{r}}{dt} = \gamma_t v_{\text{self}} \mathbf{e} + \mathbf{F}_{\text{ext}} + \mathbf{F}_t, \quad (2.13)$$

with \mathbf{e} the orientation unitary vector of the colloid. With our definition, now $q = 6\gamma_t k_B T$, thanks to the equipartition law for three degrees of freedom. Equivalent derivation can be done for the equation for the rotational motion:

$$\gamma_r \frac{d\mathbf{e}}{dt} = [\mathbf{T}_{\text{ext}} + \mathbf{T}_t] \times \mathbf{e}, \quad (2.14)$$

where \mathbf{T}_t , \mathbf{T}_{ext} are respectively the fluctuating torque and the external torque. ABP models are commonly used to describe the motion of microswimmers, both for natural and synthetic swimmers [34, 35]; the advantage of these equation (with respect to the Fokker-Planck equation) is that they allow to resolve the dynamics of each single object [27].

2.1.3.2 Mean Squared Displacement and Diffusion

A useful quantity to distinguish between random motion, self propulsion or trapping is the Mean Squared Displacement (MSD). For a Brownian particle in n dimensions with $\mathbf{v} = 0$ and for large times, it can be shown that [33]:

$$MSD = \langle (\mathbf{r}(t) - \mathbf{r}(0))^2 \rangle = \langle \Delta \mathbf{r}^2 \rangle = 2nDt, \quad D := \frac{k_B T}{\gamma_t}, \quad (2.15)$$

where D is the translational diffusion coefficient. Equivalently, it can be shown that the typical re-orientation angle is given by $\langle \theta^2 \rangle \sim 6D_r t$, with $D_r := \frac{k_B T}{\gamma_r}$. The inverse of D_r gives the characteristic time scale for the rotational brownian motion of Equation 2.5.

To check if a swimmer is undergoing Brownian motion, the standard procedure is to plot the natural logarithm of the MSD versus the natural logarithm of time. From Equation 2.15, $\ln(MSD) = \ln(2nD) + \ln(t)$, so if the plot is linear with slope 1, then the swimmer is purely Brownian and the diffusion constant can be determined from the intercept of the linear fit. If instead the

slope is 2, the swimmer is purely active with no Brownian motion: for active propulsion, $x = vt$ thus $MSD \sim x^2 = v^2 t^2$, and $\ln(MSD) \sim 2\ln(t) + \ln(v^2)$. For an Active Brownian Particle more regimes can be identified in the MSD: at small times (depending on the particle size and velocity) a Brownian regime can be seen, followed by a slope of 2 caused by the active propulsion; at large times, thermal rotational diffusion randomizes the direction and the slope becomes 1 again. If the swimmer makes active changes of directions or if the dynamics is complicated by external forces, chemotaxis and wall interactions, the MSD changes [2, 36]. See the Appendix B for more details.

In general, the diffusion constant is used to describe diffusion processes. As we saw from the mean squared displacement, Brownian particles undergo diffusion. In this thesis I am also interested in the diffusion of chemicals in water, in particular of oxygen. The time-evolution equation describing diffusion of a certain chemical compound with concentration $C(t, \mathbf{r})$ is the so called second Ficks law [2]:

$$\frac{\partial C(t, \mathbf{r})}{\partial t} = D \nabla^2 C(t, \mathbf{r}), \quad (2.16)$$

where D is the diffusion constant of the diffusing chemical. The solutions of the equation varies according to the boundary conditions. In the thesis, these equations will be used to calculate the oxygen flow in a capillary, therefore they will be solved numerically, without the need of an analytical solution.

2.1.3.3 Method of Integration for the Langevin Equation

In the thesis, I want to numerically integrate the Langevin equations for an active Brownian particle 2.13. The deterministic term is trivial to integrate (for example with a simple Euler method or Runge Kutta methods [37]). Since I want to numerically solve the equations with an Euler method, I am interested in the increments $\Delta \mathbf{r}$, that for a deterministic particle are:

$$\Delta \mathbf{r} = v_{\text{self}} \mathbf{e} \Delta t + F_{\text{ext}} \gamma_t^{-1} \Delta t. \quad (2.17)$$

The increments $\Delta \tilde{\mathbf{r}}$ that are given by the thermal noise and that contribute to the total displacement $\Delta \mathbf{r}$ should also be added. This increment has to satisfy Equation 2.15. Then, we can define a Wiener process $W(t)$ [33, 27], which is a Gaussian variable with zero mean $\langle W(t) \rangle = 0$ and time correlation $\langle W(t)W(t') \rangle = \min(t, t')$. Its increments are Gaussian variables satisfying $\langle \Delta W \rangle = 0$, $\langle \Delta W^2 \rangle = \Delta t$. According to this relation, $\Delta W = \sqrt{\Delta t}$. Then, the increment due to the noise can be rewritten such as:

$$\Delta \tilde{\mathbf{r}} = H \cdot \Delta \mathbf{W}, \quad (2.18)$$

where \mathbf{W} is a vector of n independent Wiener increments, and H is a matrix. To satisfy Equation 2.15, it must be:

$$H \cdot H^T = 2nD. \quad (2.19)$$

In a naive vision, we can simply add $\Delta \tilde{\mathbf{r}} = \Delta \mathbf{W} H = \boldsymbol{\xi} \sqrt{2nD\Delta t}$ to the deterministic part, where now $\boldsymbol{\xi}$ is a vector of n Gaussian distributed numbers and $\Delta \mathbf{W} = \boldsymbol{\xi} \sqrt{\Delta t}$. The total displacement would become:

$$\Delta \mathbf{r} = v_{\text{self}} \mathbf{e} \Delta t + F_{\text{ext}} \gamma_t^{-1} \Delta t + \boldsymbol{\xi} \sqrt{2nD\Delta t}. \quad (2.20)$$

This is actually the final result that will be used throughout the thesis (and a similar equation holds for the rotational motion); nevertheless, two considerations should be done [27]: First of

all, technically dW/dt does not exist, due to the properties of the Wiener process and of the white noise. In fact, $\Delta W/\Delta t = 1/\sqrt{\Delta t}$ diverges for the limit $\Delta t \rightarrow 0$, used to define derivatives. This means that actually, Equation 2.13 has no meaning if it is interpreted as a differential equation. The only sense that we can attribute to it is if we rewrite it as a stochastic integral, and use the Itô interpretation; secondly, the differential of the stochastic integral for the noise term is given by $d\mathbf{r} = [(k_B T)^{-1} D \cdot \mathbf{F} + \partial_{\mathbf{r}} \cdot D]dt + \mathbf{H} \cdot d\mathbf{W}$ [27]. For a sphere (which was used in this thesis to describe an Active Brownian Particle), D is a constant in space; as a consequence, the spacial derivative disappears, and we obtain our naive Equation 2.20, that can be integrated through an Euler step.

2.1.4 Magnetism for Microswimmers

In this thesis I concentrate on magnetic microswimmers, meaning microswimmers that possess a magnetic moment \mathbf{M} . This magnetic moment reacts to external magnetic field (denoted by the symbol \mathbf{B} and measured in Tesla) through the force \mathbf{F} and the torque \mathbf{T} :

$$\mathbf{F} = M\nabla\mathbf{B}, \quad \mathbf{T} = \mathbf{M} \times \mathbf{B}, \quad (2.21)$$

where $\nabla\mathbf{B}$ indicates the spacial gradient of the magnetic field. With a gradient field $\nabla\mathbf{B} \neq 0$, magnetic objects feel a dragging force; however, the velocity achieved in this way over long distances is lower than any other activation methods such as rotating magnetic fields or oscillating fields [38]. Oscillating magnetic fields can be also used to activate deformable synthetic magnetic swimmers [12].

For a homogeneous non-oscillating field, as it will be used in the thesis, the force is reduced to 0 and only the torque survives. The torque can be used in two separate ways: for alignment/direction purposes or for activation purposes. As for the first point, magnetic fields can be used to direct the swimmer through passive alignment, thanks to the torque, as it happens for magnetotactic bacteria, magnetic biohybrids or other synthetic magnetic swimmers [12]. The typical time-scale of the alignment to a magnetic field is given by $\tilde{\tau} = \gamma_r(MB)^{-1}$ [32] (see derivation in Chapter 4), where γ_r is the rotational friction constant. For systems in which thermal fluctuation is present, there will be a competition between this alignment time-scale and the rotational diffusion time-scale $\tau_{\text{rot.diffusion}} = \gamma_r k_B^{-1} T^{-1}$ [32] (see Chapter 4). As for the second point, these magnetic fields can be used also to activate a rigid magnetic propeller: If the magnetic field rotates, also the propeller rotates thanks to the torque, trying to follow the field. If the shape of the propeller is suitable, the mobility matrix presents a coupling between rotation and translation, thus the propeller swims.

To maximize the interaction with these external magnetic fields, the microswimmers should possess a strong, permanent magnetic moment. One way would be to possess a magnetic element that is ferromagnetic and in the single magnetic domain. In ferromagnetism, the material possess a permanent net magnetic moment even in the absence of external magnetic fields, thanks to the internal alignment of the electron spins. When the spins are all directed in the same way, it is defined as single domain; this can happen at small sizes, depending on the material. If the size increases, more domains are formed, each of them with all the spins internally aligned (Figure 2.1) [39, 12]. Few elements are ferromagnetic, among them the iron.

Magnetic fields can be exerted on the microswimmers in the lab with the use of coils and permanent magnets, to control them [12]. In Nature magnetotactic bacteria exploit the Earth

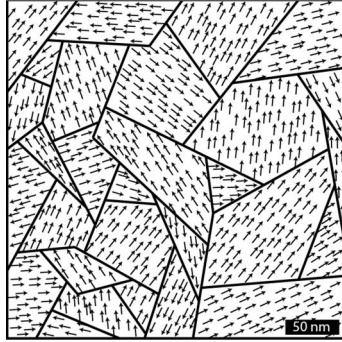


Figure 2.1: Spin domains in a ferromagnetic materials. Reproduced with permission from [12], Rightslink order number 4404770362545.

magnetic field for direction purposes [16] (see Section 2.2.3 for more details). The Earth possess a magnetic field, with the magnetic South pole being close to the geographic North pole and *viceversa*. The Earth magnetic field lines are thus entering in the North geographic pole, pointing downwards with respect to the ground. The actual inclination I of the field lines depends on the latitude θ : $\tan(I) = 2 \tan \theta$ [32]. For example, in Berlin the angle between the vertical to the ground and the Earth field lines is of 23° [40]. The strength of the Earth magnetic field is in good approximation $50\mu\text{T}$.

2.1.4.1 Applications for Magnetic Microswimmers

Magnetic microswimmers can find application in the biomedical field, mainly for tumor and biofilms targeting, biopses and drug delivering [3, 41, 12, 42]. Magnetism helps directing, actuating and imaging the swimmers once inside the body. The main advantage of using magnetic field consists in their biocompatibility and in their ability to penetrate in the human body [12]. To achieve drug-delivery, biohybrids can be employed: they consist of a biological component (mainly a cell) and a synthetic part (the drugs themselves and/or a magnetic synthetic component). Such a biohybrid exploits the motility and sensing mechanisms of a cell, while it could take advantage of the magnetic component given by the synthetic part for directionality purposes. Some remarkable examples include magnetotactic bacteria functionalized with drug-filled liposomes used *in vivo* for cancer targeting in mice [17]; *E. coli* biohybrids in which an external magnetic bead is attached to the cell body, without hindering its motion [18]; sperm-cells attached to a magnetic tube used to direct them for fertilization purposes [7, 43]; and biohybrids based on magnetotactic bacteria inserted in tubes for biofilm targeting [41]. Also synthetic swimmers could be employed once functionalized as drug carriers [12], with the main advantage being the higher resistance to cell-prohibitive environments.

2.2 Natural Swimmers

In this section, I will present the state-of-the-art information regarding natural microswimmers, more specifically about bacteria. Motile bacteria can be swimmers, *i.e.* that self-propel in the bulk, or they could possess gliding/twitching motility, where they need a surface to move [44]. In the thesis, I will deal with swimmers only. Bacteria, whose typical size ranges between $0.5\ \mu\text{m}$ and $4\ \mu\text{m}$ (but with exceptions up to $600\ \mu\text{m}$) [44], can achieve swimming velocities of several body lengths per second, 30 or more [12]. The model organism *E. coli* reaches velocities of $14.2\ \mu\text{ms}^{-1}$ [45]. Bacterial swimming-motility is usually achieved by the use of one or more flagella, an helical organelle protruded from the cell-body, which is several micrometers long and is $20\ \text{nm}$ in diameter [44, 24]. The flagella can rotate in a screw-like fashion and thus propel onward/backward the bacterium [44]. The flagellum is rotated by a motor, activated by the proton motive force. The motor can undergo a switch that enables the flagellum to rotate in the opposite direction [44].

2.2.1 Runs and Changes of Direction

The flagella are not only used for propulsion, but also for an active change of direction. Different species show different behaviors. For example, peritrichous bacteria (*i.e.* with many flagella at random positions on one side of the cell, like *E. coli*) present a counter-clock-wise rotation (CCW) of the bundle during runs; the change of direction is achieved during tumbles, when the motor rotate clock-wise (CW), the bundle opens and stops and reorients the bacterium (for *E. coli*, the mean re-orientation angles is of 68° and the mean tumble time of $0.14\ \text{s}$) [46, 44, 45, 47]. This type of motion is called run-and-tumble. The run and the changes of direction are alternated and they are exponentially distributed, with a mean run time for *E. coli* of $0.86\ \text{s}$. For bacteria that possess polar flagellation (*i.e.* when one or two flagella are attached to one or both ends of the cell [44, 46]), one possible configuration is the following: the flagellum rotates CCW propelling the bacterium onward (pusher), and can rotate CW propelling the bacterium backward (puller configuration). The direction change is thus obtained by a reversal event, with the bacterium changing the sign of the velocity thanks to the change in the flagella-rotation, but not the body orientation. In general, the type of motion for which the bacterium changes velocity sign without reorientation of the body is called run-and-reverse. For polar-flagellated bacteria, it could also happen that the flagellum always rotate CW in pusher configuration, and the change of direction is given by a reorientation of the body [44]. More complex models can also be found [48], where the swimming velocity differs between before and after the reversal event.

2.2.2 Taxis

The change of direction is essential for the bacterial life: in fact, bacteria need a steering mechanism that allows them to bias their motion in a desired direction [2]. In other words, they need the change of direction to perform taxis, *i.e.* the ability of sensing physical or chemical gradients and responding to these gradient, moving towards the preferred chemical concentration/physical condition. Different types of taxis can be distinguished: chemotaxis towards an attractant (the bacteria swim towards the maximum of the chemical concentration), chemotaxis away from a repellent (the bacteria flee away from the chemical), aerotaxis (taxis for oxygen), osmotaxis (for high ionic strength), phototaxis (for light), gravitaxis (for gravity) and so on [44, 49, 50, 51, 2, 52, 53, 54].

2.2.2.1 Chemotaxis of *E. coli*

The most well studied bacterium performing chemotaxis is *E. coli*, a rod-shaped bacterium adapted to live in the gut of warm-blooded animals. It swims with a run-and-tumble motion. 3D tracking in the bulk allowed to obtain accurate statistics regarding its swimming behavior, such as length of the runs, angle of the tumbling events, bias towards attractants and repellents [45, 2, 55, 56, 57, 58, 59]. It was shown that *E. coli* performs chemotaxis making longer runs towards the preferred concentrations, thus diminishing the frequencies of the tumbles. To sense a certain concentration, the bacterium uses membrane receptors that once occupied by the molecules, provoke a cascade of signals that influence the sense of rotation of the motor [44, 55, 56, 59]. The cell is too small to sense a spacial difference in concentration between the 'head' and the 'tail' of the body (usually, the length is of $2\ \mu\text{m}$ and of $1\ \mu\text{m}$ in diameter); thus, the only way it could sense a gradient is comparing the present concentration with the one it sensed before, which is stored in a memory (up to 3 s) [44, 2, 60, 56, 61, 62, 49, 54, 63]. Therefore, the bacterium uses a temporal gradient to bias its walk. The classical model to describe chemotaxis is the Keller-Segel model (KS) [60], which was subsequently adapted and modified [64]. The KS model proposes a mean-field approach, where the bacteria are described by a density function, while their reversal frequency depends on the chemical concentration; chemotaxis itself is described as a diffusion process. KS models propose a complementary approach compared to Active Brownian Particles models (ABP), where the bacteria are described as individuals [65]. Taxis can also be achieved by modulating the velocity instead of/together with the change in the run lengths; this process is known as chemokinesis [66], and was *e.g.* reported for *E. coli* in response to osmotic changes [67].

In this work, chemotaxis is achieved through modulation of the run times. An effective description of the sensing process is used: the run times are a function of the spacial chemical gradient, instead that being determined by time-comparisons of the concentration. This description is equivalent to the temporal comparison of concentrations, once the correct response function (connecting run times to the spacial gradient) is known. The response function was chosen to be a simple linear function or a step-function; in fact, my goal is to describe aerotaxis for magnetotactic bacteria, for which the response function has not been determined experimentally so far.

2.2.2.2 Aerotaxis and Capillary Experiments

Aerotaxis is a special kind of chemotaxis for oxygen, also cataloged as energy taxis [44, 68]. It was first discovered in 1881 when it was shown that bacteria could accumulate around an air bubble [68]. A model organism used for aerotaxis study is *Azospirillum brasilense*, whose length is of $1\text{--}2\ \mu\text{m}$ with a single polar flagellum [69, 68]. These bacteria seek for the optimal oxygen concentration that favors their growth and metabolism, fleeing from too high or too low concentration. In the meanwhile, bacteria do also consume the oxygen, modifying the concentration profile and the preferred concentration position.

The classic experiment to study aerotaxis is the capillary assay [69, 68], illustrated in Figure 2.2. A glass capillary is filled with medium and bacteria; only one end is open and is able to exchange oxygen with the air. Oxygen diffuses into the capillary, forming a gradient. The gradient is also influenced by the consumption of the bacteria. The bacteria perform aerotaxis and accumulate in a band at high density at the preferred oxygen concentration. The side exposed to the air interface, with the concentration higher than the preferred one, is defined as the oxic side, while anoxic side



Figure 2.2: Capillary-experiment set-up: a capillary is closed on the right side, while it is left open on the left side. The oxygen flows inside, forming a gradient. The bacteria perform aerotaxis and accumulate in a band. The side exposed to oxygen is called oxic, the other is called anoxic.

is the one where the concentration is lower than the preferred one. In a classic experiment, the band position over time can be recorded, as well as its size and shape. The bacteria can also be individually tracked to obtain the statistics of their run times and biased motion.

2.2.3 Magnetotactic Bacteria

One main focus of this thesis are the magnetotactic bacteria (MTB). Magnetotactic bacteria include many species, but essentially all share a common feature: the cell produces an intra-cellular assembly (often a chain) of magnetosomes, *i.e.* organelles made of a membrane containing magnetite Fe_3O_4 nano-crystals (or alternatively, of greigite Fe_3S_4 crystals) [16, 32, 70, 71]. The crystals are ferromagnetic, in single domain with a permanent dipole [72]. The magnetosomes are connected to a MamK-protein filament, forming a chain with a total magnetic moment. The filament is rigidly connected to the cell body; in good approximation, it is parallel to the main axis of the cell and thus to its swimming direction. When an external magnetic field is applied, the cell will rotate as a whole to passively align to the magnetic field. For the model species *Magnetospirillum gryphiswaldense* MSR-1, a typical number of magnetosomes is 20 [32, 72], with a typical size of 40-50 nm [32], a mean magnetization per particle of $3.1 \times 10^{-5} \text{ A}\mu\text{m}^2$ [72], resulting in a total magnetic moment of $\sim 0.6 \times 10^{-3} \text{ A}\mu\text{m}^2$ [72, 73, 74, 75].

These bacteria present many flagella configuration, depending on the species. The most studied species, on which I based my model, is MSR-1, a spirillum of 3-5 μm in length [76] that presents a flagellum at each end of the body. The bacterium performs run-and-reverse motion. No data is available on the configuration of its flagella during motion, but for *Magnetospirillum magneticum* AMB-1, a close relative, it was demonstrated [77] that while the back flagellum rotates being extended at the back of the body, the front flagellum folds itself along the body, in what it is called a "parachute" configuration. A reverse happens when the direction of motion is inverted, the front flagellum becomes the back flagellum, extending and rotating, and the back flagellum becomes the front one in the parachute position. A tumble-like event was also observed with minor frequency, in which both flagella are extended or in the parachute position, and rotate simultaneously. Magnetotactic bacteria swimming characteristics have been studied through 2D tracking [78], thus introducing an error in the mean reversal angle due to the 2D projection. Velocities for MSR-1 were reported to be around $20 \mu\text{ms}^{-1}$ [78], with a mean reversal angle of $\sim 170^\circ$ [78], and a pause time during the reversal event of $\sim 0.14 \text{ s}$ [78].

Magnetotactic bacteria are known to perform magnetically-assisted aerotaxis, the so-called magnetotaxis [16]. The general idea is that they perform aerotaxis, while passively aligning to the Earth magnetic fields. The preferred concentration is low but not zero (the bacteria are micro-aerophilic) [16, 78, 79]. Aerotaxis can be studied through 2D tracking and by the capillary assay.

Using 2D tracking, Popp *et al.* [80] reported the run times in the presence of oxygen, an impor-

tant parameter to understand aerotaxis. An increase in the switching rate ($\sim 0.35 \text{ s}^{-1}$) was observed upon sudden injection of oxygen in an anoxic medium. This injection can be interpreted in the following way: the bacteria feel an oxygen gradient, thus performing aerotaxis to run away from too high oxygen. After a while, the bacterium feels that the condition are purely oxic again, with no gradient, and the switching rate drops off to a minimum value ($\sim 0.05 \text{ s}^{-1}$), comparable to the basal value the bacteria had in the pure anoxic condition at the beginning of the experiment ($\sim 0.1 \text{ s}^{-1}$). As useful these data can be, they lack a complete description since they provide the run times only for pure oxic and pure anoxic conditions, and for bacteria swimming towards a high oxygen concentration in a steep gradient. To properly understand aerotaxis, a complete data-set would include the biased run-times towards and away from the preferred concentration in a gradient, on both the oxic and anoxic sides. Lacking this information, we can only assume that magneto-aerotaxis works as normal aerotaxis, and thus as *E. coli* chemotaxis, with longer runs towards the preferred concentration and shorter runs away from it [16]: the oxygen behaves as repellent if the bacteria experience a concentration higher than the preferred one, or as attractant, for concentration lower than the preferred one. This type of magneto-aerotaxis, where the bacterium performs normal aerotaxis biasing their walk on the oxygen gradient and the absolute concentration, while passively aligning to an external magnetic field, is called axial [16]. The magnetic field is thus reduced in this case to a pure axis of direction. A bacterium in pure oxic or anoxic conditions, would swim in both directions of the magnetic field axis, without a preferred one. In a capillary experiment, axial bacteria would form an aerotactic band even without the need of a magnetic field, and if a magnetic field is present, they would form the band for parallel and antiparallel fields as well [78, 79].

Magnetoaerotaxis can also be studied through capillary experiments, for which it was shown that more complicated behaviors can be spotted in various species: In particular, the polar behavior or mixed polar/axial behaviors [78, 79]. While axial bacteria substantially do not care about the magnetic field orientation, polar bacteria are biasing their aerotaxis on it. In fact, they use the magnetic field not only as an axis (thanks to the passive alignment), but also as a direction. Bacteria found in the Northern hemisphere are called North Seeking (NS), since they move predominantly North when in oxic condition and South when in anoxic. Bacteria from the Southern hemisphere do the opposite and are called South Seeking. When polar NS bacteria are used for a capillary experiment, they form a band only if the magnetic field is antiparallel to the oxygen gradient, with North pointing towards the anoxic side. If the field is reversed by 180° , the band splits up and disappears [78, 79]. However, NS bacteria could be found in small percentage in the South pole, where the magnetic field lines are parallel to the oxygen gradient in the natural water environment of the bacteria [32, 81]. No data has been reported in literature for the formation of the band in the absence of magnetic fields, nor for magnetic fields at 90° with respect to the oxygen gradient. However, polar magnetotactic bacteria can be found at the Equator, where the magnetic field is at nearly 90° with respect to the oxygen gradient [32, 82, 83].

Frankel [16] proposed a two state sensory mechanism to explain polarity for a bacterium with one flagellum: the magnetic moment is directed as the bacterium main axis, with the flagellum lagging behind at the South Pole. The chain would passively align to the magnetic field, with the flagellum always oriented towards South. In the oxic side, the bacterium would swim CCW in pusher mode, thus propelling towards North; as soon as it reaches the anoxic side, the flagellum is inverted in CW rotation, going in puller mode with the body following the flagellum and thus with a velocity directed towards South. This simplistic model cannot be completely true, since

reversal (even if highly suppressed) have been observed in both oxic and anoxic conditions [80]. Therefore, the model used in this thesis incorporates switches in both oxic and anoxic conditions, with longer runs towards the preferred concentration and shorter runs away (see Section 3.1 for details on the model, and Section 7 for a discussion).

Aerotaxis is not the only effect of the oxygen gradient on MTB motion. In fact, chemokinesis (*i.e.* the ability of changing swimming speed based on a chemical gradient) was reported for MSR-1 [78]. On the oxic side of the band the velocity is $22.3 \pm 1.1 \mu\text{ms}^{-1}$, while on the anoxic $15.7 \pm 0.6 \mu\text{ms}^{-1}$. I will verify that chemokinesis does not influence my model in Chapter 5.

One of the open questions is why it is beneficial for magnetotactic bacteria to spend energy and resources to produce a magnetic chain. The general idea is that in this way they can facilitate aerotaxis in Nature, where the oxygen gradient is directed upwards in the lakes and seas where the bacteria live, while the magnetic field in the North Hemisphere at high latitudes is in good approximation antiparallel to it (in truth, the angle between magnetic field and vertical to the ground depends on the latitude [32]). The motion would then be restricted in 1D along the gradient itself thanks to the magnetic field passive alignment, speeding up the chemotaxis up towards the preferred concentration that is situated at the bottom [16]. However, the weak Earth Magnetic field of $50 \mu\text{T}$ is not strong enough to overcome totally the thermal fluctuation. As a consequence, the trajectories of the bacteria are not purely 1D, but rather follow a general direction given by the magnetic field lines. In this thesis, I aim to quantify the effect of the magnetic field on chemotaxis at the micrometer scale, expanding previous results [84, 78].

2.2.4 Sediments

To fully understand the behavior of the magnetotactic bacteria, the real natural environment should be taken into account: magnetotactic bacteria live in the oxic-anoxic transition zone (OATZ), usually situated in the first layer of sediments at the bottom of lake and seas [16, 85]. This means that studying bacteria in the bulk is not enough, and porous environment should be considered. Moreover, the study of bacteria in porous environments could be useful also for future biomedical applications, where bio-hybrids would swim in an highly complex environment such as the circulatory system, solid tumors and tissues.

Active Brownian Particles in porous, crowded environments have been studied in literature from the theoretical, computational and experimental point of view [86, 87, 35, 88, 36, 89]; full-hydrodynamic description of bacteria in confined geometries have been also proposed [90]. Many studies focused on the theoretical, computational and experimental aspects of bacteria in soil and in porous media [91, 92, 13, 93, 94, 95, 96, 97]. In general, what can be concluded is that the porous medium changes the dynamics, inducing changes of directions (the very long run times that were observed in the bulk for MTB [80] would be hindered by the interaction with obstacles, changing the actuation of chemotaxis) and modifying the diffusivity of the bacteria.

Usually magnetotactic bacteria in sediments are studied from a 'macroscopic' point of view, meaning that they are studied in a microcosmos of sediments, from which their position is sampled at different heights [85, 98, 99, 100]. Imaging the bacteria in the real sediments at the micrometer scale is impossible due to the grains of sand that would block the data acquisition. An alternative approach is to reduce the system in two dimensions; to do so, microfluidic devices could be employed that resemble the soil or a crowded environment and that reduce the motion in quasi-2D, allowing the imaging [101, 102]. Recently, this approach was adopted for the study of magne-

totactic bacteria [103]. The pillars used to represent the sand were equally spaced; this could introduce artifacts in the dynamics. Moreover, it was not paid attention at the oxygen levels, thus not excluding aerotactic influences. In another study [104], the interaction with walls of the MTB was considered to tune the hydrodynamics; however, they did not study porous environments.

For a more complete approach, a characterization of the real sediments has to be performed; in this way, the statistics of a real environment are exploited for the production of microfluidic channels closer to the reality than a regular array of pillars. To study the sediments and gain information on grain sizes and water-gaps, a MicroCT can be employed [105, 106, 107]. MicroCT stands for Micro Computed Tomography. This technique allows the imaging of a sample in 3D non-destructively. The sample is rotated while a micro-focus x-ray beam hits it. The angular-dependent images are collected by a planar x-ray detector, and are then reconstructed to produce 2D slices of the sample. The 3D reconstruction can be used to study the statistics of the sample. Another improvement that could be made to match more closely a real natural environment is the introduction of oxygen gradients. This technique is used in literature for the study of bacteria or eukaryotic cells [108, 109, 110]. Finally, fluid flow could play a major role in the sediments [13, 107, 97, 111, 112, 113, 114], with groundwater velocities up to $10\text{ }\mu\text{m}$ [13]. For MTB, fluid flow influence was recently addressed in channels [115], and in porous environments but with small regularly spaced pillars [103].

2.3 Synthetic Swimmers

Synthetic microswimmers are man-made, micron-sized object that can move in the bulk, thanks to different actuation strategies. The final goal of this research field is to produce a perfect microbot, capable of swimming thanks to an in-board motor, of sensing the environment and respond to it, perform tasks such as drug delivery or bioremediation, in environments that would be prohibitive for natural swimmers [12]. Unluckily, current synthetic microswimmers are far from this vision. In-board movement mechanisms have been often used, such as self-diffusiophoresis: local concentration gradients are produced, resulting in forces trying to compensate the balance, giving rise to net movement. An example are janus particles or nanorods that propel thanks to catalytic diffusiophoresis, where the hydrogen peroxide in the medium is decomposed in oxygen and water [116, 12]. Often the solutions used are toxic and non compatible with biomedical applications. Another way to produce movement is by external actuation [12], such as ultrasounds, thermophoresis and magnetic fields. As for magnetic fields, the best actuation strategy employs rotating magnetic fields applied to rigid clusters (see Section 2.1.4). In this thesis, a simulation method for such magnetically-activated propellers is presented. The most iconic example are magnetic helices; however, also more complex, random structures are studied.

2.3.1 Helices

The most well-studied and experimentally realized example of rigid magnetic microswimmers are helices. The helical structure was inspired by the rotating bacterial flagella, that possess a corkscrew shape [24, 117, 118, 119]. The first helical rigid swimmer activated by a rotating magnetic field at low Reynolds numbers was actually in the centimeters range: low Reynolds numbers were achieved using a viscous oil [120]. From then on, many experimental realization of micro-

helices were reported in literature, varying in size, fabrication method and envisioned application [5, 22, 6, 23, 12].

In general, the behavior of a helix can be divided in two distinct regimes [121, 38, 30]: a synchronous regime, in which the propeller rotates with the same frequency as the applied magnetic field, and an asynchronous regime, for which the propeller cannot keep up with the external frequency and rotates at some effective frequency. For helices with the magnetic moment along the short axis, the synchronous regime is purely linear, with $v_{\text{CM}} = c_v f_B$, where v_{CM} is the velocity of the cluster, f_B is the applied magnetic field frequency and c_v is the coupling [19, 30]. Thus, the velocity obtained depends on the frequency and it is always positive, where the positive sign is defined as the axis of rotation of the magnetic field. The helix propels with its main axis parallel to the magnetic field axis, with a zero wobbling angle (the angle between axis of rotation of the helix and main axis of the helix). The maximum velocity is reached at the so called step-out frequency $f_{\text{so}} = BM/(2\pi\gamma_r)$, after which the system enters the asynchronous stage, with a drop in the velocity that can be described as $v_{\text{CM}} = c_v \left(f_B - \sqrt{f_B^2 - f_{\text{so}}^2} \right)$ [19, 30]. To derive this formula, the frictional and magnetic torque are equated; moreover, it was assumed that the propeller rotates always along the same axis [19].

This does not hold anymore for more complicated cases, in which the magnetic moment is oriented differently with respect to the helix body. At low frequency a tumbling regime can be identified, with the helix rotating along the short axis and the wobbling angle being 90° . As the external frequency increases, the frictional torque increases; to compensate it, the helix tumbles with an increasing angle between the main axis and the magnetic field. The higher this angle, the higher the magnetic torque. At some point, this configuration is not favorable anymore; to compensate the increasing frequency, the helix changes its axis of rotation, diminishing the friction [122]. This regime is called wobbling, and it is characterized by wobbling angles between 90° and 0° . As the frequency increases, the helix presents a 0° wobbling angle, just before the step-out frequency. A theoretical description of all these regimes taking into account the magnetic moment direction was given by Morozov *et al.* [30]. From this theoretical model, it becomes evident that not only the shape (that alone determines the motility matrix) is influencing the motion, but also the magnetic moment. The main effects that can be seen are the presence of negative velocities and the possible presence of two branching solutions: at the same external applied frequency, a helix can have two different possible velocities. For a brief summary of the theoretical approach adopted by Morozov *et al.* [30], see Section 2.3.3.

2.3.2 Non-helical Propellers and Random Shaped propellers

Helices are not the only rigid magnetic propeller that can swim. An achiral example is a three-beads propeller, which was studied both experimentally and theoretically [31, 29, 30]. This propeller is formed by three magnetic beads distributed in a triangle with a certain aperture vertex. A propeller with this shape is achiral. Previous theories stated that only chiral propeller would be able to swim [38]. However, the propeller needs a certain degree of asymmetry that could be given by the magnetic moment orientation within the body and by pseudo-chiral elements of the mobility matrix [30] (see Section 2.3.3 for a brief theoretical introduction and Section 9.1 for the theoretical values of the mobility matrix elements calculated by Morozov *et al.* [30]). Another non-helical example are v-shaped propellers [123, 124]. All these systems (and the helices as

well) are characterized by an initial design that is then realized experimentally with sophisticated fabrication methods [125, 12].

Randomly shaped propellers are an alternative way to obtain movement at the microscale. They were first experimentally realized by Vach *et al.* [19, 126, 20, 21]. The difference between these random-shaped propellers and helices/other propellers is that there is no initial design according to which the object is fabricated, but the shapes are obtained through a random synthesis process: iron-oxide nanoparticles are coated and glued together through a hydrothermal carbonization process [19]. The resulting shapes are random, with a typical size of few microns or less [19], and they possess a magnetic moment, randomly directed with respect to the propeller body. In good approximation, the propeller can be considered to have a dipolar magnetization fixed in time [126]. Not all these random structures are "good" swimmers: to obtain good propellers, a selection is necessary. A rotating magnetic field is applied, and only the propellers that can overcome gravity are selected and studied [19]. With this method, many propellers are produced with high yield and low cost, without the need of sophisticated fabrication methods. This pool of different shapes and magnetization can be useful to experimentally explore the relationship between shape, magnetic moment and swimming characteristics [19, 126, 20, 21], allowing to select propellers with desired characteristic. These selected propellers can be 3D-imaged, reconstructed and employed for future designs [19, 21]. It was seen that these propellers show a surprising variety of behaviors: the velocity-frequency curve can correspond to the one of a helix with magnetization along the short axis, with a linear synchronous regime followed by a decaying asynchronous regime [19, 20]; but it can present more complex behaviors, including switches between negative and positive velocities, branching and atypical asynchronous regimes [21]. Recently, more attention was given to such propellers on the theoretical and computational point of view [30, 127]. The theoretical approach presented in Section 2.3.3 can be applied to the random-propellers to explain the relationship between velocity, rotating frequency and applied magnetic fields, explaining why branching and negative velocities can appear. However, the exact solution for a random shape is not easily writable, and numerical simulation are required. Morozov *et al.* [30] and Mirzae *et al.* [127] proposed simulation of computer-generated random-shapes. Matching real experimental shapes proves to be difficult, since shape and magnetic moment highly influence the dynamics; this point is not currently addressed in the literature. Moreover, the available theory cannot explain what happens in the asynchronous regime. In this thesis, I propose a method to simulate and match experimentally realized random-propellers, and I explore the influence of shape and magnetic moment in all regimes, even the less-studied asynchronous regime.

2.3.3 Theoretical Description

In this section I briefly sum-up the theoretical approach adopted by Morozov *et al.* [30]. This approach can be applied not only to helices, but also to any microswimmer, once the mobility matrix is known. To derive this general theoretical description, an homogenous magnetic field is described by the torque of Equation 2.21; then, the forces and torques are balanced out thanks to the low Reynolds numbers, meaning that we can use Equation 2.2 and 2.3:

$$\mathbf{v} = \mathbf{M}^{\text{tr}} \cdot \mathbf{T}, \quad \boldsymbol{\omega} = \mathbf{M}^{\text{rr}} \cdot \mathbf{T}, \quad (2.22)$$

with \mathbf{v} , $\boldsymbol{\omega}$ the translational and rotational velocities of the propeller. These equations can be re-written in a particular body system, in which the axis are the eigenvectors of the matrix \mathbf{M}^{tr} ordered following the crescent ordering of their eigenvalues (see Appendix I). The rotation of the body system with respect to the lab system can be described by three Euler angles φ, ψ, θ ; the final equations will depend on these angles. In the synchronous regime, these angles are time-independent; this allows to write in the lab system the velocity component along the axis of rotation of the magnetic field [30]:

$$v_{\text{B}} = \omega l [\text{Ch}_1 \sin^2(\psi) \sin^2(\theta) + \text{Ch}_2 \cos^2(\psi) \sin^2(\theta) + \text{Ch}_3 \cos^2(\theta) + \text{Ch}_{12} \sin(2\psi) \sin^2(\theta) + \text{Ch}_{13} \sin(\psi) \sin(2\theta) + \text{Ch}_{23} \cos(\psi) \sin(2\theta)] \quad (2.23)$$

where l is the characteristic size of the propeller, Ch is the chirality matrix in the body system with diagonal elements $\text{Ch}_i \equiv M_{ii}^{\text{tr}}/(lM_{ii}^{\text{tr}})$ and off-diagonal elements $\text{Ch}_{ij} \equiv \frac{1}{2l}(M_{ij}^{\text{tr}}/M_{jj}^{\text{tr}} + M_{ji}^{\text{tr}}/M_{ii}^{\text{tr}})$. The diagonal terms of this matrix give information about the chirality of the object (*i.e.* the inability of an object to superimpose with its mirrored image); the off-diagonal terms also contribute to the velocity, even for achiral objects, since they can be non-zero. Achiral objects can swim thanks to these terms. The Euler angles ψ and θ depend on the frequency and on the magnetic moment direction and modulus. To write the explicit solution of Equation 2.23 for the velocity, the behavior of the Euler angles ψ and θ should be known, and their equations (reported by Morozov *et al.* [30]) should be solved. Sometimes, the equation for the angles gives two solutions at the same frequency, therefore also the velocity presents two solutions. This is the so called branching. The equation of these angle are not easily solvable for a generic propeller [30], and they can be analytically solved only in few specific cases. I report here the solution for a cylinder-like object [38, 30] that can be applied to helices. The magnetic moment direction can be described in the body system through two angles, the polar angle θ_m and the azimuthal angle α_m . The adimensional frequency $\tilde{\omega} \equiv \omega[(M_{11}^{\text{tr}})^{-1} + (M_{22}^{\text{tr}})^{-1}]/(mB_2)$ can be also defined, as well as two characteristic adimensional frequencies, the tumbling-to-wobbling frequency $\tilde{\omega}_{\text{t-to-w}} = \cos(\theta_m)$, and the step-out frequency $\tilde{\omega}_{\text{so}} = \sqrt{\cos^2(\theta_m) + \sin^2(\theta_m)(M_{33}^{\text{tr}})^2[(M_{11}^{\text{tr}})^{-1} + (M_{22}^{\text{tr}})^{-1}]/4}$. With these definitions, the solution can be easily written. For frequencies $0 < \tilde{\omega} < \tilde{\omega}_{\text{t-to-w}}$, the propeller is tumbling, with:

$$\theta = \pi/2, \quad \psi = -\alpha_m, \quad \varphi = \omega t - \theta_m + \arccos \tilde{\omega}. \quad (2.24)$$

For higher frequencies $\tilde{\omega}_{\text{t-to-w}} < \tilde{\omega} < \tilde{\omega}_{\text{so}}$, branching is visible, with two possible solution denominated 1 and 2:

$$\theta_1 = \arcsin(\cos(\theta_m)/\tilde{\omega}), \quad \psi_1 = -\alpha_m - \arcsin[\cos(\theta_1)\tilde{\omega}/(\sin(\theta_m)p)], \quad \varphi_1 = \omega t \quad (2.25)$$

$$\theta_2 = \pi - \theta_1, \quad \psi_2 = -2\alpha_m - \psi_1, \quad \varphi_2 = \omega t, \quad (2.26)$$

with $p \equiv M_{33}^{\text{tr}}[(M_{11}^{\text{tr}})^{-1} + (M_{22}^{\text{tr}})^{-1}]/2$. After the step-out frequency, the asynchronous regime begins. These equations were used by Bachmann *et al.* [21] for random elongated propellers that were studied in the lab. The propeller is approximated by a cylinder; the mobility matrix coefficients are thus known. The step-out frequency and the tumbling-to-wobbling frequency are

determined looking at the velocity-frequency curve. Thus, the magnetic moment angles can be determined.

2.3.4 Bead Simulation

Computer simulations of micro-propellers can be useful for investigating the behavior of the propellers, even in regimes (such as the asynchronous one) that are not described theoretically in literature. They can help where theoretical descriptions fail, as it happens for non-regular shapes such as random-shaped propellers; analytic solution in fact are possible only for simple shapes [38, 30, 118, 121, 122, 128], or for strong approximations such as slender or cylindrical objects [38, 30, 127]. To simulate a propeller, a discretization is required. Beads approximations have been extensively used in literature to study the propulsion by bacterial flagella and flexible filaments [129, 27], and for the study of rigid propellers [30, 27, 130, 131, 127]. The approach that will be implemented in the thesis is based on the work by Reichert [27], and consists in approximating the propeller through a cluster of beads, calculating their mobility matrix, obtaining the mobility matrix of the propeller through a projection method, and then integrating the equation of motion, once the velocity and frequency of the propeller are known through Equation 2.2. See Chapter 8 for more details on the procedure. The main point is thus calculating the mobility matrix of N interacting spheres.

One of the possible ways to calculate the mobility matrix for interacting spheres is given by the *method of reflections* [27, 26]. The general idea is that the flow produced by one sphere will interact and influence a second sphere; this interaction produces another flow that will interact with the original sphere, in an iterative process that resembles a 'reflection'. I will briefly introduce this method [27]. The flow \mathbf{u}_v in the position \mathbf{r} produced by one translating sphere of radius a with velocity \mathbf{v} is given by the solution of the Stokes Equation 2.1 in no-slip conditions (the flow on the sphere surface should be zero): $\mathbf{u}_v = A(\mathbf{r} - \mathbf{v}t) \cdot \mathbf{v}$, with $A = \frac{3}{4}\frac{a}{r}(1 + \hat{r}\hat{r}) + \frac{1}{4}\left(\frac{a}{r}\right)^3(1 - 3\hat{r}\hat{r})$. The flow produced by a rotating sphere with angular velocity $\boldsymbol{\omega}$ is given by $\mathbf{u}_\omega = \left(\frac{a}{r}\right)^3 \boldsymbol{\omega} \times \mathbf{r}$. The total flow for a rotating and translating sphere becomes:

$$\mathbf{u} = \mathbf{u}_v + \mathbf{u}_\omega. \quad (2.27)$$

Lets consider two spheres interacting, labeled by the subscript 1, 2, subject to external forces and torques, and lets write down their translational and angular velocity. The process can be divided in more steps:

- The first sphere feels an external force and torque $\mathbf{F}_1, \mathbf{T}_1$ and no flow, thus through Equation 2.2, $\mathbf{v}_1^0 = \mu^t \mathbf{F}_1$ and $\boldsymbol{\omega}_1^0 = \mu^r \mathbf{T}_1$, where $\mu^{t,r}$ are the mobility coefficients of a sphere. The produced flow \mathbf{u}^0 is given by Equation 2.27. The apex 0 indicates the zeroth order of the iteration.
- The second sphere feels an external force and torque $\mathbf{F}_2, \mathbf{T}_2$, plus the fluid flow \mathbf{u}^0 generated by the first sphere. To determine its velocities in the presence of flow, the Faxén theorem should be used [26, 27]. The velocities thus become $\mathbf{v}_2^1 = \mu^t \mathbf{F}_2 + \mathcal{L}^t \mathbf{u}^0(\mathbf{r})|_{\mathbf{r}=\mathbf{r}_2}$ and $\boldsymbol{\omega}_2^1 = \mu^r \mathbf{T}_2 + \mathcal{L}^r \mathbf{u}^0(\mathbf{r})|_{\mathbf{r}=\mathbf{r}_2}$, where $\mathcal{L}^t = 1 + \frac{1}{6}a^2 \nabla^2$ and $\mathcal{L}^r = \frac{1}{2} \nabla \times$. The second sphere produces with \mathbf{v}_2^1 and $\boldsymbol{\omega}_2^1$ a fluid flow \mathbf{u}^1 according to Equation 2.27.

- Now the first sphere also feels the flow from the second sphere \mathbf{u}^1 ; so another correction should be added, using again the Faxén theorem but ignoring the external forces and torques $\mathbf{F}_1, \mathbf{T}_1$ that were already taken into account. The velocities thus becomes $\mathbf{v}_1^2 = \mathcal{L}^t \mathbf{u}^1(\mathbf{r})|_{\mathbf{r}=\mathbf{r}_1}$ and $\boldsymbol{\omega}_1^2 = \mathcal{L}^r \mathbf{u}^1(\mathbf{r})|_{\mathbf{r}=\mathbf{r}_1}$. It produces a flow \mathbf{u}^2 .
- The process can be iterated, and the final flow becomes $\mathbf{u} = \mathbf{u}^0 + \mathbf{u}^1 + \mathbf{u}^2 + \dots$, while the velocities for the first particle would become $\mathbf{v}_1 = \mathbf{v}_1^0 + \mathbf{v}_1^2 + \dots$ and $\boldsymbol{\omega}_1 = \boldsymbol{\omega}_1^0 + \boldsymbol{\omega}_1^2 + \dots$, and for the second particle $\mathbf{v}_2 = \mathbf{v}_2^1 + \mathbf{v}_2^3 + \dots$ and $\boldsymbol{\omega}_2 = \boldsymbol{\omega}_2^1 + \boldsymbol{\omega}_2^3 + \dots$. These series converge [27, 132]. Now, the velocities calculated with this method can be equated with the velocity obtained applying the mobility matrix on the external forces and torques (Equation 2.2). In this way, the mobility matrix elements can be determined.

When more than two spheres are involved, then each sphere influences all the others with its flux; the problems becomes a many-body problem. The series can be stopped at the order \mathbf{u}^0 ; the problem becomes a two-body problem, since many-body contribution arise only at higher orders [27]. The series is exact up to order $(a/r_{ij})^3$. The translational part of the mobility matrix is referred to as the Rotne-Prager approximation; this approximation will be employed throughout the thesis. See Chapter 8 for the mobility matrix elements.

3 Materials and Methods: Bacterial Swimming

3.1 The Theoretical Model

The motion of bacteria is described by a modified Active Brownian Particle model (see Section 2.1.3.1). The bacteria are described as spheres with position \mathbf{r} and a direction vector \mathbf{e} that determines the orientation of the bacteria. Their dynamics is given by Langevin equations:

$$\begin{aligned}\gamma_t \frac{d\mathbf{r}}{dt} &= \gamma_t \sigma v \mathbf{e} + \mathbf{F}_{\text{ext}} + \sqrt{2k_B T \gamma_t} \xi_t \\ \gamma_r \frac{d\mathbf{e}}{dt} &= \left[\mathbf{T}_{\text{ext}} + \sqrt{2k_B T \gamma_r} \xi_r \right] \times \mathbf{e},\end{aligned}\tag{3.1}$$

where γ_t and γ_r are the translational and rotational friction coefficients, respectively, v is the speed of self propulsion, σ is the sign of the self-propulsion velocity (± 1 for parallel or antiparallel to \mathbf{e} , 0 for no self-propulsion), \mathbf{F}_{ext} and \mathbf{T}_{ext} describe external forces and torques (to describe magnetic interaction, the external torque becomes $\mathbf{T}_{\text{ext}} = M\mathbf{e} \times \mathbf{B}$, with \mathbf{B} the magnetic field and $M\mathbf{e}$ the magnetic moment directed along \mathbf{e}) and ξ_t and ξ_r describe uncorrelated white noise in the translational and rotational degrees of freedom. The translational noise is purely thermal with temperature T , but the rotational noise may have additional contributions, as it will be described in the following.

Bacterial motion can be described by two general states: runs and active changes of direction. Equations 3.1 describe both states, with the following change of parameters: In the run states, the bacterium self propels with a non-zero velocity ($\sigma \neq 0$), and it swims mostly straight, apart from thermal re-orientations. In the state of active changes of direction, the bacterium stops ($\sigma = 0$), and after that picks up a new direction. The run/change times are taken from exponential distributions with mean run/change times τ_{run} , τ_{pause} . Run states and active-change states are always alternated.

This active change of direction can be of two types: tumble (for the run-and-tumble motion) or reversal events (for the run-and-reverse motion). Run-and-tumble bacteria alternate runs (for which $\sigma = 1$, meaning that the velocity is always parallel to \mathbf{e}) and active reorientation called tumbles ($\sigma = 0$), with a mean angle of 68° (for *E. coli* [45]). To simulate this reorientation, an effective temperature T_{tumble} (much higher than the room temperature T) is applied only for the rotational noise during the change of direction, providing an enhanced rotational noise and consequently lead to the desired tumbling angle [133]. Instead, run-and-reverse motion includes three states: runs, during which the velocity has the same direction as \mathbf{e} ($\sigma = 1$); reversal event (the change of direction), during which the bacterium stops ($\sigma = 0$); and reverse runs, equal to runs except for the velocity that has the opposite sign with respect to \mathbf{e} ($\sigma = -1$). During the reversal event the temperature remains unchanged, and the change of direction is given by the flipping of the velocity vector.

A few computational notes: The stochastic equation were integrated through a Euler method. More advanced techniques for stochastic equations are available, but the Euler method was pre-

ferred because it is faster. The vectors ξ_t and ξ_r (representing the uncorrelated white noise) are three-dimensional vectors of Gaussian numbers [27, 33] (see Section 2.1.3.3), numerically obtained by a Box Muller method [37].

3.2 Chemotaxis and Aerotactic Models

When chemotaxis is turned on in the presence of a chemical gradient ∇C , the bacteria bias their motion to reach the preferred chemical concentration C^* , performing longer runs towards the desired concentration and shorter away. As a consequence, the mean run time τ_{run} will depend on the chemical concentration. Temporal sensing (see Section 2.2.2.1) is hereby substituted with a spacial sensing, with the 'response function' of the run time τ_{run} depending on the spacial gradient. If $C^* = +\infty$, the chemotaxis is defined towards an attractant, $C^* = -\infty$ for a repellent; C^* can also be a finite value as happens in aerotaxis. Two main aerotactic models are used in the thesis: axial and polar.

3.2.1 Axial

Based on *E. coli* chemotaxis [45], this model is applied also for axial magnetotactic bacteria. The mean run times are not constant anymore, but depend on the spatial oxygen gradient with the following response function:

$$\text{for } C < C^*, \tau_{\text{run}} = \begin{cases} t_{\text{down}} & \text{for } \nabla C_{\parallel} \leq 0 \\ t_{\text{down}} + (t_{\text{up}} - t_{\text{down}}) \frac{\nabla C_{\parallel}}{\nabla C_0} & \text{for } 0 < \nabla C_{\parallel} \leq \nabla C_0 \\ t_{\text{up}} & \text{for } \nabla C_{\parallel} > \nabla C_0 \end{cases} \quad (3.2)$$

$$\text{for } C \geq C^*, \tau_{\text{run}} = \begin{cases} t_{\text{up}} & \text{for } \nabla C_{\parallel} \leq 0 \\ t_{\text{up}} - (t_{\text{up}} - t_{\text{down}}) \frac{\nabla C_{\parallel}}{\nabla C_0} & \text{for } 0 < \nabla C_{\parallel} \leq \nabla C_0 \\ t_{\text{down}} & \text{for } \nabla C_{\parallel} > \nabla C_0 \end{cases} \quad (3.3)$$

where t_{up} , t_{down} represent the biased run times in the desired and undesired direction, respectively; they are multiples of τ_0 , the mean run time in absence of gradients, but in the presence of chemical (the actual values are reported in Tables A.1, C.1 and D.1); ∇C_{\parallel} indicates the projection of the chemical gradient onto the direction of motion and ∇C_0 is a threshold gradient for which the maximal run time is reached. For the free-swimming bacteria Chapter 4, the choice was $\nabla C_0 \neq 0$; while for the capillary experiments and for the bacteria in confinement (Chapters 5 and 6), ∇C_0 is set to 0, thus eliminating the intermediate linear behavior and obtaining a step function for τ_{run} .

3.2.2 Polar

Polar magnetotactic bacteria bias their walk on the magnetic field direction and on the absolute value of the oxygen concentration, instead that on the oxygen gradient and absolute concentration as axial bacteria. Polar bacteria can be divided in North Seeking (NS) bacteria (running North in oxic conditions), and South Seeking bacteria (running South). The mean run times response on

the magnetic field and concentration for NS bacteria is:

$$\text{for } C < C^*, \tau_{\text{run}} = \begin{cases} t_{\text{up}} & \text{for } \hat{\mathbf{v}} \cdot \mathbf{B} < 0 \\ t_{\text{down}} & \text{for } \hat{\mathbf{v}} \cdot \mathbf{B} \geq 0 \end{cases} \quad (3.4)$$

$$\text{for } C \geq C^*, \tau_{\text{run}} = \begin{cases} t_{\text{down}} & \text{for } \hat{\mathbf{v}} \cdot \mathbf{B} < 0 \\ t_{\text{up}} & \text{for } \hat{\mathbf{v}} \cdot \mathbf{B} \geq 0 \end{cases} \quad (3.5)$$

where $\hat{\mathbf{v}}$ is the velocity versor and \mathbf{B} the magnetic field. Simulation parameters can be found in the Appendix-Table A.1, C.1 and D.1.

3.3 Oxygen Integration

If the oxygen gradient is not set to a constant $\nabla C = \text{const.}$, a dynamic oxygen concentration should be considered, with oxygen diffusing from an air-water interface and with consumption by bacteria. The equation to be integrated would become [84, 79, 78]:

$$\frac{\partial C(x, y, z, t)}{\partial t} = D_{\text{O}_2} \nabla C(x, y, z, t) - k \frac{C(x, y, z, t)}{C(x, y, z, t) + C_a} \rho(x, y, z, t) \quad (3.6)$$

where C is the oxygen concentration, D_{O_2} the oxygen diffusion constant, k the consumption rate, ρ the local number of bacteria and C_a a cutoff to avoid negative concentration (following the Michaelis-Menten rule [134]). The boundary condition are $C = 216 \mu\text{M}$ on the side open to air and 0 otherwise. To integrate the equations with an Euler method, the space is discretized in bins of size $20 \mu\text{m} \times 20 \mu\text{m} \times 20 \mu\text{m}$. Inside a single bin, oxygen concentration and oxygen gradient are considered constant. From the instantaneous position of the single bacteria, the number of bacteria per bin ρ is calculated, and used to solve the equations. For the 1D integration case, C depends only on t and x , and the space is discretized only on x . See the Appendix-Table C.1 for the parameters used.

3.4 Capillary Simulation

The capillary simulation was performed in a capillary with a length of 40 mm and a section of $0.1 \times 0.1 \text{ mm}^2$ (real capillary: $40 \text{ mm} \times 2 \text{ mm} \times 0.2 \text{ mm}$), with a typical bacterial density as in the experiment (25000 bacteria were simulated, $6.25 \times 10^7 \text{ cell mL}^{-1}$ corresponding to an $OD = 0.18$). The oxygen flows from the wall at $x = 0$. The simulations are started with completely anoxic conditions, as was done in the experiments on which the simulation data will be compared in the thesis. See the Appendix-Table C.1 for the parameters used.

3.5 Wall Interaction

In the thesis two types of wall interactions are used: an induced reverse upon contact or a WCA force and torque. The first one is used in the capillary simulations (Chapter 5), the second one in the study of bacteria in confinement (Chapter 6). In both cases, the bacterium will be confined by the presence of the wall.

3.5.1 Induced Reverse

This type of interaction was used for capillary simulations (Chapter 5), being inspired by experimental findings [103] (see Appendix H). When a bacterium encounters a flat wall (for example, for a wall situated at $x = 0$ the condition becomes $x_{\text{bacterium}} \leq 0$), the bacterium is re-positioned on the wall $x = 0$, the run is stopped and an active reversal event is started (see Figure 3.1).

3.5.2 Weeks-Chandler-Anderson Potential

This method is used for bacteria in confinement (Chapter 6), specifically for bacteria in cylindrical traps and bacteria interacting with the sand. When modified, this method can be also employed for simulating an exclusion force between bacteria at high densities, see Appendix E. When the condition of wall-trespassing is met, a WCA force (Weeks-Chandler-Anderson potential, namely a Lennard-Jones potential cut off in the minimum, to avoid the attractive part of the potential) is applied [36, 135]. The WCA potential is:

$$V_{\text{WCA}} = 4\epsilon \left[\left(\frac{\sigma}{|\mathbf{r}|} \right)^{12} - \left(\frac{\sigma}{|\mathbf{r}|} \right)^6 \right] + \epsilon, \text{ for } |\mathbf{r}| < \sigma 2^{1/6}$$

and 0 otherwise, where ϵ is the pre-factor, \mathbf{r} , $\hat{\mathbf{r}}$, $|\mathbf{r}|$ are respectively the vector between the center of the obstacle and the center of the bacterium $\mathbf{x}_{\text{obstacle}} - \mathbf{x}_{\text{bact}}$, its versor and its modulus, and σ is related to the radii of the obstacle and the bacterium, as explained in the following paragraphs. The force is obtained as $\mathbf{F}_{\text{WCA}} = -\nabla V_{\text{WCA}}$:

$$\mathbf{F}_{\text{WCA}} = -24\epsilon \frac{\hat{\mathbf{r}}}{|\mathbf{r}|} \left[2 \left(\frac{\sigma}{|\mathbf{r}|} \right)^{12} - \left(\frac{\sigma}{|\mathbf{r}|} \right)^6 \right], \text{ for } |\mathbf{r}| < \sigma 2^{1/6}$$

and 0 otherwise. Four wall interactions are to be distinguished: interaction with a sphere, interaction with a cylinder, interaction with a flat wall, interaction with a concave curved wall in a cylindrical trap (see Figure 3.1). For spheres (representing the sand-grains), \mathbf{r} is given by the 3D vector connecting the sphere center and the bacterium center, with $\sigma = \frac{R+a}{2^{1/6}}$, R being the sphere radius. For cylinders, \mathbf{r} is given by the 2D vector between the cylinder center and the bacterium center, with $\sigma = \frac{R+a}{2^{1/6}}$, R being the cylinder radius. When a flat wall is encountered, an imaginary sphere of radius equal to the bacterium radius a is set immediately behind the wall, with the vector connecting the bacterium-sphere center being perpendicular to the wall. The bacterium will interact and be repelled by this imaginary sphere; \mathbf{r} is the vector between the imaginary sphere center and the bacterium, and $\sigma = \frac{a+a}{2^{1/6}}$. For curved walls, the same imaginary sphere principle is applied. For a bacterium self-velocity of $20 \mu\text{ms}^{-1}$ and radius $1 \mu\text{m}$, it was set $\epsilon = 10^{-5}$ for the grains interaction, and $\epsilon = 10^{-10}$ for the imaginary sphere interaction, to avoid unnatural effects.

The wall interaction also includes an induced torque, mimicking a hydrodynamic torque, that was shown to exist also for magnetotactic bacteria [104]. The torque was adapted by the work of Ostapenko *et al.* [135], and is given by:

$$\mathbf{T}_{\text{WCA}} = p_{\text{T}} (\mathbf{e} \times \mathbf{F}_{\text{WCA}})$$

The pre-factor p_{T} was chosen to be 4 times bacterium radius a , to take into account the wall-

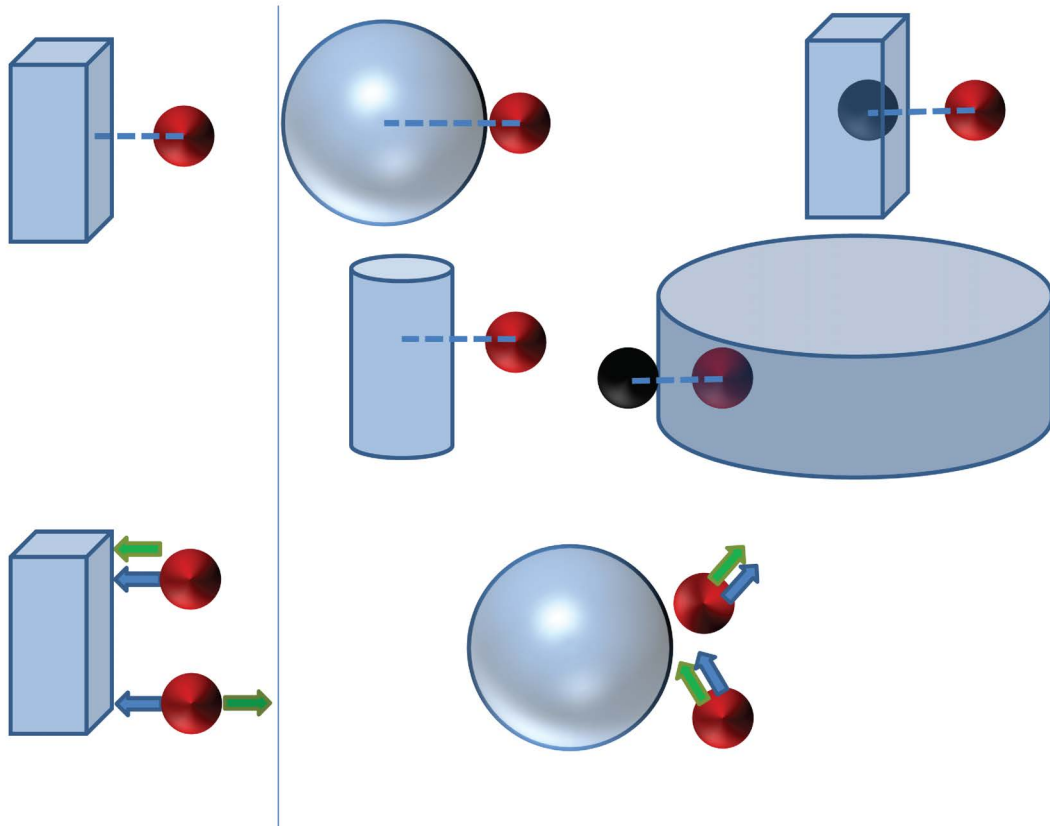


Figure 3.1: Wall interactions. First row, how the distances are calculated. Second row, how the interaction works. On the left, the induced reverse: the distance is calculated between the center of the sphere and the wall surface. When a bacterium hits the wall, a reversal event is induced, with the velocity (green arrow) changing sign, while the orientation e of the bacterium remains unchanged (blue arrow). On the right, the WCA interaction. For spheres and cylinders, the radius of the obstacle is used, while for flat walls and concave walls, an imaginary sphere (in black) is used for the interaction. The bacterium experiences hard wall exclusion and is reoriented away by the torque.

flagellum interaction. The torque reorients the bacterium away from the wall and it is applied on the border of the bacterium. This torque is an effective description necessary to reproduce the experimental circular trap results (see Section 6.1).

3.6 Sand Sample

The sand was collected in the Großer Zernsee lake (Potsdam, Germany), from the first layer of sediment (5 cm) in the shallow water nearby the shore. Macroscopic organic matter was manually removed. The sand was stored in water, and shaken before sample preparation to avoid sedimentation effects.

3.7 MicroCT of Sand

MicroCT of sediments samples can be found in literature, but was not performed in water so far: the sand was fixed by epoxy resin [105, 106, 107]. Alternatively here, the sample of sand in water was placed in a plastic cuvette of 4 mm in diameter, with a layer of water covering the top of the sand. The scan was performed by SkyScan 1172 scanner. For the scans, the following setting were used: X-ray source 89 kV, 112 μ A, Image Pixel Size (μ m)=1.56, Exposure (ms)=1400, Rotation Step ($^{\circ}$)=0.150, with frame averaging. Raw data were reconstructed using NRcon software (Version 1.6.10.4). For the reconstruction: Pixel Size (μ m)=1.56202, Reconstruction Angular Range (deg)=360.00, Angular Step (deg)=0.1500, Ring Artifact Correction=10, Smoothing=0, Filter cutoff relative to Nyquist frequency=100, Filter type description=Hamming (Alpha=0.54), Beam Hardening Correction (%)=70.

3.8 2D Sand Analysis

The 2D slices obtained from the microCT reconstruction were first processed with ImageJ: the images were cropped in the center to avoid the border effects, they were made binary to get black and white masks and a Median filtering was applied for smoothing. Then they were analyzed by a custom-made MATLAB program: erosion was applied to separate the grains from each other (settings: diamond shape and radius 9 pixels). Subsequently, the centroid function provided the center of each grain and the radius of a circle with equivalent area. The centers and radii are then used for calculating the statistics of the slide and for producing the circles-fitted masks. The percentage of sand was calculated as black pixels number over total number of pixel times 100.

3.9 3D Sand Analysis

The 3D visualization was done with the Amira software. The 3D statistics regarding the grain-size distribution and the water-gap distribution was obtained by the CTAn software (Version 1.16, Brucker). For the statistics, the first 1316 bottom slices were used (2 mm of sample), to avoid slices not completely filled by sand and distortion effects that were seen in the top slices. The images were processed by thresholding with Otsu method, despeckled (for white and black speckels, to reduce the noise) and a Median filter was applied. Then a 3D analysis was performed, in particular trabecular thickness and trabecular separation distribution were calculated to get the statistics on the grain-sizes and the gap-sizes. The distribution were fitted with MATLAB fitting tool: the grain-size follows a log-normal, and the water gaps a normal distribution.

3.10 Sphere Generation

From the 3D experimental grain-size distribution, an equivalent distribution of sphere-diameters was derived for simulation purposes. The logarithm of the diameters are distributed as a Gaussian with mean and sigma derived from the experimental analysis of Section 3.9. Random diameters were generated from this distribution. Diameters bigger than the maximal experimental diameter were discarded. Uniformly distributed positions were generated inside the box; diameters were assigned to a position in decreasing order. The spheres were all included inside the box, without overlap with the borders and between each other. If a sphere of a certain radius was not fitting in the box anymore without superposition, it was discarded and the next sphere was considered. New diameters and positions were generated till the percentage of volume occupied by the spheres reached the experimental sand percentage, given a simulation box of $500\ \mu\text{m}$ side. The procedure is illustrated in Figure 3.2.

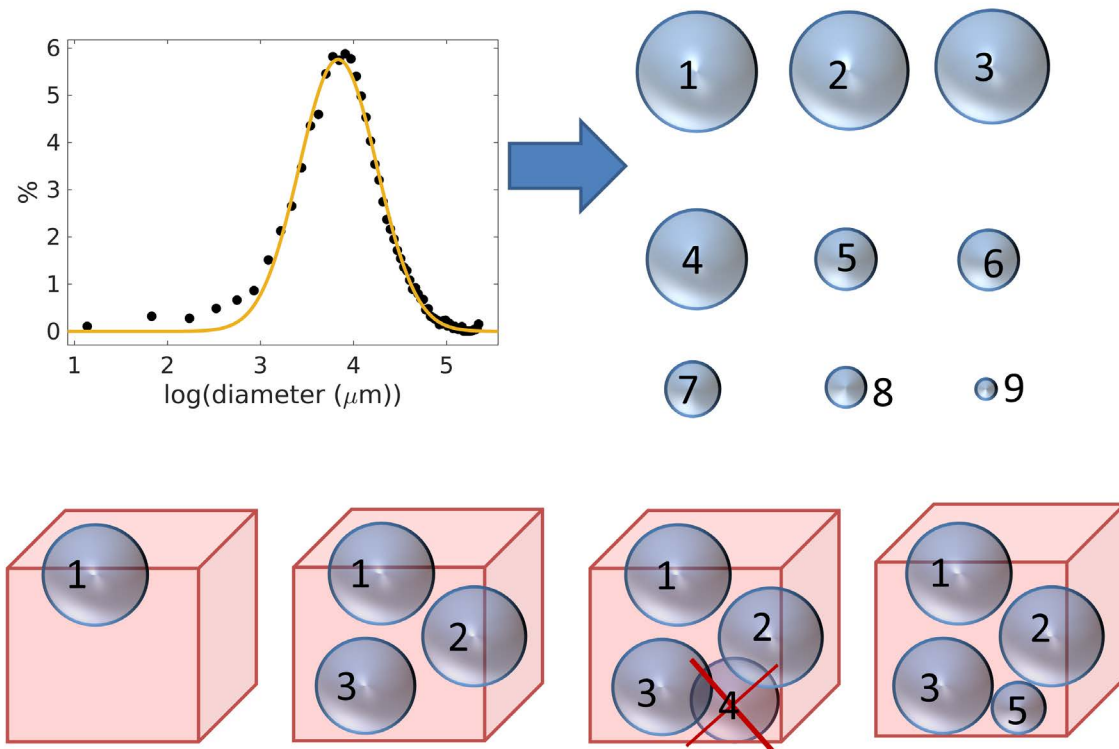


Figure 3.2: Sphere generation method: the logarithm of the experimental grain size diameters is fitted by a Gaussian; an equivalent sphere distribution is generated, with diameters smaller than the maximum experimental diameter, and they are ordered in crescent order; following this order, the spheres are randomly placed inside the simulation box; if a sphere does not fit without superposition, it is discarded.

4 Results for Free Swimming Bacteria

In this chapter, I will present the results for bacteria swimming without confinement, *i.e.* in the bulk. Since it is possible to integrate the equation of motion without the need of space-discretization, I do not have limitations regarding the size of the system and there is no need for wall interactions. The confined systems will be considered in the next chapters.

This chapter is divided in the following sections: first, I present bacteria swimming without external biases (Section 4.1). Second, I consider the interaction with external fields (Section 4.2), for which I show that the alignment angle with the magnetic field is influenced by the tumbling events, by thermal noise and by the dimensionality of the system (2D or 3D). Third, I quantify the effect of the magnetic field intensity and direction on the chemotactic velocity (Section 4.3) and I show that magnetic fields speeds chemotaxis up till magnetic fields inclinations of 60° .

The parameters used in this chapter are listed in Table A.1 of Appendix A, if not indicated otherwise. Additional results on the MSD can be found in Appendix B.

4.1 Bacterial Motion

Bacterial motion cannot be described by a simple Active Brownian Particle model. The main feature that shall be added is an active change of direction, which allows the bacteria to redirect their motion and eventually, to perform chemotaxis. I present three common strategy to achieve such an active change of direction: tumble, reverse and flick.

4.1.1 Tumble

I reproduce the tumbling motion that consists in alternating exponentially distributed runs and stops, during which the bacterium tumbles, thus re-orienting. The mean tumbling angle is experimentally 68° for *E. coli* [45], distributed as in Figure 4.1a: the circles represent the experimental distribution obtained by Berg *et al.* [45], compared to the simulated distribution (histogram). I obtain $\langle \theta_{\text{tumble}} \rangle \pm \sigma = 68 \pm 40^\circ$ for an effective temperature of $T_{\text{tumble}} = 4.2 \times 10^4$ K (see Section 3.1 for its definition). The curve is correctly right skewed as the experimental distribution; however, I obtain more events at small angles compared to the real distribution. Nevertheless, the required qualitative description of the tumbling event is sufficient for my purposes. In Figure 4.1b I show the distribution for the same effective temperature as in Figure (a), but with fixed tumbling times instead of exponential. The mean tumbling angle changes $\langle \theta_{\text{tumble}}^{\text{fixed}} \rangle \pm \sigma = 83 \pm 39^\circ$, as well as the skewness of the distribution. I will use the exponentially distributed values, since it matches the experimental data better, and since there is experimental evidence for it [45]. With these tumbling distribution, I obtain the example trajectories of Figure 4.2, with and without magnetic fields. The magnetic interaction produces a stretching of the trajectories along the direction of the magnetic field. This happens because the bacterium tends to re-align to the magnetic field after tumbles. I quantify this alignment in Section 4.2.

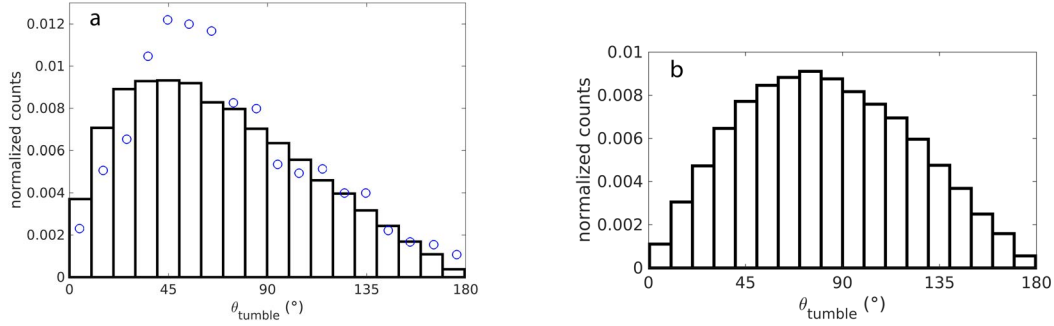


Figure 4.1: Experimental distribution (blue points in (a)) [45] compared to the normalized histogram (black bars) of the tumbling angle obtained from 50000 simulated tumbles with (a) exponentially distributed tumbling times, or with (b) constant tumbling times.

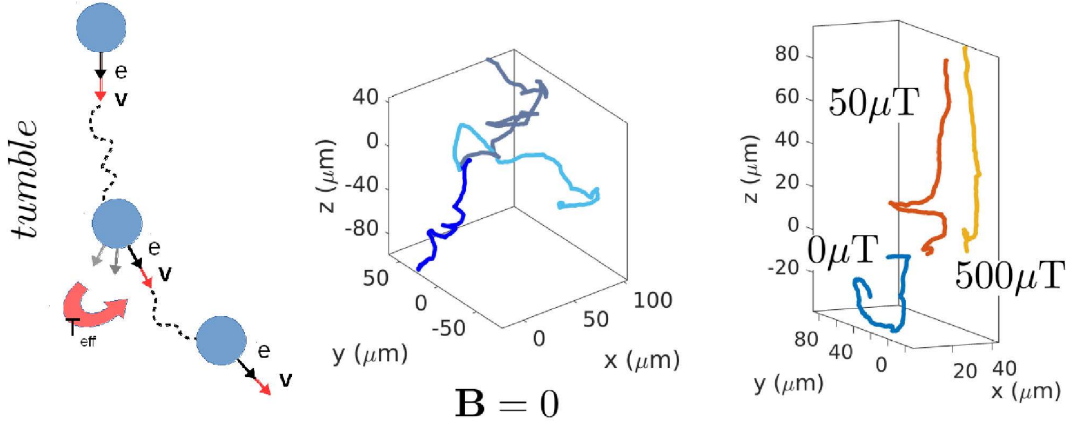


Figure 4.2: Example trajectories for tumble in the absence of magnetic fields (blue) and with magnetic fields. The cartoon illustrates the tumble process.

4.1.2 Reverse

While for tumble there is a reorientation of the body, for reverse the velocity vector changes sign, while the body orientation \mathbf{e} keeps its sign. The histogram of the reverse angle would be peaked around 0° for the body-vector \mathbf{e} , and around 180° for the velocities vectors. I report the angle between the velocity-vectors in Figure 4.3, where the mean reverse angle corresponds to $\theta_{\text{reverse}} \pm \text{sem} = 171.651 \pm 0.030^\circ$, in good agreement with the experimental observation of $\theta_{\text{reverse}} \pm \text{sem} = 166 \pm 10^\circ$ [78]. In Figure 4.4, I show some example trajectories with and without magnetic fields. The presence of the magnetic fields confines the trajectories in position. This effect is due to the body alignment that never changes, while the velocity switches. Since there is no bias, the probability of swimming up or down the magnetic field is the same, thus resulting in a motion restricted to a specific location.

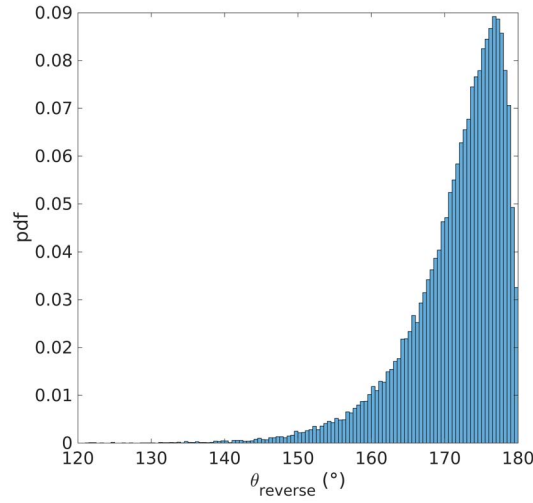


Figure 4.3: Normalized histogram of the reverse angle obtained from 50000 simulated reversal events with exponentially distributed reverse times.

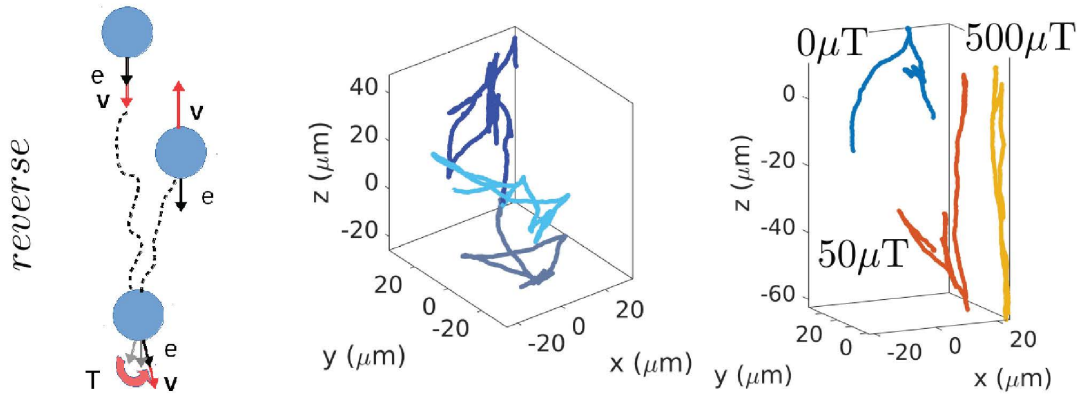


Figure 4.4: Example trajectories for reverse in the absence of magnetic fields (blue) and with magnetic fields. The cartoon illustrates the reverse process.

4.1.3 Flick

The method used to implement a tumble could be also used to implement a flick, whose mean angle is 90° [136]. In this case, I used a different set of parameters to match the behavior of MC-1 [137], a magnetotactic bacterium performing turns of 90° [138]. The flicks are of fixed length, equivalent to 0.002 s. The effective temperature needed to match the experimental data is $T_{\text{eff}} = 5. \times 10^{10}$ K. The corresponding histogram is presented in Figure 4.5a, where the mean angle corresponds to $\theta_{\text{flick}} = 89.876 \pm 0.0018^\circ$. Some example trajectories are also shown in Figure 4.5b, where the flicks are marked by a red dot. The 2D projection generates a bias in the angles: even though the distribution is tightly peaked on a 90° angle, the corresponding 2D projection biases it towards smaller angles. This effect is strong and predominant for experimental 2D tracking.

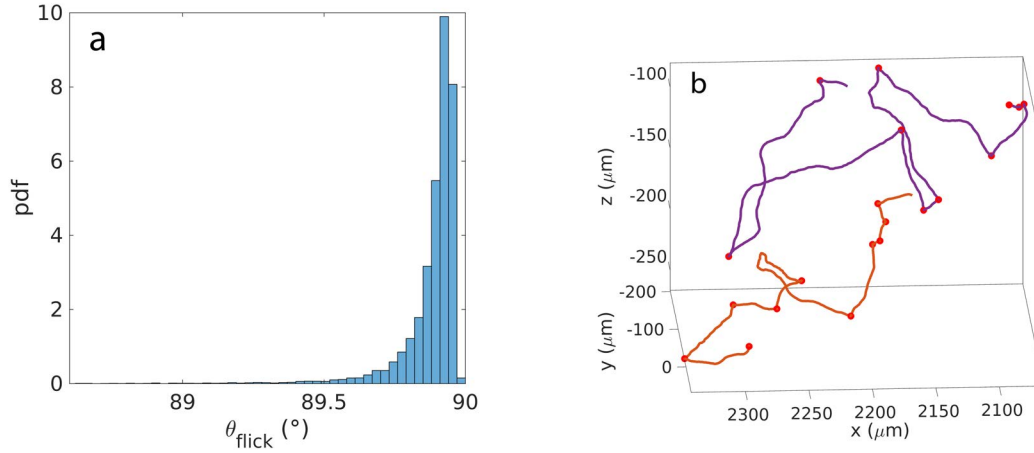


Figure 4.5: (a) Flick-angle histogram for 50000 flick events. (b) Two example trajectories in the absence of magnetic field. The red dots represent the flick event. Here $\tau_{\text{run}} = 0.86$ s, $\tau_{\text{flick}} = 0.002$ s (fixed), $v = 100 \mu\text{ms}^{-1}$.

4.2 The Magnetic Torque

Magnetic cells such as magnetotactic bacteria (performing reverse) and *E. coli* magnetic biohybrids (performing tumble) are influenced by external magnetic fields. In the previous chapter, I have shown the qualitative influence of the magnetic torque on the trajectories. Now, I want to quantify this interaction. I concentrate on the run and tumble case: the tumble event perturbs the alignment, on the contrary of the reverse event, where the alignment is preserved. Here I consider a free bacterium not performing chemotaxis: the only external influence is given by the passive alignment to the magnetic field. I characterize the alignment time and the behavior of the alignment angle there.

4.2.1 Alignment Time

First of all, I want to quantify the time needed to realign after a tumble. The theoretical alignment time to a magnetic field was obtained from the equations of motion in the following way (the approach is equivalent to that in refs. [73, 32]): I consider a run in the absence of thermal noise, but in the presence of a magnetic field, which for simplicity I take to be oriented along the z axis, \hat{z} , $\mathbf{B} = B\hat{z}$. The equations for the rotational frequency ω and for the orientation vector \mathbf{e} are

$$\begin{aligned}\omega &= \frac{d\phi}{dt} = MB\gamma_r^{-1}(\mathbf{e} \times \hat{z}) \\ d\mathbf{e} &= d\phi \times \mathbf{e}.\end{aligned}$$

Substituting the second equation into the first one and writing out equations for the components of the orientation vector, I obtain for the component e_z parallel to the magnetic field

$$\frac{de_z}{dt} + \frac{1}{\tilde{\tau}}(e_z^2 - 1) = 0, \quad (4.1)$$

where

$$\tilde{\tau} = \frac{\gamma_r}{MB} \quad (4.2)$$

is the typical relaxation time. Solving the equation for e_z , I find

$$e_z = \frac{\exp(2t/\tilde{\tau}) - c}{\exp(2t/\tilde{\tau}) + c}, \quad (4.3)$$

where $c = \frac{1-e_{z0}}{1+e_{z0}}$ is given by the initial condition $e_z(t=0) = e_{z0}$. Since I consider a magnetic field along the z axis, I can express e_z as $e_z = \cos(\theta_{e,B})$. Now I take the initial condition for e_z as resulting from a kick away from alignment with the field due to tumble, then on average I have $e_{z0} = \langle \cos(\theta_{\text{tumble}}) \rangle \simeq 0.31$ (the numerical value is from the adjusted mean tumbling angle). Our equation thus describes a decay of the (cosine of the) alignment angle back to alignment with the field. As an example, I fit the cosine of the alignment angle after a tumble for $500\mu\text{T}$ without noise, the case for which the theory was derived. With the parameters of my simulation, the expected value for $\tilde{\tau}^{-1}$ is 4.4 s^{-1} . This value is recovered by fitting the simulation data, giving $\tilde{\tau}^{-1} = 4.1\text{ s}^{-1}$ (Fig. 4.6a). The fit has been performed with the function $f(x) = \frac{e^{2b(x-d)} - (1-a)(1+a)^{-1}}{e^{2b(x-d)} + (1-a)(1+a)^{-1}}$, where b evaluates $\tilde{\tau}^{-1}$, a evaluates e_{z0} and d is needed to re-scale the times to 0. I use the same procedure in the presence of noise, using for the fit the function $g(x) = f(x) + g_0$. The constant $g_0 = \langle \cos\theta_{e,B} \rangle$ reflects the nonzero mean value of the cosine in thermal equilibrium. The fit in this case leads to $\tilde{\tau}^{-1} \simeq 4.0\text{ s}^{-1}$, still in good agreement with the theory derived in absence of noise (Fig. 4.6b). For a magnetic field of $B = 50\mu\text{T}$, the strength of the magnetic field of the Earth, the relaxation constant is $\tilde{\tau}^{-1} = 0.44\text{ s}^{-1}$, corresponding to a decay time of $\tilde{\tau} \simeq 2.3\text{ s}$. However, in that case, the fluctuations around that decay are considerably more pronounced when the thermal noise is present.

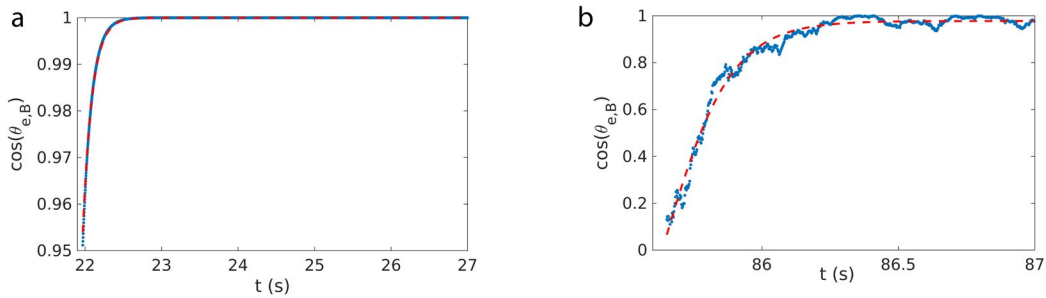


Figure 4.6: Cosine of the alignment angle $\theta_{e,B}$: (a) in the absence of thermal noise after a tumble event at $B = 500\mu\text{T}$ (blue curve). In red the fit $f(x)$; (b) in the presence of thermal noise (blue curve). In red the fit $g(x)$.

4.2.2 Alignment Angle

In my model, the motion during a run corresponds to a simple Active Brownian Particle motion, with passive alignment to the magnetic field in the presence of thermal noise. The thermal fluctuations are characterized by the corresponding energy $E = -MB \cos \theta_{e,B}$ [32], and the Boltzmann statistics $\propto \exp(-E/k_B T)$ can be used to describe the system. Using spherical coordinates, I obtain the following distribution for the alignment angle $\theta_{e,B}$:

$$p(\theta_{e,B}) = \frac{MB}{k_B T} \frac{1}{2 \sinh(\frac{MB}{k_B T})} \sin \theta_{e,B} \exp(\frac{MB}{k_B T} \cos \theta_{e,B}), \quad (4.4)$$

where the term $\sin \theta_{e,B}$ comes from the area element. This expression is normalized as $\int_0^\pi d\theta p(\theta, T) = 1$. Using this distribution to calculate the mean cosine of the alignment angle, I obtain the Langevin function [32, 139]:

$$\langle \cos(\theta_{e,B}) \rangle = \int_0^\pi \cos(\theta_{e,B}) p(\theta_{e,B}) d\theta_{e,B} = \coth(MB/k_B T) - (MB/k_B T)^{-1}. \quad (4.5)$$

These equations remain true only during the runs un-interrupted by changes of directions, or in the overall motion if the change of direction does not alter the alignment to the magnetic field. As a consequence, a bacterium performing run and reverse will follow Equation 4.4 and Equation 4.5 at the room temperature T , since the alignment angle $\theta_{e,B}$ remains always close to 0 (green line in Figure 4.7). Instead, a bacterium performing run and tumble will not follow exactly the Equations 4.4 and 4.4 at room temperature, because of the 'tumble-kicks' that push $\theta_{e,B}$ far from 0 (purple line in Figure 4.7).

I want to determine $p(\theta_{e,B})$ and $\langle \cos(\theta_{e,B}) \rangle$ in the case of tumble. To do so, I have to consider the competition between two different time scales: the run time and the relaxation time $\tilde{\tau}$. After a tumble, the bacterium is kicked away from alignment and it takes a time $\tilde{\tau}$ to realign back. If the run time is shorter than the relaxation time, the bacterium never reaches full alignment. Thus the $\langle \cos(\theta_{e,B}) \rangle$ will depend on the mean run times (Figure 4.8a). For very long runs $\tau_{\text{run}} \gg \tilde{\tau}$, the tumble has less influence, thus the cosine approaches the ideal Langevin function 4.5 for the room temperature T . For very small run times $\tau_{\text{run}} \ll \tilde{\tau}$ the bacterium is almost always in the tumble state, and the curve approaches the ideal Langevin function 4.5 for the tumbling temperature T_{tumble} . All the other curves at different run times fall in the middle, and can be fitted by Equation 4.5 with an effective temperature T_{eff} . If I use these effective temperature to rescale the curves, I obtained a collapsed plot (Figure 4.8b), showing that for any run time I can consider the Langevin function 4.5 as a good approximation for the simulated mean cosine curves. I can also plot the dependence of this effective temperature on the mean run times (Figure 4.9a), where I can see that T_{tumble} is obtained for $\tau_{\text{run}} = 0$, and T for $\tau_{\text{run}} = +\infty$. Scaling the times by the relaxation time $\tilde{\tau}$ (Figure 4.9b) shows that T_{eff} has an inflection point at $\tau_{\text{run}} = \tilde{\tau}$.

While I have seen that for the cosine the theoretical description given by Equation 4.5 remains true if an effective temperature is used, the distribution of the alignment angle $\theta_{e,B}$ changes drastically in the presence of tumble (Figure 4.10). The thermal distribution given by Equation 4.4 at the effective temperature obtained from the Langevin fit of $\langle \cos(\theta_{e,B}) \rangle$ (continuous curve of Figure 4.10a) does not represent the simulated data (purple diamonds of Figure 4.10a). The simulated distribution presents a peak due to the thermal distribution during runs after relaxation, and

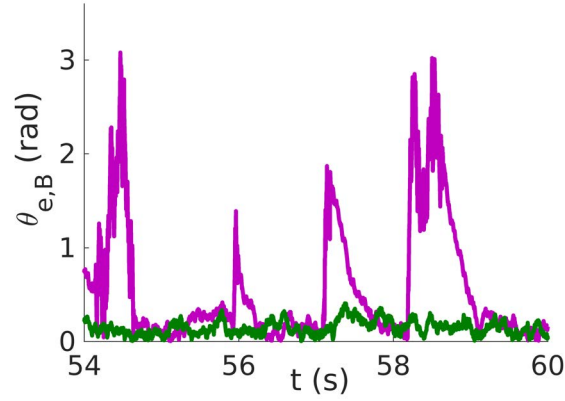


Figure 4.7: Alignment angle vs time for tumble (in purple) and reverse (in green) for a mean run time of 0.86 s at 500 μ T.

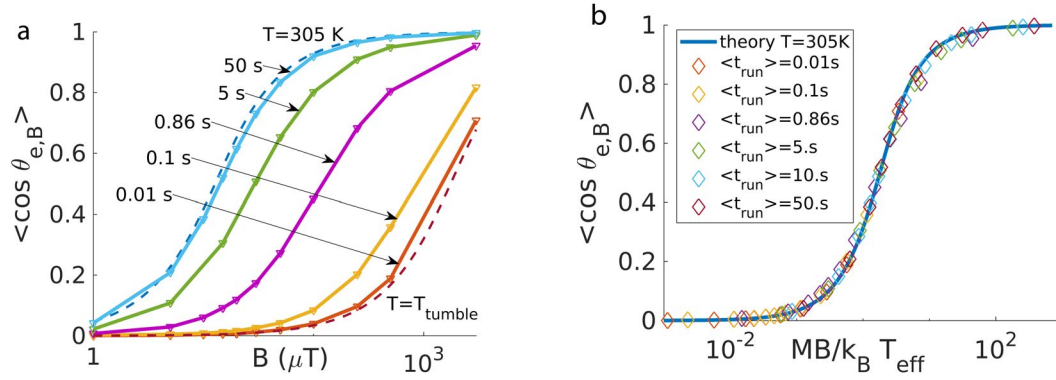


Figure 4.8: (a) Langevin plots for tumble compared to theoretical Langevin function at T and T_{tumble} . Each line corresponds to a different mean run time. (b) The same curves can be scaled by the effective temperature T_{eff} obtained by a Langevin fit, obtaining a collapsed plot. The full line corresponds to the theoretical curve at room temperature.

a broad tail that depends on tumbling and relaxation and is not explainable with a thermal distribution. This observation suggests that measuring the distribution of the alignment angle might provide a way to distinguish the non-thermal noise due to discrete tumble events from non-thermal noise that might be present continuously due to the active swimming motion. Recently, other fitting distributions were proposed by Rupprecht *et al.* [140]: $P_\theta \sim \theta^{-1+1/\beta}$ at small angles with $\beta \equiv \tau_{\text{run}}/\tilde{\tau} = \tau_{\text{run}}MB/\gamma_r$, both in 2D and 3D with different normalizations. The formula holds for values $\beta > 1$, as it is the case for MTB. This result was obtained considering a run-and-tumble random walk, with deterministic runs without thermal noise, during which the magnetic fields realign the bacteria with characteristic time $\tilde{\tau}$, interrupted by tumbles; the duration of each run is drawn by a given probability density, each run is independent of the previous ones and it is independent of the alignment direction (thus this formula cannot be used for chemotaxis). My simulated distribution in 3D and with noise (purple diamonds of Figure 4.10 a and b) presents discrepancies with this

functional form (blue continuous curve of Figure 4.10b). To understand where these discrepancies come from, I run a 3D simulation without thermal noise during runs (purple stars), and I also calculated the 2D projection of the angle with and without noise (respectively, light blue diamonds and light blue stars). The 2D projection of the angle $\cos \theta^{2D} = \frac{\cos \theta^{3D}}{\sin(\cos^{-1}(e_z))} = \frac{\mathbf{e} \cdot \mathbf{B}}{\sin(\cos^{-1}(e_z))}$ (with \mathbf{B} along $+\hat{z}$ and $e_z = \mathbf{e} \cdot \hat{z}$) is hereby considered since often the experimental data are 2D tracking of real 3D trajectories. Interestingly, the distribution present a good fit with $P_\theta \sim \theta^{-1+KT/mB}$ only if the thermal noise is turned off. This is consistent with derivation of the formula proposed by Rupprecht *et al.* [140], which was obtained in the absence of thermal noise. For real systems where noise is present, both in 2D and 3D, the distributions change shape, since the peak moves from 0 to higher values.

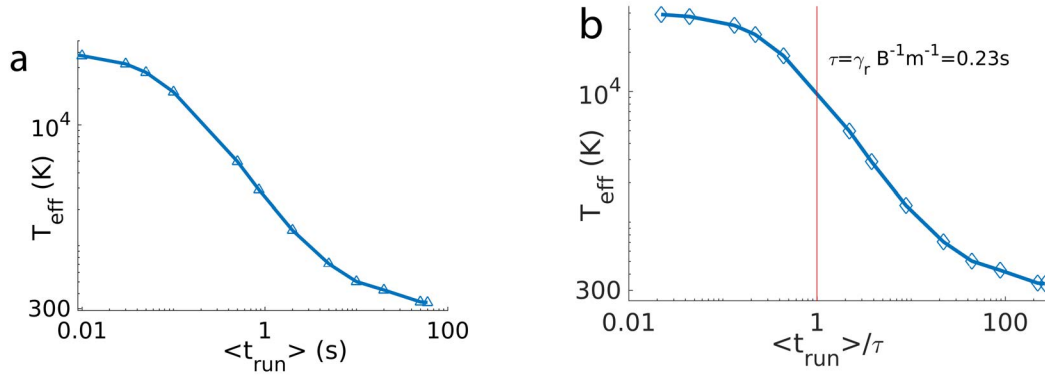


Figure 4.9: (a) The effective temperature obtained by the Langevin fit are plotted against the mean run time. (b) The same curve as function of the rescaled times $\tau_{\text{run}}/\tilde{\tau}$.

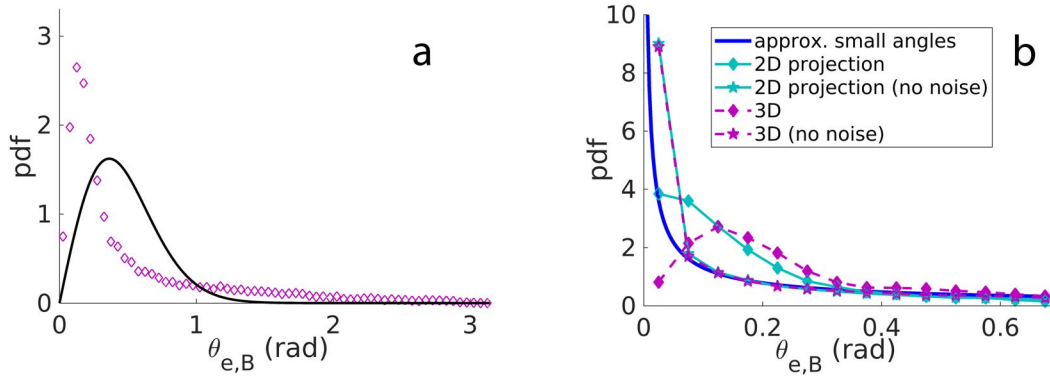


Figure 4.10: (a) The distribution of the alignment angle for tumble and a mean run time of 0.86 s at $500 \mu\text{T}$ (data points) deviates from the thermal distribution with the corresponding effective temperature 2896K (solid line) (b) Alignment angle for tumble at $B = 500 \mu\text{T}$, for 3D motion with and without thermal noise during runs compared to a 2D projection with and without thermal noise. The blue line corresponds to $P_\theta \sim \theta^{-1+1/\beta}$ [140].

4.3 Chemotaxis in Constant Gradients

The next step is to consider walks that are biased due to a chemical gradient. I choose a gradient that is constant in space and time for simplicity. More complex gradients will be considered in the next chapters. I consider here the interplay between external interactions like forces or torques and chemotaxis.

Here, the chemotactic model is based on *E. coli* (see Section 3.2.1), and it is thought to represent the axial behavior of magnetotactic bacteria [32]. The chemotactic parameters were adapted from *E. coli*, since I used it as my test organism (Table A.1).

4.3.1 Attractant

In this section I present the results for the attractant case. The repulsive case is totally equivalent to the attractant, and will not be presented here. In fact, all the same conclusions can be drawn just considering that the bacteria would swim down the gradient (so antiparallel to it) instead than up as in the attractant case.

4.3.1.1 Forces

I briefly consider the effect of forces on chemotaxis. Typical forces that could act on a magnetic bacterium are the ones exerted by magnetic gradients, fluid flow, and optical or magnetic tweezers. Under a constant force, the run and tumble trajectories become biased (stretched out) in the direction of the force. As a consequence, forces parallel to the gradient will enhance chemotaxis, on the contrary forces antiparallel to the gradient would hinder chemotaxis (Figure 4.11). Chemotactic swimming up the gradient is impossible for opposing forces exceeding a threshold value $F^* = -\gamma_t v_{\text{taxis}}(F=0) / \cos \theta_{e,F}$, where $\theta_{e,F}$ is the angle between the orientation of the bacterium and the force. For reverse, the trajectories also biased in the direction of the force, with a similar effect as for tumble.

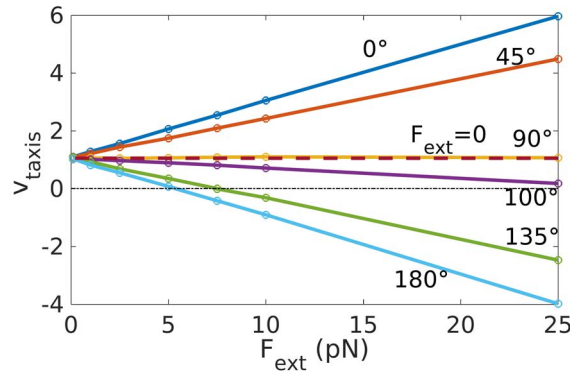


Figure 4.11: Taxis velocities in presences of a constant force at different angles $\theta_{e,B}$ and intensities.

4.3.1.2 Magnetic Torque

I want to consider now the influence of the magnetic torque on the taxis velocity for both tumble and reverse, at different orientations of the magnetic field. In general, a magnetic field parallel to the chemical gradient enhances the taxis velocity both for reverse and tumble (Figure 4.12), already at the Earth magnetic field intensity. However, the reverse presents lower velocities, due to the greater contributions of backward motion. This enhancement of velocities continues up to rather large angles (approximately 60° in Figure 4.12). For angles close to 90° , the chemotactic velocity is lower than without the field for both reverse and tumble, therefore raising the question whether magnetotaxis is beneficial at such high field inclinations. For even larger angles, tumble achieves negative velocities, meaning that the bacterium is pushed to follow the antiparallel magnetic component that cannot be overcome by the taxis. On the contrary, reverse presents a symmetrical curve, and achieves a correct taxis even for antiparallel magnetic fields. This could explain why magnetotactic bacteria do not choose tumble as their main reorientation strategy. For stronger magnetic fields, the velocities get higher (Figure 4.13 and Table 4.1), because a stronger magnetic field provides better alignment, contrasting the thermal noise and the internal bacterial noise (the tumble events).

For a bacterium making infinite runs, with a very strong magnetic field and without thermal noise, I suppose perfect alignment of the trajectories to the magnetic field. As a consequence, the only component that plays a role in the determination of the taxis velocity should be the projection of the magnetic field along the gradient $\cos(\theta_{B,\nabla C})$, as demonstrated by the scaled taxis velocities of Figure 4.14, where the tumble follows a cosine and the reverse follows the modulus of the cosine (since parallel and antiparallel fields generate the same behavior). The scaling is needed to filter out the effect of thermal noise and changes of direction and normalize the velocities for parallel fields to 1; in fact, these noise components perturb the alignment, thus the motion is not totally directed along the magnetic field and only a component of the self-velocity contributes to the taxis velocity. When only thermal noise is present (for infinite un-interrupted runs), the thermal perturbation can be described by $\langle \cos \theta_{e,B} \rangle$ (Equation 4.5). So for parallel fields, the expected percentage of self velocity along the gradient (equivalent to the taxis velocity)

would be $\langle \cos \theta_{e,B} \rangle$. As it can be seen from Table 4.1, these values are not reached. For tumble, this is due to the fact that the re-orientations events induce a higher effective temperature, so the correct theoretical solution would be $\sim \langle \cos(\theta_{e,B})(T_{\text{eff}}) \rangle$. In the Table 4.1 the cosine values are obtained for $T_{\text{eff}} = 1342 \text{ K}$: this effective temperature is extrapolated from Figure 4.9 at 2 s without chemotaxis, considering that for chemotaxis holds $(t_{\text{up}} + t_{\text{down}})/2 = 2.22 \text{ s}$. The match proves to be good. Instead, for reverse I have to consider not only the thermal noise contribution at room temperature, but also the backward-motion contribution. This means that the velocity needs to be reduced by a factor $R_{\text{time}} \equiv \frac{t_{\text{up}} - t_{\text{down}}}{t_{\text{up}} + t_{\text{down}}} = 1/3$, since $t_{\text{up}} = 2\tau_0$ and $t_{\text{down}} = \tau_0$. The match with theory results very good. It further improves taking into consideration the stop time due to the reversal event; the formula then becomes $R_{\text{time}}^* \equiv \frac{t_{\text{up}} - t_{\text{down}}}{t_{\text{up}} + t_{\text{down}} + 2t_{\text{pause}}} = 1/3.19$ since $t_{\text{pause}} = \tau_0/10.57 = 0.14 \text{ s}$ (values in Table 4.1).

The final formula for the taxis velocity up a constant gradient for reverse becomes:

$$v_{\text{taxis}}^{\text{reverse}} \simeq v_{\text{self}} |\cos(\theta_{B,\nabla C})| \left(\coth\left(\frac{MB}{k_B T}\right) - \left(\frac{MB}{k_B T}\right)^{-1} \right) \frac{t_{\text{up}} - t_{\text{down}}}{t_{\text{up}} + t_{\text{down}} + 2t_{\text{pause}}}, \quad (4.6)$$

B (μT)	thermal noise effect	tumble	theory for tumble	reverse	theory for reverse
0	/	0.07	/	0.08	/
50	0.8751	0.49	0.46	0.25	0.27
500	0.9857	0.88	0.94	0.30	0.31
5000	0.9986	0.95	0.99	0.31	0.31

Table 4.1: Percentage of self velocity $v_{\text{taxis}}/v_{\text{self}}$ achieved for tumble and reverse at different parallel magnetic fields, compared to the thermal noise effect $\langle \cos(\theta_{e,B}) \rangle(T)$, and the theoretical predictions for tumble $\sim \langle \cos(\theta_{e,B}) \rangle(T_{\text{eff}})$ and reverse $\sim 1/3.19 \langle \cos(\theta_{e,B}) \rangle(T)$.

while for tumble it becomes:

$$v_{\text{taxis}}^{\text{tumble}} \simeq v_{\text{self}} \cos(\theta_{B,\nabla C}) \left(\coth \left(\frac{MB}{k_B T_{\text{eff}}} \right) - \left(\frac{MB}{k_B T_{\text{eff}}} \right)^{-1} \right), \quad (4.7)$$

where the pause time and the relaxation times are taken into account by the effective temperature.

To fully understand the influence of magnetic fields on taxis, I consider the dependence of the taxis velocity on the run times. There are hints that magnetotactic bacteria actually prefer very long run times compared to the ones of *E. coli* [80, 32]. For non-magnetic species, very long run times are actually negative, because due to thermal noise, the bacteria would lose their orientations after a time $\tau_{\text{rot. diffusion}}$ (see Section 2.1.3). The thermal-induced reorientation in a

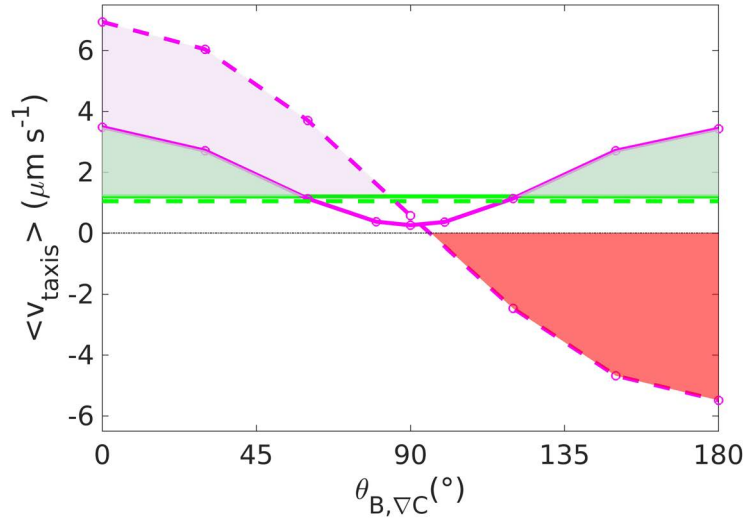


Figure 4.12: Taxis velocity up the gradient for reverse (filled lines) and tumble (dashed lines) at $B = 0\mu\text{T}$ (green line) and $B = 50\mu\text{T}$ (purple line). Tumble with the field performs better than reverse with field for small angles (the pink area shows the gap between tumble curve and reverse curve). Reverse with field performs better than without (the green area shows the gap between curves with and without field for reverse). Tumble with field obstacles chemotaxis at high angles (the red area shows the gap between zero velocity and tumble curve).

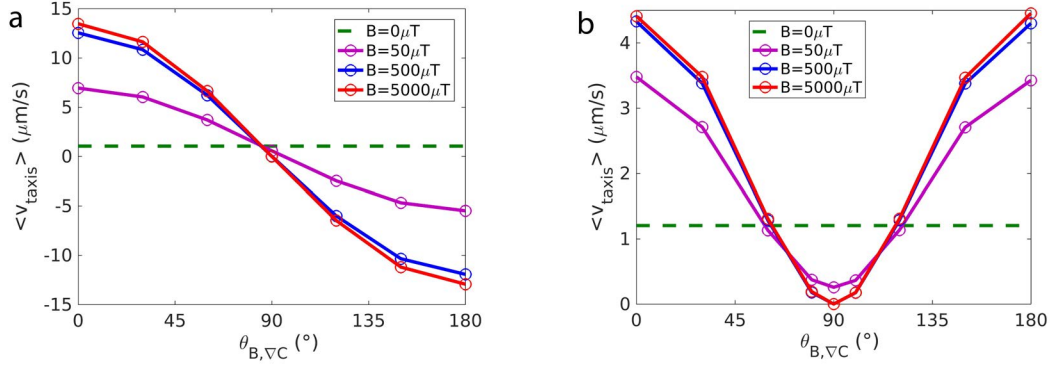


Figure 4.13: Taxis velocity as function of the angle between magnetic field and gradient for (a) tumble and (b) reverse, at four different magnetic field intensities.

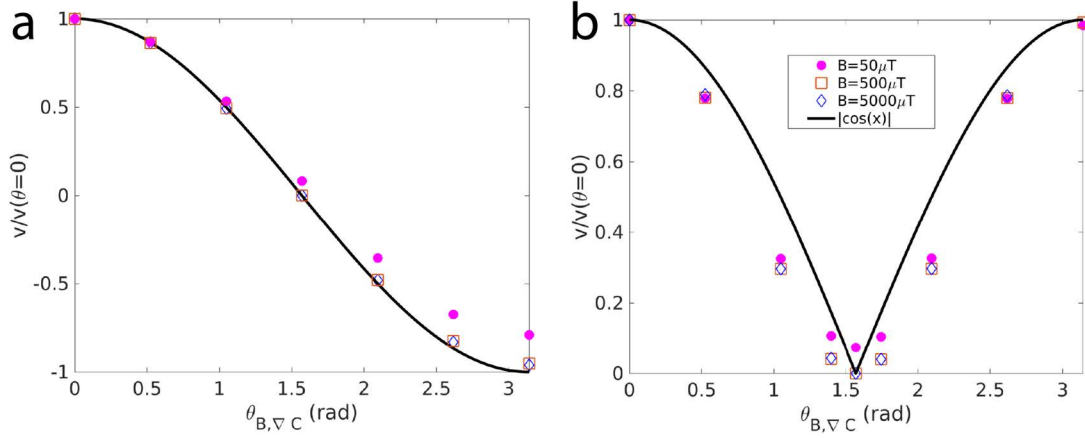


Figure 4.14: Scaled taxis velocity as function of the angle between magnetic field and gradient for (a) tumble and (b) reverse, at four different magnetic field intensities. The black lines represent the cosine (a) and the absolute value of the cosine (b).

time t is equivalent to $\langle \theta^2 \rangle = 6D_{\text{r}}t$ [2]: for a sphere of radius $1 \mu\text{m}$ it takes 1.7 s to reorient of 45° , thus losing the intended direction. Consistently, the taxis velocity presents a sharp peak at values close to 2 s in the absence of magnetic fields (red curve in Figure 4.15), after which the velocity drops to 0. With a parallel magnetic field, higher velocities can be reached; moreover, the peak is less pronounced and shifted to higher run times, and it is followed by a slow decay for long run times, still maintaining high taxis velocities at 100 s (blue curve). For the Earth magnetic field inclination present in Berlin ($\theta_{B, \nabla C} \simeq 157^\circ$) [40] (purple curve), the same behavior is obtained as in the parallel case, even though the velocities are smaller, as expected from the previous results of Figure 4.12. In conclusion, magnetic fields seem to allow the bacteria to perform longer runs without getting reoriented. The open question is why such long runs are convenient for bacteria. In principle, this might allow them to use the spacial sensing of chemical gradients, but without further experiments this is just speculation.

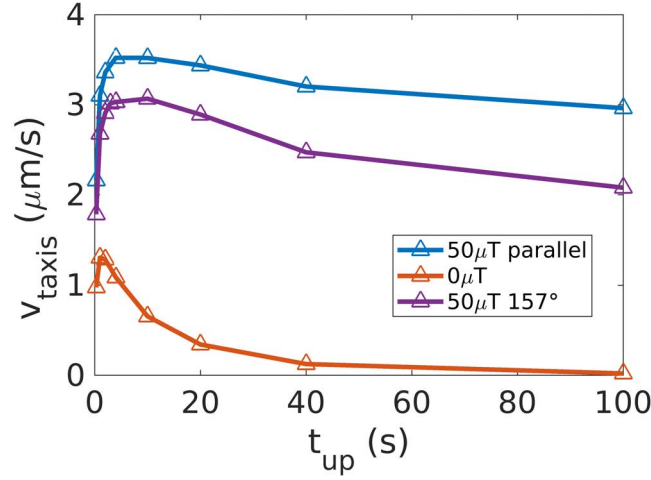


Figure 4.15: Taxis velocity as function of t_{up} without a magnetic field (red), with a 50 μT magnetic field at 0° (blue) and at 157° (violet) respect to the gradient.

4.3.2 Preferred Concentration

In this section I concentrate on the chemotaxis towards a preferred concentration. Aerotaxis is believed to belong to this category, where the oxygen acts both as attractant at concentrations $C < C^*$ and as a repellent at concentrations $C > C^*$. As a consequence, bacteria accumulate around the preferred concentration, and form a band there (a simulated band is depicted in Figure 4.16a). I systematically studied the band formation in constant gradients with and without magnetic fields, for tumble and for reverse. The band can be formed by both tumble and reverse strategies without magnetic fields, even though for tumble the resulting band is more dispersed. When magnetic fields are added, tumble fails to form a band, consistently with my previous results where the tumble is compelled to follow the magnetic field. For reverse instead, the band is formed in almost every case. To quantify the band formation process, I look at two parameters: the band-size and the equilibrium time. To obtain them, I look at the standard deviation of the swimmer position in the direction of the gradient as a function of time (Fig. 4.16b). This quantity relaxes quickly as the band is formed. I fit this quantity with an exponential decay to a constant $\sigma(t) = (\sigma(0) - \sigma_{eq}) * \exp(-t/t_{eq}) + \sigma_{eq}$ and I obtain therefore the decay time t_{eq} and the standard deviation at equilibrium σ_{eq} , representing the dispersion and thus the dimension of the band. The band width can also be estimated from the density profile of the band after the equilibrium time (Figure 4.17a) applying a symmetric Laplace distribution $f(x) = \frac{1}{2L} \exp(-\frac{|x-m|}{L})$, where the free fitting parameters are m , the position of the preferred concentration and L , the decay length of the curve. L is thus a good estimator of the size of the band, since 68% of the density is situated in $[m - L, m + L]$. I see a strong dependence of these quantities on the magnetic field angle and intensity. For angles up to 60° , the band forms faster compared to the case without field, while it is slightly larger (Figure 4.16c and d and Figure 4.17b). For angle close to 90° , the band forms at longer times, while it is tighter. In the extreme case of a very strong field at 90° , the band failed to form, while for the Earth magnetic field intensity, the band can still form within an hour, indicating that magneto-aerotaxis (based on run and reverse) remains functional even at 90° . I can conclude that

the presence of magnetic fields is beneficial for the band formation for reverse, making chemotaxis faster for angles up to 60° , while it slows down the dynamics at greater angles, even though it does not prohibit it. Therefore, axial bacteria could live at the Equator.

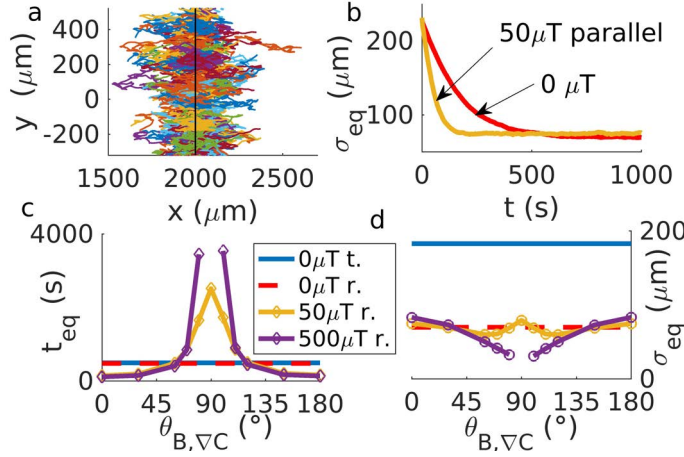


Figure 4.16: a) 100 examples trajectories for chemotaxis towards a preferred concentration (black line). b) Relaxation of the band width, estimated by σ_{eq} . c) Equilibration time t_{eq} and d) steady-state width of the band for tumble (t.) and reverse (r.) at different intensities and orientations of the magnetic field.

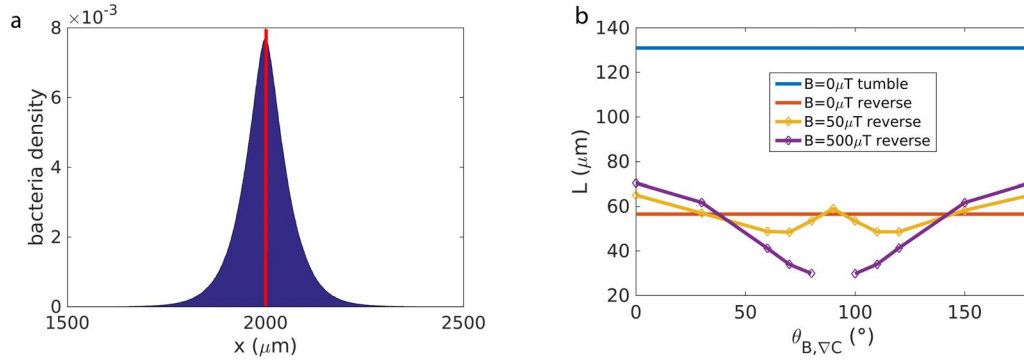


Figure 4.17: (a) Density of the bacteria after the equilibrium time of 477 s for run and reverse with $B = 0$. The curve is symmetrical with respect to the preferred concentration, which is situated at $2000 \mu\text{m}$ and indicated by the red line. (b) Band width obtained by the fit with the Laplace distribution.

5 Capillary Simulations

In the previous chapter, I presented the behavior of free-swimming bacteria, where no boundaries are present. Here I want to reproduce the capillary experiments done for magnetotactic bacteria [78, 79], where the bacteria are confined by the capillary walls and where the oxygen gradient is changing in time and space (see Section 2.2.2.1). I concentrate on reverse, since it is preferred by my model organism MSR-1, and also because I have shown in the previous chapter that a run and tumble strategy does not form a band with magnetic fields. I also change the parameters to adapt them to MSR-1 (see Table C.1 of Appendix C). With these simulations, I want to match as close as possible the experiments to study the influence of magnetic fields, but also I want to test my aerotactic models, since a direct comparison with the experimental results is possible for this system. Moreover, the models tested in this way can be subsequently used as a predictive tool.

The Chapter is structured in the following way. At first, I adapt my simulation for this new system (Section 5.1). To do so, I introduce the interactions with the capillary walls for a constant oxygen gradient, and I see that the walls do not influence the dynamics (Section 5.1.1). After this, I consider a dynamic oxygen gradient that changes due to oxygen diffusion and consumption of oxygen by bacteria, ignoring eventual anisotropies in the capillary cross-sections, thus considering a 1D integration of the concentration equations (Section 5.1.2). I see that to obtain band formation with such a dynamic gradient, the response function of the run times should become a step-function. I test if this works also with a 3D integration of the concentration, allowing for anisotropies on the cross-sections (Section 5.1.3). After this tuning, I consider axial (Section 5.2) and polar (Section 5.3) behavior; I quantify the effects of the magnetic field intensity and direction (0° , 180° and 90°) on the band formation, showing that the magnetic fields in the correct configurations speed up aerotaxis. Finally, I consider alternative aerotactic models for completeness (Section 5.4).

5.1 Tuning

In this Section, I want to tune my program for the capillary case. I check if the walls interactions have any effect, and if the chemotactic model works also for a dynamic oxygen gradient. The findings of this Section are the basis for the following sections with the main results for axial and polar bacteria.

5.1.1 Constant Gradient

First of all, I want to verify if the wall interactions produce any effect on the band formation. Therefore, I run the simulation with a constant gradient (in space and time), and induced reverse on the walls upon contact. I set the following parameters: $t_{up} = 6\tau_0$, $\tau_0 = 1$ s, $v = 20 \mu\text{ms}^{-1}$, $\nabla C = 6 \mu\text{Mmm}^{-1}$, $L_x = 40$ mm, $L_y = L_z = 2000 \mu\text{m}$, $B = 0$. The band forms without problems at the expected preferred concentration, and the density of the band grows in time (Figure 5.1, 5.2).

The bacteria keep swimming towards the peak, and a wave of bacteria fleeing from to high oxygen concentration is formed (Figure 5.2a). The peak of bacteria in the band is symmetrical. However, a depletion of bacteria can be observed where the oxygen concentration turns to 0 (Figure 5.2b). The bacteria remain trapped in the anoxic end, where the oxygen gradient and concentration are 0. This oxygen gradient is not representative of what happens in a real capillary, therefore I simulate a dynamic oxygen gradient in the next sections. Nevertheless, the band can form and is not disturbed by the wall interactions

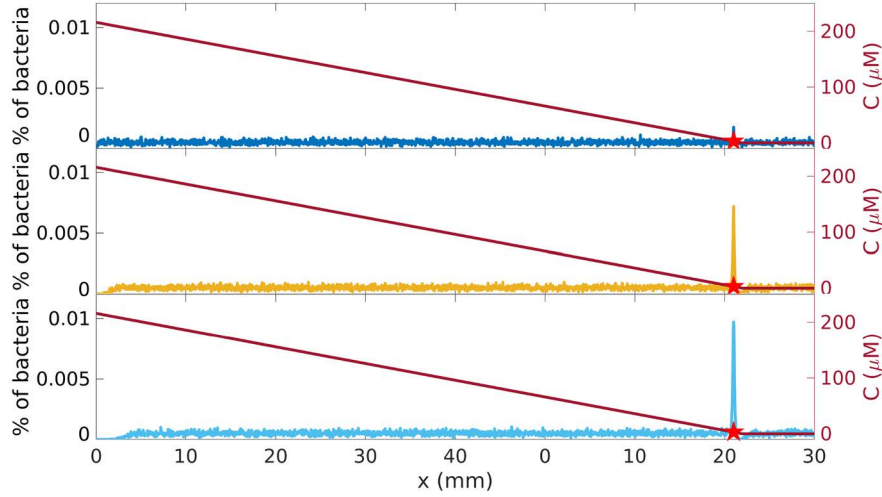


Figure 5.1: Bacteria percentage $n_{\text{bact}}(x)/n_{\text{TOT}}$ (left y axis) and oxygen concentration (right y axis) plotted against the position along the capillary at 1 min (blues), 10 min (yellow) and 20 min (light blue). A red star indicates the preferred concentration position.

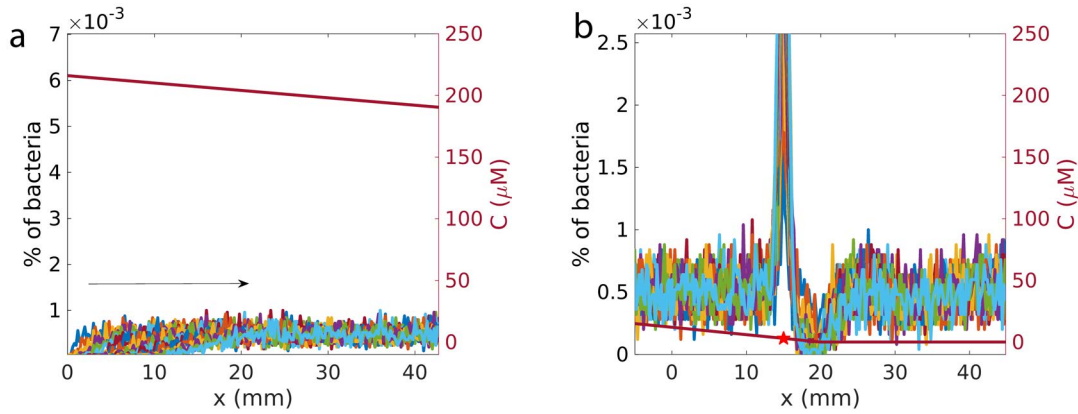


Figure 5.2: Zoom of Figure 5.1 with a curve at every minute (different colors): (a) at the air interface; (b) at the preferred concentration position. The black arrow in (a) indicates the movement of the bacteria in time.

5.1.2 Dynamic Gradient with 1D Integration

For real systems, the oxygen gradient is not constant in time, nor in space. In fact, the oxygen is diffusing from the open end of the capillary, and bacteria also consume it. Therefore, I included an equation describing the oxygen dynamics in my system. I first present a tuning of the aerotactic response function (Equations 3.2 and in 3.3 Chapter 3) in one dimension, where the oxygen concentration is only a function of the position along the capillary, to pass then to the final results in three dimensions, where the concentration is a function of all the three spacial coordinates. First, a simple 1D integration of the oxygen concentration was attempted, where the concentration is only function of the position along the capillary $C = C(x, t) \forall y, z$. The yz cross-section has the same concentration given a certain x , and the oxygen flows from the open end $x = 0$. At first, I use my model for which the response of the run time on the gradient $\tau(\nabla C)$ presents a intermediate linear behavior 3.1, with the reference gradient $\nabla C_0 \gg 0 \mu\text{Mmm}^{-1}$ (see Equations 3.2 and 3.3). The band is not forming (Figure 5.3a), and the distribution of bacteria remains random for any time. This is due to an oxygen gradient much smaller than the reference gradient ∇C_0 . To start seeing a band, I diminish the intermediate linear behavior, reducing ∇C_0 (Figure 5.3b,c). The band forms faster and denser for smaller values of ∇C_0 , until the limiting case where $\nabla C_0 = 0$ and $\tau(\nabla C)$ becomes a step-function (Figure 5.3d). I also notice that the depletion point on the anoxic side is present for $\nabla C_0 \neq 0$, while it disappears for the step-function. Moreover, a wave of bacteria fleeing the anoxic side is present only for the step-function case. Therefore, I can distinguish different aerotactic models, just looking at how the band-shape is experimentally. Since we do not observe experimentally a depletion on the anoxic side of the band, I choose to use the step-function approach, consistently with what done previously in literature [78, 79]: while for *E. coli* the response to the gradient is widely known [45, 24, 56], the aerotactic response of magnetotactic bacteria is poorly studied, so I keep the simple step-function model as an effective description of the system.

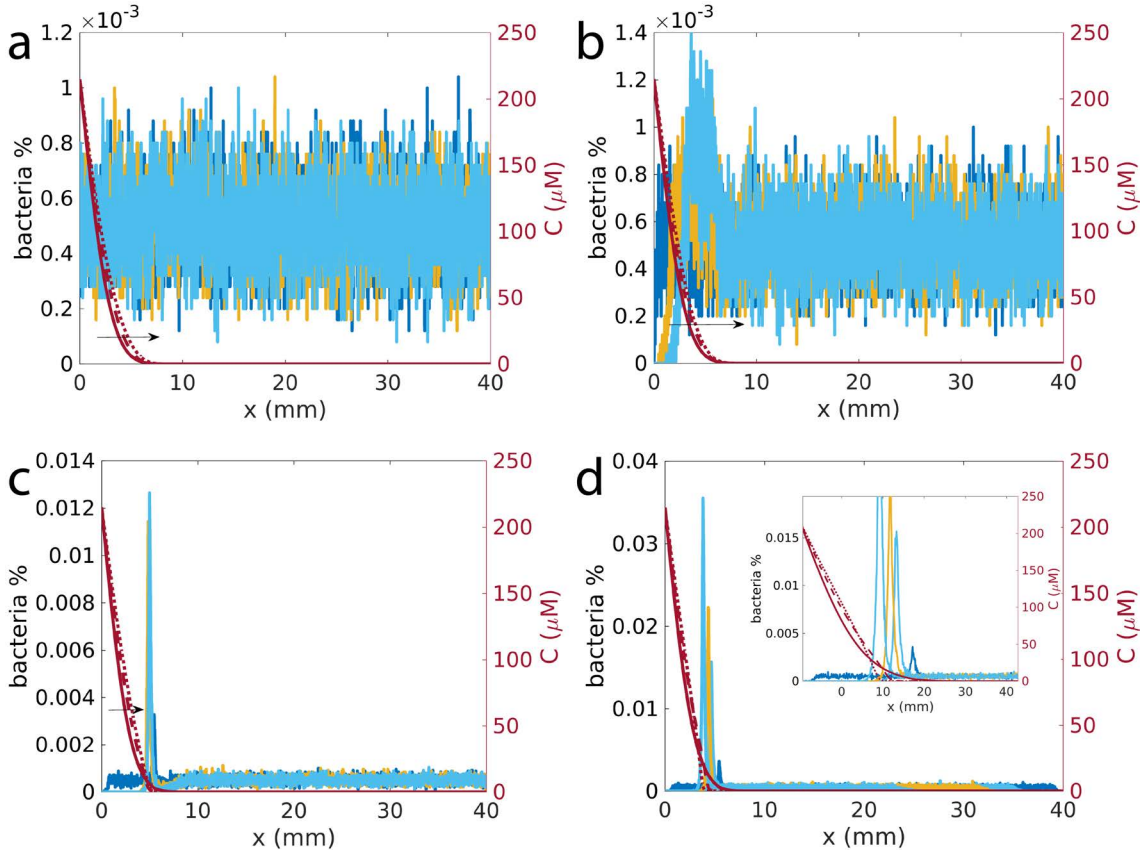


Figure 5.3: Band at 1 min (blue), 10 min (yellow) and 20 min (light blue) and the corresponding oxygen concentration (filled line, dashed line and dotted line) for a) $\nabla C_0 = 100 \mu\text{Mmm}^{-1}$, b) $\nabla C_0 = 1 \mu\text{Mmm}^{-1}$, c) $\nabla C_0 = 0.01 \mu\text{Mmm}^{-1}$, d) Step-function. The black arrow shows the time direction. The inset shows the zoom of the band in d).

5.1.3 Dynamic Gradient with 3D Integration

In general, the oxygen concentration and gradient will depend not only on x , but also on the other two spacial coordinates $C = C(x, y, z, t)$. This is of minor importance if the magnetic fields are directed along x , since there is no anisotropy and asymmetry in the yz plane. If I want to consider any angle between long axis of the capillary and the magnetic field, then I must take into account that the bacteria can concentrate in an anisotropic way along the yz cross-sections, modifying the local oxygen gradient. Therefore, I need to take into consideration also the dependence of the oxygen concentration along yz , and perform a 3D integration. To perform integration in space, I divide the 3D space in cubes of dimensions $20 \times 20 \times 20 \mu\text{ms}^3$ (Figure 5.4a). In each cube, the gradient (the arrows in the first plot), the oxygen concentration (color code of the second plot) and the local density of bacteria (dimension of the circles in the third plot) are calculated. In this example, no magnetic field was turned on: as a consequence, there is no anisotropy in the yz plane, as it can be seen from the gradient arrows, all pointing along x . The same data can be represented averaging away the y and z dimensions (Figure 5.4b), thus obtaining the bacteria density and the oxygen concentration as function of x , equivalently to the 1D integration.

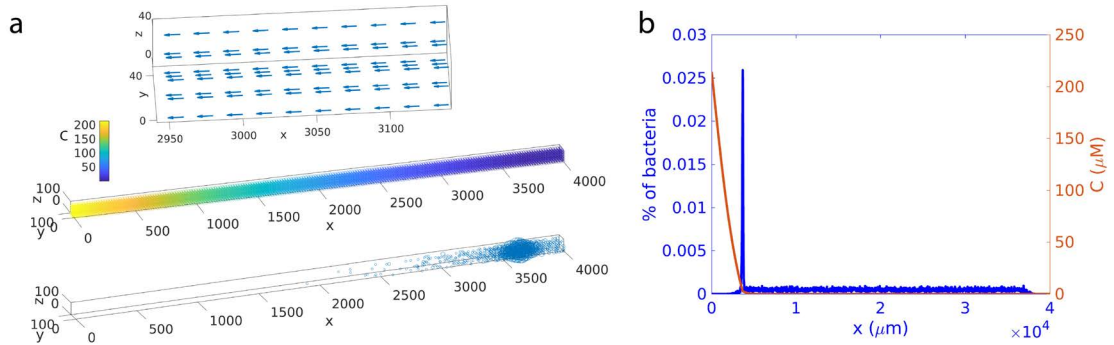


Figure 5.4: (a) 3D plot for axial bacteria after 20 min from the start of the experiment, with no magnetic field. In the first row, a zoom of the capillary with the oxygen gradient represented by arrows. The arrow gives the direction, and its length gives the intensity. In the second row, the oxygen concentration C as a heat plot (scale in μM). In the third row, the bacteria density as circles, whose dimension is representative of the bacteria number in the cell. (b) Percentage of bacteria $n_{\text{bacteria}}^{\text{bin}}/n_{\text{bacteria}}^{\text{tot}}$ (in blue) and oxygen concentration profile (in red) at 20 min of simulation for $B = 0$. The distance from the air interface is represented by x .

5.2 Axial

Axial bacteria bias their motion on the oxygen concentration only in a similar way as *E. coli*, and the magnetic field gives an axis of orientation through passive alignment. Since axial bacteria use the magnetic field only for passive alignment, chemotaxis can be performed correctly even in the absence of magnetic fields, as we saw in Chapter 4. The band forms at the correct preferred concentration (Figure 5.5a1), but in general the dynamics is slower with respect to the case with parallel or antiparallel magnetic fields (Figure 5.5a2): with a magnetic field, the band forms faster (it is better defined and denser at shorter times). The pdf of the band $n_x/(n_{\text{tot}}\delta_x)$ (with n_x the number of bacteria at a certain x and δ_x the size of the integration cell) can be fitted by a Laplace distribution $f = I \exp(-|x - m|/b)$, from which I obtain the position m , band-size b and intensity I . If I look at b in time (Figure 5.5c) I notice that without magnetic fields, the equilibrium size is smaller compared to the antiparallel magnetic field case, and the stronger the field, the faster the decay. Stronger magnetic fields lead to a broader equilibrium size, as seen in Chapter 4. The field forces the trajectories to be parallel to the capillary axis, thus making the band broader. As for the intensity of the band I (Figure 5.5d), without magnetic field, it grows slower. However, the velocity of growth does not depend on the intensity of the magnetic field. Finally, I study the band position m over time (data points in Figure 5.5e) and compare them to the preferred oxygen position (lines in Figure 5.5e). For all the magnetic fields, the band follows the preferred concentration position. At small times (less than 5 min in my simulation), the main influence on the dynamics is given by the flow of oxygen (all the curves follow the green curve obtained for pure oxygen flow, with no consumption by bacteria). After the first 5 minutes, when the density of bacteria in the band is increased, the consumption of oxygen increases at the band position, modifying the dynamics. For stronger fields, the band stabilizes earlier and closer to the air interface, due to the larger number of bacteria present in the band within $m \pm 3b$ (given by $2Ib0.95$). The band position seems to reach a plateau, but actually it keeps evolving with time (see yellow curve for $50 \mu\text{T}$). This is caused by the continuous flowing of bacteria to the band. I can compare the simulated band position (where the density corresponds to an OD of 0.18) to the experimental one obtained for axial WT MSR-1 at OD 0.18 (Figure 5.5f). The simulated time scales and equilibrium position are off with respect to the experiments. This could be due to different parameters such as the velocity or the run times, or to the aerotactic model (see section 5.3.1). Nevertheless, the qualitative behavior matches with the experiments. I can also study the wave of bacteria fleeing from the anoxic end of the capillary (Figure 5.5b), where oxygen concentration and gradient are 0. I can plot this quantity as function of time (Figure 5.5g) and I can linearly fit it to obtain the wave velocity (blue lines in Figure 5.5h). I compare these velocities with the theoretical prediction of Equation 4.6 (red stars), and I observe a certain discrepancy. This could be due to the fact the Equation 4.6 was calculated for constant gradients and for a different response function of the run-times on the gradient, which included an intermediate linear behavior. Here, there is no gradient since the oxygen is 0, but I still observe the wave of bacteria driven by chemotaxis towards the band.

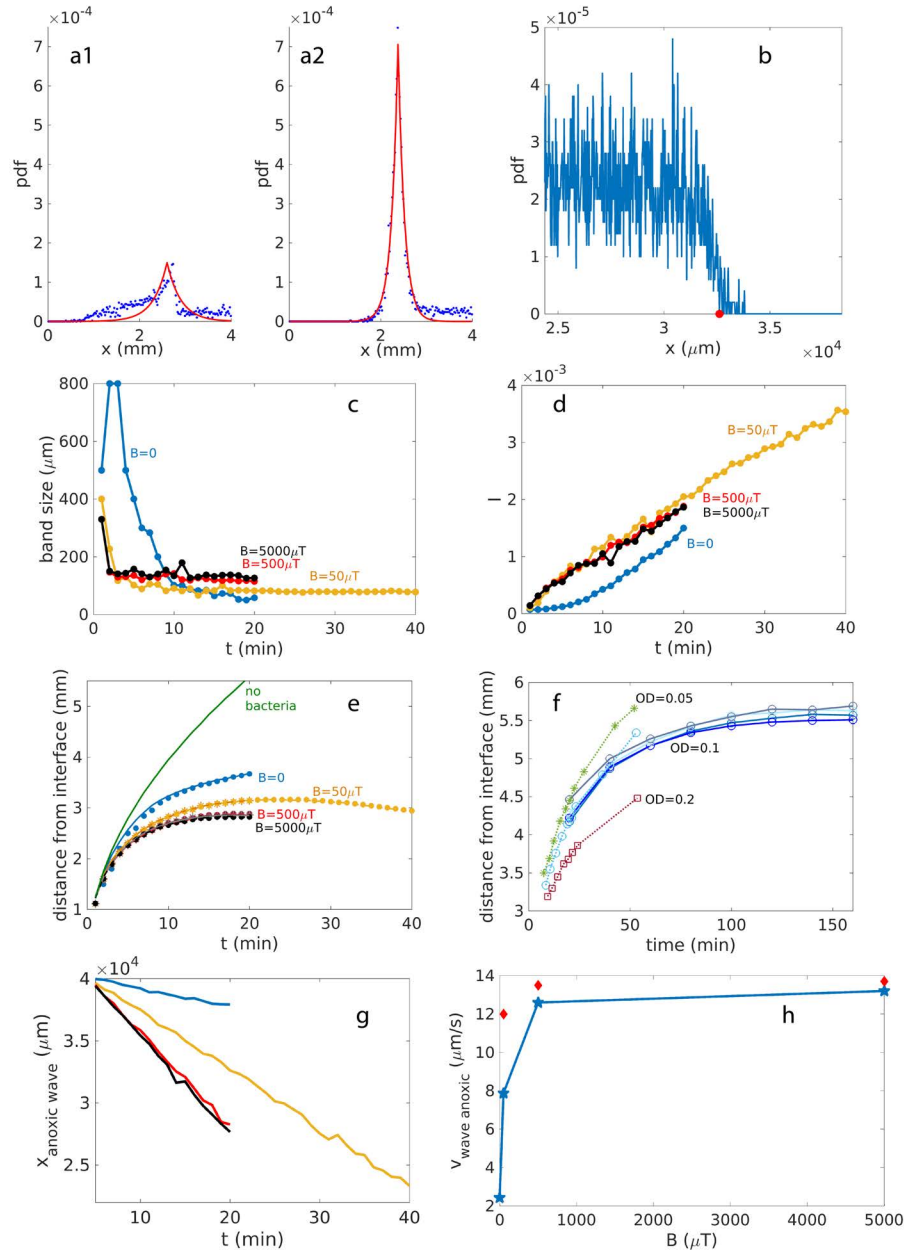


Figure 5.5: Parallel and antiparallel magnetic fields. (a) Band of bacteria at 6 min for $B = 0$ (a1) and $B = 500 \mu T$ antiparallel (a2). In blue the simulation data-points, in red the corresponding Laplace distribution fitting. (b) Bacteria density at the anoxic end. A wave of bacteria is formed, fleeing from the closed end of the capillary. The red dot indicates the wave position. (c) Band-size evolution in time for $B = 0, 50, 500, 5000 \mu T$ antiparallel. (d) Intensity of the peak of bacteria in pdf units (μm^{-1}) plotted against time $B = 0, 50, 500, 5000 \mu T$ antiparallel. (e) Time-dependence of the simulated band position (dots) and preferred concentration position (lines) in the case of no bacteria (green), or 25000 bacteria at different magnetic fields, $B = 0, 50, 500, 5000 \mu T$ (parallel and antiparallel coincide). (f) Experimental band position as function of time at different concentrations (green, blue and red) and for different days (filled and dotted lines) for an antiparallel field of $50 \mu T$. Experimental data: courtesy of Klaas Bente (paper in preparation). (g) Anoxic wave position against time for various magnetic fields. (h) Anoxic wave velocity as function of the magnetic field intensity (blue). In red, the theoretical prediction of Equation 4.6.

Until now, I ignored the effects on the yz cross-sections. I can now analyze them. In the absence of magnetic field and of chemotaxis (first row of Figure 5.6), there is no significant oxygen gradient along the y and z directions, and the distribution of bacteria is random. Turning on chemotaxis produces a wall effect that is visible only when the bacteria distribution is averaged over all the x cross-sections (row 2 plot 3). The bacteria accumulate at the walls and this effect is even more accentuated in the corners. Changing the size of the capillary (third row) does not eliminate the problem. Since this wall effect is not visible looking at the single cross-section at the band center (row 2 and 3 plot 2), I consider it as irrelevant for my purposes. Turning on an antiparallel magnetic field (Figure 5.7) does not change this effect if the field is of $50 \mu\text{T}$ (row 1). However, for stronger magnetic field the effect disappears (row 2). In any case, I can conclude that a significant anisotropy can not be seen.

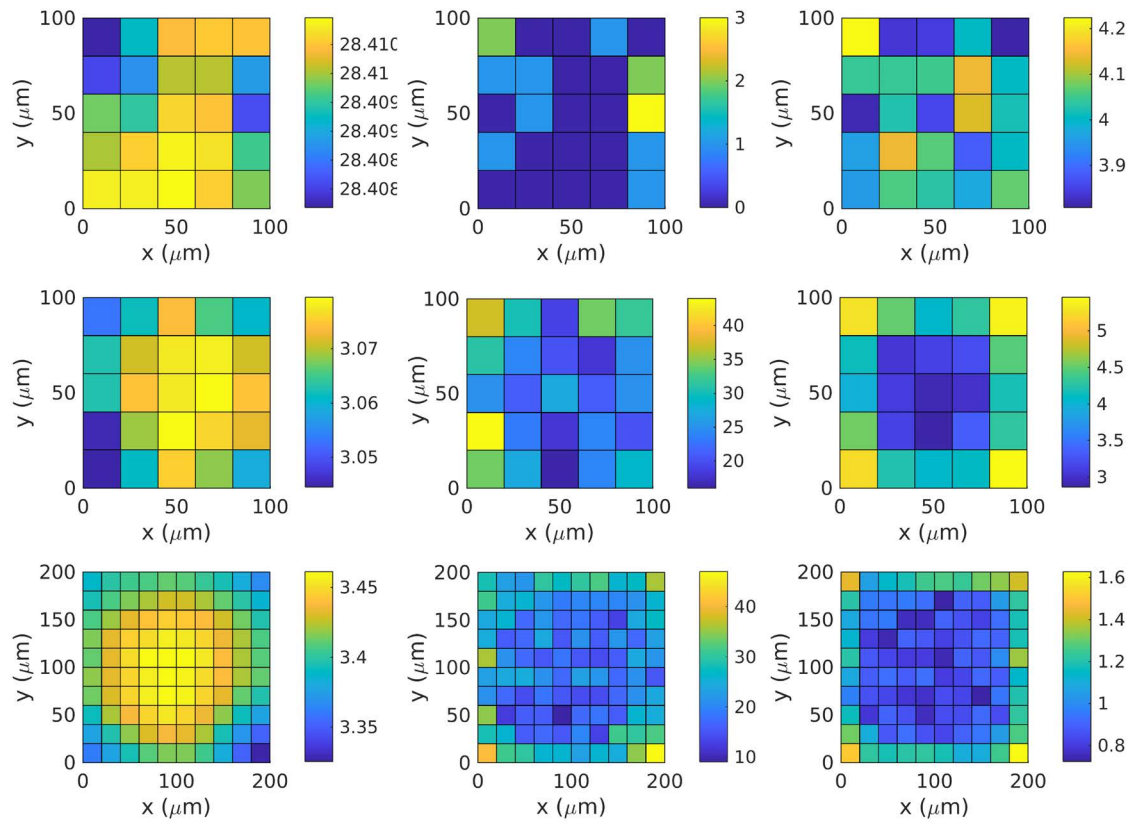


Figure 5.6: Yz section of the band profile at 20 min for no chemotaxis (first row), $0 \mu\text{T}$ (first row), $0 \mu\text{T}$ (second row) with a four times wider sections (third row). In the first column, oxygen concentration at the band position (μM), in the second column, bacteria percentage at the band position, in the third column the average over all the cross-sections along the x direction of the bacteria percentage.

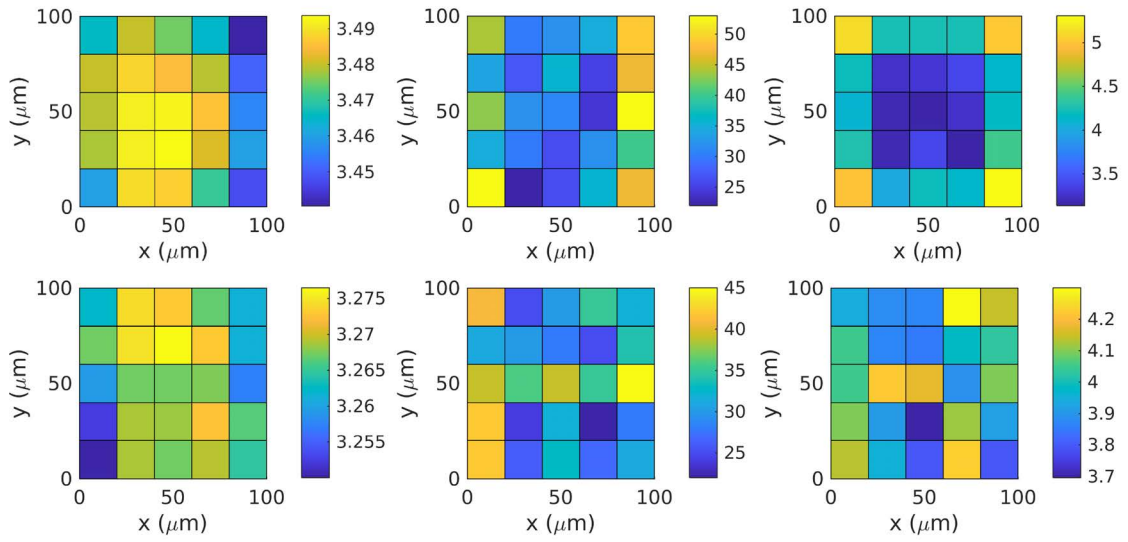


Figure 5.7: Yz section of the band profile at 20 min for 50 μT (first row) and 500 μT antiparallel (second row). In the first column, oxygen concentration at the band position (μM), in the second column, bacteria percentage at the band position, in the third column the average over all the cross-sections along the x direction of the bacteria percentage.

I can then turn the magnetic field at 90° along +y, after a normal band was formed for an antiparallel field. For a $50\ \mu\text{T}$ magnetic field, the band shrinks in size while increasing in density (Figure 5.8a), still retaining the same number of bacteria (32% of bacteria is in the band before turning, and 30% after turning). The shrinking happens in the first minute. After that, the band size remains almost constant in time (Figure 5.8c), while the band intensity increases (Figure 5.8c), indicating that bacteria keep populating the band. The preferred concentration position (Figure 5.8b) changes due to the change in the band behavior; nevertheless, the band keeps following the preferred concentration. This means that with a weak field the bacteria still retain a certain freedom of motion. For stronger fields instead, the band is stuck in position and the size does not change, nor the intensity. Looking at the yz sections (Figure 5.9), it can be noticed how no significant anisotropy in the band can be seen for weak fields, but only for strong: the bacteria accumulate on the -y side of the section. This result is interesting since axial bacteria should not have a preference for the direction of the magnetic field. To better understand what is going on, it is useful to look at the yx sections (Figure 5.10). For stronger fields, there is actually an asymmetry of accumulation on the oxic and anoxic side, with more bacteria accumulating at +y on the anoxic, and on -y on the oxic.

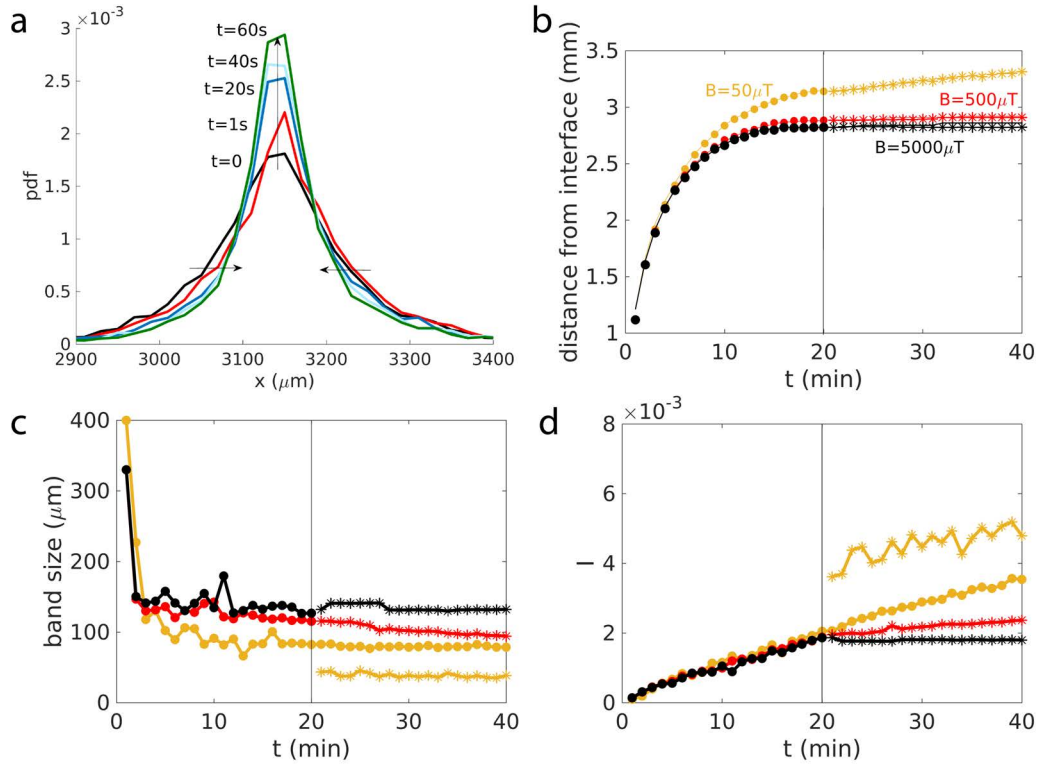


Figure 5.8: (a) Band profile for $50\ \mu\text{T}$: the band is formed in the AP (antiparallel) setting (first 20 min) and then the magnetic field is turned at 90° along +y. Each curve is plotted at a different time after the switching, and the arrows indicate the band evolution in time. (b) Band position (data points) and preferred concentration position (lines), (c) band size and (d) intensity for $50\ \mu\text{T}$ (yellow), $500\ \mu\text{T}$ (red) and $5000\ \mu\text{T}$ (black). The circles represent the system with an AP magnetic field; after 20 min, the field is switched to 90° along +y (stars).

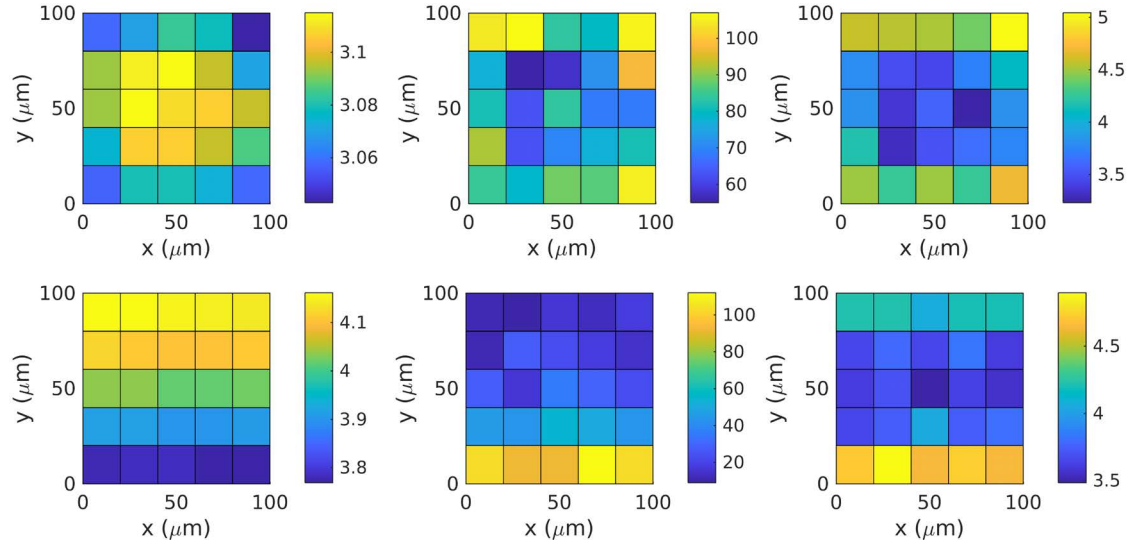


Figure 5.9: Yz section of the band profile at 20 min after the inversion of the magnetic field to 90° in the $+y$ direction (previously the band was formed with an antiparallel magnetic field), for $50 \mu\text{T}$ (first row) and $500 \mu\text{T}$ (second row). In the first column, oxygen concentration at the band position (μM), in the second column, bacteria percentage at the band position, in the third column the average over all the cross-sections along the x direction of the bacteria percentage.

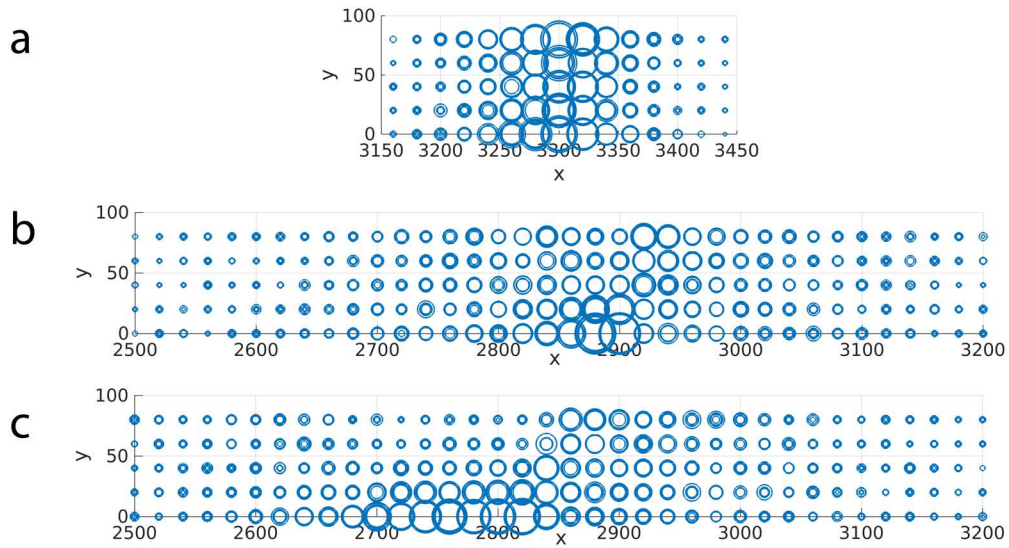


Figure 5.10: Xy section of the band profile at 20 min after the inversion of the magnetic field to 90° in the $+y$ direction (previously the band was formed with an antiparallel magnetic field), for $50 \mu\text{T}$ (a), $500 \mu\text{T}$ (b) and $B = 5000 \mu\text{T}$ (c). The blue circles are proportional to the number of bacteria in the cell.

Finally, I can look at the band formation for which I set the magnetic field at 90° from the beginning, starting with a random distribution of bacteria (Figure 5.11). In this case, a weak magnetic field slows sensibly down the band formation, with a band profile at 20 min similar to the one obtained in the absence of fields at 5 min (a). Stronger fields inhibit the band formation, with no band being formed at 20 min (b). The result with the weak magnetic field confirm that axial bacteria can still perform aerotaxis even at the Equator.

In conclusion, some important results can be learned from the simulations on axial bacteria: first, I am able to reproduce the band position dynamics in time as it happens in the experiments but on faster time scales, meaning that either the model or some parameters are off; second, the velocity of the wave of bacteria fleeing the anoxic side follows only partially the equations 4.6 and 4.7 that I obtained for the taxis velocity in Section 4, meaning that this equations depend on the type of gradient and on the response function of the run times; third, parallel and antiparallel magnetic fields allow to form well-defined bands at shorter times, fastening up aerotaxis, confirming the results of Chapter 4 with constant gradients; fourth, aerotaxis can still correctly happen for magnetic fields at 90° , but the dynamics is slowed down, confirming the results of Chapter 4; last, anisotropies in the cross-sections for the bacteria distribution and for the oxygen gradient can be ignored for parallel and antiparallel fields, but become an important feature for fields at 90° .

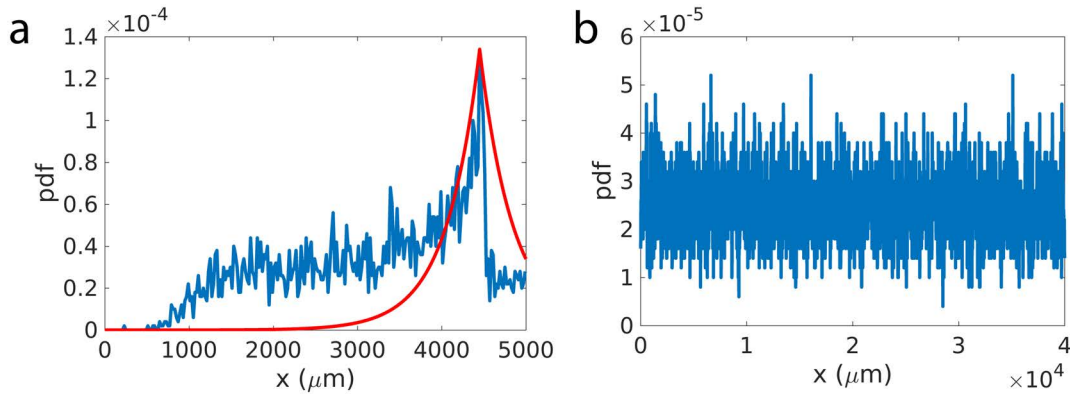


Figure 5.11: Bacteria density profile for (a) $B = 50 \mu\text{T}$ and (b) $B = 500 \mu\text{T}$ at 20 min with the magnetic field at 90° along $+y$ from the start of the simulation. The red line represent the corresponding Laplace fit.

5.3 Polar

Polar bacteria bias their walk on the absolute oxygen concentration and on the magnetic field direction. I implement here North Seeking (NS) bacteria, for which the correct configuration is an antiparallel magnetic field. With my model, the band cannot be formed without magnetic field. Experimental data are not reported in literature regarding this point. The band can be correctly formed only in the natural configuration with the antiparallel magnetic field (Figure 5.12), with a comparable behavior with respect to the axial model. Stronger fields produce a tighter band (b), while the velocity of population of anoxic wave is moving faster (c). The yz sections are also comparable to the axial case (Figure 5.13).

The model reproduces what happens to an already formed band after an immediate switch to a parallel field: the band splits up, an two traveling peaks are formed, one towards the oxic and one towards the anoxic side (Figure 5.14a). The two peaks are not symmetrical, and this behavior is reproducible (Figure 5.14b).

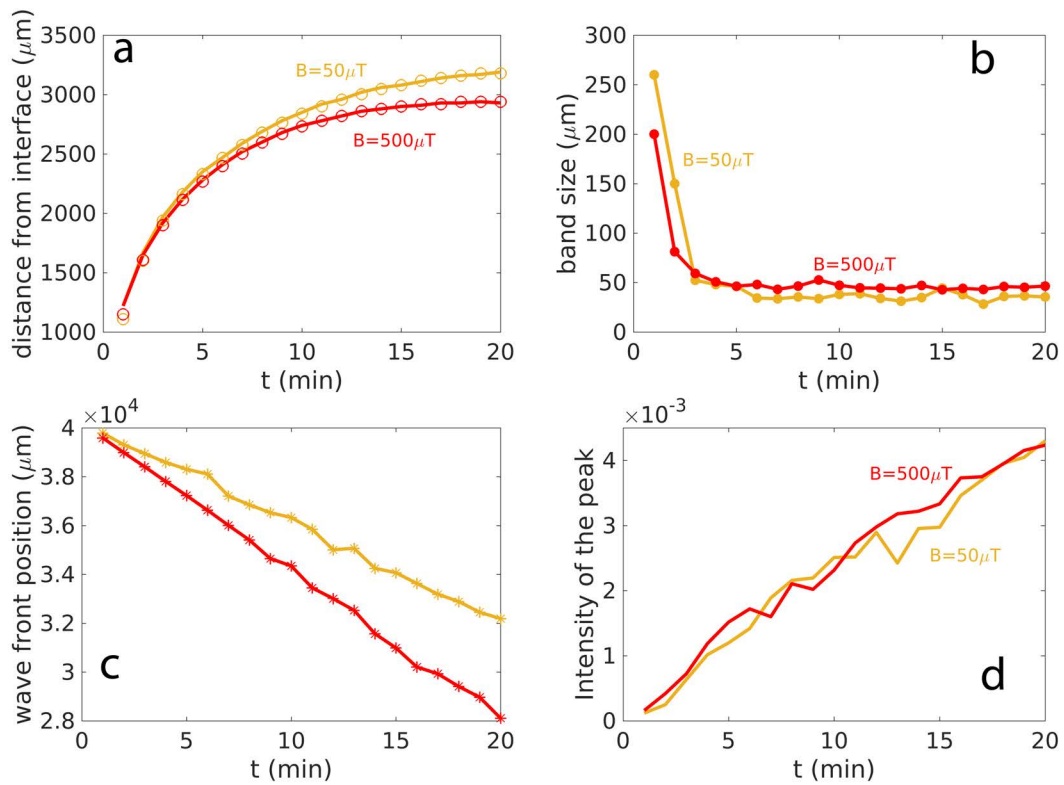


Figure 5.12: Band position (data points) and preferred concentration position (lines) (a), band size (b), band intensity (c) and anoxic wave position (d) for 50 μT (yellow) and 500 μT (red), for an antiparallel magnetic field.

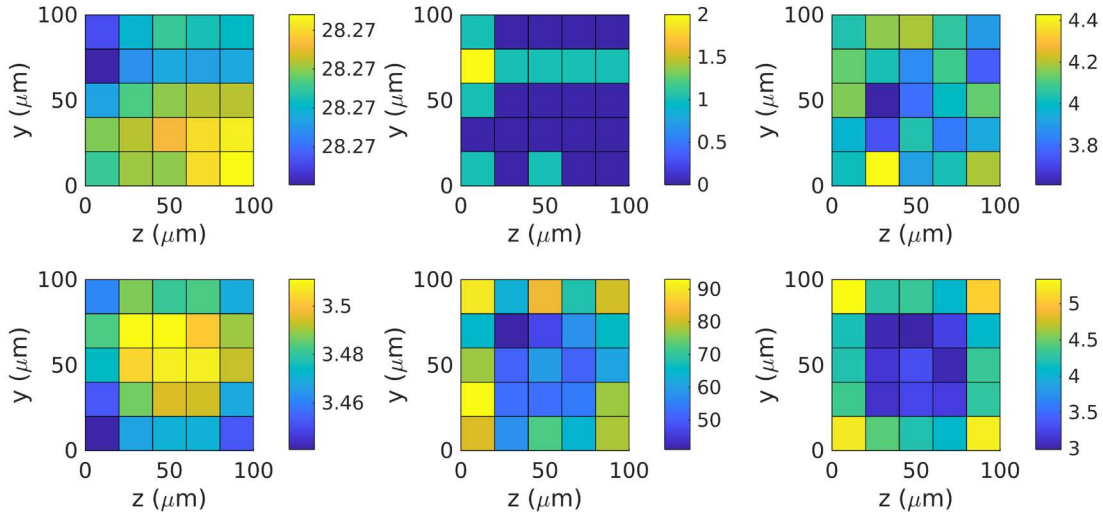


Figure 5.13: Yz section of the band profile at 20 min for $0\ \mu\text{T}$ (first row) and $50\ \mu\text{T}$ antiparallel (second row). In the first column, oxygen concentration at the band position (μM), in the second column, bacteria percentage at the band position, in the third column the average over all the cross-sections along the x direction of the bacteria percentage.

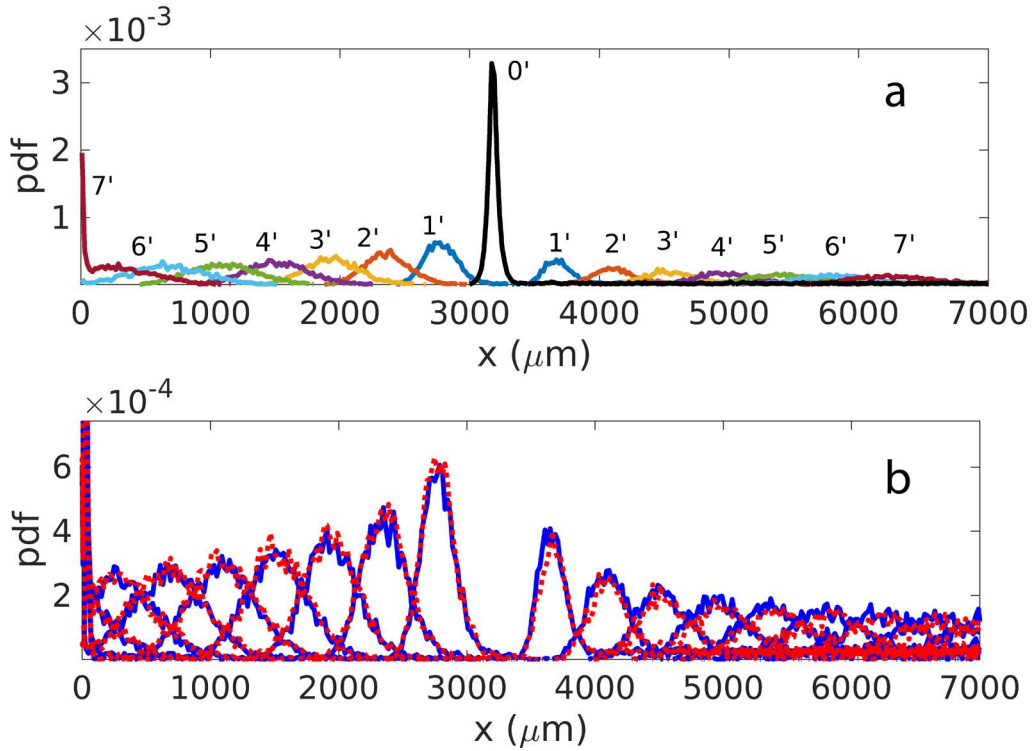


Figure 5.14: (a) After a band is formed with an antiparallel magnetic field (20 min), the magnetic field is switched to parallel. The numbers indicate the minutes from the switch. (b) Two independent repetitions of the same switching experiment.

When the field is set to parallel from the beginning, I still observe the bacteria traveling towards the sides of the capillary, and forming two peaks there (Figure 5.15a). The bacteria are split in two groups: the bacteria on the oxic side will all accumulate on the air-water interface and remain stuck there, and viceversa for the bacteria on the anoxic side. Since bacteria on the anoxic side are much more than on the anoxic, the intensity of the peak will still keep growing till all the bacteria have reached the end of the capillary (Figure 5.15c). The wave of bacteria traveling towards the anoxic end (red point in Figure 5.15a) presents a velocity dependent on the magnetic field (Figure 5.15d). The preferred concentration position is the same for the two magnetic fields (Figure 5.15b), and differs from the case of $B = 0$, for which the bacteria remain randomly distributed.

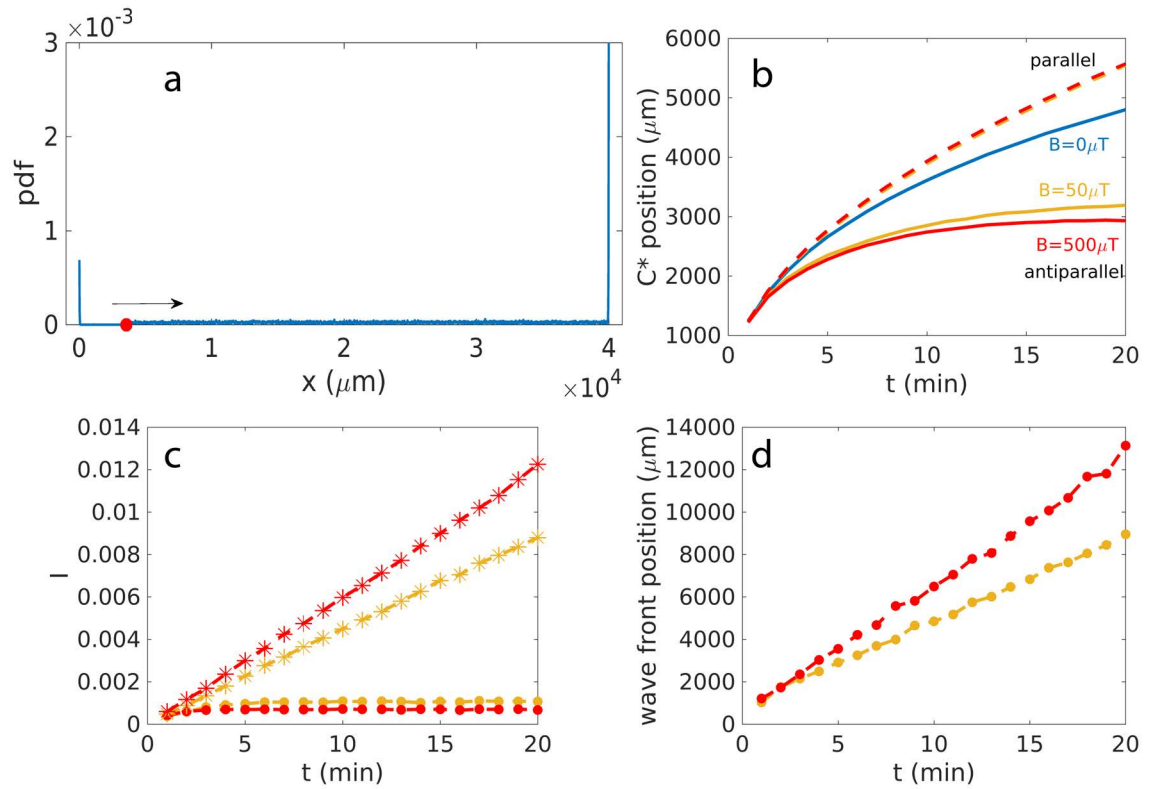


Figure 5.15: A random distribution of bacteria is exposed to a parallel magnetic field from time 0. (a) A typical bacteria density profile, where the red dot indicates the position of the anoxic wave and the arrow indicates the motion of the wave in time. (b) Preferred concentration position for $B = 0$ (blue), $B = 50 \mu\text{T}$ (yellow) and $B = 500 \mu\text{T}$ (red) in the antiparallel (filled lines) and parallel case (dashed). (c) Intensity of the peaks: dots for the peak on the oxic side, and stars for the anoxic. (d) Anoxic wave position.

I can also turn the magnetic field at 90° after the band is formed. Pronounced differences can be spotted with respect to the axial case. Here the band remains completely stuck in position, unable to follow the preferred concentration (Figure 5.16a), while the band size increases (b) and the intensity drops (c), meaning that the band is dissolving. Looking at the sections (Figure 5.17), it can be noticed that a small oxygen gradient ($0.005 \mu\text{M}\mu\text{m}^{-1}$ for the $50 \mu\text{T}$ and $0.01 \mu\text{M}\mu\text{m}^{-1}$ for the $500 \mu\text{T}$) is present in the yz cross-section at the band, and that bacteria accumulate at the +y direction, since here the oxygen is higher than the preferred concentration (which is situated further away from the air interface).

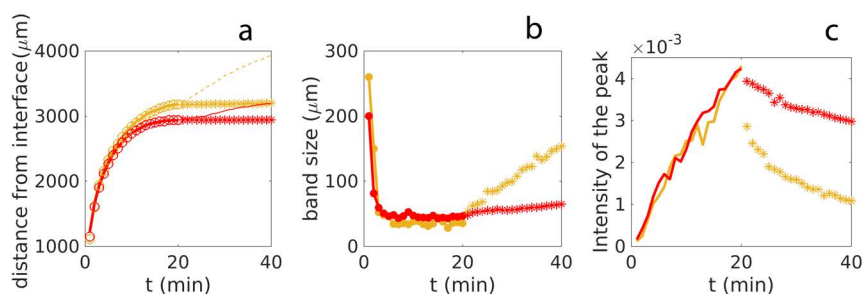


Figure 5.16: Band position (data points) and preferred concentration position (lines) (a), band size (b) and intensity (c) for $50 \mu\text{T}$ (yellow) and $500 \mu\text{T}$ (red). The circles represent the band formed with an antiparallel magnetic field; after 20 min, the field is switched to 90° along +y (stars).

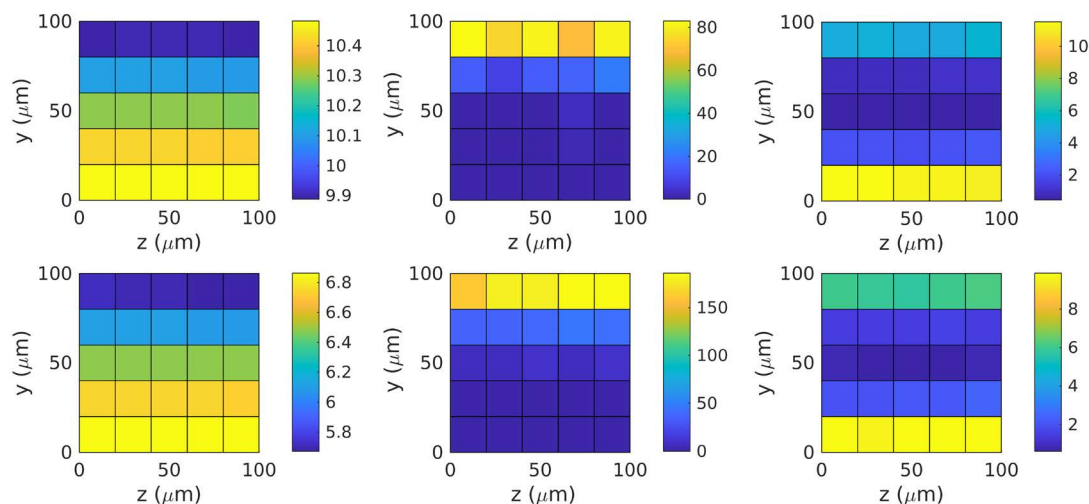


Figure 5.17: Yz section of the band profile at 20 min after the inversion of the magnetic field to 90° in the +y direction (previously the band was formed with an antiparallel magnetic field), for $50 \mu\text{T}$ (first row) and $500 \mu\text{T}$ (second row). In the first column, oxygen concentration at the band position (μM), in the second column, bacteria percentage at the band position, in the third column the average over all the cross-sections along the x direction of the bacteria percentage.

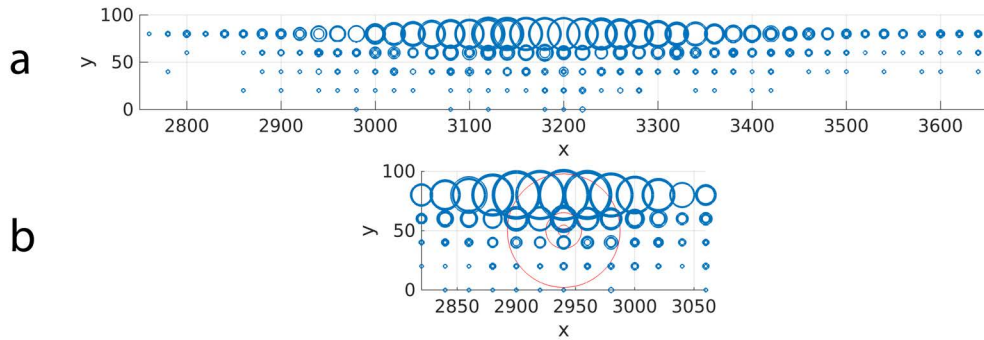


Figure 5.18: Xy section of the band profile at 20 min after the inversion of the magnetic field to 90° in the +y direction (previously the band was formed with an antiparallel magnetic field), for $50 \mu\text{T}$ (a) and $500 \mu\text{T}$ (b). The blue circles are proportional to the number of bacteria in the cell. In red, reference circle for 1, 10, 100, 1000 bacteria.

Instead, in the mean over all cross-sections, bacteria accumulate at the -y side; this is due to the higher percentage of bacteria present in the anoxic side, where they follow the - direction of the field. The xy cross-sections (Figure 5.18) show that the band all accumulates on the +y side, since the oxygen concentration here is higher than the preferred one. Finally, if a 90° field is set from the beginning for a random distribution of bacteria, no band can be formed.

Summing up the main results for NS polar bacteria, I can conclude that: first, the model reproduces the experimental observations of the band splitting up after the magnetic fields have been reversed from antiparallel to parallel [79], and of bacteria accumulating Nord in the oxic side and South in the anoxic [16]; second, the model qualitatively behaves like the axial model for antiparallel fields, with the band following the preferred concentration position, and the magnetic fields fastening up the dynamics; third, the absence of magnetic fields, parallel magnetic fields and magnetic fields at 90° hinder aerotaxis, impeding the correct band formation; finally, anisotropies becomes even more evident in the cross-sections with magnetic fields at 90° compared to the axial case.

5.3.1 Change of Parameters and Comparison Polar and Axial

I saw that there is a discrepancy in the time scales and position of the axial band with respect to the experiments (see section 5.2). To understand where this discrepancy comes from, I try to vary parameters such as the velocity of the bacteria and the run times, and I compare it to the polar model. First I vary the self-velocity for the axial bacteria with an antiparallel field of $50 \mu\text{T}$. I see that the equilibrium band size increases (Figure 5.19a), accordingly to the higher spacial excursions that the bacteria are doing around the preferred concentration. The increase in the intensity instead slows down (b), while the wave velocity increases (d). The dynamics of the band position is also affected (c), being faster for higher velocities. Thus, a possible factor that could rescale this plot is the self-velocity of the bacteria. The effect is not drastic though, and cannot be the only factor explaining my discrepancy.

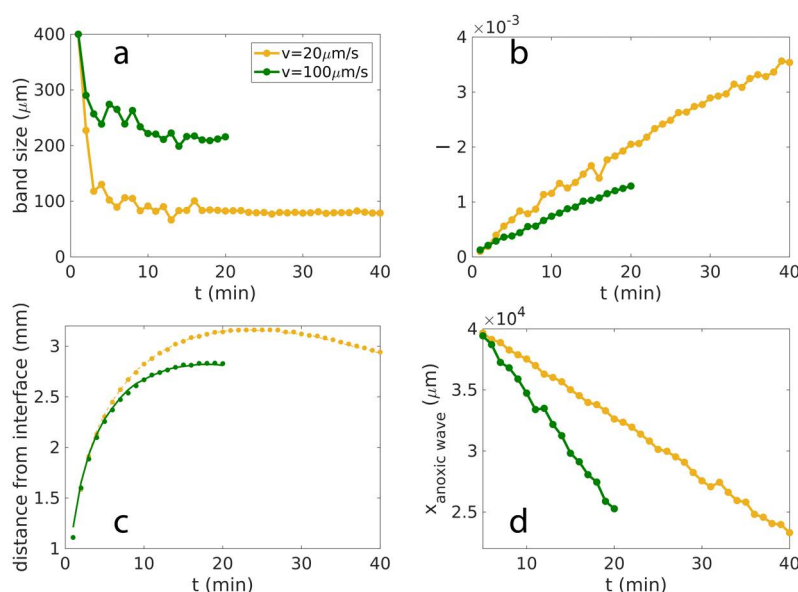


Figure 5.19: Effect of the bacterial velocity on band size (a), band intensity (b), band position (data points) and preferred concentration position (lines) (c) and anoxic wave position (d) for an axial model and a $50 \mu\text{T}$ antiparallel field.

I then vary run times and to compare the results between axial (in yellow) and polar (in red, Figure 5.20). I consider two sets of parameters. For set 1 (continuous line, used in my polar simulation in Section 5.3), $t_{\text{up}} = 2\tau_0$, $t_{\text{down}} = \tau_0/2$ ($R_{\text{time}} = 0.6$); and set 2 (dashed line, used for axial in section 5.2), for which $t_{\text{up}} = 6\tau_0$, $t_{\text{down}} = \tau_0$ ($R_{\text{time}} = 0.7$). The following quantities depend on the run-times parameters and not on the model: the band-size at equilibrium (a), the rate of increase in the peak intensity (b), the dynamics of the band position (c) and the velocity of the anoxic wave (c). It depends on the model the band size at small time (a) and the anoxic wave position at small times (d). In any case, I can conclude that the differences in the dynamics of the band position are not related to the model (axial or polar) but rather to the factor R_{time} . Here the change is small due to the small difference of the R_{time} . To perfectly match the data, I need to determine these values experimentally.

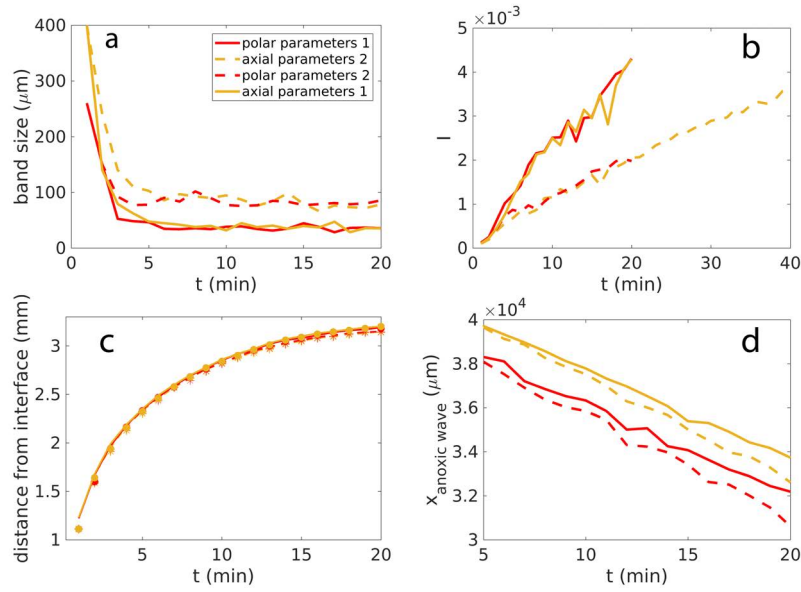


Figure 5.20: Comparison between axial (yellow) and polar (red) models, with two different sets of parameters: $R_{\text{time}} = 0.6$ for the continuous line/filled dots, and $R_{\text{time}} = 0.7$ for the dashed line/stars. Dependence on time of the band size (a), band intensity (b), band position (data points) and preferred concentration position (lines) (c), and anoxic wave position (d) for an antiparallel field of $50 \mu\text{T}$.

5.4 Alternative Aerotactic Models

Many experimental questions are still open; for example, there is no precise measurement of the biased run times towards the band for both axial and polar. Nevertheless, some data on the run time lengths are available. For example, there are hints that polar bacteria suppress reversal events and prefer very long runs in constant oxygen conditions (oxic or anoxic), where the oxygen gradient is 0 [80]. Therefore I implemented a model for which the run times depend on the presence or on the absence of the oxygen gradient: the run times become $t_{\text{up}} = 2\tau_0$, $t_{\text{down}} = \tau_0/2$ for a gradient different from 0 ($R_{\text{time}} = 0.6$), and $t_{\text{up}} = 30\tau_0$ where there is no gradient at all ($R_{\text{time}} = 0.97$). I compare it with the two controls with $R_{\text{time}} = 0.6$ and $R_{\text{time}} = 0.97$ everywhere (first row of Figure 5.21). While the band is symmetrical for the controls, broader for the higher R_{time} factor, the peak of bacteria is asymmetrical for the new model (Figure 5.21a), with a sharper cut on the anoxic side. The size and intensity are intermediate with respect to the two controls. The velocity of the anoxic wave instead, where the gradient is 0, is the same for the new model and the control with $R_{\text{time}} = 0.97$ (Figure 5.21b). Since I see experimentally that the band is sharper on the oxic side, this model most probably does not represent what is happening in reality.

For axial bacteria, chemokinesis was observed, meaning that an higher bacterial velocity was observed on the oxic side with respect to the anoxic [78]. To understand if this could influence the dynamics of the band, I include chemokinesis in my axial model. In principle, the same could also be done for the polar. I use the difference in velocity measured in our lab, where the oxic side present $v = 23 \mu\text{ms}^{-1}$ and on the anoxic where $v = 19 \mu\text{ms}^{-1}$. As it can be seen in Figure 5.21c and d, no difference can be spotted between the axial model with and without chemokinesis (respectively, red and blue curve). As a control, the distribution of bacteria remains random for all the duration of the experiment if only chemokinesis is used, and chemotaxis is turned off (yellow). I also tried a model with chemokinesis and a faster switching around the band (purple), but also in this case the band cannot form. Here the run times are reduced to 0.45 s close to the preferred concentration ($\pm 150 \mu\text{m}$, typical band size), and are of 0.65 s away from it (data obtained experimentally without considering differences in t_{up} and t_{down} , but averaged to obtain a single run time). I conclude that with this small velocity difference that was observed experimentally, my model is not affected by chemokinesis. Experimental data courtesy of Mohammad Charsooghi.

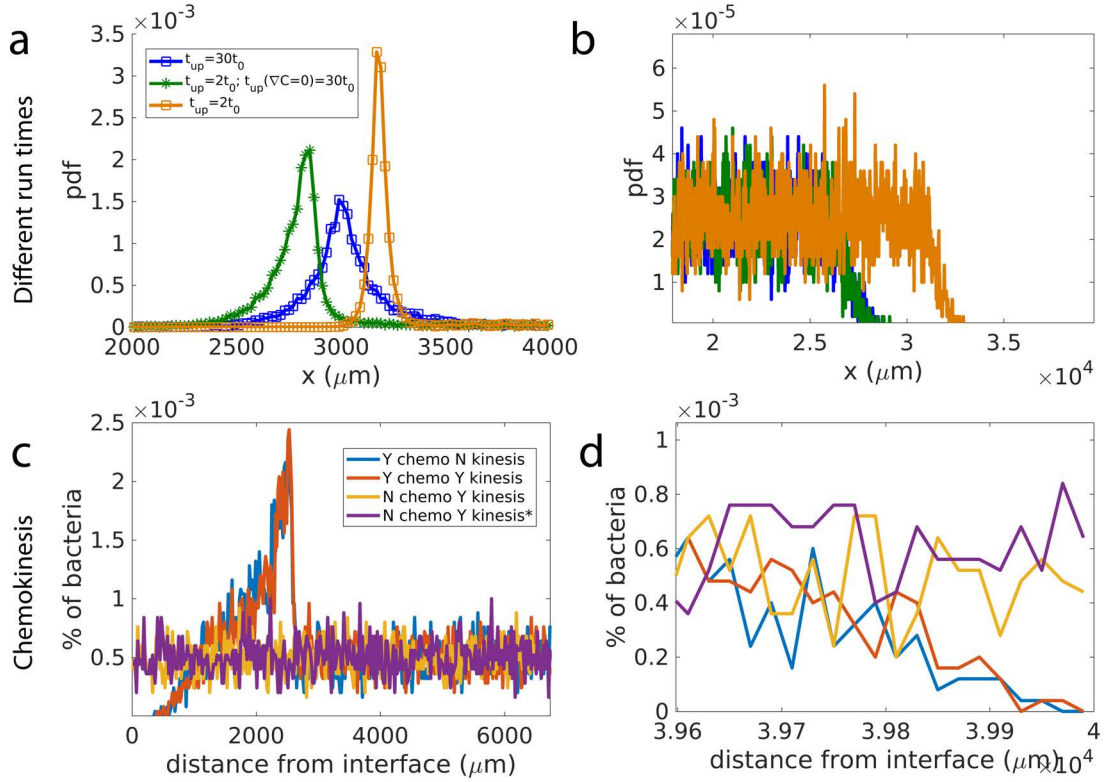


Figure 5.21: Alternative models. Different run times: band profile (a) and anoxic wave (b) for polar bacteria with an antiparallel field of $50 \mu\text{T}$ for a mixed model with $R_{time} = 0.97$ in the absence of oxygen gradient and $R_{time} = 0.6$ otherwise (green), compared to the controls (blue $R_{time} = 0.97$ and yellow $R_{time} = 0.6$). Chemokinesis: band profile (c) and anoxic wave (d) for axial bacteria without magnetic field in the control case with only chemotaxis (blue) compared to chemotaxis plus chemokinesis (orange), only chemokinesis (yellow), and only chemokinesis with higher switching rate nearby the preferred concentration (purple).

6 Bacteria In Confinement

MTB often live in the first layer of sediments (see Section 2.2.4); also, many envisioned biomedical applications include crowded systems. Therefore, in this chapter I consider bacteria that move in confinement, *i.e.* where the interactions with walls becomes of major importance. I concentrated on two systems. First, I consider bacteria swimming in round microtraps of few micrometers of diameter (Section 6.1). Tuning the wall interaction, I am able to reproduce the experimental data for such traps. Second, I consider bacteria swimming in sediments. A sediments sample was analyzed with a microCT scan (Sections 6.2.1 and 6.2.3); the data were then used to run 2D (Section 6.2.2) and 3D simulations (Section 6.2.4), and to plan future microfluidic experiments (Section 6.2.1). The simulation parameters used are listed in Table D.1, if not stated otherwise.

6.1 Circular Traps

The motility of bacteria can be studied in cylindrical microtraps closed on all the sides, with radii ranging between $15\text{ }\mu\text{m}$ and $80\text{ }\mu\text{m}$, and heights of $10\text{ }\mu\text{m}$, making it a quasi-2D circular system. These microtraps are experimentally realized in our lab (experimental data courtesy of Elisa Cerdá Doñate), and the trajectories of the bacteria can be extracted to study their motion (Figure 6.1 first row). A similar study is reported in literature for algae [135]. The main difference with my system is the dimensions (algae are bigger than bacteria), the hydrodynamic characteristics (algae are pullers and possess a round shape), and the impossibility of applying magnetic fields. Studying magnetotactic bacteria in such microtraps allows us to apply magnetic fields to gain an insight on wall interactions under external torques. Moreover, I can use the data acquired experimentally to tune my simulated interactions.

6.1.1 Simulations

I want to replicate the experimental results (Figure 6.1 first row). Bacteria swim along the borders of the microtraps, as it can be inferred from the trajectories (first column), the heat-map that indicates how probable is to find a bacterium there, and the radial distribution histogram (third column) with a clear peak close to the border of the trap. These are preliminary experimental data; in particular, it can be seen that some trajectories are outside of the expected border of the trap (green line). This can be due to traps that are not perfectly cylindrical. Nevertheless, I can use these preliminary data to get an idea of the wall interaction, since the general behavior inferred from these experiments agrees with what reported in literature for algae [135].

To simulate wall interactions, a WCA potential can be used to calculate the force acting on the bacterium upon contact [36, 135] (see Section 3.5). The force is not only exerted by the curved walls, but also by the flat walls closing the trap. The simulation is thus not equivalent to a pure 2D simulation, where the effect of the flat walls would be neglected. This WCA force produces few crossings of the center of the trap, while the bacterium can be localized most of the time at

the wall (row 2 6.1). The corresponding heat-map and histogram show an unnatural peak at the border, because the bacterium does not get reoriented by the wall interactions and keeps pushing against the wall while sliding along it. Introducing a torque that mimicks hydrodynamic interaction (see Section 3.5) leads to reorientation of the bacterium and a decreased density along the border (third row). Tuning the parameters leads to a good match with the experimental data (fourth row). Therefore, I used this interaction on the following sand study. Finally, I can predict the behavior

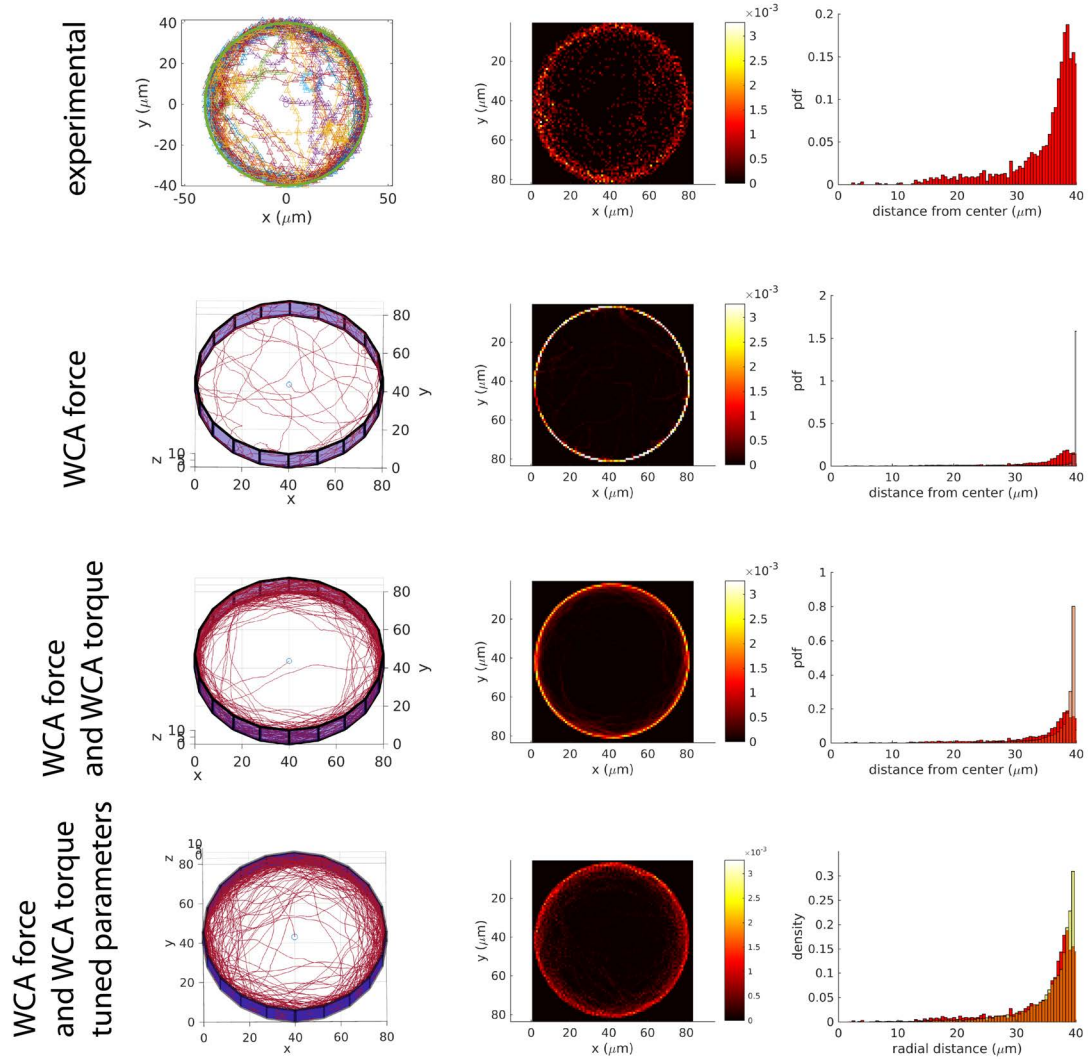


Figure 6.1: For a trap of $40\ \mu\text{m}$ in diameter, comparison between the experimental results (first row, courtesy of Elisa Cerdá Doñate) and different simulations. First column, the trajectories; second, heat-map where the colorbar is proportional to $n_{\text{counts}}/(n_{\text{tot}}\text{bin} - \text{size}^2)$, with bin of $1\ \mu\text{m}^2$; third, histogram of the radial distribution of bacteria, compared to the experimental histogram in red.

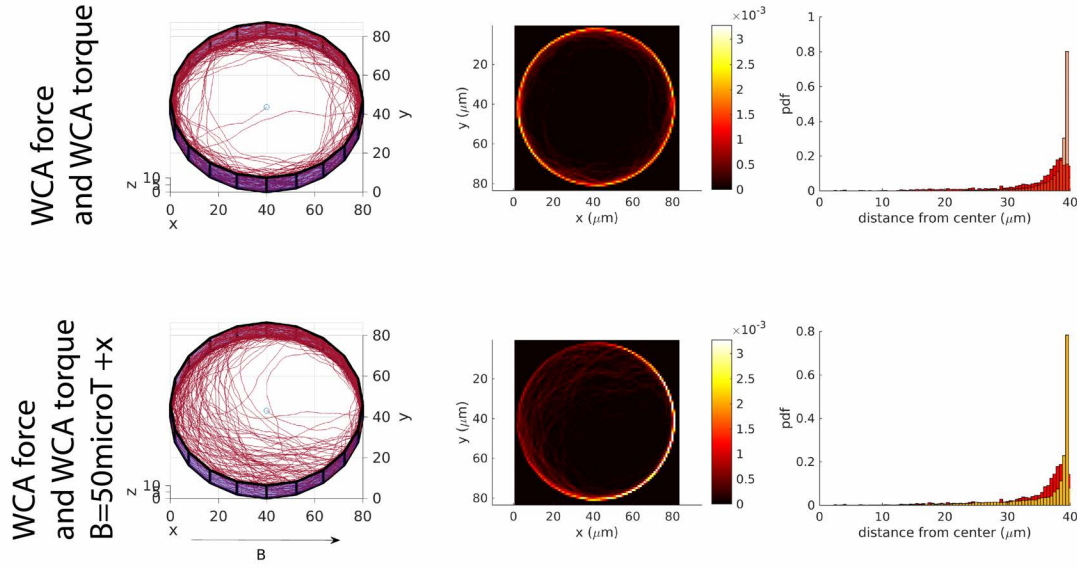


Figure 6.2: Effect of a 50 μT magnetic field on the trajectories, heat-map and histogram of the radial distribution.

of a bacterium exposed to magnetic fields (second row Figure 6.2). The bacterium would swim closer to the wall on the side where the magnetic field points, and spread towards the center on the other side, with an effect visible already at the Earth magnetic field.

6.2 Bacteria in Sediments

I characterized a real sand sample from Großer Zernsee lake (Potsdam, Germany), where MTB can be found, and used the data for the simulations. The strength of this approach is that I did not assume random parameters for the sand grains and distribution as previous studies [36, 103, 35], but rather I adjusted them to the real environment where these bacteria live. The use of the experimental distribution of the grains-size and of the water-gaps dimensions prevents artificial effects due to regular spacing of pillars of the same dimensions, and more closely resemble the maze-like environment in which the bacteria live. To characterize the sediments, a sample of sand in water was analyzed through microCT with a resolution of $1.56 \mu\text{m}$ (we thanks Zaslansky Paul for the help in preparing and running the experiment and for the reconstruction of the raw data). The microCT technique allows a three dimensional characterization of the sample, allowing us to study the real gap-size distribution in water. Two dimensional slices of the sample are obtained; these slices can be used for a 2D or a 3D characterization, as explained in the following sections. The simulation results in this chapter are preliminary, and lay the basis for future studies. In particular, I use a constant oxygen gradient, ignoring the bacteria consumption and the oxygen flow. Moreover, I neglect fluid flow. Magnetotactic bacteria were recently studied under fluid flow [115, 103]. While the influence of fluid flow was proved for bacteria living in ground-water environments [13], the influence on the sediment environment of magnetotactic bacteria is a open debate. Nevertheless, fluid flow can be studied in the optics of biomedical applications.

6.2.1 2D Experimental Characterization

The 2D sections of the microCT reconstructed data can be analyzed as described in Section 3.8, and used to produce 2D microfluidic channels. The slices (Figure 6.3a) can be processed to obtain a black and white mask (b), the equivalent circles distribution (red circles in (c)), the radii distribution (d), as well as the mean radius and the percentage of sand respect to water, which is 60% for all the analyzed slices of the sample at different depths (see Table 6.1). The fitted circles can be used as an equivalent mask approximating the real sand (e), with only a slight loss in the sand percentage (see Table 6.1). Then, the two masks (the real sand one and the circle-approximated one) can be used to produce a quasi-2D microfluidic channel (f). In a central channel of depth $10\ \mu\text{m}$ (enough to have the bacteria always in focus for tracking, see Appendix F), the bacteria are injected on one side and are left free to swim between the obstacles (the pillars with the section provided by the masks). The two side channels could be used to flow medium rich and poor in oxygen to create an oxygen gradient on the short section of the central channel. These future experiments can be compared to the simulation of the following chapter.

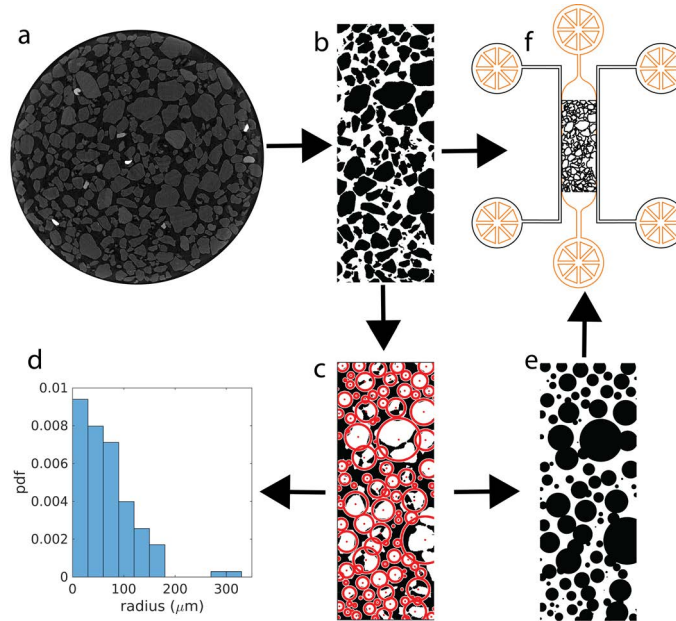


Figure 6.3: Experimental 2D study of the sand. The microCT slices (a) are cropped out as to ignore border effect due to the reconstruction, and binarized (b). The binarized image can be fitted with circles (see methods) (c), from which the statistics (d) and an equivalent mask (e) can be obtained. (b) and (e) then can be used to design microfluidic channels (f), in which the bacteria are injected in the middle channel ($3.5\ \text{mm} \times 1.2\ \text{mm} \times 10\ \mu\text{m}$) where they encounter cylindrical obstacles, while the two side channels can be used to create an oxygen gradient.

name	height (μm)	sand %	circles %	mean radius (μm)	s.e.m. (μm)
1	0	62.4	59.3	67.8	5.1
2	624	61.6	57.9	64.4	4.4
3	1248	64.3	57.3	62.3	3.7
4	1872	66.4	62.0	61.7	3.9

Table 6.1: 2D analysis of the sand. For each slice are given: the distance from the bottom, the percentage of sand $\text{area}_{\text{sand}}/\text{area}_{\text{tot}} \times 100$ for the processed sand image, for the fitted circles, and the mean radius from the fitted circles with its standard mean error.

6.2.2 2D Simulation

The circles-fitted masks of Figure 6.3e can be used to run a simulation that would exactly resemble the experimental set-up, simplifying the simulation-experiments comparison. Since we lack experimental data, I use the wall interactions that I tuned in the circular traps Section 6.1. Here a different force prefactor is used for the cylindrical pillars respect to the walls, to tune the interaction and avoid unnatural effects (see Table D.1). In fact, if I use the same prefactor for both interaction with flat walls and with sand grains, unnatural displacements are calculated ('explosions'). This is due to the fact that the mean grain size is much bigger than the bacteria radius that I used as the radius of the imaginary sphere for the flat walls (see Methods 3.5). For my simulation, I run 100 trajectories of 1000 s, with random starting position at $x=0$. I run two sets of experiments: a control without pillars (first column of Figure 6.4) and with the circles-fitted mask of Figure 6.3e (second column). The control without pillars is needed to take into account possible effects due to the interactions with the two flat walls that could change the results compared to the pure bulk. The basic case of axial bacteria without magnetic field or chemotaxis is shown in the first row. Only half millimeter is explored in both cases, with and without sand. When chemotaxis towards an attractant is turned on (second row, with the gradient pointing towards $+x$) the bacteria further explore the space; the obstacles hinder the diffusion of the bacteria. Then, I run a control without chemotaxis but with a parallel magnetic field along $+x$ (third and fourth row, 50 and 500 μT respectively) and I compare them to the case with chemotaxis (fifth and sixth row). Magnetic fields alone help to explore more space. For 500 μT however, the effect is smaller. When chemotaxis is turned on together with magnetic fields, the bacteria perform chemotaxis faster. The presence of the sand has two major effects in this case: some bacteria get stuck in some points and cannot escape, and preferred pathways ('streamlines') are selected (see Appendix H for a comparison with the experimental data of Rismani Yazdi *et al.* [103]). This effect is more visible looking at the heat-map (Figure 6.5): the points in which bacteria would get stuck are in yellow, the preferred streamlines are brighter then the blue background. The effect is stronger for stronger magnetic fields.

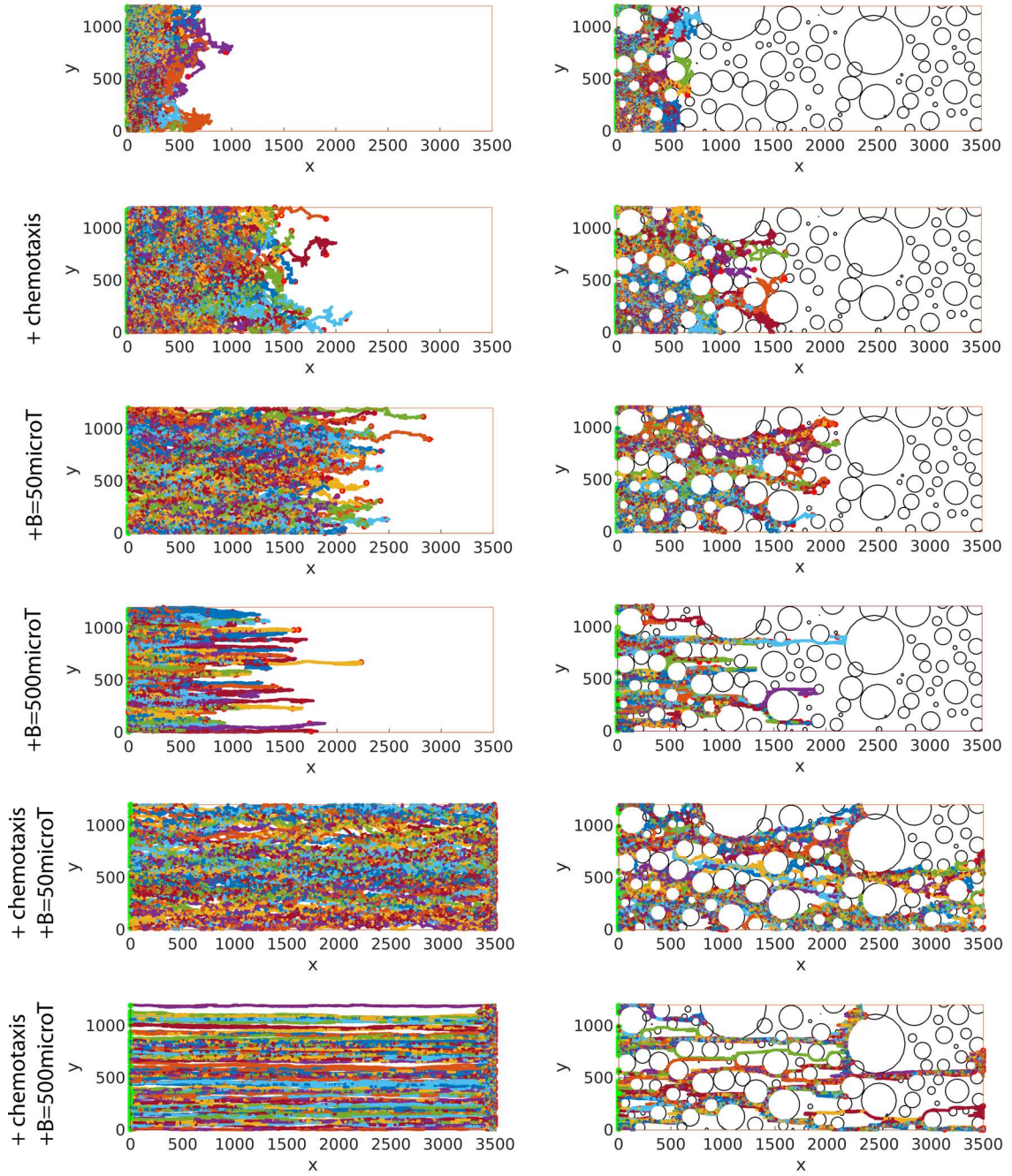


Figure 6.4: 100 example trajectories of 1000 s all starting at $x = 0$, with sand and without sand, in a channel with $10 \mu\text{m}$ depth (measuring $1.2 \text{ mm} \times 3.5 \text{ mm}$), for various cases: reference, chemotaxis towards an attractant, a magnetic field of $50 \mu\text{T}$ and $500 \mu\text{T}$, and chemotaxis towards an attractant together with a magnetic field of $50 \mu\text{T}$ and $500 \mu\text{T}$.

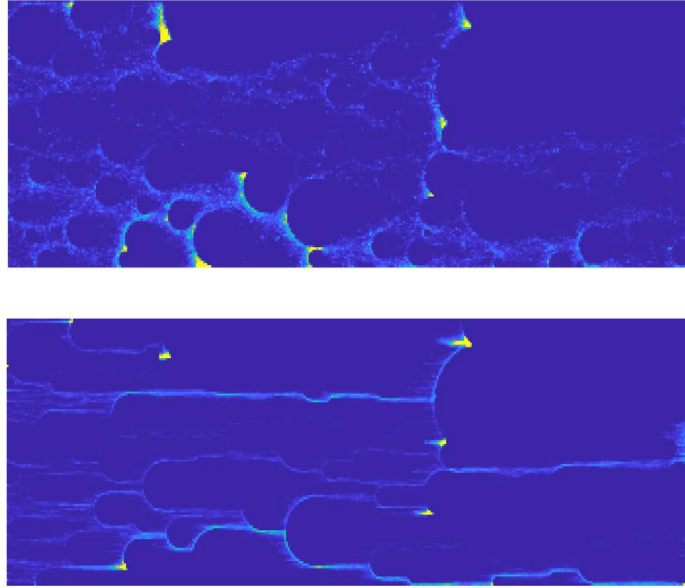


Figure 6.5: Heath-plots for 100 bacteria trajectories performing chemotaxis towards an attractant and a magnetic field of $50 \mu\text{T}$ (first row) and $500 \mu\text{T}$ (second row). Brighter colors indicate higher probability to occupy that point in time.

To extract information from these data, such as velocity and diffusion constant, the usual procedure would include the calculation of the mean squared displacement. However, I aim to compare these data to the experiments. To obtain a good mean squared displacement, the tracks must be followed for very long times and wide spacial range, such as to include the effect of the sand. In fact, if short tracks are considered, no difference would be visible respect tracks in the bulk, due to the high dimension of the channels. Experimentally is problematic to follow a bacterium for such long time and for such wide spacial ranges, because the limited field of view (around $270 \mu\text{m}$ for 40X magnification and $180 \mu\text{m}$ for 60X, necessary to perform a good tracking) would include only few sand grains (whose mean radius is $60 \mu\text{m}$) and thus only few channels. Since tracking cannot be used, alternative methods should be implemented. One solution would be to consider a small field of view where to count the bacteria over time. In Figure 6.6 this method is applied to my simulations. I consider a field of view of $200 \mu\text{m} \times 200 \mu\text{m}$ centered at $x = 500 \mu\text{m}$ and $y = 600 \mu\text{m}$ (in the insets). I count the number of bacteria other time, in the case of chemotaxis towards an attractant, with or without sand (dark and light colors), for three magnetic fields (red $0 \mu\text{T}$, green $50 \mu\text{T}$ and blue $500 \mu\text{T}$). The signal presents a peak at a certain time. The peak can be fitted with a Gaussian, and the center can be taken as a measure of the mean passage time t_{passage} at $500 \mu\text{m}$. From this the chemotactic velocity can be calculated, as $500 \mu\text{T}/t_{\text{passage}}$. Even though the field of view is small and mainly occupied by the sand grains, still the peak is visible, proving that this method can be applied in the experiments, too. The sand is slowing down the wave of bacteria, and reduces the counts. It could also enhances the counts if the field of view is centered on one of the streamlines. The magnetic fields fasten up the dynamics and narrows the wave.

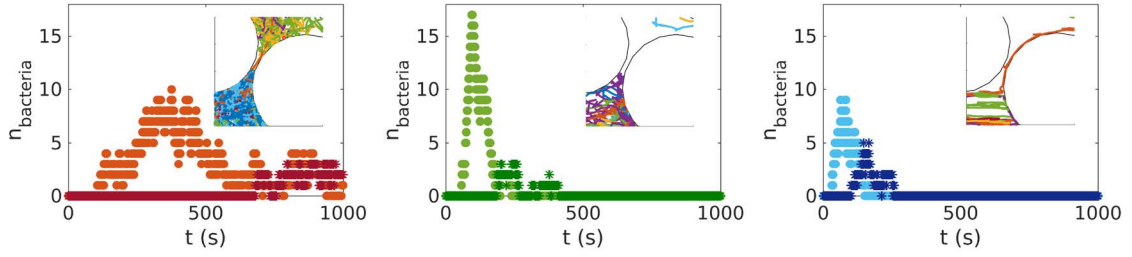


Figure 6.6: Number of bacteria as function of time in a window of $200 \mu\text{m}^2$ situated at $x = 500 \mu\text{m}$, for bacteria in bulk (dots in light colors) and with sand (stars in dark colors), for chemotaxis towards an attractant for three different magnetic field intensities: $0 \mu\text{T}$ (red), $50 \mu\text{T}$ (green), $500 \mu\text{T}$ (blue). The insets show the area considered for the bacteria counting in the presence of sand.

The velocities obtained with this method are compared to the ones obtained as the slope of the linear fit of the mean x position versus time (Table 6.2), and can be also compared with the Appendix G. While for the bulk the two methods are equivalent, for the sand I observe a certain discrepancy, with the field of view-method overestimating the velocities; most probably there is a dependence on where the field of view is situated, thus a mean over a bigger field of view is desirable. In general, the velocities are lower than the predicted values of Equation 4.6; this could be attributed to the wall interactions, even in the case without sand since the channel is so low that provides confinement.

B (μT)	sand	v (μms^{-1}) (f.o.v.)	v (μms^{-1}) (mean x)	theory (μms^{-1})
0	Y	0.74	0.65	/
50	Y	4.3	2.3	12.1
500	Y	5.9	4.8	13.6
0	N	1.3	1.0	/
50	N	4.5	4.4	12.1
500	N	5.8	6.2	13.6

Table 6.2: Taxis velocities calculated with the field of view method (f.o.v.), with the mean x method, and compared to the theoretical results of Equation 4.6.

6.2.3 3D Experimental Characterization

While the 2D analysis could be useful to actually compare the simulated results to 2D experiments, a 3D analysis helps us to get as close as possible to Nature. 3D experiments are not possible since the sediments would prevent the bacteria visualization, but simulation can be still performed. To reproduce an environment as close as possible to the natural one, the 2D slices obtained from the microCT can be visualized in 3D using for example the Amira software (Figure 6.7). The grains of sand present smooth surfaces and rounded shapes. The grains can get up to $500\ \mu\text{m}$ in dimension, while the gaps range from few micrometers to hundreds of μm . The distribution of the grain sizes and of the gaps sizes can be obtained through the CTAn software respectively looking at the trabecular thickness and trabecular separation, where spheres are fitted as to remain inside the volume of the grain/gap.

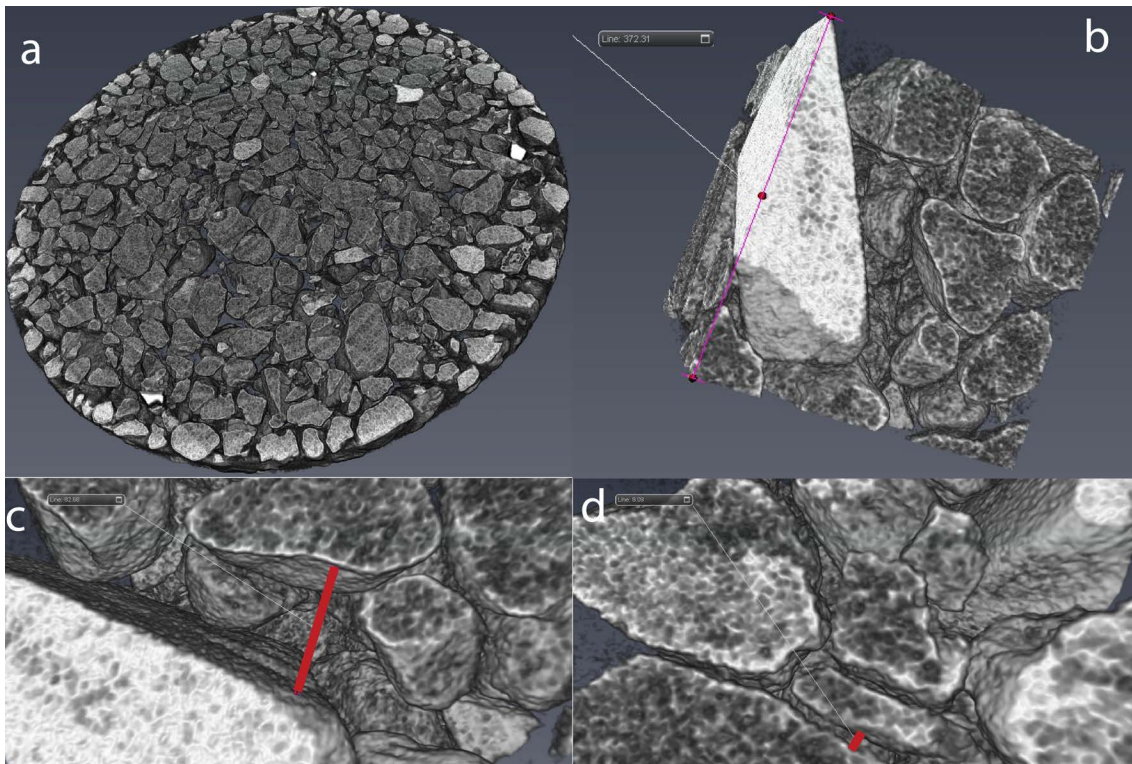


Figure 6.7: 3D visualization of the sand in water with Amira software. (a) In the 3D visualization of the bottom slices, a border effect is visible due to the reconstruction as a dark external ring. (b) A cube of $580\ \mu\text{m}$ from the center of the cuvette. (c) and (d) Two examples of gaps, respectively of $129\ \mu\text{m}$ and $13\ \mu\text{m}$ (red line).

The obtained distributions (Figure 6.8) give the statistics of the minimum dimension of the grains/gaps. This means the grain size is under-estimated, while the gap sizes are well represented. The grain size follows a log-normal distribution with a mean size of $46\mu\text{m}$ (many sediments follow a log-normal distribution [141]); with this mean dimension, the sediment is cataloged as silt [141]), while the gaps follow a normal distribution with mean $\sim 43\mu\text{m}$, and the percentage of sand is around 61%. To better estimate the grain size, an equivalent radius using a centroid method could be calculated. The problem is that most grains are touching, and the water/sand contrast is not high, so this method is not applicable since it would detect just a big sphere and not the single grains of sand.

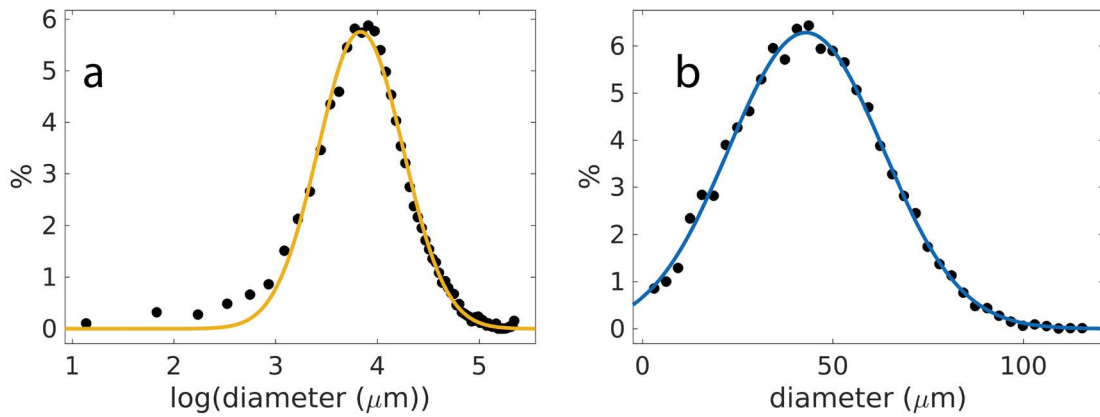


Figure 6.8: Statistics of the sand in water obtained through CTAn software, for the bottom layers of the cuvette (first 2 mm). The trabecular thickness gives the statistics of the sand-grain smallest diameter (a), while the trabecular separation represents the water-gaps between grains (b). The solid lines correspond to Gaussian fit $a \exp(-(x - \mu)^2/c^2)$. Yellow $\mu = 3.83$, $c = 0.5903$ corresponding to a mean sand diameter of $46\mu\text{m}$; blue $\mu = 42.94\mu\text{m}$, $c = 28.66\mu\text{m}$.

6.2.4 3D Simulation

From the statistics obtained from the 3D analysis, an equivalent set of spheres can be generated as described in the methods Section 3.10. The statistics is shown in Figure 6.9a, compared to the original log-normal distribution from which the grain sizes were sampled. This results in a box of side of $500\ \mu\text{m}$, filled with spheres representing the grains of sand (Figure 6.9b). The simulations are performed fixing a starting position, and setting a constant chemotactic gradient along $+x$. An example trajectory without magnetic field is shown in (c), while in (d) an example interaction with the spheres is shown. Three example trajectories at $0\ \mu\text{T}$ (red), $50\ \mu\text{T}$ (green) and $500\ \mu\text{T}$ (blue) are visualized without sand (e). There is a border effect: the bacteria seem to prefer to slide along the border of the box rather than to enter inside the grain maze. To avoid this effect, the spheres could be taken to overlap the box-boundaries. In figure (e), the interaction between a bacterium and a flat wall for strong magnetic fields is visible in the blue curve: the bacterium slides along the wall and then reverses with trajectories perpendicular to the wall. This behavior resembles the one observed experimentally by Rismani Yazdi *et al.* for flat walls [103] (see Appendix H). From these simulation I can conclude that the walls interactions seem to give reasonable results compared to the experiments; moreover, there is a hint that magnetic fields fasten up chemotaxis also for this 3D case. These preliminary data should be integrated to understand deeper the behavior of bacteria in such complex porous systems.

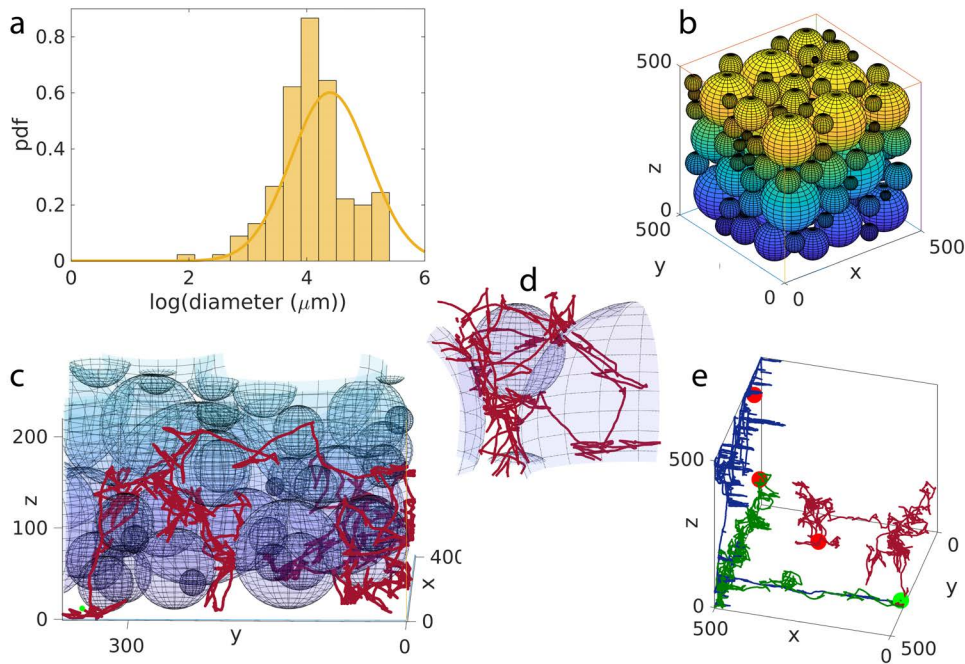


Figure 6.9: 3D sand simulation. (a) From a typical Gaussian distribution of the logarithm of the grain-diameters ($\mu = 4.393$, $c = 0.99389$) (yellow line), a correspondent distribution of spheres is obtained (histogram). (b) The spheres in the simulation box. (c) Typical trajectory in the box ($0\ \mu\text{T}$). (d) The interaction with the spheres. (e) Trajectories of 1000 s obtained in the sand for $0\ \mu\text{T}$ (red), $50\ \mu\text{T}$ (green), $500\ \mu\text{T}$ (blue). The sand is not shown for better visualization. The green and red dots correspond to the starting and ending position.

7 Discussion: Bacterial Swimming Behavior

In this chapter, I will discuss the results of Chapters 4, 5, 6 regarding the bacterial swimming behavior. The discussion will be divided as follows: comparison between tumble and reverse, the aerotactic models, advantage of magnetic fields for chemotaxis, and the behavior in porous environments.

7.1 Tumble vs. Reverse: the Change of Direction

In my thesis, I consider a run-and-tumble mechanism. *E. coli* run-and-tumble has been thoroughly studied in literature, providing all the parameters of motion, such as run times and the tumbling angle distribution in 3D [45, 24, 56, 2, 58]. Often, to describe the motion, ABP models are used for the runs, which are interrupted by tumbles. The tumble can be implemented in more ways, for example drawing the angle from a certain distribution [142, 89, 140], or considering an enhanced thermal noise effect [133]. Respect normal ABP models, the presence of tumble affects the motion: in fact, tumbles change the diffusion constant, which inversely depends on one minus the cosine of the tumbling angle [2, 50]. Moreover, when magnetic fields are present, the tumbles change the distribution of the alignment angle (the angle between the bacterial dipole and the external magnetic field). For magnetic cells performing straight deterministic runs without noise, interrupted by tumbles, the histogram of the alignment angle shows a peak at zero, an effect called in literature 'velocity-condensation' [140]. This histogram differs from the Langevin distribution expected for a dipole passively aligning with magnetic fields in the presence of noise [32]. With my simulation, I quantified all these effects on the motion, too. My model for tumbling magnetic cells combines an ABP model interrupted by tumbles, where tumbles are implemented thanks to an enhanced rotational noise [133]. This method is equivalent to the ones that use angles drawn from a distribution, once the thermal noise is correctly tuned. The parameters were adapted from *E. coli* [45]. I verify that the diffusion constant is affected by the tumbles (Appendix B), as shown in literature. Moreover, I also quantify the effect of tumbles on the alignment angle in the presence of magnetic fields. When there is no noise, I replicate the 'velocity-condensation' phenomenon for the alignment angle distribution [140]; however, I show that noise modifies this distribution, producing a peak at angles different from zero; moreover, the dimension of the system (3D or 2D) influences the distribution when noise is present, an effect not shown in the absence of noise [140].

Another possible change of direction is the reverse [46, 136], often performed by MTB [80]. Therefore, I also considered reversal events in my model, instead of the tumbles. The reverses are implemented as a stop followed by a switch in the sign of velocity without reorientation of the body, as proven experimentally for many bacteria [46, 80, 136, 103]. The reverse does not influence the alignment angle distribution.

Theses changes of direction are crucial for the correct outcome of chemotaxis in the presence of magnetic fields [45, 2]. I have shown that reverse and tumble lead to different behaviors for

axial bacteria: while a reversal strategy allows the bacterium to reach its preferred concentration (being it the maximum for an attractant or a finite value for aerotaxis), no matter the direction of the magnetic field, a tumbling strategy would impend chemotaxis towards an attractant with an antiparallel magnetic field, and would completely hinder the band formation for aerotaxis with any magnetic field direction. This is due to the fact that a tumble pushes the bacterium out of alignment, reorienting its body, with a mean angle of 68° [45]; the magnetic field at that point realigns the bacterium to the magnetic field itself always in the parallel direction, obtaining a trajectory that follows the magnetic field. On the contrary, reverse preserves the body orientation and changes just the sign of the velocity [32], allowing the bacterium to swim both parallel or antiparallel to the field. I can imagine chemotaxis and magnetic fields as two 'signals' that can be contrasting or reinforcing each other and that determine the bacterium swimming direction. With this interpretation, an axial bacterium performing tumble would prioritize the 'signal' from the magnetic field with respect to the chemotaxis pathway; while axial bacteria performing reverse would give more importance to chemotaxis. These findings support the experimental evidence for which no magnetotactic bacteria species perform tumble as main change of direction motion (while it was observed under certain conditions as a minor strategy [77, 80]). These findings are crucial for future biomedical applications envisioning biohybrids: the change of direction strategy matters to ensure the correct chemotaxis in the presence of magnetic fields, as well as the aerotactic model (polar or axial). For example, in a typical cancer-targeting application, magnetic cells are directed with magnetic fields towards the solid tumor, while chemotaxis or aerotaxis allow the biohybrid to infiltrate inside the solid tumor. For such a situation, a magnetic biohybrid based on *E. coli* [18], performing tumble, would encounter difficulties for wrong orientations of the magnetic fields; the task can be correctly performed only if the fields are parallel to the chemical gradients. On the contrary, bacteria performing reverse and axial aerotaxis are able to reach the target both for parallel and antiparallel magnetic fields.

7.2 The Aerotactic Models

With my model, axial aerotaxis is represented as a simple chemotaxis towards a preferred concentration, together with passive alignment to magnetic fields [16]. The model for chemotaxis was adapted from *E. coli* [45], from which I took the parameters such as run times, tumble times, and velocities, and the general concept of longer runs towards a preferred concentration and shorter away. In my model, the run times depend on the chemical species concentration and on the spacial gradient, while for *E. coli* it was demonstrated that a temporal gradient is sensed [44, 2, 60, 56, 61, 62, 54, 49, 63]. Experimental data on the MTB aerotaxis are not complete though, for this reason a chemotactic response in time as it was done for *E. coli* was not determined. Therefore, I use my model with a spacial gradient as an effective approximation of the unknown temporal response.

When simulating aerotaxis, things are complicated even more compared to *E. coli* chemotaxis, since aerotaxis was shown to be both a direct kind of taxis (*i.e.* behaving like *E. coli* chemotaxis, with the bounding of the chemical producing a direct cascade of signals that affects the flagellar motor) and indirect (*i.e.* an energy taxis, where the bacteria monitors the internal energy that is affected by the oxygen presence, indirectly influencing the flagella rotation) [68]. Moreover, simple KS models are not adequate to describe the aerotactic capillary assay, since they do not

take into account a strong oxygen gradient with diffusion and consumption of the oxygen [68]. An alternative model was proposed for the aerotaxis performed by *Azospirillum brasilense* [68]. This model is strongly based on this particular bacterium behavior: reversal rates are higher out of the band and lower in the band, and the bacteria change direction as soon as they exit the band. This model cannot be applied directly to MSR-1; in fact, in our lab it was seen that axial MSR-1 do the opposite, and they have higher switching rates inside the band and lower outside (unpublished data, courtesy of Mohammad Charsooghi). In my thesis, I tried to implement this model, showing that this kind of response alone is not sufficient to form a band (see Section 5.4).

Modification of the aerotactic model for *Azospirillum brasilense* [68] have been used in literature to simulate the MTB aerotactic behavior. Smith *et al.* [84] proposed an increased switching rate whenever bacteria find themselves in oxic conditions and they swim up the spacial gradient. These simulations show that the bacteria do not form a stationary band, and that the band is asymmetrical [84, 78]. The model was further improved by Bennet *et al.* [78], including increased switching rates also when the bacteria is found in anoxic conditions and they swim down the gradient. This model allows the formation of a stationary, symmetrical band. My model is based on the one of Bennet *et al.* as far as it regards the chemotactic response; however, instead of integrating the equations for the density of bacteria as it is done in literature [68, 84, 78], I integrate the equation of motion of each single bacterium, obtaining their trajectories. This allows me to obtain the same type of data that are given by tracking experiments; moreover, it allows me to simulate changes of directions and thermal noise in 3D. This consists in an improvement, since the MTB model based on the density equations are accurate only for very strong magnetic fields that hinder the noise effect and reduce the motion in 1D [78], while with my simulation I can provide an accurate description of a 3D motion subjected to noise and with weak magnetic fields.

I do not only study axial aerotaxis, but also polar. In my model, the main difference between axial and polar bacteria performing reverse is that axial bacteria prioritize the chemotaxis, and use the magnetic field just as an axis of direction; instead, polar bacteria bias their chemotaxis directly on the magnetic fields themselves, in agreement with previous formulations [16, 79]. This model confirms precedent experiments, where it has been observed that polar bacteria with the wrong magnetic condition do not form a band [79]. The polar model used in this thesis incorporates switches in both oxic and anoxic conditions, with longer runs towards the preferred concentration and shorter runs away (see Section 3.1 for details on the model). This is used as a working hypothesis, since experimental data on the run time lengths as function of the direction of motion are lacking. The bacterium measures the absolute concentration to decide if it is above or below the preferred one, but then it biases its motion on the magnetic field direction. As a consequence, the magnetic field provides the orientation through passive alignment and thanks to the magnetic chain configuration with respect to the flagellum, and no active sensing of the magnetic field is involved. To explain how such a mechanism is possible, a solution similar to the one that Frankel proposed for bacteria with one flagellum [16, 137] (see Section 2.2.3 for details) can be proposed. The difference with the model proposed by Frankel (in which the flagellum changes its sense of rotation and thus its direction of motion only when passing from oxic to anoxic conditions or *viceversa*) is that the flagellum mainly rotates CCW in the oxic area but it is still able to change to CW, and it rotates mainly CW in the anoxic but it is still able to switch to CCW motion. My models thus allows reversal events in oxic/anoxic conditions, which were observed experimentally [80] and that are not be incorporated in the model by Frankel. For bacteria with two polar flagella, this model would still work if an asymmetry in the behavior of the two flagella would be present.

There is at the moment no available data on this point. In literature, both for polar and axial bacteria, magnetic fields are recognized to have a passive influence on the dynamics, with no active sensing [32]. This point is controversial, and an active influence of magnetic fields on the aerotactic sensing was proposed by Popp *et al.* [80]. Since this model was not reproduced by other experiments, and since the accepted idea in the field is that no active effect is visible, I did not consider this effect in my thesis.

My polar model makes some prediction on the bacteria behavior that could be easily verified experimentally. For example, it predicts no band formation if the magnetic field is absent. It has not been reported in literature yet what happens to polar bacteria when no magnetic field is present. If a band would be formed even without magnetic fields alternative considerations should be done. Also, the model predicts no band formation for a misleading magnetic field at 90° with respect to the oxygen gradient. However, polar magnetotactic bacteria can be found at the Equator, where the magnetic field is at nearly 90° with respect to the oxygen gradient [32, 82, 83]. The model predicts that NS bacteria cannot perform correct chemotaxis with parallel magnetic fields. However, NS bacteria could be found in small percentage in the South pole, where the magnetic field lines are parallel to the oxygen gradient in the water environment of bacteria [32, 81]. Considering that polar bacteria are found in Nature also in completely unfavorable conditions, a possible explanation could be that my model is partially wrong; or that environmental fluctuation (such as fluid flow etc.) could prevent the bacteria from reaching harmful oxygen concentrations; or that bacteria can switch between polar and axial behavior according to the environmental condition. MSR-1 itself changes between axial or polar according to the growth conditions or from polar north seeking to south seeking [79, 80], but there are no data in favor of the hypothesis that a bacterium can change from polar to axial during its life without undergoing division.

More experiments are also needed to confirm if axial and polar bacteria perform chemotaxis biasing their run times as *E. coli* does, with longer runs towards the preferred concentration and shorter away from it; in fact, there are no data in literature measuring the run times in a favorable direction t_{up} and run times towards an unfavorable direction t_{down} . Knowing these parameters would help us in the tuning of the model, to understand how the time-scale discrepancies seen in the capillary experiments are arising. From more detailed experiments, in principle we could also distinguish between different response function for the mean run times as function of the concentration and the gradient (axial), or as function of the concentration and the magnetic fields (polar). I have seen in fact that changing this response function changes the band formation dynamics. I can conclude that my simulations together with future experiments could be useful to understand the aerotactic models of magnetotactic bacteria.

7.3 Advantages in the Use of Magnetic Fields in the Bulk

One of the questions at the basis of this thesis is to quantify the advantage that the interaction with magnetic field gives to magnetotactic bacteria. The general idea in literature is that the Earth magnetic field restrains the motion in one dimension, making chemotaxis faster [16, 32, 84]. I see with my model that axial chemotaxis in the bulk is faster for angles between magnetic field and oxygen gradient up to 60° , but the motion is not one dimensional for the weak Earth magnetic field, as usually stated. Moreover, I see a strong dependence on the magnetic field orientation that was not quantified before. Previous experiments [137, 84, 79] do not deal with non-trivial angles

(meaning not 0 or 180°), or they consider few other angles (45° and 90°) [78], with scarcely reproducible results. Previous simulations [78, 79, 84] work with 1D mean-field approaches, not considering the trajectories of the single bacteria (thus ignoring noise effects, weak magnetic fields); the dependence on magnetic angles on simulations was considered by Bennet *et al.* [78], but with the strong simplifications of a 1D motion, which could be accurate only for very strong magnetic fields. With my 3D model, I provide a theoretical description (Equations 4.6 and 4.7) to predict taxis velocity in constant gradients, including thermal noise, noise effects due to active changes of direction, and magnetic field-angles effects. These formulas can be used to modify the previous 1D simulations to include the missing effects if constant gradients are assumed. This would lead to more accurate mean-field approaches, resulting in faster simulations with respect to the all-body resolution of my approach. With my theoretical description, I show that aerotaxis is possible for magnetic field inclinations of 90° for axial bacteria; these findings match with the discovery of magnetotactic bacteria at the Equator [82, 83]. However, for polar bacteria the band formation at 90° is hindered; so if polar bacteria are present at the Equator, there should be some strategy that allows them to survive.

Magnetic fields do not only influence the tactic velocity, but also the width of the aerotactic band. In theory, a smaller band means that bacteria spend less time performing excursion far from the preferred concentration. This could represent an advantage for the bacteria, since they would spend more time in the most favorable condition. However, the changes in the band width that I measured at big angles are not high enough to justify a natural selection towards magneto-aerotaxis.

Chemotaxis is faster with the help of the correct magnetic fields not only in the bulk for constant gradients, but also in the capillaries experiments, for both axial and polar bacteria. These set of simulations aim to reproduce more accurately previous experimental and simulation work [78, 79, 84], since it includes a dynamic oxygen gradient. Still, the effects of the magnetic field are the same compared to the ones I have shown for axial bacteria with constant gradients in the bulk. These set of simulation could help to understand if the aerotactic model is correct, for example comparing the formation time-scales and the band characteristics with experiments. Future experiments should address this points.

When quantifying the effect of magnetic fields on magnetotaxis, special consideration should be given to polar bacteria, since they do not only benefit from the passive alignment as axial bacteria do, but also they base their aerotactic strategy on the magnetic fields [16, 79]. This means that without magnetic fields they could not perform aerotaxis. Therefore, the advantage would be that instead of sensing the oxygen gradient, they can sense absolute oxygen concentrations, still performing aerotaxis in the correct direction thanks to the magnetic fields. This could be an advantage whenever the oxygen gradient is not stable as it happens in Nature, due to flow perturbations, for example. The effects of flow will be discussed in the following Section.

Finally, I observed that the magnetic fields allow to perform long runs in the bulk without much loss in the tactic velocity. Without magnetic fields, long runs are not to be preferred for the chemotactic bias, because the thermal noise reorientation would make a bacterium lose its initial direction. With magnetic fields instead, long runs preserve the original direction, with an increase in the tactic velocity. Still it is not clear why a bacterium should prefer long runs (as reported in literature [80]) to short ones. It could be that long runs facilitate the spacial chemotactic sensing, but without further proofs, this is just a speculation. Moreover, the interaction with sediments would shorten up these runs due to collisions, meaning that maybe in Nature the chemotactic

strategy is completely different from the bulk. I give a brief discussion about sediments in the following paragraph.

7.4 Confined and Porous Environments

From my results in the bulk, I can see that the magnetic fields could influence the band-width without significant advantages, while there is a consistent gain in the tactic velocity up to an inclination of 60° . However, most of the magnetotactic bacteria spend part of their lives in more crowded environments and not in the bulk: they occupy the oxic-anoxic transition zone that is situated in the first layer of sediments at the bottom of lakes and seas [143, 85, 144, 145, 42], where obstacles as the grains of sand, fluid flow and non-linear oxygen gradients influence their motion [95, 104]. Therefore, I studied MTB in such a porous environment.

Previous studies considered MTB in the sand, but only in tanks of water and sediments, where the bacterial vertical distribution were analyzed in the millimeter and centimeter ranges [85, 98, 99, 100]. To understand the dynamics though, a microscopic approach should be adopted. In literature, few studies of this kind have been done. MTB were studied under the influence of fluid flow in the bulk [146, 115]; or they were studied in a regular sets of pillars without flow, or in a set of pillars regularly spaced with different sizes and flow [103].

To diversify from these studies and for better completeness, I decided to apply a 'bottom-up' approach, meaning that I start from the characterization of a real sand sample that constitutes the environment of the magnetotactic bacteria, from which statistics of the sand-grains dimension and water-gaps can be obtained. My approach consists in a microCT scan of the sample in water; in this way, the real gap-size should be preserved, avoiding artifacts that can arise from the use of resins for fixing the sediments used in the previous studies [105, 106, 107].

Subsequently, I use these results to project future two-dimensional microfluidic experiments, and to perform 2D and 3D simulations, where the porous environment is as close as possible to the Natural one, with realistic grain and water-gaps sizes, and a random distribution of the obstacles. In this way, I do not use regularly spaced pillars (which were employed for the only study of MTB in such environments [103]), therefore avoiding the effects due to regular pillars that were demonstrated for active particles [88, 147], and the effects of gap-sizes and grain sizes that are not significant when compared to the real environment. The water gaps that I measured are usually much bigger than the typical bacterium size (5 to 100 times), so in principle the motion at the micro-scale is not influenced. However, the obstacles force changes of directions, reducing the length of very long run times. Very long runs, as observed in the bulk for MTB [80], should not be possible. The influence of wall interactions on the bacteria motility has been shown previously [95, 96], also for MTB [104]. With my simulations, I can reproduce in a qualitative way the interaction with curved and flat walls shown experimentally for MTB by Rismani Yadzi *et al.* [103]. Moreover, I successfully reproduce the motility in circular microtraps, which we observed in our lab for MTB, and that were previously reported for algae [135].

The effect of walls interactions, together with the fact that the sand is actually a maze that the bacterium has to solve to reach the preferred concentration, influences the dynamics at the millimeter range: the sand slows down the dynamics with respect to the bulk. This result is consistent with previous studies that show that the diffusivity of active particles in complex porous media is lower compared to the bulk [35, 36].

Also in the sand, the magnetic fields allow to perform faster chemotaxis. Compared to the bulk though, I can see that a certain percentage of bacteria could be blocked by the grains in specific 'hot-points'; while the tactic velocity is higher for the bacteria able to escape the sand-maze, for some bacteria the motion is impeded by the magnetic fields. Moreover, the presence of magnetic fields does not allow the bacteria to explore all the available space, but restricts their motion in some preferential paths ('streamlines'). This could disadvantage the bacteria, preventing them to reach food-rich location, for example. The presence of 'hot-points' and 'stream-lines' was not observed in the work by [103]; the regular spacing of the pillars and the absence of closed paths could eliminate these effects; moreover, these effects are stronger in the presence of chemotaxis, which was not considered in the cited work. The presence of these 'stream-lines' was reported for 2D microfluidic channels for MTB in a conference-abstract [148], but no peer-reviewed paper is published at the present date.

In conclusion, more simulations and experiments are needed to understand the motion in porous media, such as to determine the run times in the presence of obstacles, aerotaxis and magnetic fields. My simulations can help in the planning of future 2D microfluidic experiments; in fact, I demonstrated that the passage times can be calculated counting the number of bacteria in a restricted field of view in time. From the simulation point of view, the future work should include the fluid-flow and a non-constant oxygen gradient, to take in consideration all the parameters influencing the bacterial behavior. Regarding fluid flow, its presence was demonstrated in sea-beads [113, 112] and lake-beads [114], and the influence on bacterial motility was shown in groundwater environments [13]. Hopefully, my simulations could help to decipher the importance of fluid flows in the MTB world.

8 Materials and Methods: The Synthetic Propellers

8.1 The Theoretical Model

To describe the motion of a magnetic rigid micro-propeller, a mobility matrix approach was used. In the following, thermal noise is ignored and deterministic equations are used. The mobility matrix \mathbf{M}_{CM} of a propeller connects the applied forces \mathbf{F}_{CM} and torques \mathbf{T}_{CM} to the propellers velocities (translational \mathbf{v}_{CM} and rotational $\boldsymbol{\omega}_{\text{CM}} = 2\pi f_{\text{CM}}$, with f_{CM} being the frequency of rotation) in the following way:

$$\begin{pmatrix} \mathbf{v}_{\text{CM}} \\ \boldsymbol{\omega}_{\text{CM}} \end{pmatrix} = \mathbf{M}_{\text{CM}} \begin{pmatrix} \mathbf{F}_{\text{CM}} \\ \mathbf{T}_{\text{CM}} \end{pmatrix}, \quad (8.1)$$

where CM stands for the center of mass. The matrix itself (6×6) can be subdivided in four 3×3 matrices:

$$\mathbf{M}_{\text{CM}} = \begin{pmatrix} \mathbf{M}^{\text{tt}} & \mathbf{M}^{\text{tr}} \\ \mathbf{M}^{\text{rt}} & \mathbf{M}^{\text{rr}} \end{pmatrix}, \quad (8.2)$$

where the upper index t stands for translational and r for rotational. The matrix is symmetrical, with $\mathbf{M}^{\text{tr}} = (\mathbf{M}^{\text{rt}})^T$. When an external magnetic torque is applied as propulsion source, with $\mathbf{F}_{\text{CM}} = 0$ and $\mathbf{T}_{\text{CM}} = \mathbf{m} \times \mathbf{B}$ (being \mathbf{m} the magnetic moment of the cluster and \mathbf{B} the magnetic field), a non-zero translational-rotational coupling \mathbf{M}^{tr} is needed to have a non-zero translational velocity \mathbf{v}_{CM} . The translational velocity will have a main component along the axis of rotation of the magnetic field; since the magnetic field rotates counterclockwise in the yz -plane in the lab frame of reference, $\mathbf{B} = (0, B \cos(2\pi f_{\text{B}} t), B \sin(2\pi f_{\text{B}} t))$ (with f_{B} is the frequency of the field), the main component of the velocity will be along x .

It is problematic to theoretically calculate the mobility matrix of random shaped propellers. For this reason, it was chosen to approximate the propeller as a cluster of rigid spheres possessing a total magnetic moment. The spheres could be adapted to discretize any shape; moreover, the mobility matrix for interacting spheres $\boldsymbol{\mu}$ is easily writable through a Rotne-Prager approximation [27, 26, 149], which leads to equations that are exact up to order $(a/r_{ij})^3$ [27] (see Section 2.3.4). The $6N \times 6N$ mobility matrix becomes:

$$\boldsymbol{\mu} = \begin{pmatrix} \boldsymbol{\mu}^{\text{tt}} & \boldsymbol{\mu}^{\text{tr}} \\ \boldsymbol{\mu}^{\text{rt}} & \boldsymbol{\mu}^{\text{rr}} \end{pmatrix} \quad (8.3)$$

where the $\boldsymbol{\mu}^{ij}$ are $3N \times 3N$ mobility matrices (with superscripts 't' and 'r' for translational and rotational degrees of freedom as described above), whose elements are:

$$\boldsymbol{\mu}_{ii}^{\text{tt}} = \mu^{\text{t}} \mathbf{1} \quad (8.4)$$

$$\boldsymbol{\mu}_{ii}^{\text{rr}} = \mu^{\text{r}} \mathbf{1} \quad (8.5)$$

$$\boldsymbol{\mu}_{i \neq j}^{\text{tt}} = \mu^{\text{t}} \left[\frac{3}{4} \frac{a}{r_{ij}} (\mathbf{1} + \hat{\mathbf{r}}_{ij} \hat{\mathbf{r}}_{ij}) + \frac{1}{2} \left(\frac{a}{r_{ij}} \right)^3 (\mathbf{1} - 3 \hat{\mathbf{r}}_{ij} \hat{\mathbf{r}}_{ij}) \right], \quad (8.6)$$

where $i, j = 1, \dots, N$ is the index of the bead, $\mathbf{1}$ is the 3×3 identity matrix, $\mu^{\text{t}}, \mu^{\text{r}}$ are the mobility coefficients for a sphere, a is the radius of the bead, r_{ij} is the distance between the i -th and j -th bead, and $\hat{\mathbf{r}}_{ij} = \frac{\mathbf{r}_i - \mathbf{r}_j}{r_{ij}}$ is the unit vector connecting the i -th and j -th bead. $\hat{\mathbf{r}}_{ij} \hat{\mathbf{r}}_{ij}$ is a 3×3 matrix, in which the elements $[\hat{\mathbf{r}}_{ij} \hat{\mathbf{r}}_{ij}]_{lk} = \hat{\mathbf{r}}_{ij}(l) \hat{\mathbf{r}}_{ij}(k)$, where $\hat{\mathbf{r}}_{ij}(1) = x_{ij}$, $\hat{\mathbf{r}}_{ij}(2) = y_{ij}$ and $\hat{\mathbf{r}}_{ij}(3) = z_{ij}$. In the present paper, rotational-translational couplings $\mu^{\text{tr}}, \mu^{\text{rt}}$ are neglected, which are known to result in artifacts for elastic structures [27], as well as the off-diagonal terms $\mu_{i \neq j}^{\text{tr}}$ [27] (see Section 8.3).

This beads-mobility matrix can be converted to the propeller center-of-mass mobility matrix with a projection method [27, 150]:

$$\mathbf{M}_{\text{CM}} = (\mathbf{C}^{\text{T}} \cdot \boldsymbol{\mu}^{-1} \cdot \mathbf{C})^{-1}, \quad (8.7)$$

with the $6N \times 6$ projection matrix

$$\mathbf{C} = \begin{pmatrix} \mathbf{1} & (\mathbf{r}_{\text{c}} - \mathbf{r}_1) \times \\ \vdots & \vdots \\ \mathbf{1} & (\mathbf{r}_{\text{c}} - \mathbf{r}_N) \times \\ \mathbf{0} & \mathbf{1} \\ \vdots & \vdots \\ \mathbf{0} & \mathbf{1} \end{pmatrix}, \quad (8.8)$$

Here $\mathbf{r}_{\text{c}} = \frac{\sum_i \mathbf{r}_i}{N}$ is the position of the center of mass and \times indicates the vector product. The relationship 8.7 holds because it can be seen that $(\mathbf{F}_{\text{CM}}, \mathbf{T}_{\text{CM}}) = \mathbf{C}^{\text{T}} \cdot (\mathbf{F}_i, \mathbf{T}_i)$ and $(\mathbf{v}_i, \boldsymbol{\omega}_i) = \mathbf{C} \cdot (\mathbf{v}_{\text{CM}}, \boldsymbol{\omega}_{\text{CM}})$, where the i subscript refers to the forces, torques and velocities of the single spheres of the cluster. From these relationships, and remembering that $(\mathbf{v}_i, \boldsymbol{\omega}_i) = \boldsymbol{\mu} \cdot (\mathbf{F}_i, \mathbf{T}_i)$, it can be easily obtained Equations 8.8 and 8.7.

Once obtained the mobility matrix of the center of mass \mathbf{M}_{CM} , the position of the propeller can be easily obtained integrating:

$$\frac{d\mathbf{x}_{\text{CM}}}{dt} = \mathbf{v}_{\text{CM}}. \quad (8.9)$$

The orientation of the object is described by a triad of orthogonal unit vectors $\hat{\boldsymbol{\alpha}}, \hat{\boldsymbol{\beta}}, \hat{\boldsymbol{\gamma}}$ rigidly attached to the body, which rotates due to the angular velocity of the propeller, according to

$$\frac{d\hat{\boldsymbol{\alpha}}}{dt} = \boldsymbol{\omega}_{\text{CM}} \times \hat{\boldsymbol{\alpha}} \quad (8.10)$$

and likewise for $\hat{\boldsymbol{\beta}}, \hat{\boldsymbol{\gamma}}$ is obtained from the other two vectors through orthogonality.

8.2 The Simulation Algorithm

The simulation was implemented in Fortran 90, based on the following algorithm: the mobility matrix of the center of mass is calculated once in the body system at the beginning of the simulation [27] and is fixed in the body system. To calculate the inverted matrices, a Gauss-Jordan method with pivoting was used [37]. At each time-step, the instantaneous body system is considered, where the mobility matrix is known and the magnetic moment is fixed. The torque is calculated in this system, too. From the torque, the velocity and frequency in the instantaneous body system can be derived via Equation (8.1). The displacement of position and of the unitary vectors are computed in this body system from integration of Equations 8.9 and 8.10 using the second-order Runge-Kutta scheme [37], and then transformed into the lab system, in which the new position of the center of mass and the new orientation of the triad are obtained as the present-time value plus the corresponding displacement. For Visual Molecular Dynamics (VMD) videos, the position of the beads in the lab system is calculated at each time-step from their fixed position (a_i, b_i, c_i) in the body system defined by $\hat{\alpha}, \hat{\beta}, \hat{\gamma}$ as $\mathbf{x}_i = \mathbf{x}_{CM} + a_i\hat{\alpha} + b_i\hat{\beta} + c_i\hat{\gamma}$. Alternatively, all calculations can be done in the lab system, but then the mobility matrix needs to be re-calculated at each time-step, because of its dependence on the orientation in the lab frame. Thus, this approach requires much longer computation times, but the results of the two algorithms are equivalent. In both approaches, I included a check of the orthogonality of the triad $\hat{\alpha}, \hat{\beta}, \hat{\gamma}$ over time, because Euler integration of the unit vector $\hat{\alpha}_{new} = \hat{\alpha}_{old} + \boldsymbol{\omega}_{CM} \times \hat{\alpha}_{old} dt$ does not preserve orthogonality: if $\hat{\alpha}_{old} \cdot \hat{\beta}_{old} = 0$, then after integration $\hat{\alpha}_{new} \cdot \hat{\beta}_{new} = -dt^2(\hat{\beta}_{old} \cdot \boldsymbol{\omega}_{CM})(\hat{\alpha}_{old} \cdot \boldsymbol{\omega}_{CM})$. This problem is kept under control by the second order Runge-Kutta scheme for integration as well as a small time-step $dt \simeq 10^{-5}$ s. Simulations were stopped if the error accumulated to $\hat{\alpha} \cdot \hat{\beta} > 10^{-2}$.

8.3 Approximations

The model implies a series of approximations: (i) the continuous surface is approximated with beads; (ii) the Rotne-Prager equations are an approximation themselves, valid for spheres at sufficiently large distances, but used here also for rather small distances (spheres touching each other); (iii) some terms in the equations are neglected, in particular the rotational-translational terms and the off-diagonal rotational-rotational terms, (iv) rigid bonds correction were not used. I will go through these points in the following.

(i) The approximation with beads of a continuous surface was previously used in the literature [30, 27, 131, 130]. Artifacts can arise due to gaps between the beads. Since the aim is a qualitative description of the behavior of the propeller and not the exact flow of the fluid around the object, this problem is of minor relevance.

(ii) The Rotne-Prager approximation is also common in the literature. It is good for spheres that are sufficiently distant from each other [27, 26] due to lubrication problems that could arise when the gap between them is too small. For a rigid cluster though, lubrication problems are not present, since the spheres are fixed with respect to each other. There are order $O(1)$ effects [26] that are considered negligible in the simulation, since tuning the number of spheres (see Chapter 9) caused no significant difference for distant or touching beads. Moreover, these terms would influence only the near-surface flow, but not the overall behavior of the object that I want to represent with an effective motion. Thus, these expressions for the entries of the mobility

matrix will be used here also for spheres touching each other.

(iii) The rotational-translational terms and the off-diagonal rotational-rotational terms are neglected following the approach of ref. [27], where this was done consistently for flexible chains.

(iv) Rigid bonds corrections have not been considered in my approach. This was done in ref. [27] through the HYDROLIB library [150]. Here, instead I used self-written code without the use of that library. Compared to the other approximations I made (such as the discretization), these corrections are, however, of minor importance.

Overall these approximation can lead to quantitative changes in the velocity-frequency curves, but with the qualitative behavior unchanged.

8.4 Discretization with Beads

The propellers were approximated with spheres with radius a . The spheres were usually touching, if not specified otherwise. The way to discretize the propeller with spheres changed according to the type of propeller: a helix, a generated random propeller or experimentally-realized propellers. The number of beads was chosen taking in consideration two factors: on one side, too few beads would lead to a poor discretization of the object; on the other side, too many beads would slow down the initial mobility matrix calculation and the production of the VMD video.

8.4.1 Helices

The helix-beads position \mathbf{r}_v (v being the bead index) were generated with the following algorithm [27]: $\mathbf{r}_v = \left(\frac{p}{m} \left(v - \frac{nm-1}{2} \right), r \cos \left(\frac{2\pi}{m} v \right), r \sin \left(\frac{2\pi}{m} v \right) \right)$, where p is the pitch of the helix, r the radius of the helix, m the number of beads per turn and n the number of turns. m was varied to get touching beads, once the value of the bead-radius a was decided.

8.4.2 Generated Random Propellers

A growth algorithm was self-written in Fortran 90. Equivalent algorithms were proposed in literature [30, 127]. Initially, the radius a of each bead and the total number of beads are set. After the first bead is generated, a second bead is attached to the first one, in a random direction. The following beads are then randomly chosen to be attached to one of the previous beads, in a random direction. If the new bead is superimposing with the other beads, it is discarded and the process is repeated. The algorithm is iterated until all beads are attached.

8.4.3 Experimental Random Propellers

To model the random-shaped propellers of Bachmann *et al.* [21] as clusters of beads, an initial bead configuration must be determined. To do so, the shape of the rotating propeller is obtained with a three dimensional tomographic reconstruction from 2D microscope images by Bachmann *et al.* [21]. The best approximation is to assign one bead to each voxel (3D pixel), but the number of beads can be reduced to run faster simulations. Through appropriate binning and thresholding, the propellers can be approximated and coarse-grained, reducing the total number of pixels in the 3D reconstruction. The position of each pixel obtained after binning and thresholding has been taken as the center of a bead, and the radius as half of the pixel size. In this way the procedure of

reconstruction has been automatized, providing a reproducible way to approximate any shape with beads. The beads are not only positioned on the surface, but also inside to avoid empty spaces that could lead to unwanted interactions.

8.5 Inferring the Magnetic Moment from Experimental Data

In general, it is necessary to know the magnetic moment of the experimental random-shaped propellers. Since the magnetic moment cannot be easily determined by direct measurements (it is difficult to isolate the propeller from the bulk to perform further tests), alternative methods could be used to infer it from the experimental data.

8.5.1 The Cylindrical Approximation

The direction of the magnetic moment is determined by analyzing videos that are taken at low frequencies of the magnetic field, when the propeller is aligned in the plane of the field rotation, using a cylindrical approximation. I use the magnetic moment norm and direction that were determined by Bachmann *et al.* [21] with the cylindrical approximation according to the method previously reported [151, 122]. With this method, an elongated propeller is approximated by a cylinder, and knowing the propeller parameters (such as how the propeller is oriented in the magnetic field and its characteristic frequencies), the magnetic moment is determined in the hydrodynamic center reference system [122, 38] and is then rotated to the lab reference system of the simulation.

8.5.2 Inferring from the Comparison with Simulations

Since the intensity of the magnetic moment just re-scales the velocity-frequency curve of the propeller, the major effort was done to determine the orientation of the magnetic moment within the propeller. To do so, 100 random orientations of the magnetic moment were run to obtain the correspondent velocity-frequency curves. These curves were compared with the experimental curve; the curves with a matching characteristic behavior were re-scaled by their step-out frequency and their maximum velocity, and compared with the re-scaled experimental curve. The best match was then selected. To assess the stability of this measurement, small deviations of the magnetic-moment direction were run and compared to the original curve. A perturbation was considered as significant when evident changes in the curve behavior appeared.

8.6 Determining the Step-out Frequency

The frequency of the center of mass is in sync with the applied external frequency below the step-out, thus the curve of the center of mass frequency as a function of time is a constant. In the asynchronous regime above the step-out, the center of mass frequency oscillates in time. The last applied external frequency whose curve is still in sync is defined to be the step-out frequency. For experimental curves, usually the step-out is determined at the velocity-frequency curve: when a drop in velocity is detected, then the last frequency before the drop is the step-out frequency.

8.7 Reproduce Branching in Simulations

Since the thermal noise is not included in this model, branching (*i.e.* two velocities at the same applied frequency) can be obtained playing with the initial orientation of the propeller respect to the magnetic field. To individuate the branches, usually three initial orientations are implemented. Usually, for a fixed initial orientation, the velocity jumps between branches. To obtain all the complete branch, new simulations are run, where the last configuration at one frequency is used at initial configuration for a nearby frequency. This method allows to 'walk' along a branch, determining all the data-point along it.

9 Synthetic Propellers

In this chapter¹, I will apply my bead-based hydrodynamic simulation (section 8) to the study of rigid magnetic clusters in the micrometer range. I present the computational results for various propellers that were realized also experimentally. At first, I will introduce a three-beads propeller (Section 9.1), for which experimental data and theoretical descriptions are available. I show that the approximations I made in the model give a good qualitative match. I then consider the helices (Section 9.2); again, I can successfully reproduce the theoretical predictions, and I explore less known features such as the appearance of negative velocities. Finally, I simulate two random-shaped propellers for which the experimental data are available (Section 9.3); I propose a method to reproduce their shape and to determine the magnetic moment direction. Throughout the Chapter, I highlight the importance of the magnetic moment direction and of the shape on the dynamics.

9.1 Three-beads Propeller

I choose to test my program on a three-beads propeller [29, 31, 30] (Figure 9.1a), first of all because the bead representation matches well the experimental shape, and second because for such a simple cluster the mobility matrix has been determined analytically [30]. More details on how this achiral shape moves can be found in the Background Sections 2.1.2, 2.3.2 and 2.3.3. Using this simple propeller, I support the approximation choice I made in section 8.3.

I run my simulation for a three-bead swimmer (its beads are disposed as a triangle with an aperture vertex of 90°), a radius $a = 0.24 \mu\text{m}$, a magnetic moment of $m = 1. \times 10^{-15} \text{ m}^2\text{A}$ directed with $\theta_m = 90^\circ$, $\alpha_m = 45^\circ$, and a magnetic field $B = 3 \text{ mT}$. I obtain a branching velocity-frequency curve (Figure 9.1), in qualitative agreement with the theoretical prediction of [30]. To obtain branching, I run the curve with three different initial orientations (different colors in Figure 9.1b).

To quantify the match between theory and my simulation, I look at the mobility matrix of the center of mass in center of hydrodynamic mobility, where the rotational-rotational mobility matrix is diagonal and the translational-rotational part is symmetrical [30] (see Appendix I):

$$M_{\text{theo}} = \left(\begin{array}{ccc|ccc} 0 & 0 & 0 & 0 & 0 & -G \\ 0 & 0 & 0 & 0 & 0 & 0 \\ 0 & 0 & 0 & -G & 0 & 0 \\ \hline 0 & 0 & -G & F_1 & 0 & 0 \\ 0 & 0 & 0 & 0 & F_2 & 0 \\ -G & 0 & 0 & 0 & 0 & F_3 \end{array} \right)$$

and considering $a = 0.24 \mu\text{m}$ and $\eta = 8.9 \times 10^{-4} \text{ Pas}$ I obtain, for theory and simulation for vertex 122.7° in the center of hydrodynamic mobility (Appendix I), the values shown in Table 9.1.

¹The chapter is based on: A. Codutti *et al.*, *Front. Robot. AI*, doi: 10.3389/frobt.2018.00109

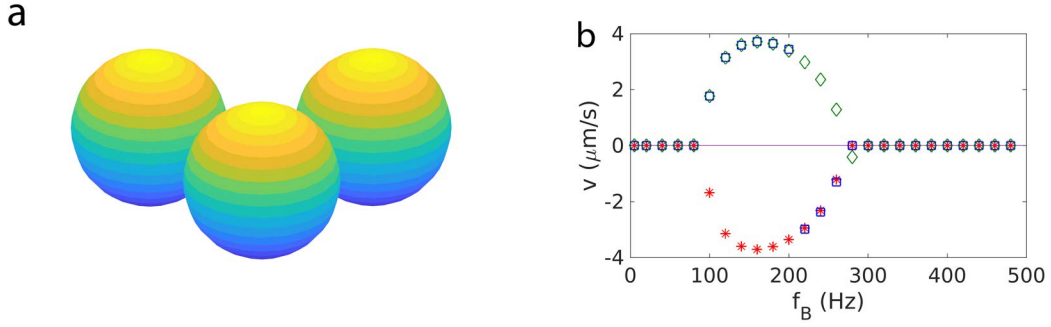


Figure 9.1: (a) Three-beads propeller with a vertex of 90° ; (b) Results for $a = 0.24 \mu\text{m}$, $m = 1. \times 10^{-15} \text{ m}^2\text{A}$, $\theta_m = 90^\circ$, $\alpha_m = 45^\circ$, $B = 3 \text{ mT}$, and a vertex of 90° (set param1) for 3 initial orientations (green, blue, red).

matrix entry	theory	simulation
$G \text{ (sKg}^{-1}\text{m}^{-1}\text{)}$	$-3.13 \times 10^{-4}/(\eta a^2) = -6.1 \times 10^{+12}$	$-5.2 \times 10^{+12}$
$F_1 \text{ (sKg}^{-1}\text{m}^{-2}\text{)}$	$4.97 \times 10^{-3}/(\eta a^3) = 4.0 \times 10^{+20}$	$3.4 \times 10^{+20}$
$F_2 \text{ (sKg}^{-1}\text{m}^{-2}\text{)}$	$5.18 \times 10^{-3}/(\eta a^3) = 4.2 \times 10^{+20}$	$3.6 \times 10^{+20}$
$F_3 \text{ (sKg}^{-1}\text{m}^{-2}\text{)}$	$12.62 \times 10^{-3}/(\eta a^3) = 10.0 \times 10^{+20}$	$8.2 \times 10^{+20}$

Table 9.1: Three-beads propeller with 122.7° vertex, and $a = 0.24 \mu\text{m}$ and $\eta = 8.9 \times 10^{-4} \text{ Pas}$

From these values I notice that the approximation used to calculate the mobility matrix terms (Section 8.3) induce a shift in the coupling values, while preserving the correct shape of the matrix. The shift corresponds to a reduction of $\sim 15\text{-}18\%$ with respect to the theory values. This reduction could justify the shift in frequencies and velocities with respect to theoretical prediction in the velocity-frequency curve. I observe this shift in Figure 9.2a, where for an aperture vertex of 90° and $a = 2.2 \mu\text{m}$, $B = 10.12 \text{ mT}$, $m = 1. \times 10^{-15} \text{ m}^2\text{A}$, $\theta_m = 90^\circ$, $\alpha_m = 45^\circ$ I plot the theoretical velocity-frequency curve [30] (in yellow), together with the computational results with different approximations (refer to section 8.3 for an overview of the cases): (a) including all terms in the mobility matrix (red curve); (b) neglecting off-diagonal rotational-rotational terms as well as rotational-translational terms (blue curve, the approximation used throughout the thesis). To further investigate these discrepancies, I rescale the curves of Figure 9.2a as described in [30]: in Figure 9.2b I plot $v/(\omega_0 a |\tilde{C}h|)$ as a function of ω_B/ω_0 , where $\omega_0 = mBF_\perp$, with $F_\perp = 2/(F_1^{-1} + F_2^{-1})$, $|\tilde{C}h| = G(F_1^{-1} + F_3^{-1})/2a$. To obtain the rescaling parameters, I calculate the matrix elements in the hydrodynamic center [30] (Appendix I), obtaining the values of Table 9.2:

matrix entry	approximation b	approximation a
$G \text{ (sKg}^{-1}\text{m}^{-1}\text{)}$	$-2.9 \times 10^{+10}$	$-4.2 \times 10^{+10}$
$F_1 \text{ (sKg}^{-1}\text{m}^{-2}\text{)}$	$5.0 \times 10^{+17}$	$3.9 \times 10^{+17}$
$F_2 \text{ (sKg}^{-1}\text{m}^{-2}\text{)}$	$5.8 \times 10^{+17}$	$5.1 \times 10^{+17}$
$F_3 \text{ (sKg}^{-1}\text{m}^{-2}\text{)}$	$8.5 \times 10^{+17}$	$7.5 \times 10^{+17}$

Table 9.2: Three-beads propeller with 90° vertex, and $a = 2.2 \mu\text{m}$ and $\eta = 8.9 \times 10^{-4} \text{ Pas}$

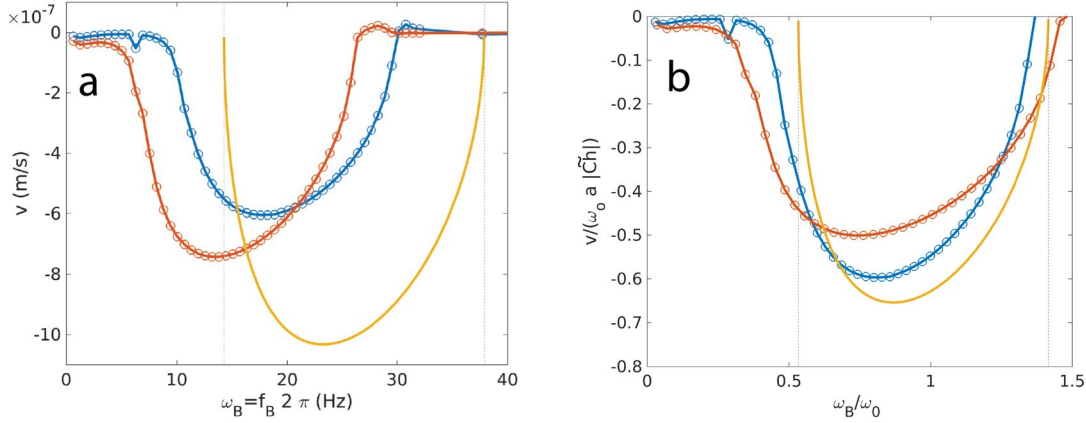


Figure 9.2: (a) Velocity-frequency curve for a three-bead propeller, with a vertex of 90° , $a = 2.2 \mu\text{m}$, $B = 10.12 \text{ mT}$, $m = 1. \times 10^{-15} \text{ m}^2\text{A}$, $\theta_m = 90^\circ$, $\alpha_m = 45^\circ$, $\eta = 8.9 \times 10^{-4} \text{ Pas}$, in the case of approximations b (blue) and with full terms in the mobility matrix (approximation a, red), compared with theory (yellow) [30]. (b) The same curves where rescaled according to what propose in [30]

From the rescaled data (Figure 9.2b) I can infer that the set of approximations b (blue curve) is closer to the theoretical description (yellow curve) compared to the full terms in the matrix (approximation a, red curve). Therefore, I will use approximation b throughout the thesis.

9.2 Systematic Study of the Parameters Influence on Helices

After studying the three-beads propeller, I focus on helices, one of the most well studied propellers, both from the analytical, computational and experimental point of view [117, 119, 121, 5, 122, 128, 118, 38, 30, 12]. On one side, I aim at showing that my model is reliable, therefore I make a systematic variation of the computational parameters. On the other side, I explore results that were less considered in the past, such as negative velocities and branching. In the following section on helices, I use the basic set of parameters specified in Table J.1, if not stated differently.

9.2.1 Helix Regimes for a Perpendicular Magnetization

First, I want to reproduce the behavior of a helix with a magnetization along the short axis $\theta_m = 0^\circ$ and $\alpha_m = 0^\circ$. The velocity-frequency curve (data points in figure 9.3) presents two distinct regimes: a linear synchronous regime, for which $v = c_v f_B$, where c_v is the coupling constant. In this regime the helix rotates in a synchronized fashion with the external magnetic field; a decaying asynchronous regime, for which the propeller cannot keep the synchronization with the external magnetic field, causing a drop in the velocity. The frequency that divides these two regimes is called the step-out frequency f_{so} . The maximum velocity v_m is reached at this point, and for higher frequencies it decays to 0^+ .

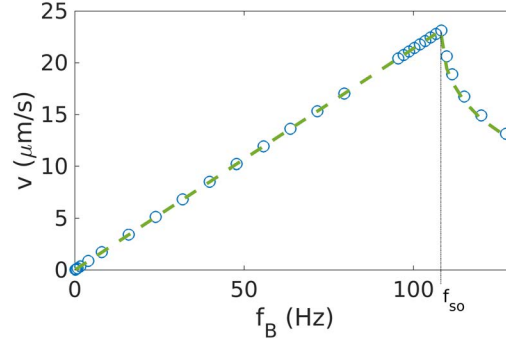


Figure 9.3: Velocity-frequency curve for a helix with the basic set of parameters of Table J.1 (blue data points). In green, the fit for 9.1, resulting in $c_v = 0.2138 \mu\text{m} \pm 0.0001$ at 95% confidence level, and $f_{so} = 108$ Hz.

This magnetization case is theoretically well studied [30, 19], and its velocity-frequency curve can be described by the following functional form [19]:

$$v_{CM} = \begin{cases} c_v f_B & \text{if } f_{CM} \leq f_{so} \\ c_v \left(f_B - \sqrt{f_B^2 - f_{so}^2} \right) & \text{if } f_{CM} \geq f_{so}. \end{cases} \quad (9.1)$$

I obtain the constant c_v from a linear fit below the step-out frequency, and I use this value as to plot the decay curve after step-out. The resulting fit (green line of Figure 9.3) shows an excellent agreement between this functional form and simulation.

The coupling coefficient c_v assumes a particularly simple form for a one-dimensional system where the axis of rotation is not changing (such as for an helix with the magnetic moment along the short axis). The coupling coefficient becomes $c_v = 2\pi\mu^{tr}/\mu^{rr}$ [126], where the 2X2 mobility matrix components μ^{tr} and μ^{rr} are the rotation-translation coupling and the rotation rotation coupling, respectively. For more complex cases, it is not easy to obtain a simple form for the coupling coefficient.

To distinguish the two regimes, I can also consider the wobbling angle, defined as the angle between the long axis of the helix and its axis of rotation. This angle is 0 in good approximation in the synchronous regime, while it presents oscillations in the asynchronous one, due to oscillations of the axis of rotation. These simple distinction in two regimes fails when the magnetic moment orientation is changed, as I will discuss in the next sections.

9.2.2 Effect of the Mobility Matrix Approximations

As for the three-beads swimmer (Section 9.1), I decided to test the influence of the approximations in the mobility matrix for a helix with magnetization along the short axis. I use the parameters of Table J.1. In Figure 9.4 I plot four different cases, with different degrees of simplifications (refer to section 8.3): (a) including all terms in the mobility matrix; (b) neglecting off-diagonal rotational-rotational terms as well as rotational-translational terms; (c) neglecting off-diagonal rotational-rotational terms and rotational-translational terms and additionally approximating up to order $(a/r_{ij})^1$ only; (d) neglecting only rotational-translational terms.

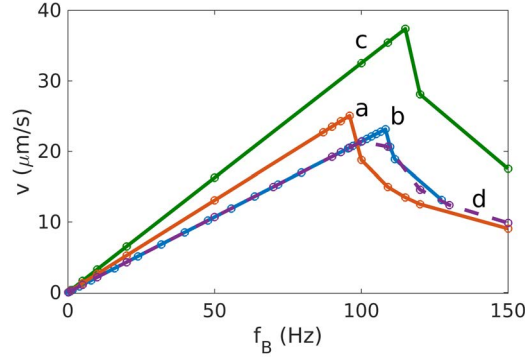


Figure 9.4: Influence of the approximations in the mobility matrix for a helix with $\theta_m = 0$. The green curve corresponds to the case c), the blue curve to the case b), the red curve to the case a), and the purple dashed curve to the case d).

Figure 9.4 shows that the qualitative behavior, in particular the shape of the curve, is the same for all cases, but I observe small shifts in both velocity and frequency. Interestingly, adding the rotational-rotational terms to (b) (thus obtaining case (d)) does not change the velocity-frequency curve. The biggest shift is observed when also the rotational-translational terms are included. The quantitative differences between the approximations are relatively small. Throughout the study, I used approximation (b), since for the three-beads swimmers I observed a best match with theory.

9.2.3 Bead Size and Number of Beads per Turn

The first parameter that I decide to vary for my systematic study is the bead size. I keep the helix geometry unvaried from the one given in Table J.1, and I vary the radius of the beads ($a' = 1.5a$), as well as the number of beads per turn ($n = 6$ as to keep the beads touching). I observe how bigger beads shift the velocity-frequency curve to smaller velocities and frequencies (red curve in Figure 9.5), compared to the basic simulation with the parameters of Table J.1 (blue curve).

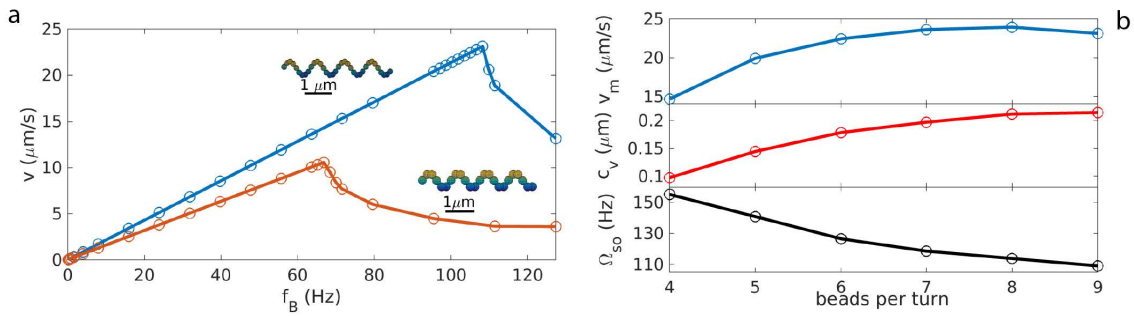


Figure 9.5: (a) Variation of bead size, blue $a = 0.1 \mu\text{m}$ and red $a' = 1.5a$. (b) Variation of the number of beads per turn: effect on the characteristic values of the velocity-frequency curve c_v , $\Omega_{so} = 2\pi f_{so}$ and v_m .

This shift can be attributed to the overall higher surface exposed to friction due to bigger beads, and to the total thickness of the helix, which is increased respect the basic case. Therefore, when approximating a real helix shape, all geometrical parameters must be taken in account, as not to produce unwanted shifts in the curves.

The next test I performed consists in keeping fixed the geometry of the helix and the dimension of the beads, but to reduce their number as to obtain larger gaps between the spheres (the spheres are equally spaced). I test the effect on three characteristic values of the velocity-frequency curve, such as c_v , $\Omega_{so} = 2\pi f_{so}$ and v_m . All three parameters show a dependence on the discretization, which however, saturates for large n . In particular, a discretization with beads touching each other ($n = 9$) gives essentially the same results as the case $n_{pt} = 6$, where the gap is big enough to use the Rotne-Prager approximation. For large gaps however, the velocity is noticeably reduced, indicating that the continuous structure of the helix is poorly represented. Thus, a sufficient density of beads is needed for a good representation of the continuous geometry, but the precise choice of the discretization is unimportant if the beads are sufficiently dense. Given these considerations, I will use touching beads throughout the thesis.

9.2.4 Magnetic Moment Orientation

Experimentally, the magnetization of a helix could be directed with any orientation, consequently differing from the ideal case presented in section 9.2.1. Therefore, I vary systematically the polar magnetization angle θ_m , as an example of the effect that magnetic moment orientation can have on the overall behavior. In Figure 9.6, I show the basic example with parameters from Table J.1 in black, and I compare it with the other degenerate case with magnetization along the long axis $\theta_m = 90^\circ$ (in gray). I notice that the velocity frequency curves presents the same behavior as the case at 0° , with the linear synchronous regime and the decaying asynchronous one, but now the velocities are all negative and smaller in absolute value, and the frequencies are also smaller. Moreover, in the synchronous regime, the wobbling angle θ_{wobb} is 0° for $\theta_m = 0^\circ$ (meaning that the helix propels in the direction of the long axis), while $\theta_{wobb} = 90^\circ$ for $\theta_m = 90^\circ$, meaning that the helix is tumbling.

For intermediate magnetization angles (an example at $\theta_m = 50^\circ$ in blue in Figure 9.6), I see a transition between the two extreme cases, giving rise to three different regimes:

1. At small frequencies, the helix tumbles (yellow snapshots): the wobbling angle is at 90° and the velocities are negative, as for the helix with $\theta_m = 90^\circ$. The velocity reaches a minimum at the end of this linear regime.
2. After this regime, the velocity increase again in a quasi-linear fashion, crosses zero and becomes positive again, till the step-out frequency, where it reaches the maximum. The wobbling angle is here decreasing, and the helix presents the so-called wobbling (red snapshots). Close to the step-out frequency, the wobbling decreases and the helix propels mainly onward parallel to the long axis (violet snapshots), as happened for $\theta_m = 0^\circ$.
3. After the step-out, the asynchronous regime starts, with the velocities decaying to 0, and an oscillating wobbling angle (green snapshots).

This negative peak was never reported experimentally before, but it was predicted theoretically [30]. Since the peak is small, it could have been covered by thermal noise, or it could be not

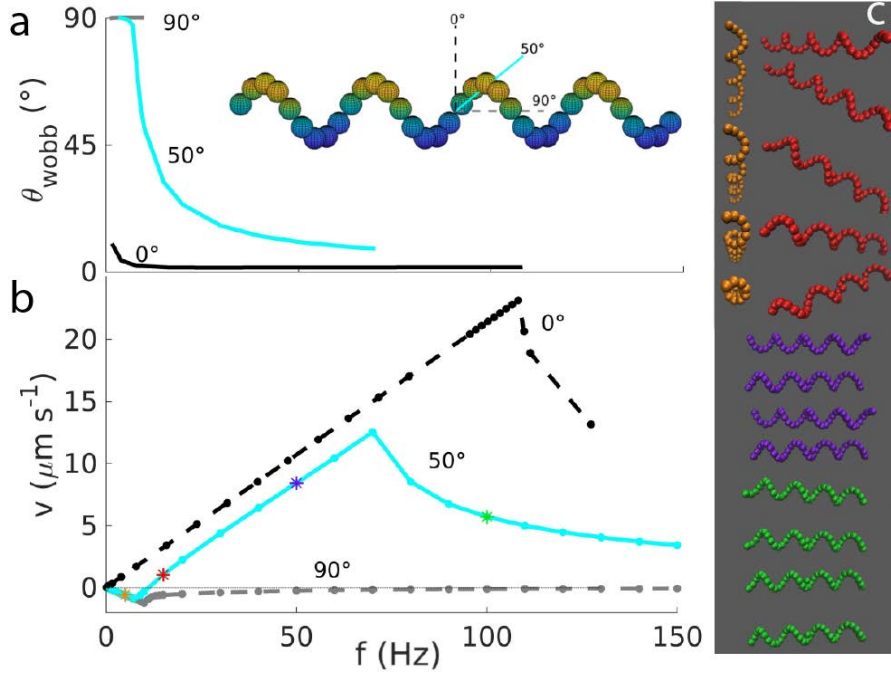


Figure 9.6: (a) Wobbling angle and (b) velocity as functions of the frequency for helices with different orientations of the magnetic moment ($\theta_m = 0^\circ, 50^\circ, 90^\circ$, as depicted in the inset). (c) Snapshots of the helix motion for frequencies of 5 Hz (yellow), 15 Hz (red), 50 Hz (violet), 100 Hz (green) illustrate tumbling at 5 Hz, wobbling at 15 and 50 Hz, and asynchronous rotation at 100 Hz.

present for real helices in which the geometry is not exact as in my case (for example, a big 'head' could be present, modifying the behavior). This negative velocities are not exclusive of helices, but they can be found also for random shaped propellers, where it can be enhanced.

I then start to vary systematically θ_m . First of all, I notice that the magnetic moment \mathbf{m} behaves as $-\mathbf{m}$ [30], thus a helix with $\theta_m = 80^\circ$ is equivalent to one at 260° , while 100° behaves as 280° (Figure 9.7a). Moreover, it matters if the displacement angle from the long axis is considered from above or below (80° differs from 100° even though they both differ 10° from the long axis). After this consideration, I concentrate my attention on the results between 0° and 180° (Figure 9.7b), since the remaining angles are equivalent. The negative peak gets deeper when it gets closer to 90° from both limits 90^- and 90^+ . The minimum points (v_{\min}, f_{\min}) can be isolated for each magnetic moment angle, and plotted separately (Figure 9.8a). Two distinct linear fits can be done for angles $0^\circ < \theta_m < 90^\circ$ (Figure 9.8b) and $90^\circ < \theta_m < 180^\circ$ (not shown). The fit $v_{\min} = c_{v,-} f_{\min}$ gives $c_{v,-} \simeq -0.11 \mu\text{m}$ for the 0° - 90° case. Then I derive a dimensionless velocity U_- for the propulsion in negative direction. The dimensionless velocity is defined as $U = 1000 \times \frac{v}{L f}$, which here becomes $U_- = 1000 c_{v,-} / L$. With a characteristic length of the propeller of $L \simeq 4 \mu\text{m}$, I obtain $U_- \simeq -30$. This dimensionless velocity is independent of the polar angle $\theta_m = 0$ (but changes of the azimuthal angle could lead to changes [30]). The dimensionless velocity U_+ achieved in the positive direction is approximately twice U_- , thus this negative velocity is significant. In conclusion, I have shown the importance of the orientation of the magnetic moment even for a simple

propeller has a helix. Moreover, negatives velocities could be also achieved for helical propellers.

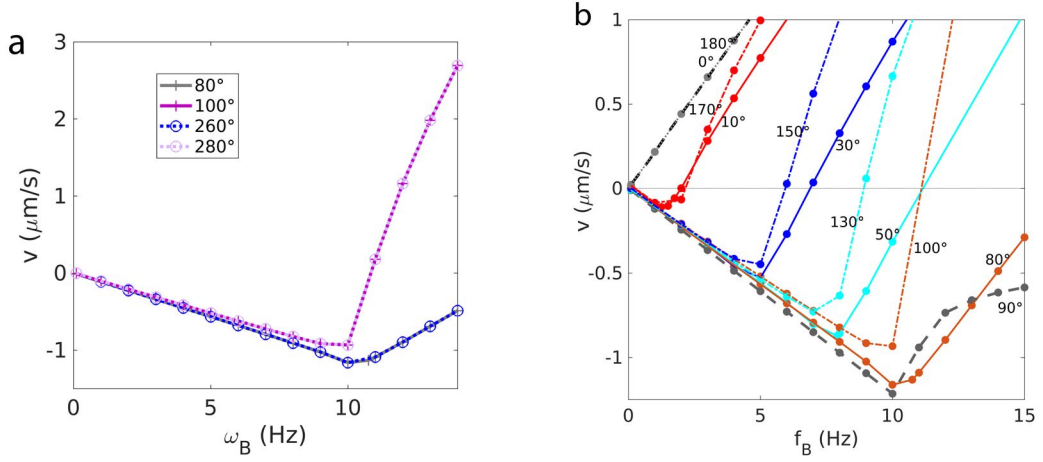


Figure 9.7: (a) Negative peaks for helices with $\theta_m = 80, 100, 260, 280^\circ$. (b) Negative peaks for angles between 0 and 180° .

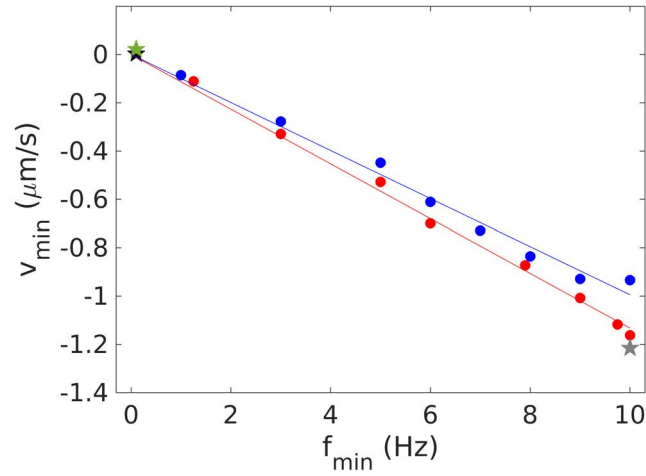


Figure 9.8: Plot of the isolated minima points (v_{\min}, f_{\min}) : the stars correspond to the 0° (black), 90° (gray) and 180° (green). For $0^\circ < \theta_m < 90^\circ$ (red data points) and $90^\circ < \theta_m < 180^\circ$ (blue data points), I show the corresponding fit $y = c_{v,-}x$, with $c_{v,-} = -0.1133 \mu\text{m}$ and $c_{v,-} = -0.0995 \mu\text{m}$.

9.2.5 Asynchronous Behavior

I focus briefly on the asynchronous behavior, a regime still lacking a full theoretical description. As previously stated, below step-out, the propeller is synchronized with the external magnetic field, thus the frequency of the center of mass and the external one are the same, while above step-out the frequency of the center of mass oscillates (Figure 9.9a). Not only the absolute value of the frequency oscillates, but also the direction of the axis of rotation changes in time, consequently the wobbling angle oscillates in time too (Figure 9.9b). To determine when the step-out frequency is reached, it is sufficient to look at the frequency of the center of mass, or at the wobbling angle. Alternatively, the step-out can be inferred from the velocity-frequencies curves, as the point after which the velocity drops. While it can be easy to identify this point in curves as the one with basic parameters in Figure 9.3, it proves to be difficult for curves as the ones in Figure 9.10, in which θ_m is close to 90° . For example, at 87° , the step-out point (a star) seems to lie on the decay part of the curve, and does not show a clear peak. I also notice from Figure 9.10 that not always a positive step-out velocity corresponds to a 0^+ limit at high frequencies, nor a negative step-out velocity corresponds to a 0^- limit: for 83° I observe a transient behavior, for which a positive step-out velocity is followed by a 0^- limit. This decay after the step-out cannot be described by formula 9.1 (Figure 9.11a), nor by a more advanced theoretical explanation (Figure 9.11b) given by [38], where the proposed fit is:

$$v_{CM} = \begin{cases} c_v f_B (1 - f_c^2 / f_B^2) & \text{if } f_B \leq f_{so} \\ c_v f_B (1 - f_c^2 / f_B^2) (1 - \sqrt{f_B^2 - f_{so}^2} / \sqrt{f_B^2 - f_c^2}) & \text{if } f_B \geq f_{so}, \end{cases} \quad (9.2)$$

where parameters c_v and f_c can be determined from the behavior for $f_B \leq f_{so}$. In conclusion, the asynchronous behavior appears even more complicated and rich of phenomenology respect what believed before.

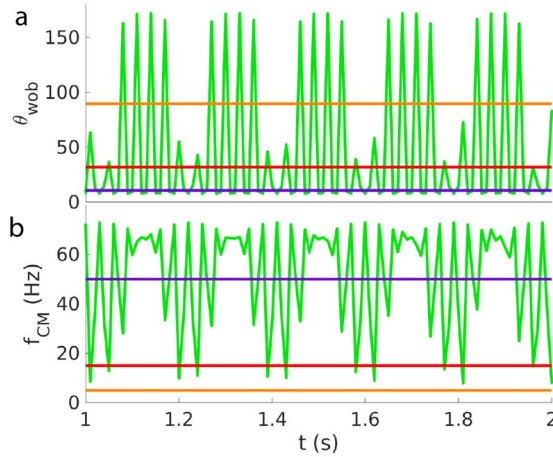


Figure 9.9: (a) Wobbling angle and (b) frequency of the center of mass for a helix with $\theta_m = 50^\circ$ as functions of time for four different applied frequencies (5 Hz yellow, 15 Hz red, 50 Hz violet, 100 Hz green). While for frequencies below step-out both quantities are constant, they oscillated above the step-out frequency.

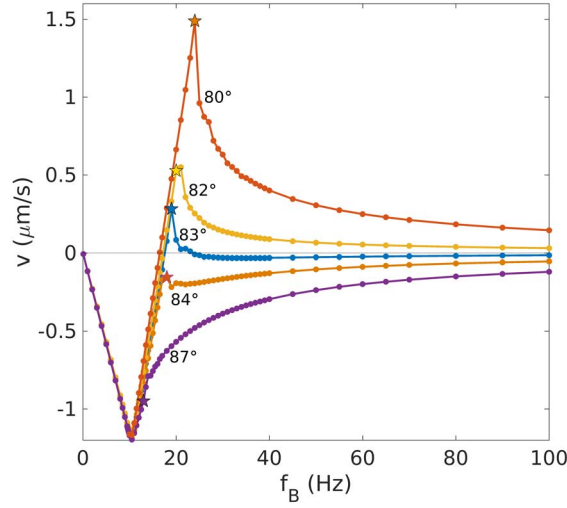


Figure 9.10: Dependence of the behavior in the asynchronous regime on the orientation of the magnetization. The limit $v = 0$ for large frequencies can be reached from above or below. Note the velocity reversal for the case of 83° , with a positive step-out velocity (indicated by a star) and negative velocities at large frequencies.

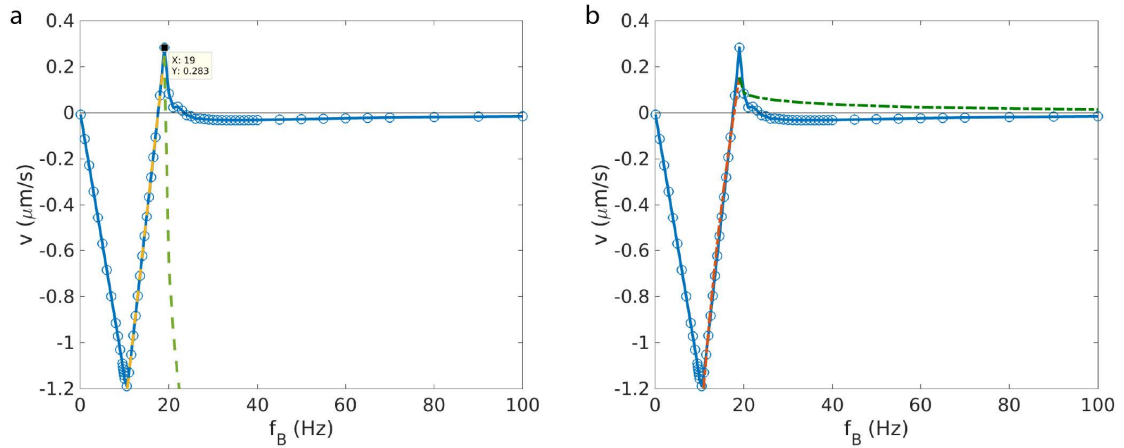


Figure 9.11: Fit of the step-out behavior for a helix with $\theta_m = 83^\circ$. (a) Fit function from equation 9.1. To obtain the parameters for that expression, I determined f_{so} as described in section 8.6 and c_v from a linear fit to the behavior for $f_B < f_{so}$. (b) Fit function proposed in ref. [38].

9.3 Random Propellers

Not all the propellers present helical shape: I can find three-beads propeller [29] (see Section 9.1), a v-shaped propeller [123, 124], or random-shaped propellers [19, 20, 21]. The strength of my method lies in the ability to approximate any shape through a coarse graining based on spheres, overcoming the difficulties that could be encountered with an analytical solution. I will apply it in this section to some random-shaped examples: I demonstrate that to reproduce the experimental behavior, it is important to know not only the shape, but also the magnetic moment orientation. The mobility matrix elements written in the center of hydrodynamic mobility for the propellers of this chapter can be found in Appendix K.

9.3.1 Generated by a Growth Algorithm

I can generate random shapes with a growth algorithm (see Section 8.4). The propeller obtained in this way could present internal gaps and can be less compact than a shape obtained from a 3D reconstruction (see sections 8.4, 9.3.2 and 9.3.3). Nevertheless, this could actually better match real propellers produced in the lab [19, 20, 21], where independent magnetic sub-units are glued together through a carbon coating, thus presenting an irregular shape with most probably internal gaps, too. These randomly generated shapes can reach velocities comparable to the one obtained in real experiments, as well as negative velocities (Figure 9.12). A gap of $0.05 \mu\text{m}$ between beads (red curve) shifts the velocity curve towards higher absolute velocities compared to the case with touching beads (blue curve), leaving unchanged the qualitative behavior.

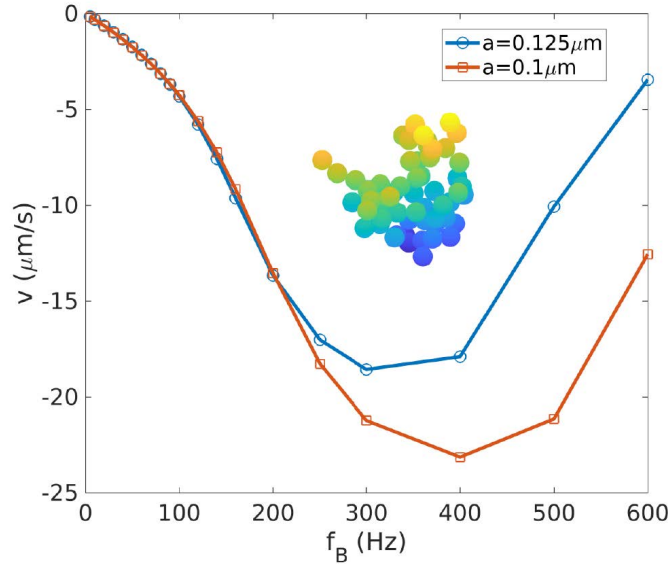


Figure 9.12: The velocity-frequency curve for a random generated propeller (60 beads of radius $a = 0.1 \mu\text{m}$, $|\mathbf{m}| = 24.5 \times 10^{-15} \text{ m}^2 \text{A}$, $B = 2 \text{ mT}$). For the blue curve, the beads are touching ($a = 0.125 \mu\text{m}$), while for the red curves the beads present a gap of $0.05 \mu\text{m}$ between each other. Inset: the propeller with touching beads.

9.3.2 Experimentally Realized Propeller - 1

Next, I want to simulate random propellers produced in the lab by Bachmann *et al.* [21], for which I know the 3D reconstruction. In this paragraph I concentrate on a random-shaped propeller that presents two almost-spherical parts connected by a bridge (reconstruction in gray in Figure 9.13). For this propeller, a switch between positive and negative velocities was shown experimentally when the frequency is varied [21]. In principle, I know the shape through the reconstruction, but I do not know the magnetic moment intensity and orientation. I decide to try different orientations to see if the experimentally qualitative behavior can be matched.

I first use an approximation with few beads (49 touching beads and $a = 0.24 \mu\text{m}$, first approximation in Figure 9.13), obtained through coarse graining of the 3D reconstruction [21] (see section 8.4). I choose to simulate four different magnetic moment orientations (m_1, m_2, m_3 and m_4 of figure 9.13) with $|\mathbf{m}| = 24.5 \times 10^{-15} \text{ Am}^2$, $B = 3 \text{ mT}$. The corresponding velocity-frequencies curves are reported in Figure 9.14.

The curves present very distinct behaviors. This underline the importance of knowing the exact orientation of the magnetic moment. In contrast, the intensity of the magnetic moment results less crucial since it just provides a rescaling factor in the curves. I also notice from these curves how there are both positive and negative velocities at different frequencies, a behavior comparable with the negative peak of the helices, but that here is emphasized for some cases.

Moreover, branching is observed. I also notice that m_3 and $-m_3$ present the same behavior, thus it is the axis of the magnetization and not its orientation that determines the dynamics [30]. Another important result regards the asynchronous behavior (empty points in the graph). The decay to 0 can be achieved in different ways (for example 0^+ for m_2 and m_3 , or 0^- for m_1), and it can present branching too (m_1, m_2, m_3 and $-m_3$). In conclusion, none of this curves matches qualitatively the experimental data, but I could infer from them the existence of the atypical asynchronous behavior, and the importance of knowing the direction of the magnetic moment.

For these magnetic moment orientations, I can study the behavior of the wobbling angle θ_{wobb} defined as the angle between the main axis of the propeller and the rotational axis. The wobbling angle gives information of the orientation of the propeller with respect to the lab frame. Different magnetic moment orientation can lead to different swimming modes of the propeller (Figure 9.15a), for example in the upper branch of configuration m_1 the propeller is tumbling, while for m_4 the propeller is moving forwards. The angle can also change according to the branch [21]. In Figure 9.15a I report the wobbling angle below step-out, since in the asynchronous regime it

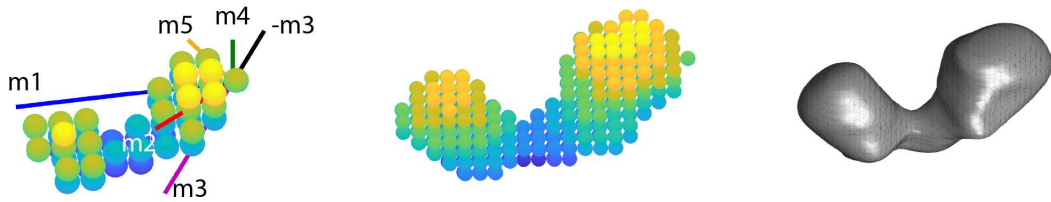


Figure 9.13: Random shaped propeller coarse-graining with 49beads ($a = 0.24 \mu\text{m}$), 501 beads ($a = 0.11 \mu\text{m}$), and the corresponding 3D reconstruction. The axis indicate the magnetic moment orientations used for the results in Figure 9.14, 9.15, and 9.16.

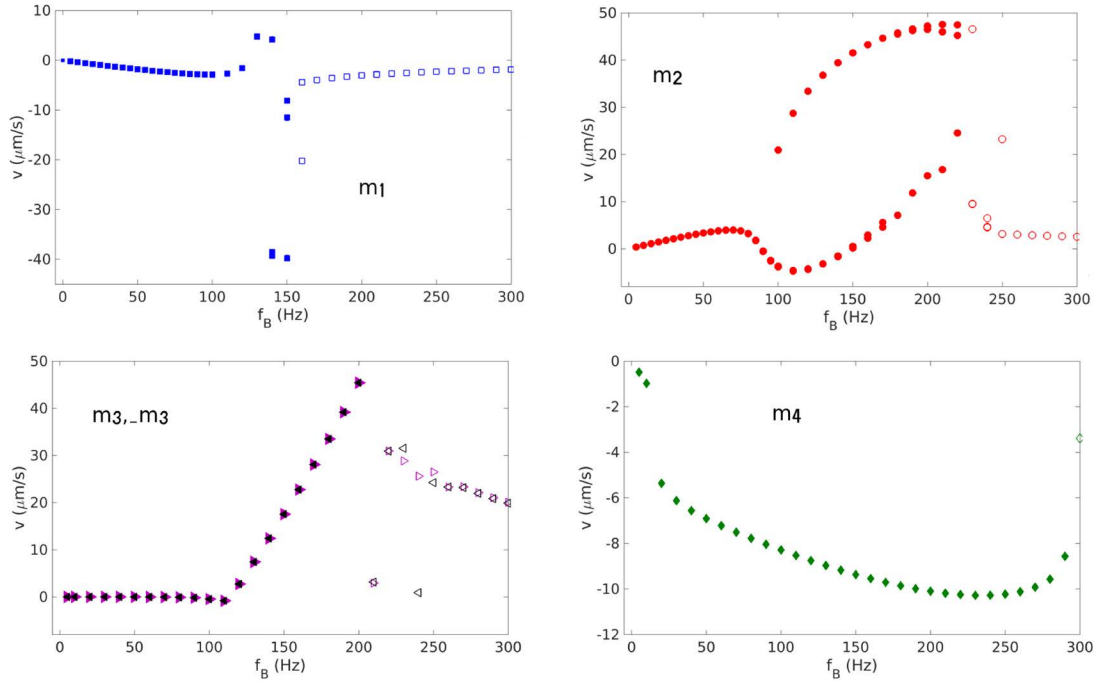


Figure 9.14: velocity-frequency curve for the 49 beads propeller at four different magnetic moment orientations m_1 , m_2 , $\pm m_3$, m_4 . Full data points are below step-out, empty data points are in the asynchronous regime.

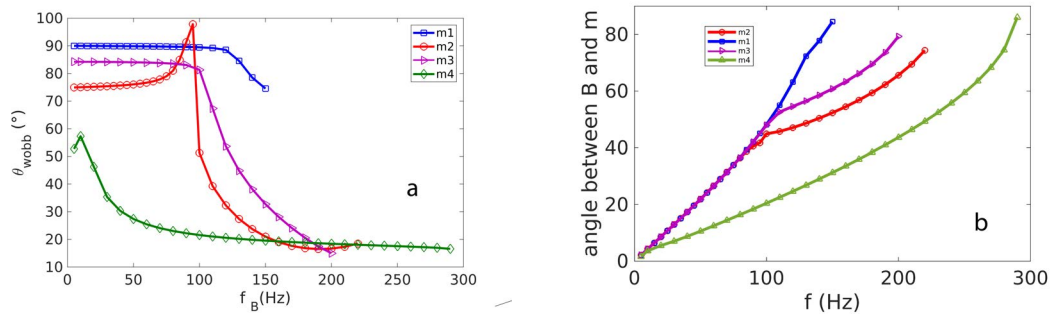


Figure 9.15: (a) Wobbling angle for the positive branches of m_1 , m_2 and m_3 and for the negative branch of m_4 . (b) Lag between magnetic field and magnetization axis for the four magnetization orientations m_1 , m_2 , m_3 , m_4 .

oscillates, as happened for the helices. Below step-out I can distinguish two regimes for all curves: there is a certain frequency after which the curve changes drastically. This change can also be seen when I quantify the lag $\theta_{B,m}$ between the rotating magnetic field B and the magnetic moment axis (Figure 9.15b). The changing point separates a semi-linear behavior from clear deviations from linearity at higher frequencies. The point roughly corresponds to the beginning of the branching of the velocity-frequency curve (the Ω_0 described by Morozov *et al.* [30]).

Since the velocity-frequency curves does not match the experimental data, I used the magnetic moment orientation calculated through a cylindrical approximation [21, 30] (m5 of Figure 9.13). I compare the experimental data [21] (black diamonds in Figure 9.16), to the coarse-graining with 49 beads and m5 (yellow stars) and to the propeller with 501 beads and m5 (yellow crosses). The experimental behavior differs from the simulated one, although it does not depend on the shape discretization, meaning that the shape was well represented even with fewer beads. Again, I can conclude that the magnetic moment orientation is the main parameter to be considered.

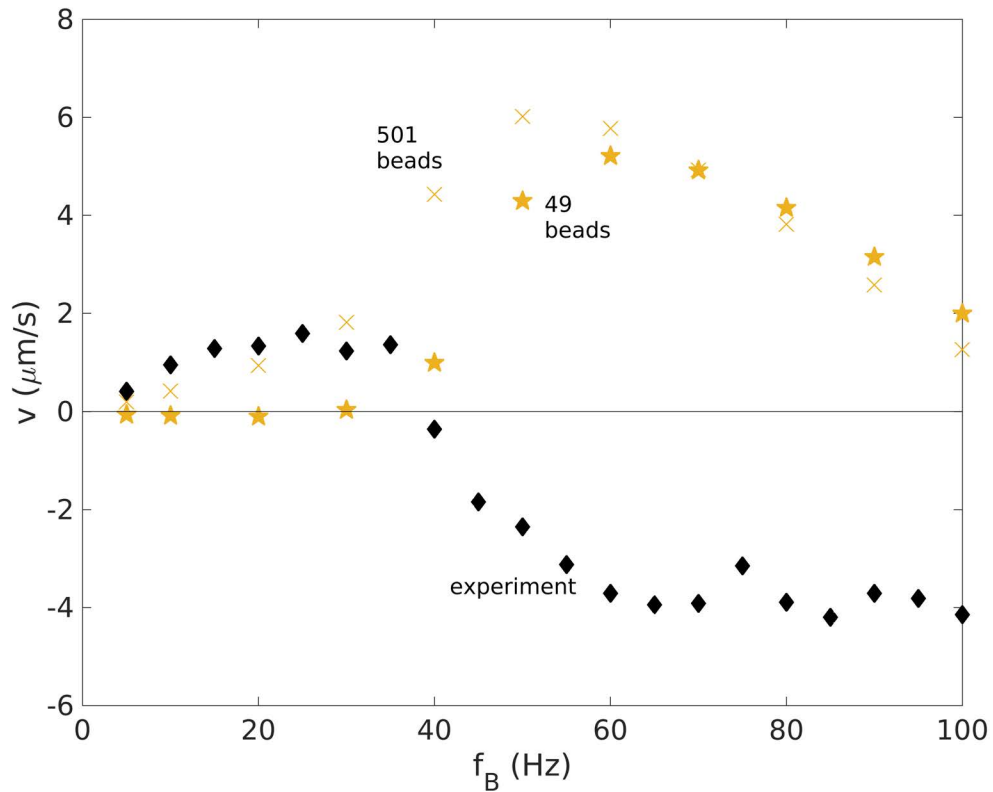


Figure 9.16: The experimental data [21] in black are compared to the simulation with 49 beads (yellow stars) and with 501 beads (yellow crosses), with magnetic moment orientation m5.

9.3.3 Experimentally Realized Propeller - 2

I concentrate then on a second example also reported by Bachmann *et al.* [21], for which a more complete data-set was reported, including the behavior after step-out (panel a of Figure 9.17). This propeller presents an elongated shape with an irregular surface (3D reconstruction in the inset in Figure 9.17). Since the surface presents these irregularities, as first step I want to test if the discretization process influences the outcome. Therefore, I run the simulation for three different cases: 55 beads and $a = 0.177 \mu\text{m}$; 518 beads and $a = 0.0903 \mu\text{m}$; 4276 beads and $a = 0.04425 \mu\text{m}$ (one bead each voxel), all of them with the magnetic moment calculated through the cylindrical approximation and $|\mathbf{m}| = 10.8 \times 10^{-15} \text{ Am}^2$ (direction indicated as a blue axis in the inset in Figure 9.17b) and $B = 2 \text{ mT}$ as used in the experiment. The velocity frequency curve present a mismatching qualitative behavior with the experimental data (Figure 9.17). This indicates that the magnetic moment calculated through the cylindrical approximation does not reproduce the experimental results with my coarse-graining.

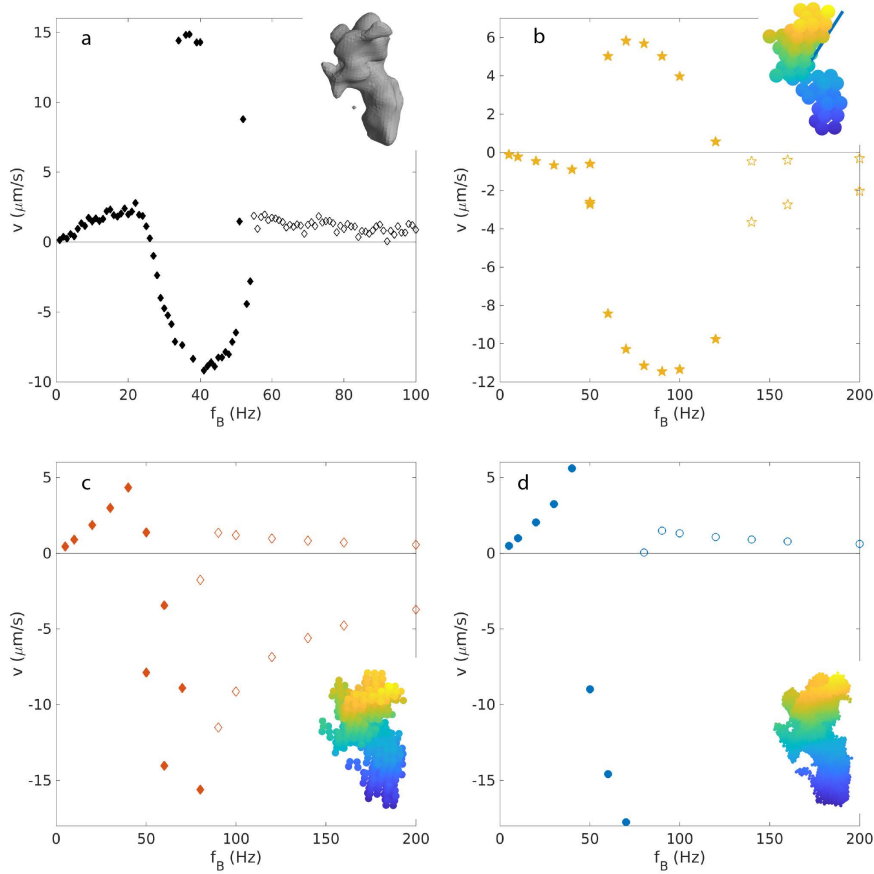


Figure 9.17: Velocity frequency curve for the 3D reconstructed paper shown in the inset [21]: (a) experimental; (b) coarse graining at 55 beads, (c) 518beads and (d) at 4276 beads. The blue axis in the inset shows the direction of the magnetic moment calculated through the cylindrical approximation. Full points indicate the synchronized regime, empty the asynchronous one.

Moreover, the curves with higher number of beads are similar, while they differ from the fewer beads curve. This hints that the poorer discretization with 55 beads does not well represent the reconstructed shape, therefore more beads must be chosen. I choose to use in the following the discretization with 501 beads since the computation of the mobility matrix is faster in this case. I underline how, for the first propeller of Section 9.3.2, the discretization with 49 beads was already providing a good result. As a conclusion, it must be paid attention to the level of coarse-graining, to match the reconstruction as well as possible.

Even though these curves do not match the experimental results, some interesting features can be read: switching between positive and negative velocities, branching before and after the step-out, different limits at high frequencies. Moreover, instability can be seen at the step-out frequency: in fact, for the same frequency, the propeller can be in synchronization or not, depending on the initial conditions (Figure 9.17c at 80 Hz). This results in a blurred transition between the two regimes, an aspect observed experimentally [21, 121] but not reported theoretically.

To match the experimental behavior, I need to determine the correct magnetic moment. This is not easily done experimentally, since the propeller cannot easily be isolated from the bulk sample for experimental determination of the magnetic moment. Even if isolation is successful, determining the exact orientation of the magnetic moment inside the propeller geometry with the required precision would be difficult. The cylindrical approximation failed to reproduce the data for my coarse-grained propellers. I propose an alternative method that consists in running 100 random orientation of the magnetic moment, which results in a high variability of the velocity-frequency curves (Figure 9.18a). The resulting velocity-frequency curves are then inspected, and the best matches with the qualitative behavior of the experiments (initial semi-linear positive behavior, branching, a positive velocity at step-out and a 0^+ limit at high frequencies) are selected (Figure 9.18b).

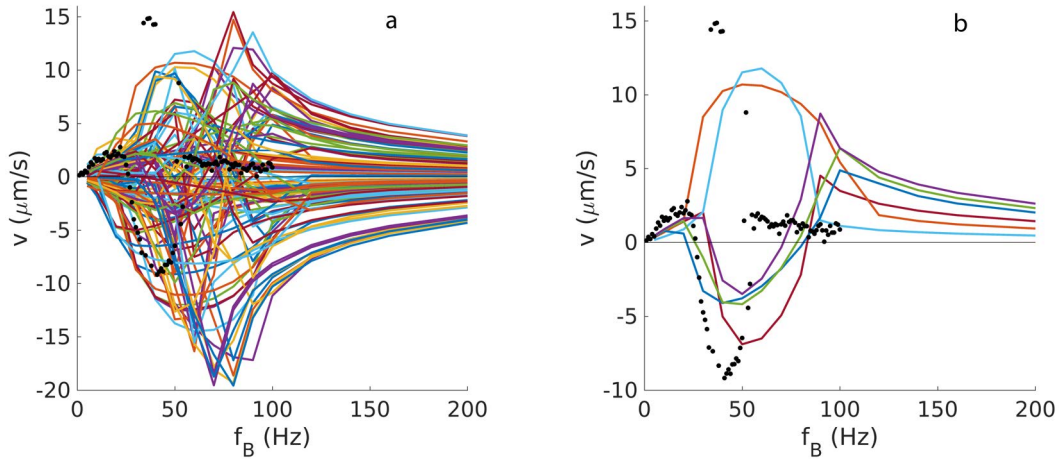


Figure 9.18: (a) For the random shaped propeller with 518-beads, propulsion is simulated with 100 randomly chosen orientations of the magnetic moment. The plot shows the curves in comparison with the un-scaled experimental data (black dots). (b) The magnetic moment orientations that result in the closest correspondence with the experimental data were selected.

These curves were then rescaled with v/v_{\max} and f_B/f_{so} , then compared with the rescaled experimental data (black points in Figure 9.19a). The best match is equivalent to the red axis of magnetization in the inset a of Figure 9.19 (blue data points). The match with the experimental behavior is largely improved, even though small discrepancies can be seen in the lower branch.

Since the direction of the magnetization emerges as a crucial parameter needed to describe the experimental behavior, I tested how sensitive the results are to changes in this direction. I perturbed the best-matching magnetic moment by small random deviations of the azimuthal and polar angle (as shown by the black and red arrows in the inset b of Figure 9.19). I obtained the corresponding velocity-frequency curves 9.19b for deviations of $\pm 1^\circ$, 5° , 10° and 20° . The qualitative behavior remains the same for perturbation up to 5° , while for bigger angles deviations can be observed. In conclusion, the direction of the magnetic moment must be known with an accuracy of 5° for this propeller.

In conclusion, I showed that to reproduce the behavior of an experimental propeller the shape influences the outcome, so an accurate 3D reconstruction is needed; that the coarse graining influences the result; an insufficient coarse graining would modify the behavior; that the magnetic moment direction determines the velocity-frequency curve; and that the direction can vary of 5° without changing the qualitative behavior. Therefore, to design and produce customized propellers, all these elements must be taken in consideration. As future outlook, an automation of the best matching magnetic moment could be implemented.

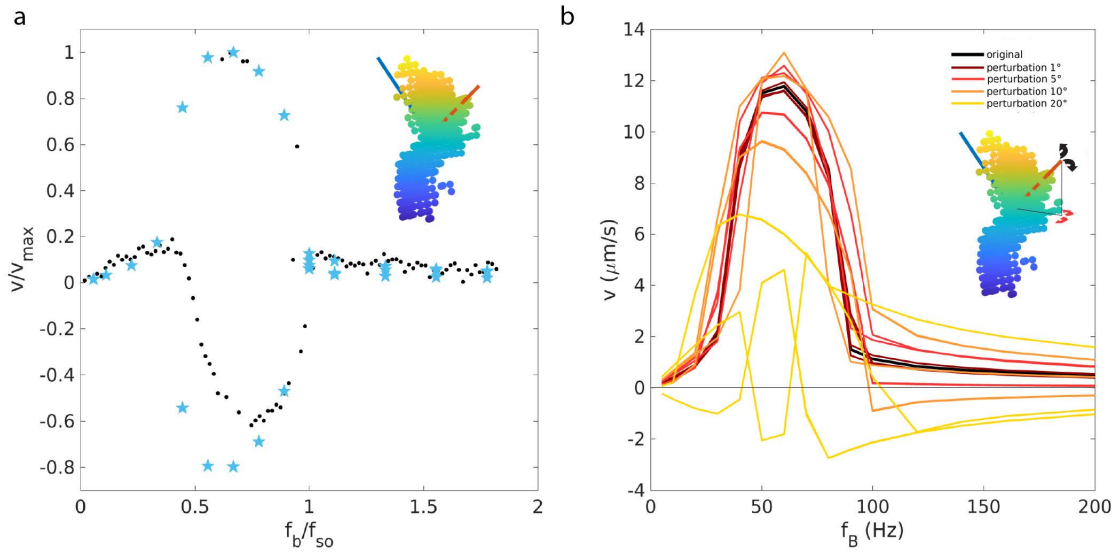


Figure 9.19: (a) Rescaled velocity-frequency curve for the 518 beads-approximation (light blue stars) with magnetic moment direction indicated by the red vector (best matching vector with experimental data), compared to rescaled experimental data (black dots). The direction of the magnetic moment from the cylindrical approximation is in blue. (b) The direction of the magnetic moment (red vector) has been perturbed by small angles in the direction of the black and red arrows. Five random perturbation are shown as five distinct curves for each angle of perturbation.

10 Discussion: Magnetic Propellers

Here I will discuss the results presented in Chapter 9 about the hydrodynamic simulation of rigid magnetic micro-propellers, from three-beads swimmers to helices and random-shaped propellers. The main successes that I achieved with this method are the ability to reproduce the qualitative behavior of helices and random-shaped propellers; the possibility of accurately approximate and simulate experimentally-realized propellers; the possibility to determine unknown parameters of these propellers through a comparison with the simulations; and the acquired knowledge on less well-studied phenomena such as negative velocities, branching and atypical asynchronous regimes, and of the influence of the magnetic moment on these phenomena. I divide the discussion in the following sections: general aspects of the model, qualitative behavior of the propellers below and above step-out, and challenges for the study and production of experimental propellers.

10.1 Validation of the Model

The model I used presents a series of approximations of the mobility matrix terms (see Section 8.3) that can influence the outcome of the simulation. The mobility matrix terms and the velocity-frequency curve of a simulated three-bead propeller present discrepancies from the theoretical results presented by Morozov *et al.* [30]. These discrepancies amount to a reduction of 15% of the mobility matrix terms (section 9.1), resulting in a shift of velocity and frequencies. Although these shifts are present, the behavior matches qualitatively with the theoretical prediction, both for the three-beads swimmer and the helices, thus proving my method to be semi-quantitative. I also test other types of approximations of the mobility matrix both for helices and the three-beads propeller (Figures 9.2, 9.4), and I show that the approximation I use throughout the thesis present the closest match to theory (Figure 9.1). To reduce the discrepancies between simulation and theory, rigid-bonds corrections could be implemented through the HYDROLIB library [150]. As an alternative, instead of using the method of reflections for the calculation of the spheres-mobility matrix, other methods could be used [27].

Once the mobility matrix is chosen, the simulation parameters such as the bead-size and the bead-separation still influence the outcome. The bead-size can modify the aspect of the propeller, so it must be chosen carefully as to obtain the correct geometry, together with the beads number. This is true for helices (Figure 9.5), where a single thread of beads could be thicker or thinner than a real helical shape, but also for propellers, as I will discuss further on. As for the bead-separation, I show how a discretization with beads touching each other gives essentially the same results as the case of separate beads (Figure 9.5), if the beads are sufficiently dense.

10.2 Features of the Propellers Behavior

The propellers behavior in the synchronous regime present features that were reported experimentally and theoretically only in recent years [21, 30, 29]. I successfully reproduce these features for the three-beads swimmer, helices and random-shaped propellers. The rich phenomenology includes branching, *i.e.* the presence of multiple solutions at the same frequency for the velocity-frequency curve, and a frequency-dependent sign of the velocity that can switch between positive and negative values. These features are not determined only by the geometry (through the mobility matrix), but are also highly dependent on the magnetic moment orientation. In fact, with the same geometry but different magnetization, the behavior can totally change, as I observe for helices and random-shaped propellers (section 9.2.4 and 9.3), confirming and expanding previous experimental and theoretical results [30, 121]. This fact is of major importance for future design of customized propellers for biomedical applications: shape and magnetic properties should be both determined to produce the correct behavior.

The asynchronous regime is less studied theoretically due to its complexity; in this regime, the propellers cannot keep up with the external magnetic field and thus they undergo a loss of velocity [122]. Previous studies describe the asynchronous behavior for simple cases, for example for a helix with magnetization along the short axis [30, 121, 122, 19, 126, 72]. With my work, I obtained results for more complex geometries. Why does this regime matter for practical applications? In principle, we could limit the frequency to remain in a synchronous regime, where the dynamics is well understood. The problem is that for actual experimentally-realized propellers, it is hard to obtain always the same magnetization; and according to the magnetic moment direction, the asynchronous regime can start at different frequencies. If such a mixture of propellers with different properties are employed together in a swarm, there would be frequencies for which some propeller are synchronized and others are not. As a consequence, the asynchronous regime also requires systematic studies and characterizations in the optic of future applications. Moreover, another challenge for practical applications consists in being able to direct and steer a single propeller along independent trajectory with respect to the other propellers in a swarm, using the same external activating magnetic field; this can be overcome by the use of propeller with different step-out frequencies [152], proving once more the importance of the asynchronous regime. With my simulation I obtain many interesting characteristics, such as the presence of two typical frequencies: a 'twitching' frequency (that slows down the motion) and an effective frequency that makes the propeller swim (see videos 1 and 2); instability of the step-out passage point (Section 9.3), confirming previous experimental results [121, 122]; 0^+ but also to 0^- high-frequency limits of the velocity-frequency curve, with different decay laws with respect to theoretical predictions [38, 19] (Section 9.3 and 9.2.4); branching (Section 9.3). In our lab, we see experimentally all these features (unpublished data from Bachmann *et al.* [21]), while they were not explained theoretically yet. This proves how the asynchronous regime is much richer in phenomenology than what previously expected and supposed, thus posing future challenges regarding its theoretical description and characterization.

10.3 Challenges for the Study and Production of Experimental Propellers

From my simulations, we can learn important lessons for the study of experimental propellers and for their future design: first, the shape must be known with good accuracy, for example thanks to 3D reconstructions, since it determines the mobility matrix and thus the overall behavior of the system. Second, the discretization process should represent the main features of the propeller, since a poor discretization negatively affects the results. Moreover, the discretization process should be automatized to be reproducible. I propose an automation based on the 3D reconstruction, for which the coarse graining can be easily changed. Third, while a difference in the magnetic moment intensity leads to a rescaling of the velocity-frequency curve, the magnetic moment orientation is crucial to determine the behavior itself. The precision at which it should be known is around 5° for my random-shaped propeller. All these points must be taken into account to accurately predict and simulate the motion of a given propeller. Moreover, my computational work could provide a strong method to determine a missing parameter as the magnetic moment direction, difficult to determine experimentally in many cases. I also predict the accuracy needed in the production of the magnetization direction, a technical detail usually underestimated.

11 Conclusions and Outlook

In this thesis, I presented two distinct simulations method to reproduce and study magnetic microswimmers. Microswimmers have many envisioned future applications, from cancer targeting [6, 7, 11, 12] to bioremediation [13, 14, 15]. To make these applications possible, a deep knowledge of the swimmers' behavior and of the systems in which they should operate is required. Simulation methods help to integrate experimental results when lab techniques and theory cannot provide the complete picture, and also help to gain knowledge on the underlying physics and biology processes, helping to develop effective models, necessary for the correct design and manipulation of the systems. One promising field regards magnetic swimmers. In fact, magnetism is a bio-compatible and powerful method to either direct and control, image or actuate the microswimmers [12]. Two systems were considered: one natural, *i.e.* magnetic cells including magnetic biohybrids and magnetotactic bacteria, and one synthetic, *i.e.* rigid magnetic propellers, in particular random-shaped propellers.

Magnetic cells have been simulated with a modified Active Brownian Particle approach, thus resolving the single trajectories and the single-cell-behavior of the swimming cells. The aim was to study the interplay between magnetic interactions and chemotactic strategies, to answer some fundamental questions: what is the advantage for magnetotactic bacteria given by magnetism in Nature? Can we model their chemotactic strategies? What kind of microswimmer would be the best for biomedical applications that involve magnetism? As main results, I have shown that bacteria performing tumble can be hindered in their chemotactic response by the magnetic fields; therefore, special attention should be posed on magnetic bio-hybrids based on *E. coli* like the one proposed by Park *et al.* [18], if their are applied in biomedical conditions where chemotaxis plays an important role. I have shown that in the presence of constant gradients and in the bulk, axial magnetotactic bacteria perform faster aerotaxis up to angles of 60° , with a strong angle dependence. I have highlighted the challenges in the determination of the aerotactic model for axial and polar bacteria, underlying how further experiments should be done to have a complete dataset for the model determination; in particular, capillaries experiments with unconventional magnetic fields orientations. Finally, I presented some preliminary results on the behavior in porous media, such as the one in which the magnetotactic bacteria live (sediments), or equivalently, in the environments of some envisioned applications, such as bioremediation (soil) or biomedical purposes (blood-vessels and solid tumors). The porous environment slows down the chemotaxis with respect to the bulk; with magnetic fields, bacteria present a higher tactic velocity respect the case with no field, but they could also undergo 'jamming' episodes, with some bacteria stuck and unable to perform a correct chemotaxis. Further simulations and experiments are needed, such as 2D microfluidic assays in the presence of oxygen gradient, or 2D and 3D simulations.

Rigid magnetic propellers were simulated thanks to a hydrodynamic approach through the use of the mobility matrix; the simulation was thoroughly tested and the influence of the approximations on the outcome have been systematically studied. The final aim was to understand the influence of the shape and the magnetic moment on the propelling abilities, and to compare the

simulation with real experimental propellers. All these points would lead to a better planning, design and realization of future propellers with biomedical applications. I have shown that my applied method successfully reproduces the qualitative rigid-magnetic-helix behavior, and I explored less known features such as the possibilities of obtaining negative velocities, in this way underlying the importance of the magnetic field direction; I proposed a method to model and simulate real experimental propellers and coarse grain them, matching their qualitative behavior; I finally highlighted the importance of knowing not only the shape, but also the magnetic moment orientation, and I shown a method to determine this orientation through comparison with the simulated data. Future works could benefit from these findings to design the next-generation propeller, adapted to perform specific tasks.

In conclusion, my thesis highlights the great influence that magnetic fields can have in the microswimmers life. I propose models and simulation methods that can help future design of micro-bots, but that can also throw some light on the behavior of existing natural and synthetic systems.

List of Figures

2.1	Background Information: Magnetization Domains	9
2.2	Background Information: Capillary Experiment	12
3.1	Methods: the Wall Interaction	25
3.2	Methods: Sphere Generation	27
4.1	Tumgling Angle Distribution	29
4.2	Trajectories for Tumble	29
4.3	Reversal Angle Distribution	30
4.4	Trajectory for Reverse	30
4.5	Flick: Distribution and Trajectories	31
4.6	Cosine of the Alignment Angle	32
4.7	Alignment Angle as Function of Time	34
4.8	Langevin Plots	34
4.9	Effective Temperatures from Langevin Plots	35
4.10	Alignment Angle Distributions	35
4.11	Taxis Velocities with Force	36
4.12	Taxis Velocities with Magnetic Fields	38
4.13	Taxis Velocities with Magnetic Fields - part 2	39
4.14	Taxis Velocities with Magnetic Fields - part 3	39
4.15	Taxis Velocity as Function of t_{up}	40
4.16	Band Formation for a Constant Gradient	41
4.17	Band Formation for a Constant Gradient - part 2	41
5.1	Capillary with a Constant Gradient	43
5.2	Capillary with a Constant Gradient- part 2	43
5.3	Capillary with 1D Integration	45
5.4	Capillary with 3D Integration	46
5.5	Axial Bacteria with Parallel and Antiparallel Magnetic Fields in a Capillary	48
5.6	Axial Bacteria with no Magnetic Fields in a Capillary - yz sections	49
5.7	Axial Bacteria with Parallel and Antiparallel Magnetic Fields in a Capillary - yz sections	50
5.8	Axial Bacteria with a 90° Magnetic Fields in a Capillary	51
5.9	Axial Bacteria with a 90° Magnetic Fields in a Capillary - yz sections	52
5.10	Axial Bacteria with a 90° Magnetic Fields in a Capillary - xy sections	52
5.11	Axial Bacteria with a 90° Magnetic Fields in a Capillary from Time 0	53
5.12	Polar Bacteria with an Antiparallel Magnetic Fields in a Capillary	54
5.13	Polar Bacteria with an Antiparallel Magnetic Fields in a Capillary - yz sections	55

5.14	Polar Bacteria with an Parallel Magnetic Fields in a Capillary	55
5.15	Polar Bacteria with an Parallel Magnetic Fields in a Capillary from Time 0	56
5.16	Polar Bacteria with a 90° Magnetic Fields in a Capillary	57
5.17	Polar Bacteria with a 90° Magnetic Fields in a Capillary - yz sections	57
5.18	Polar Bacteria with a 90° Magnetic Fields in a Capillary - xy sections	58
5.19	Effect of the Bacterial Velocity	59
5.20	Effect of the Run Times for Polar and Axial	60
5.21	Alternative Models	62
6.1	Circular Traps	64
6.2	Circular Traps with Magnetic Fields	65
6.3	Experimental 2D Study of the Sand	66
6.4	Simulated Trajectories in 2D with Sand	68
6.5	Heath Plot of the Simulated Trajectories in 2D with Sand	69
6.6	Number of Bacteria as a Function of Time	70
6.7	3D Visualization of Sand	71
6.8	3D Sand Analysis	72
6.9	3D Sand Simulation	73
9.1	Three-Beads Propeller	88
9.2	Three-beads propeller with theory	89
9.3	Velocity-Frequency Curve for a Basic Helix	90
9.4	Influence of the Approximations for a helix	91
9.5	Bead-size and Gaps Influence for a helix	91
9.6	Helix with Different Magnetic MOment Orientations	93
9.7	Negative Peaks for Helices	94
9.8	Minimum Velocity for Helices	94
9.9	Wobbling Angle and Frequency of a helix in Time	95
9.10	Magnetization Orientation Effect on the Asynchronous Regime	96
9.11	Helix Asynchronous Behavior	96
9.12	Generated Random Propeler	97
9.13	Propeller 1 - Shape	98
9.14	Propeller 1 - Velocity-Frequency Curves	99
9.15	Propeller 1 - Wobbling and Lagging Angles	99
9.16	Propeller 1 - Comaprison with the Experiment	100
9.17	Propeller 2 - Velocity-Frequency Curves	101
9.18	Propeller 2 - Determination of the Magnetic Moment	102
9.19	Propeller 2 - Best Matching Magnetic Moment	103
B.1	MSD	127
B.2	MSD for Fixed Run Times	128
B.3	MSD for Tumble and Reverse	129
E.1	High Density of Bacteria in Confinement	132
F.1	Tracking Performance	133

G.1	2D Sand Simulation: Passage Times	134
G.2	2D Sand Simulation: Final Positions without Sand	135
G.3	2D Sand Simulation: Final Positions with Sand	135
H.1	Experimental Data in a 2D microfluidic Channel -1	136
H.2	Experimental Data in a 2D microfluidic Channel -2	137

List of Tables

4.1	Taxis Velocities with a Parallel Magnetic Field	38
6.1	2D Analysis of the Sand	67
6.2	Taxis Velocities for the 2D Simulated Sand	70
9.1	Mobility Matrix for a Three-Beads Propeller	88
9.2	Mobility Matrix for a Three-Beads Propeller - influence of approximations	88
A.1	Simulation Parameters: free swimming bacteria	126
C.1	Simulation Parameters: capillary assay	130
D.1	Simulation Parameters: bacteria in confinement	131
J.1	Simulation Parameters: helices	140

Abbreviations

1D (2D, 3D) One (two, three) dimensional
AMB-1 *Magnetospirillum magneticum* strain AMB1
AP Antiparallel
ABP Active Brownian Particle
CCW Counter Clock Wise
CW Clock Wise
e.g. for example
f.o.v. field of view
i.e *id est*, that is
KS Keller-Segel model
MamK Magnetosome associated membrane protein - filament protein
MicroCT Micro Computed Tomography
MSD Mean Squared Displacement
MSR-1 *Magnetospirillum gryphiswaldense* strain MSR-1
MTB Magnetotactic Bacteria
NS North Seeking Polar Bacteria
OATZ Oxic-Anoxic Transition Zone
OD Optical Density
pdf Probability Density Function
s.e.m Standard Error of the Mean
TAMSD Time-Averaged Mean Squared Displacement
WCA Weeks-Chandler-Anderson (force or potential)
WT Wild Type

List of Publications

The thesis was partly based on the following papers in which I am first author or coauthor:

1. Bente, K., **Codutti, Agnese**, Bachmann, F. & Faivre, D., "Biohybrid and Bioinspired Magnetic Microswimmers", *Small*, 1704374 (2018)
2. **Codutti, Agnese**, Bachmann, F., Faivre, D. & Klumpp, S., "Bead-based hydrodynamic simulation of rigid magnetic micropropellers" *accepted, Frontiers Robotics and AI* (2018), doi: 10.3389/frobt.2018.00109
3. **Codutti, Agnese**, Bente, K., Faivre, D. & Klumpp, S., "Chemotaxis in External Fields". *in preparation* (2018)
4. Bachmann, F., **Codutti, Agnese**, Bente, K. & Faivre, D. "Using Shape Diversity on the Way to New Structure-Function Designs for Magnetic Micropropellers", *submitted* (2018)
5. Bente, K., Mohammadinejad, S., Bachmann, F., **Codutti, Agnese**, Lefèvre, C. T., Klumpp, S. & Faivre, D. "High-speed Helical Microswimming and Rapid Reorientation of Bacteria", *in preparation* (2018)

Bibliography

- [1] E. M. Purcell. Life at low reynolds number. *American Journal of Physics*, 45(1):3–11, 1977.
- [2] H. C. Berg. Random walks in biology. *Princeton Paperbacks*, 1993.
- [3] J. J. Abbott, K. E. Peyer, M. Cosentino Lagomarsino, L. Zhang, L. Dong, I. K. Kaliakatsos, and B. J. Nelson. How should microrobots swim? *The International Journal of Robotics Research*, 28(11-12):1434–1447, 2009.
- [4] P. Fischer and A. Ghosh. Magnetically actuated propulsion at low reynolds numbers: towards nanoscale control. *Nanoscale*, 3:557–563, 2011.
- [5] S. Tottori, Li. Zhang, F. Qiu, K. K. Krawczyk, A. Franco-Obregón, and B. J. Nelson. Magnetic helical micromachines: Fabrication, controlled swimming, and cargo transport. *Advanced Materials*, 24(6):811–816, 2012.
- [6] K. E. Peyer, L. Zhang, and B. J. Nelson. Bio-inspired magnetic swimming microrobots for biomedical applications. *Nanoscale*, 5:1259–1272, 2013.
- [7] V. Magdanz and O. G. Schmidt. Spermbots: potential impact for drug delivery and assisted reproductive technologies. *Expert Opinion on Drug Delivery*, 11(8):1125–1129, 2014. PMID: 24882224.
- [8] M. Sitti, H. Ceylan, W. Hu, J. Giltinan, M. Turan, S. Yim, and E. Diller. Biomedical applications of untethered mobile milli/microrobots. *Proceedings of the IEEE*, 103(2):205–224, Feb 2015.
- [9] J. Elgeti, R. G. Winkler, and G. Gompper. Physics of microswimmers—single particle motion and collective behavior: a review. *Reports on Progress in Physics*, 78(5):056601, 2015.
- [10] E. Lauga. Bacterial hydrodynamics. *Annual Review of Fluid Mechanics*, 48(1):105–130, 2016.
- [11] L. Schwarz, M. Medina-Sánchez, and O. G. Schmidt. Hybrid biomicromotors. *Applied Physics Reviews*, 4(3):031301, 2017.
- [12] K. Bente, A. Codutti, F. Bachmann, and D. Faivre. Biohybrid and bioinspired magnetic microswimmers. *Small*, 0(0):1704374, 2018.
- [13] R. M. Ford and R. W. Harvey. Role of chemotaxis in the transport of bacteria through saturated porous media. *Advances in Water Resources*, 30(6-7):1608–1617, 2007.

- [14] K. N. Timmis and D. H. Pieper. Bacteria designed for bioremediation. *Trends in biotechnology*, 17(5):201–204, 1999.
- [15] D. H. Pieper and W. Reineke. Engineering bacteria for bioremediation. *Current opinion in biotechnology*, 11(3):262–270, 2000.
- [16] R. B. Frankel, T. J. Williams, and D. A. Bazylinski. *Magneto-Aerotaxis*, pages 1–24. Springer Berlin Heidelberg, Berlin, Heidelberg, 2007.
- [17] O. Felfoul, M. Mohammadi, S. Taherkhani, D. de Lanauze, X. Y. Zhong, D. Loghin, S. Essa, S. Jancik, D. Houle, M. Lafleur, L. Gaboury, M. Tabrizian, N. Kaou, M. Atkin, T. Vuong, G. Batist, N. Beauchemin, D. Radzioch, and S. Martel. Magneto-aerotactic bacteria deliver drug-containing nanoliposomes to tumour hypoxic regions. *Nature Nanotechnology*, 11:941, August 2016.
- [18] B.-W. Park, J. Zhuang, O. Yasa, and M. Sitti. Multifunctional bacteria-driven microswimmers for targeted active drug delivery. *ACS Nano*, 0(0):null, 2017.
- [19] P. J. Vach, N. Brun, M. Bennet, L. Bertinetti, M. Widdrat, J. Baumgartner, S. Klumpp, P. Fratzl, and D. Faivre. Selecting for function: solution synthesis of magnetic nanopropellers. *Nano letters*, 13(11):5373–5378, 2013.
- [20] P. J. Vach, P. Fratzl, S. Klumpp, and D. Faivre. Fast magnetic micropropellers with random shapes. *Nano Letters*, 15(10):7064–7070, 2015.
- [21] F. Bachmann, K. Bente, A. Codutti, and D. Faivre. Frequency-induced reversal of swimming direction of magnetic micropropellers. *submitted*, 2018.
- [22] K. E. Peyer, S. Tottori, F. Qiu, L. Zhang, and B. J. Nelson. Magnetic helical micromachines. *Chemistry—A European Journal*, 19(1):28–38, 2013.
- [23] G. Huang and Y. Mei. Helices in micro-world: Materials, properties, and applications. *Journal of Materiomics*, 1(4):296–306, 2015.
- [24] H. C. Berg and R. A. Anderson. Bacteria swim by rotating their flagellar filaments. *Nature*, 245(5425):380, 1973.
- [25] O. Reynolds. Xxix. an experimental investigation of the circumstances which determine whether the motion of water shall be direct or sinuous, and of the law of resistance in parallel channels. *Philosophical Transactions of the Royal Society of London*, 174:935–982, 1883.
- [26] J. K. G. Dhont. *An introduction to dynamics of colloids*. Elsevier, 1996.
- [27] M. Reichert. Hydrodynamic interactions in colloidal and biological systems. *Dr. rer. nat. dissertation*, page Konstanz University, 2006.
- [28] S. Kim and S. J. Karrila. *Microhydrodynamics: principles and selected applications*. Courier Corporation, 2013.

- [29] U. K. Cheang, F. Meshkati, D. Kim, M. J. Kim, and H. C. Fu. Minimal geometric requirements for micropropulsion via magnetic rotation. *Physical Review E*, 90:033007, Sep 2014.
- [30] K. I. Morozov, Y. Mirzae, O. Kenneth, and A. M. Leshansky. Dynamics of arbitrary shaped propellers driven by a rotating magnetic field. *Physical Review Fluids*, 2:044202, Apr 2017.
- [31] U Kei Cheang, Dejan Milutinović, Jongeun Choi, and MinJun Kim. Chapter 7 - control of three bead achiral robotic microswimmers. In M. Kim, A. A. Julius, and U. K. Cheang, editors, *Microbiorobotics (Second edition)*, Micro and Nano Technologies, pages 115 – 131. Elsevier, Boston, second edition edition, 2017.
- [32] R. B. Frankel. Magnetic guidance of organisms. *Annual review of biophysics and bioengineering*, 13:85–103, 1984.
- [33] H. Risken. *The Fokker-planck equation*. Springer, 1989.
- [34] P. Romanczuk, M. Bär, W. Ebeling, B. Lindner, and L. Schimansky-Geier. Active brownian particles. *The European Physical Journal Special Topics*, 202(1):1–162, 2012.
- [35] C. Bechinger, R. Di Leonardo, H. Löwen, C. Reichhardt, G. Volpe, and G. Volpe. Active particles in complex and crowded environments. *Reviews of Modern Physics*, 88(4):045006, 2016.
- [36] M. Zeitz, K. Wolff, and H. Stark. Active brownian particles moving in a random lorentz gas. *The European Physical Journal E*, 40(2):23, Feb 2017.
- [37] W. H. Press, S. A. Teukolsky, W. T. Vetterling, and B. P. Flannery. *Numerical Recipes in FORTRAN (2Nd Ed.): The Art of Scientific Computing*. Cambridge University Press, New York, NY, USA, 1992.
- [38] K. I. Morozov and A. M. Leshansky. The chiral magnetic nanomotors. *Nanoscale*, 6:1580–1588, 2014.
- [39] R. P. Feynman, R. B. Leighton, and M. L. Sands. *The feynman lectures on physics*. Addison-Wesley, 1979.
- [40] <https://www.ptb.de/cms/nc/en/ptb/fachabteilungen/abt2/fb-25/ag-251/live-data-earths-magnetic-field.html>.
- [41] M. M. Stanton, B.-W. Park, D. Vilela, K. Bente, D. Faivre, M. Sitti, and S. Sánchez. Magnetotactic bacteria powered biohybrids target e. coli biofilms. *ACS Nano*, 0(0):null, September 2017. PMID: 28933815.
- [42] S. Mann, N. H.C. Sparks, and R. G. Board. Magnetotactic bacteria: Microbiology, biomineralization, palaeomagnetism and biotechnology. volume 31 of *Advances in Microbial Physiology*, pages 125 – 181. Academic Press, 1990.
- [43] H. Xu, M. Medina-Sánchez, V. Magdanz, L. Schwarz, F. Hebenstreit, and O. G. Schmidt. Sperm-hybrid micromotor for targeted drug delivery. *ACS nano*, 12(1):327–337, 2017.

- [44] M.T. Madigan. *Brock Biology of Microorganisms/ Fourteenth Edition*. Prentice Hall, 2015.
- [45] H. C. Berg and D. A. Brown. Chemotaxis in *Escherichia coli* analysed by three-dimensional tracking. *Nature*, 239:500–504, 1972.
- [46] B. L. Taylor and D. E. Jr. Koshland. Reversal of flagellar rotation in monotrichous and peritrichous bacteria: Generation of changes in direction. *Journal of bacteriology*, 119 (2):640–642, 1974.
- [47] L. Turner, W. S. Ryu, and H. C. Berg. Real-time imaging of fluorescent flagellar filaments. *Journal of bacteriology*, 182(10):2793–2801, 2000.
- [48] M. Theves, J. Taktikos, V. Zaburdaev, H. Stark, and C. Beta. A bacterial swimmer with two alternating speeds of propagation. *Biophysical journal*, 105(8):1915–1924, 2013.
- [49] A. Celani and M. Vergassola. Bacterial strategies for chemotaxis response. *Proceedings of the National Academy of Sciences*, 107 (4):1391–1396, 2010.
- [50] P. S. Lovely and F. W. Dahlquist. Statistical measures of bacterial motility and chemotaxis. *Journal of theoretical biology*, 50(2):477–496, 1975.
- [51] W. Alt. Biased random walk models for chemotaxis and related diffusion approximations. *Journal of mathematical biology*, 9:147–177, 1980.
- [52] V. Sourjik and N. S. Wingreen. Responding to chemical gradients: bacterial chemotaxis. *Current opinion in cell biology*, 24 (2):262–8, 2012.
- [53] M. J. Schnitzer. Theory of continuum random walks and application to chemotaxis. *Physical Review E*, 48 (4):2553, 1992.
- [54] T. Krell, J. Lacal, F. Muñoz-Martínez, J. A. Reyes-Darias, B. H. Cadirci, C. García-Fontana, and J. L. Ramos. Diversity at its best: bacterial taxis. *Environmental Microbiology*, 13(5):1115–1124, 2010.
- [55] D. A. Brown and H. C. Berg. Temporal stimulation of chemotaxis in *Escherichia coli*. *Proceedings of the National Academy of Sciences*, 71 (4):1388–1392, 1974.
- [56] H.C. Berg and E.M. Purcell. Physics of chemoreception. *Biophysical journal*, 20(2):193 – 219, 1977.
- [57] Y. V. Kalinin, L. Jiang, Y. Tu, and M. Wu. Logarithmic sensing in *Escherichia coli* bacterial chemotaxis. *Biophysical journal*, 96(6):2439–2448, 2009.
- [58] K. M. Taute, S. Gude, S. J. Tans, and T. S. Shimizu. High-throughput 3d tracking of bacteria on a standard phase contrast microscope. *Nature Communications*, 6:8776, 2015.
- [59] G. Si, T. Wu, Q. Ouyang, and Y. Tu. Pathway-based mean-field model for *Escherichia coli* chemotaxis. *Physical review letters*, 109:048101, Jul 2012.
- [60] E. F. Keller and L. A. Segel. Model for chemotaxis. *Journal of Theoretical Biology*, 30(2):225 – 234, 1971.

-
- [61] J. E. Segall, S. M. Block, and H. C. Berg. Temporal comparisons in bacterial chemotaxis. *Proceedings of the National Academy of Sciences*, 83(23):8987–8991, 1986.
- [62] M. A. Rivero, R. T. Tranquillo, H. M. Buettner, and D. A. Lauffenburger. Transport models for chemotactic cell populations based on individual cell behavior. *Chemical Engineering Science*, 44(12):2881 – 2897, 1989.
- [63] J.-B. Masson, G. Voisinne, J. Wong-Ng, A. Celani, and M. Vergassola. Noninvasive inference of the molecular chemotactic response using bacterial trajectories. *Proceedings of the National Academy of Sciences*, 109(5):1802–1807, 2012.
- [64] T. Hillen and K. J. Painter. A user’s guide to pde models for chemotaxis. *Journal of Mathematical Biology*, 58(1):183, Jul 2008.
- [65] P. Romanczuk, U. Erdmann, H. Engel, and L. Schimansky-Geier. Beyond the keller-segel model. *The European Physical Journal Special Topics*, 157(1):61–77, Apr 2008.
- [66] I. B. Zhulin and J. P. Armitage. Motility, chemokinesis, and methylation-independent chemotaxis in *azospirillum brasilense*. *Journal of bacteriology*, 175(4):952–958, 1993.
- [67] J. Rosko, V. A. Martinez, W. C. K. Poon, and T. Pilizota. Osmotaxis in *escherichia coli* through changes in motor speed. *Proceedings of the National Academy of Sciences*, 114(38):E7969–E7976, 2017.
- [68] B. C. Mazzag, I. B. Zhulin, and A. Mogilner. Model of bacterial band formation in aerotaxis. *Biophysical journal*, 85(6):3558–3574, 2003.
- [69] R. Barak, I. Nur, Y. Okon, and Y. Henis. Aerotactic response of *azospirillum brasilense*. *Journal of bacteriology*, 152(2):643–649, 1982.
- [70] S. Klumpp and D. Faivre. Magnetotactic bacteria. *The European Physical Journal Special Topics*, 225 (11-12):2173–2188, 2016.
- [71] R. B. Frankel and D. A. Bazylinski. Magnetosome mysteries. *ASM news*, 70(4):176, 2004.
- [72] S. Klumpp, B. Kiani, P. Vach, and D. Faivre. Navigation with magnetic nanoparticles: magnetotactic bacteria and magnetic micro-robots. *Physica Scripta*, 2015(T165):014044, 2015.
- [73] E. L. De Barros and D. Acosta-Avalos. A simple method to estimate the magnetic moment of magnetic micro-particles. *Journal of Magnetism and Magnetic Materials*, 320, 2008.
- [74] C. Zahn, S. Keller, M. Toro-Nahuelpan, P. Dorscht, W. Gross, M. Laumann, S. Gekle, W. Zimmermann, D. Schüler, and H. Kress. Measurement of the magnetic moment of single magnetospirillum gryphiswaldense cells by magnetic tweezers. *Scientific Reports*, 7, 2017.
- [75] R. Nadkarni, S. Barkley, and C. Fradin. A comparison of methods to measure the magnetic moment of magnetotactic bacteria through analysis of their trajectories in external magnetic fields. *PLOS One*, 8 (12), 2013.

- [76] H. A. Hassan, M. Pichel, T. Hageman, L. Abelmann, and I. S. M. Khalil. Influence of the magnetic field on the two-dimensional control of magnetospirillum gryphiswaldense strain msr-1. In *Intelligent Robots and Systems (IROS), 2016 IEEE/RSJ International Conference on*, pages 5119–5124. IEEE, 2016.
- [77] D. Murat, M. Hérisse, L. Espinosa, A. Bossa, F. Alberto, and L.-F. Wu. Opposite and coordinated rotation of amphitrichous flagella governs oriented swimming and reversals in a magnetotactic spirillum. *Journal of bacteriology*, 197 (20):3275—3282, 2015.
- [78] M. Bennet, A. McCarthy, D. Fix, M. R. Edwards, F. Repp, P. Vach, J. W. C. Dunlop, M. Sitti, G. S. Buller, S. Klumpp, and D. Faivre. Influence of magnetic fields on magneto-aerotaxis. *PLOS ONE*, 9(7):1–10, 07 2014.
- [79] C. T. Lefèvre, M. Bennet, L. Landau, P. Vach, D. Pignol, D. A. Bazylinski, R. B. Frankel, S. Klumpp, and D. Faivre. Diversity of magneto-aerotactic behaviors and oxygen sensing mechanisms in cultured magnetotactic bacteria. *Biophysical journal*, 107(2):527 – 538, 2014.
- [80] F. Popp, J. P. Armitage, and D. Schüler. Polarity of bacterial magnetotaxis is controlled by aerotaxis through a common sensory pathway. *Nature communications*, 5, 2014.
- [81] P. Leão, L. C. R S. Teixeira, J. Cypriano, M. Farina, F. Abreu, D. A. Bazylinski, and U. Lins. North-seeking magnetotactic gammaproteobacteria in the southern hemisphere. *Applied and environmental microbiology*, 82(18):5595–5602, 2016.
- [82] F. F. T. de Araujo, F. A. Germano, L. L. Goncalves, M. A. Pires, and R. B. Frankel. Magnetic polarity fractions in magnetotactic bacterial populations near the geomagnetic equator. *Biophysical journal*, 58:549–555, 1990.
- [83] R. B. Frankel, R. P. Blakemore, F. F. T. De Araujo, and J. Esquivel, D. M. S .and Danon. Magnetotactic bacteria at the geomagnetic equator. *Science*, 212 (4500):1269–70, 1981.
- [84] M. J. Smith, P. E. Sheehan, L. L. Perry, K. O’Connor, L. N. Csonka, B. M. Applegate, and L. J. Whitman. Quantifying the magnetic advantage in magnetotaxis. *Biophysical journal*, 91 (3):1098–1107, 2006.
- [85] C. B. Flies, H. M. Jonkers, D. de Beer, K. Bosselmann, M. E. Böttcher, and D. Schüler. Diversity and vertical distribution of magnetotactic bacteria along chemical gradients in freshwater microcosms. *FEMS Microbiology Ecology*, 52(2):185–195, 2005.
- [86] T. Bauer, F. Höfling, T. Munk, E. Frey, and T. Franosch. The localization transition of the two-dimensional lorentz model. *The European Physical Journal Special Topics*, 189(1):103–118, 2010.
- [87] G. Volpe, I. Buttinoni, D. Vogt, H.-J. Kümmerer, and C. Bechinger. Microswimmers in patterned environments. *Soft Matter*, 7(19):8810–8815, 2011.
- [88] A. Chamolly, T. Ishikawa, and E. Lauga. Active particles in periodic lattices. *New Journal of Physics*, 19(11):115001, 2017.

-
- [89] T. Bertrand, Y. Zhao, O. Bénichou, J. Tailleur, and R. Voituriez. Optimized diffusion of run-and-tumble particles in crowded environments. *Physical Review Letters*, 120(19):198103, 2018.
- [90] G. Guccione, D. Pimponi, P. Gualtieri, and M. Chinappi. Diffusivity of e. coli-like microswimmers in confined geometries: The role of the tumbling rate. *Physical Review E*, 96(4):042603, 2017.
- [91] K. J. Duffy, P. T. Cummings, and R. M. Ford. Random walk calculations for bacterial migration in porous media. *Biophysical journal*, 68(3):800, 1995.
- [92] R. Dillon, L. Fauci, and D. Gaver III. A microscale model of bacterial swimming, chemotaxis and substrate transport. *Journal of theoretical biology*, 177(4):325–340, 1995.
- [93] S. Torkzaban, S. S. Tazehkand, S. L. Walker, and S. A. Bradford. Transport and fate of bacteria in porous media: Coupled effects of chemical conditions and pore space geometry. *Water Resources Research*, 44(4), 2008.
- [94] C. Reichhardt and C. J. O. Reichhardt. Active matter transport and jamming on disordered landscapes. *Physical Review E*, 90(1):012701, 2014.
- [95] M. Raatz, M. Hintsche, M. Bahrs, M. Theves, and C. Beta. Swimming patterns of a polarly flagellated bacterium in environments of increasing complexity. *The European Physical Journal Special Topics*, 224(7):1185–1198, 2015.
- [96] M. Theves, J. Taktikos, V. Zaburdaev, H. Stark, and C. Beta. Random walk patterns of a soil bacterium in open and confined environments. *Europhysics Letters*, 109(2):28007, 2015.
- [97] A. Dehkharghani. *Hindered Transport of Bacteria in Porous Media Flows*. PhD thesis, Tufts University, 2017.
- [98] X. Mao. *Magnetotactic bacteria in sediment*. PhD thesis, lmu, 2013.
- [99] X. Mao, R. Egli, N. Petersen, M. Hanzlik, and X. Liu. Magneto-chemotaxis in sediment: First insights. *PLoS One*, 9(7):e102810, 2014.
- [100] X. Mao, R. Egli, N. Petersen, M. Hanzlik, and X. Zhao. Magnetotaxis and acquisition of detrital remanent magnetization by magnetotactic bacteria in natural sediment: first experimental results and theory. *Geochemistry, Geophysics, Geosystems*, 15(1):255–283, 2014.
- [101] A. Anbari, H.-T. Chien, S. S. Datta, W. Deng, D. A. Weitz, and J. Fan. Microfluidic model porous media: Fabrication and applications. *Small*, 14(18):1703575, 2018.
- [102] K. Aleklett, E. T. Kiers, P. Ohlsson, T. S. Shimizu, V. E. A. Caldas, and E. C. Hammer. Build your own soil: exploring microfluidics to create microbial habitat structures. *The ISME journal*, 12(2):312, 2017.
- [103] S. Rismani Yazdi, R. Nosrati, C. A. Stevens, D. Vogel, and C. Escobedo. Migration of magnetotactic bacteria in porous media. *Biomicrofluidics*, 12(1):011101, 2018.

- [104] C. J. Pierce, E. Mumper, E. E. Brown, J. T. Brangham, B. H. Lower, S. K. Lower, F. Y. Yang, and R. Sooryakumar. Tuning bacterial hydrodynamics with magnetic fields. *Physical Review E*, 95(6):062612, 2017.
- [105] J. Fonseca, C. O’Sullivan, M. R. Coop, and P. D. Lee. Non-invasive characterization of particle morphology of natural sands. *Soils and Foundations*, 52(4):712–722, 2012.
- [106] J. Fonseca, W. Sim, T. Shire, and C. O’sullivan. Microstructural analysis of sands with varying degrees of internal stability. *Géotechnique*, 64(5):405–411, 2014.
- [107] H. F. Taylor, C. O’Sullivan, and W. W. Sim. Geometric and hydraulic void constrictions in granular media. *Journal of Geotechnical and Geoenvironmental Engineering*, 142(11):04016057, 2016.
- [108] Y.-H. Chen, C.-C. Peng, Y.-J. Cheng, J.-G. Wu, and Y.-C. Tung. Generation of nitric oxide gradients in microfluidic devices for cell culture using spatially controlled chemical reactions. *Biomicrofluidics*, 7(6):064104, 2013.
- [109] B. J. Kim, I. Chu, S. Jusuf, T. Kuo, M. A. TerAvest, L. T. Angenent, and M. Wu. Oxygen tension and riboflavin gradients cooperatively regulate the migration of shewanella oneidensis mr-1 revealed by a hydrogel-based microfluidic device. *Frontiers in microbiology*, 7:1438, 2016.
- [110] H. Uchida, A. Sato, A. Miyayama, and K. Tsukada. Generation of an oxygen gradient in a microfluidic device and cellular analysis in hypoxia. *Advanced Biomedical Engineering*, 2:143–149, 2013.
- [111] J. C. Conrad and R. Poling-Skutvik. Confined flow: Consequences and implications for bacteria and biofilms. *Annual review of chemical and biomolecular engineering*, (0), 2018.
- [112] M. Hutnak. Seabed fluid flow. *Geofluids*, 7(4):468–469, 2007.
- [113] R. Luff and K. Wallmann. Fluid flow, methane fluxes, carbonate precipitation and biogeochemical turnover in gas hydrate-bearing sediments at hydrate ridge, cascadia margin: numerical modeling and mass balances. *Geochimica et Cosmochimica Acta*, 67(18):3403 – 3421, 2003.
- [114] Q. Qian, Clark J. J., V. R. Voller, and H. G. Stefan. Depth-dependent dispersion coefficient for modeling of vertical solute exchange in a lake bed under surface waves. *Journal of Hydraulic Engineering*, 135(3):187–197, 2009.
- [115] S. Rismani Yazdi, R. Nosrati, C. A. Stevens, D. Vogel, P. L. Davies, and C. Escobedo. Magnetotaxis enables magnetotactic bacteria to navigate in flow. *Small*, 14(5):1702982, 2017.
- [116] T. R. Kline, W. F. Paxton, T. E. Mallouk, and A. Sen. Catalytic nanomotors: remote-controlled autonomous movement of striped metallic nanorods. *Angewandte Chemie International Edition*, 44(5):744–746, 2005.

-
- [117] L. Zhang, J. J. Abbott, L. Dong, B. E. Kratochvil, D. Bell, and B. J. Nelson. Artificial bacterial flagella: Fabrication and magnetic control. *Applied Physics Letters*, 94(6):064107, 2009.
- [118] Y. Man and E. Lauga. The wobbling-to-swimming transition of rotated helices. *Physics of Fluids*, 25(7):071904, 2013.
- [119] A. Ghosh and P. Fischer. Controlled propulsion of artificial magnetic nanostructured propellers. *Nano Letters*, 9(6):2243–2245, 2009. PMID: 19413293.
- [120] T. Honda, K. I. Arai, and K. Ishiyama. Micro swimming mechanisms propelled by external magnetic fields. *IEEE Transactions on Magnetics*, 32(5):5085–5087, 1996.
- [121] A. Ghosh, D. Paria, H. J. Singh, P. L. Venugopalan, and A. Ghosh. Dynamical configurations and bistability of helical nanostructures under external torque. *Physical Review E*, 86:031401, Sep 2012.
- [122] A. Ghosh, P. Mandal, S. Karmakar, and A. Ghosh. Analytical theory and stability analysis of an elongated nanoscale object under external torque. *Physical Chemistry Chemical Physics*, 15:10817–10823, 2013.
- [123] J. Sachs, K. I. Morozov, O. Kenneth, T. Qiu, N. Segreto, P. Fischer, and A. M. Leshansky. The role of symmetry in driven propulsion at low reynolds number. *arXiv:1708.01140*, 2017.
- [124] S. Tottori and B. J. Nelson. Controlled propulsion of two-dimensional microswimmers in a precessing magnetic field. *Small*, 0(0):1800722, 2018.
- [125] H. Wang and M. Pumera. Fabrication of micro/nanoscale motors. *Chemical reviews*, 115(16):8704–8735, 2015.
- [126] P. Vach. *Solution synthesis and actuation of magnetic nanostructures*. PhD thesis, Humboldt-Universität zu Berlin, Mathematisch-Naturwissenschaftliche Fakultät, 2015.
- [127] Y. Mirzae, O. Dubrovski, O. Kenneth, K. I. Morozov, and A. M. Leshansky. Geometric constraints and optimization in externally driven propulsion. *Science Robotics*, 3(17):eaas8713, 2018.
- [128] E. E. Keaveny, S. W. Walker, and M. J. Shelley. Optimization of chiral structures for microscale propulsion. *Nano Letters*, 13(2):531–537, 2013. PMID: 23317170.
- [129] M. Manghi, X. Schlagberger, and R. R. Netz. Propulsion with a rotating elastic nanorod. *Physical review letters*, 96:068101, Feb 2006.
- [130] A. V. Filippov. Drag and torque on clusters of n arbitrary spheres at low reynolds number. *Journal of Colloid and Interface Science*, 229(1):184 – 195, 2000.
- [131] B. Carrasco and J. García de la Torre. Hydrodynamic properties of rigid particles: Comparison of different modeling and computational procedures. *Biophysical journal*, 76(6):3044 – 3057, 1999.

- [132] J. H. C. Luke. Convergence of a multiple reflection method for calculating stokes flow in a suspension. *SIAM Journal on Applied Mathematics*, 49(6):1635–1651, 1989.
- [133] J. Saragosti, P. Silberzan, and A. Buguin. Modeling e. coli tumbles by rotational diffusion. implications for chemotaxis. *PLoS ONE*, 7(4), 2012.
- [134] L. Nátr. Murray, J. D.: Mathematical biology. I. an introduction. *Photosynthetica*, 40(3):414–414, 2002.
- [135] T. Ostapenko, F. J. Schwarzendahl, T. J. Böddeker, Christian T. Kreis, J. Cammann, M. G. Mazza, and O. Bäumchen. Curvature-guided motility of microalgae in geometric confinement. *Physical Review Letters*, 120:068002, Feb 2018.
- [136] R. Stocker. Reverse and flick: Hybrid locomotion in bacteria. *Proceedings of the National Academy of Sciences*, 108(7):2635–2636, 2011.
- [137] R. B. Frankel, D. A. Bazylinski, M. S. Johnson, and B. L. Taylor. Magneto-aerotaxis in marine coccoid bacteria. *Biophysical journal*, 73(2):994–1000, 1997.
- [138] K. Bente, S. Mohammadinejad, F. Bachmann, A. Codutti, C. T. Lefèvre, S. Klumpp, and D. Faivre. High-speed helical microswimming and rapid reorientations of bacteria. *in preparation*, 2018.
- [139] R. B. Frankel and R. P. Blakemore. Navigational compass in magnetotactic bacteria. *Journal of Magnetism and Magnetic Materials*, 15-18:1562–1564, 1980.
- [140] J.-F. Rupprecht, N. Waisbord, C. Ybert, C. Cottin-Bizonne, and L. Bocquet. Velocity condensation for magnetotactic bacteria. *Physical review letters*, 116:168101, Apr 2016.
- [141] S. J. Boggs. *Principles of sedimentology and stratigraphy*. Pearson Education, 2011.
- [142] M. Khatami, K. Wolff, O. Pohl, M. R. Ejtehad, and H. Stark. Active brownian particles and run-and-tumble particles separate inside a maze. *Scientific Reports*, 6, 2016.
- [143] Y. Dong, J. Li, W. Zhang, W. Zhang, Y. Zhao, T. Xiao, L.-F. Wu, and H. Pan. The detection of magnetotactic bacteria in deep sea sediments from the east p acific m anganese n odule p rovince. *Environmental microbiology reports*, 8(2):239–249, 2016.
- [144] D. A. Bazylinski and T. J. Williams. Ecophysiology of magnetotactic bacteria. In *Magnetoreception and magnetosomes in bacteria*, pages 37–75. Springer, 2006.
- [145] L. Yan, S. Zhang, P. Chen, H. Liu, H. Yin, and H. Li. Magnetotactic bacteria, magnetosomes and their application. *Microbiological Research*, 167(9):507 – 519, 2012.
- [146] N. Waisbord, C. Lefèvre, L. Bocquet, C. Ybert, and C. Cottin-Bizonne. Destabilization of a flow focused suspension of magnetotactic bacteria. *Physical Review Fluids*, 1, 02 2016.
- [147] T. Jakuszeit, O. A Croze, and S. Bell. Diffusion of active particles in a complex environment: Role of surface scattering. *arXiv preprint arXiv:1807.04117*, 2018.

- [148] N. Waisbord, A. Dehkharghani, T. Coons, and J. S. Guasto. Directed transport of active magnetotactic bacteria in porous media flow. In *APS Division of Fluid Dynamics Meeting Abstracts*, 2017.
- [149] J. Rotne and S. Prager. Variational treatment of hydrodynamic interaction in polymers. *The Journal of Chemical Physics*, 50(11):4831–4837, 1969.
- [150] K. Hinsén. Hydrolib: a library for the evaluation of hydrodynamic interactions in colloidal suspensions. *Computer physics communications*, 88(2-3):327–340, 1995.
- [151] A. Ortega and J. García de la Torre. Hydrodynamic properties of rodlike and disklike particles in dilute solution. *The Journal of Chemical Physics*, 119(18):9914–9919, 2003.
- [152] P. J. Vach, S. Klumpp, and D. Faivre. Steering magnetic micropropellers along independent trajectories. *Journal of Physics D: Applied Physics*, 49(6):065003, 2015.

A Appendix: Simulation Parameters for Free Bacteria

For bacteria freely swimming in the bulk, the following parameters of Table A.1 were used throughout Chapter 4, if not stated otherwise.

name	object	value	reference
a	cell size (sphere radius)	$1 \mu\text{m}$	[45]
T	room temperature	305 K	[45]
T_{tumble}	effective tumbling temperature	$4.2 \times 10^4 \text{ K}$	see 3
M	magnetic moment modulus	$0.6 \times 10^{-3} \text{ A } \mu\text{m}^2$	[72, 75]
v	self velocity modulus	$14.2 \mu\text{m s}^{-1}$	[45]
η	water viscosity	0.027 Pa s	[2]
γ_t	translational friction coefficient	$5.1 \times 10^{-8} \text{ Kg s}^{-1}$	calculated from a
γ_r	rotational friction coefficient	$6.8 \times 10^{-8} \text{ Kg s}^{-1} \mu\text{m}^2$	calculated from a
$\tau_{\text{run}}, \tau_{\text{reverse}}$	mean run/reverse time in the absence of chemicals	0.86 s	[45]
$\tau_{\text{tumble}}, \tau_{\text{pause}}$	mean tumble/reversal-pause time in the absence of chemicals	0.14 s	[45]
τ_0	mean run time with chemicals and no gradient	1.48 s	[45]
t_{up}	max. mean run time up a gradient	$2\tau_0$	
t_{down}	min. mean run time down a gradient	τ_0	
∇C	modulus of the gradient	$25 \mu\text{M mm}^{-1}$	[45]
∇C_0	modulus of the reference gradient	$25 \mu\text{M mm}^{-1}$	the same as ∇C
C^*	prefered concentration at position $x = 0$	$10 \mu\text{M}$	[78, 79]
dt	timestep of integration	0.002 s	

Table A.1: Simulation parameters for free swimming bacteria of Chapter 4

B Appendix: Mean Squared Displacement for Free Bacteria

The Mean Squared Displacement is a useful quantity to discern which type of motion is taking place, as briefly introduced in Section 2.1.3.2. To obtain the MSD in this section, I calculate the Time-Averaged MSD (TAMSD) over each trajectory of ~ 5000 s and then I take a mean over an ensemble of 1000 trajectories; this quantity is indicated by $\langle TAMSD \rangle$. The MSD can be calculated in one dimension or in three. Usually, chemical gradients and magnetic fields are set along the x axis, so the x component of the MSD is taken into consideration.

In all the figure of this appendix, the $\langle TAMSD \rangle$ is plotted in a loglog scale as function of time; in Figure B.1a, the typical behavior for a brownian particle is showed, with a slope of 1; this is compared to an ABP, where initially the slope is of 2 (indicating direct self-propulsion) and then changes to 1 due to the thermal rotational diffusion. A more general case is depicted in figure In Figure B.1b, where the fitted slopes are indicated; an active brownian particle undergoes a first brownian regime with slope close to 1 for very small times (this regime is suppressed if the self-velocity is high); then an intermediate regime with a slope close to 2 indicates the self-propulsion; it is followed by a regime where the brownian motion is taking over with a slope close to 1; and finally another regime can appear at very high time if the motion is biased by an external stimulus, with slopes close to 2, indicated a 'intentional' motion.

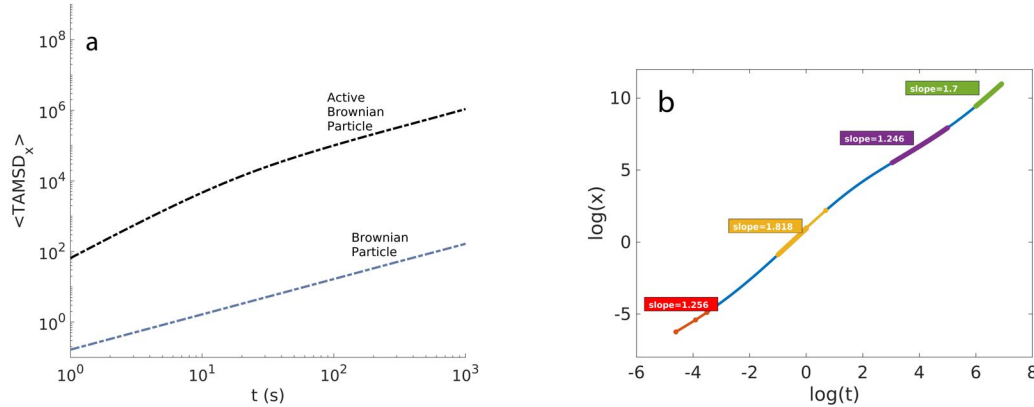


Figure B.1: (a) Ensemble Average of the Time-Averaged MSD versus time in a loglog scale for a Brownian Particle (gray) and for an Active Brownian Particle (black) (b) General behavior of an Active Brownian particle, with a first Brownian regime (red), followed by the directed motion (yellow), then by thermal noise reorientations (purple) and finally, a biased regime towards an external stimulus (green). The numbers indicate the slope of the linear loglog fit of the interested section.

When a bacterium performs also changes of direction, the diffusion constant changes, and for the run-and-tumble it assumes the following form: $D_{\text{eff}} \simeq \frac{v^2 \tau_{\text{run}}^2}{3\alpha(\tau_{\text{run}} + \tau_{\text{tumble}})}$, with $\alpha = (1 - \langle \cos \theta_{\text{tumble}} \rangle)$ [50]; therefore, this changes the MSD and its intercept, compared to what happens for a pure active particle without changes of direction. The corresponding curve is the blue curve in Figure B.2a.

The effect of chemotaxis towards an attractant (with a gradient along $+x$) can be seen in Figure B.2a for a run-and-tumble strategy (in red) compared to the case without chemotaxis (blue). While the initial behavior at small times is the same, at intermediate times the red curve shows a super-diffusive behavior, meaning with a slope between 1 and 2; at higher times, the bias due to chemotaxis takes over and the slope is close to 2 again. In the inset, three example trajectories of run-and-tumble with chemotaxis are shown. For these curves, exponentially distributed run times were used. In figure B.2b, the difference between curves with and without exponentially distributed times is presented. The effect of the exponentially distributed times is to postpone the transition between active and diffusive behavior.

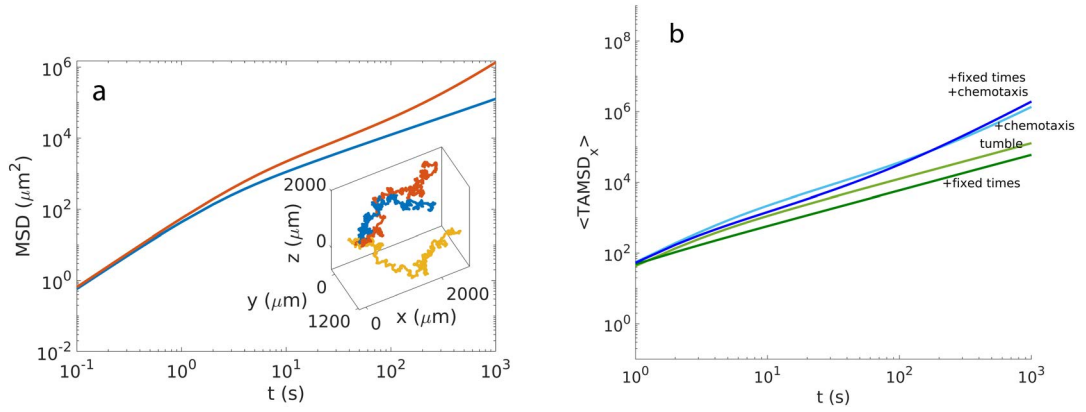


Figure B.2: (a) MSD for a run-and-tumble particle with chemotaxis for an attractant with the gradient along $+x$ (red), and without chemotaxis (blue). In the inset, three example trajectories with chemotaxis. (b) Effect of the exponentially distributed run times (light curves) and of the fixed run times (dark curves), with (blue) and without chemotaxis (green) for a run-and-tumble particle.

In figure B.3a and b I present the effect of a magnetic field parallel to the chemical concentration, respectively for run-and-tumble and for run-and-reverse. Magnetic fields lead to faster velocities along the magnetic field direction that can be seen by the higher intercept. The main difference between tumble and reverse is the following. For reverse, the bacterium keeps the alignment of the body with the magnetic field all the time; the only resulting effect is an effective reduction of the thermal noise, with an higher velocity along the magnetic field direction; the curves are thus translated up. For tumble instead, the motion is completely changed by the magnetic field; the magnetic field stretches the trajectories along the field direction; provoking a directed motion at all times, thus a slope of 1.

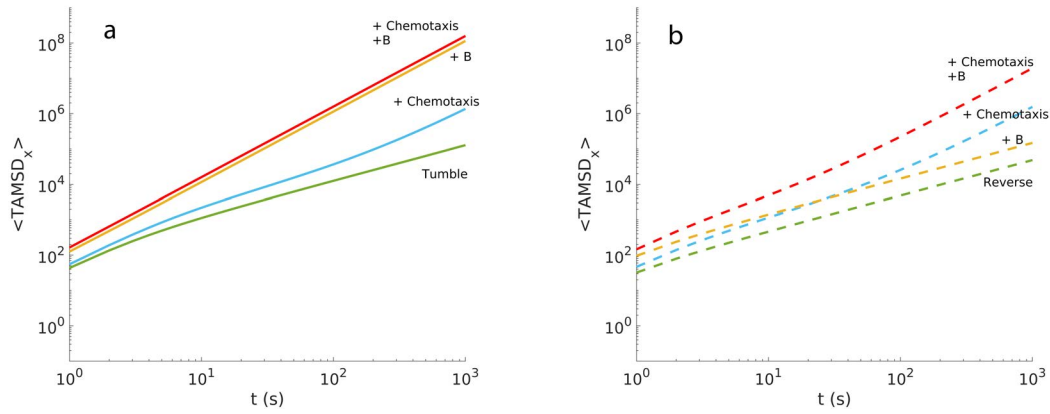


Figure B.3: Effect of the magnetic fields for (a) run-and-tumble and (b) run-and-reverse. In green, the basic case; in blue, with chemotaxis; in yellow, with a parallel magnetic along x ; in red, with chemotaxis and a parallel magnetic field.

C Appendix: Simulation Parameters for Capillaries

For the capillary simulations of Chapter 5, some parameters were changed with respect to the free-swimming bacteria. If not stated here, the parameters are unchanged with respect to Table A.1. For Chapter 5, the concentration and gradient are dynamic and not constant. The run-time response function to the gradient is a step function, thus the reference gradient ∇C_0 is 0.

name	object	value	case
v	self velocity modulus	$20 \mu\text{m s}^{-1}$	axial, polar
C^*	preferred concentration at position $x = 0$	$3 \mu\text{M}$	axial, polar
k	oxygen consumption rate	$0.75 f \text{ mol min}^{-1} \text{ cell}^{-1}$	axial, polar
$C(x = 0)$	oxygen concentration at $x = 0$	$216 \mu\text{M}$	axial, polar
C_a	concentration cutoff	$0.75 \mu\text{M}$	axial, polar
D_{O_2}	oxygen diffusion constant	$2100 \mu\text{m}^2 \text{s}^{-1}$	axial, polar
τ_0	mean run time with chemicals and no gradient	1 s	axial, polar
t_{up}	max. mean run time up a gradient	$6\tau_0$	axial
t_{down}	min. mean run time down a gradient	τ_0	axial
t_{up}	max. mean run time up a gradient	$2\tau_0$	polar
t_{down}	min. mean run time down a gradient	$0.5\tau_0$	polar

Table C.1: Simulation parameters for capillary assays used in chapter 5

D Appendix: Simulation Parameters for Bacteria in Confinement

For bacteria in confinement in Chapter 6, some changes were done in the parameters. If not stated differently, the parameters are the same as Table A.1. For the circular traps simulation, no chemotaxis was included and no reversal events were included. For the 2D and 3D sand simulations, the oxygen gradient was a constant and the response function was a step-function, with chemotaxis performed towards an attractant and axial bacteria.

name	object	value	case
v	self velocity modulus	$20 \mu\text{m s}^{-1}$	circular trap, 2D, 3D
$\tau_{\text{run}}, \tau_{\text{reverse}}$	mean run/reverse time in the absence of chemicals	∞	circular trap
C	concentration	$0 \mu\text{M}$	circular trap
ϵ	prefactor for wall interaction	10^{-10}	circular trap
p_T	prefactor for wall torque prefactor	$4a$	circular trap
τ_0	mean run time with chemicals and no gradient	1 s	2D, 3D
t_{up}	max. mean run time up a gradient	$6\tau_0$	2D, 3D
t_{down}	min. mean run time down a gradient	τ_0	2D, 3D
ϵ	prefactor for flat wall interaction	10^{-10}	2D, 3D
ϵ	prefactor for cylinder/grain interaction	10^{-4}	2D, 3D
p_T	wall torque prefactor	$4a$	2D, 3D

Table D.1: Simulation parameters for bacteria in confinement, as used in Chapter 6

E Appendix: High Density of Bacteria

The WCA force that was used to model the interaction between the bacteria and the hard obstacles such as walls or sediment-grains can be used to simulate the self-exclusion interaction between bacteria. In all the thesis, bacteria do not interact between themselves and in principle they can overlay. For the densities used in all the simulations, the bacteria are diluted enough to ignore the interaction between them. This is not true when simulations at high bacterial density should be performed, for example if we want to study pattern formation. In this case, the WCA force can come in hand, and allows to simulate self-excluding particle as in figure E.1. For such simulations, the time-step should be reduced to prevent unphysical interactions: if the time-step is too big, even with a small WCA force, the displacement calculated can be very big, making the bacteria 'jump'.

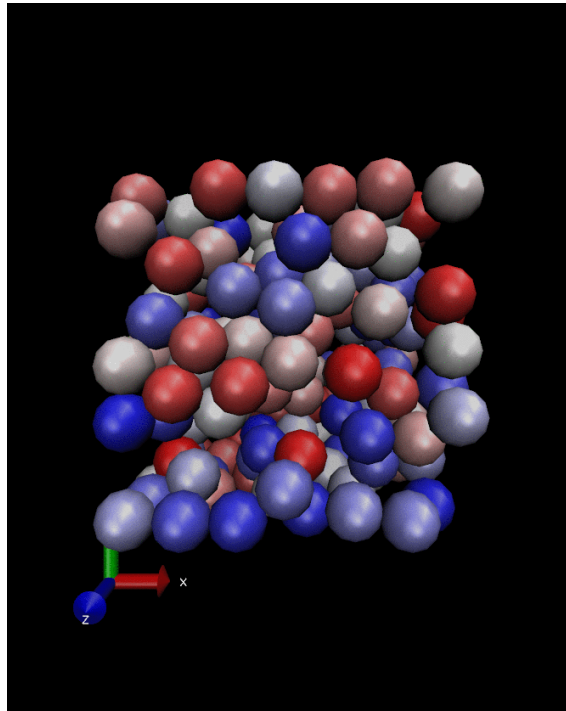


Figure E.1: In a cube of $12^3 \mu\text{m}^3$, 200 bacteria of radius $1 \mu\text{m}$ undergo a WCA interaction between them, and an induced reverse on the borders of the box.

F Appendix: Focus Depth for 2D Tracking

To plan future experiments with quasi-2D microfluidic channels, the height of the channel should be taken carefully into consideration. If 3D tracking would be available for spirilla-shaped bacteria, the ideal channel height would be of at least of 100 times the size of the bacteria; in this way, the bacteria would be swimming freely in the bulk, without perturbation of their motion from the walls. Since 3D tracking proves to be problematic, the other solution is to have 2D tracking. With 2D tracking in the bulk, the main problem is that bacteria can swim out of focus, and the tracks get interrupted. To avoid this, the experiment can be reduced in quasi-2D, to have the bacteria always in focus and no breaks in the tracks. The only problem is that the wall interaction can influence the motion of the bacteria due to hydrodynamics, so reference controls should be done with bacteria in such small heights. To decide the optimal height for our porous-environment microfluidic channels, a simple experiment was performed by Klaas Bente in our lab. Some glass bead of $1\ \mu\text{m}$ radius were imaged with our set-up at different heights: in focus, out of focus of $\pm 5\ \mu\text{m}$ or of $\pm 10\ \mu\text{m}$. Subsequently, I employed the self-written Matlab code that was used before in our lab to track the bacteria [78, 79]. The code applies a background subtraction followed by thresholding, obtaining a black and white image, where the white parts are the beads. Then, the code recognizes a minimum number of white pixels as bacteria. As it can be seen in Figure F.1, particles that are easily recognized by the program in focus (examples are indicated by a red and yellow circle) are still recognized when the image is out of focus of $5\ \mu\text{m}$, while they are lost for $10\ \mu\text{m}$. Thus, the ideal height for our set-up and for our tracking algorithm is of $10\ \mu\text{m}$.

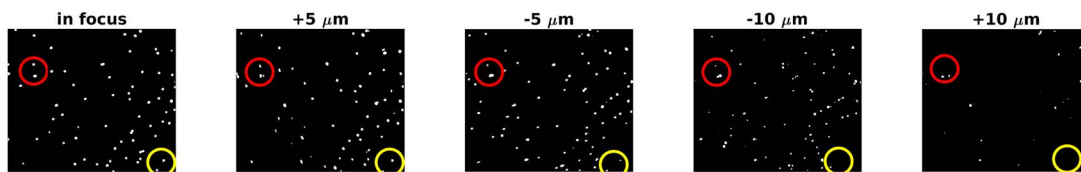


Figure F.1: Tracking performance at different depth of a glass sphere of $1\ \mu\text{m}$ of radius (check). The tracking works good if the spheres are situated at $\pm 5\ \mu\text{m}$ from the focal plane. According to this result, the microfluidic channel will be produced with an height of $10\ \mu\text{m}$ to have the bacteria always in focus. The simulation were run with that depth, too.

G Appendix: Passage Times for 2D simulations

For quasi-2D simulations in a porous environment of Chapter 6 (Figure 6.4), there are more ways to calculate the passage time. In the main part of the thesis, I show this method for which the number of bacteria in a certain window is counted over time; the profile looks like a Gaussian that can be fitted to obtain the main peak. The peak position gives an idea of the mean passage time. This method is employable in the experiments, too. Other solutions that are adapt for simulations but are less practical in the experiments are presented in Figure G.1. For each different case (no magnetic field and no chemotaxis; with only magnetic fields; with only chemotaxis; and with chemotaxis combined with magnetic fields) the time at which the first bacterium passes a 'finish line' can be calculated (blue curve) with and without sand (respectively, stars with filled lines and circles with dashed line). No big differences can be seen between sand and without sand for a finish line at $500\mu\text{m}$ (Figure G.1a). Instead of taking the time of the first bacterium, the mean time of all the bacteria that passed the finish line can be considered (red lines). Again, no big differences can be seen between the case with and without sand. It can also be considered the percentage of bacteria that managed to reach the 'finish line' (green curves). Here, some differences can be spotted between with and without sand. In general, the differences for these three measurements (minimum passage

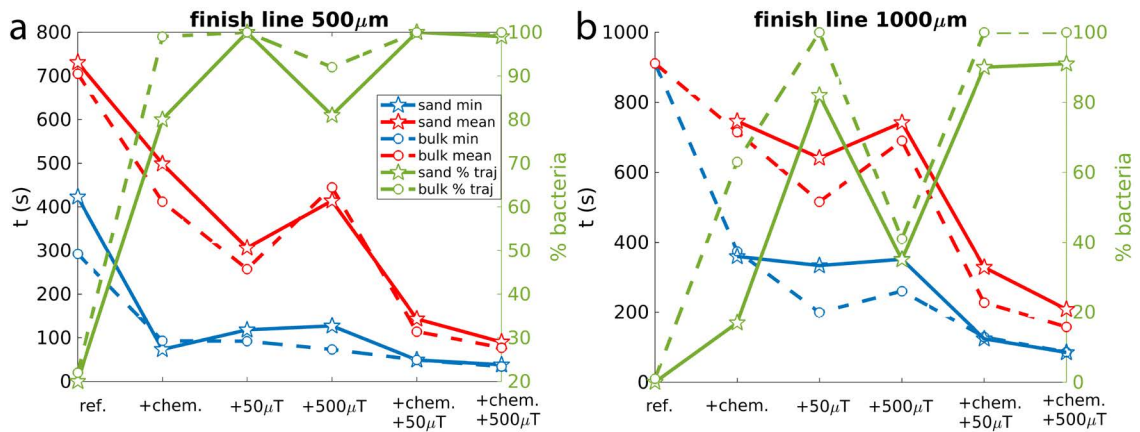


Figure G.1: Minimum passage time (blue), mean passage time (red), percentage of bacteria that reached the finish line (green), for the case without sand (circles with dashed line) and with sand (stars with filled line), for a 'finish line' of (a) $500\mu\text{m}$ and (b) $1000\mu\text{m}$, for different simulations: a reference without chemotaxis nor magnetic fields, with magnetic fields, with chemotaxis, or with magnetic fields and chemotaxis combined. All the bacteria started at $x = 0$, with 1000 s of simulated trajectories. The chemotaxis is for an attractant with a gradient along $+x$, and magnetic fields are parallel to that. See Figure 6.4 for the trajectories.

time, mean passage time and percentage of bacteria) become higher when the finish line is set further away at $1000\ \mu\text{m}$ (Figure G.1b). In fact, differences in the diffusivity become stronger further away from the source. Here it becomes visible that the sand hinders the motion, slowing down the diffusion process, with smaller passage times and less bacteria that reached the 'finish line'. Another interesting effect is that a strong magnetic field alone hinders the motion of the bacteria, slowing them down with respect to the case with a weak magnetic field or without magnetic field. Instead, when a strong magnetic field is coupled with chemotaxis, the dynamics is fastened up even for strong magnetic fields.

Another way to visualize how the sand obstacles the motion of the bacteria, is to plot the final position of 100 trajectories simulated for 1000 s (Figure G.2 without sand and G.3 with the sand). It can be clearly seen that the sand slows down the process since the corresponding positions are at smaller x with respect to the ones without sand. Again, a strong magnetic field without chemotaxis hinders the motion, with many final configurations at smaller x with respect to the case with a weak field. For chemotaxis with sand and a strong magnetic field, many bacteria get stuck in some 'hot points', while with a weak field they can more easily escape.

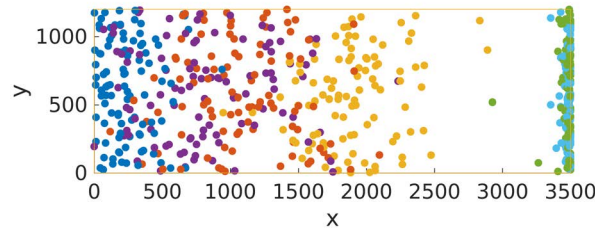


Figure G.2: Final positions of 100 trajectories started in $x = 0$ after 1000 s of simulations, without sand, for various cases: a reference without chemotaxis nor magnetic fields (blue), with magnetic fields (red $50\ \mu\text{T}$ and purple $500\ \mu\text{T}$), with chemotaxis (yellow), or with magnetic fields and chemotaxis combined (green $50\ \mu\text{T}$ and light blue $500\ \mu\text{T}$). X and y are measured in μm .

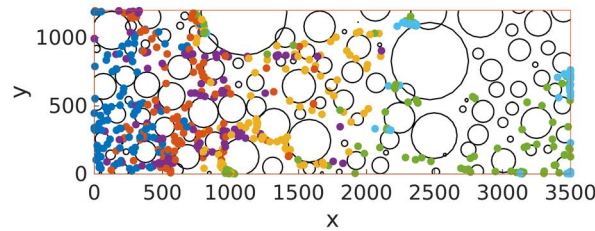


Figure G.3: Final positions of 100 trajectories started in $x = 0$ after 1000s of simulations, with the pillars resembling the sand, for various cases: a reference without chemotaxis nor magnetic fields (blue), with magnetic fields (red $50\ \mu\text{T}$ and purple $500\ \mu\text{T}$), with chemotaxis (yellow), or with magnetic fields and chemotaxis combined (green $50\ \mu\text{T}$ and light blue $500\ \mu\text{T}$). X and y are measured in μm .

H Appendix: Comparison between Simulated and Experimental Data for MTB in a 2D Porous Environment

Rismani Yazdi *et al.* performed experiments with MTB in 2D microfluidic channels resembling a porous environment [103]. The simulations that I performed in Chapter 6 can be compared with their results. First of all, my simulated wall-interactions (WCA force and torque) resemble in good approximations the wall-interactions observed by them: the bacteria 'slide' around a cylinder in the presence of a magnetic field (see Figure H.1 for the experimental data compared to Figure 6.9d for the simulated data); the bacteria under a strong magnetic field alternate sliding with a 'reverse' motion on flat walls (see Figure H.1 for the experimental data at 300 μT compared to Figure 6.9e for the simulated data at 500 μT). For this last point, they observe a real induced reverse at flat walls that was not taken into account in my simulation; the final effect is although similar.

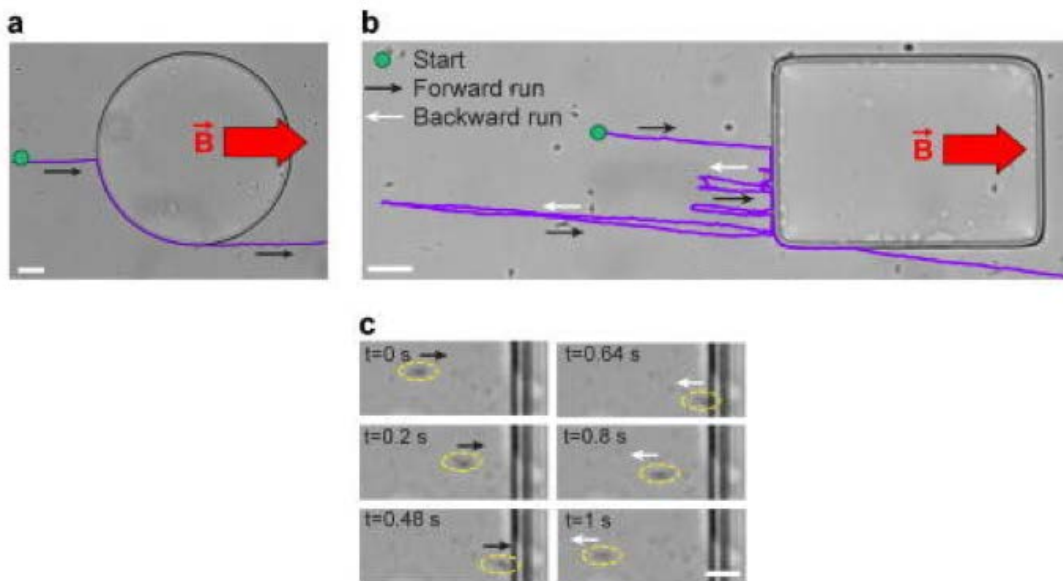


Figure H.1: Interaction of MTB with (a) curved and (b) flat obstacles, $B=0.3$ mT. (c) A bacterial reversal event at a flat obstacle. The bacterium is marked by a yellow ellipse. Reproduced with permission from Rismani Yazdi *et al.* [103] RightsLink Order Number: 4398750548293.

For the trajectories inside a porous environment in a 2D microfluidic channel, they didn't see the presence of 'stream-lines': all the trajectories are equally distributed between the gaps (see Figure H.2), while on the contrary, I observed some path that were more used (see Figure 6.4). This could be due to some differences between their setup and mine: for example, the regular spacing of their pillars and the lack of obstructed paths. The regular spacing leads also to 'unnatural motions', with the bacteria following a diagonal path; this would be avoided with our construction, in which the pillars are random sized and distributed. We plan future experiments with microfluidic channel with random distributed and random sized pillars.

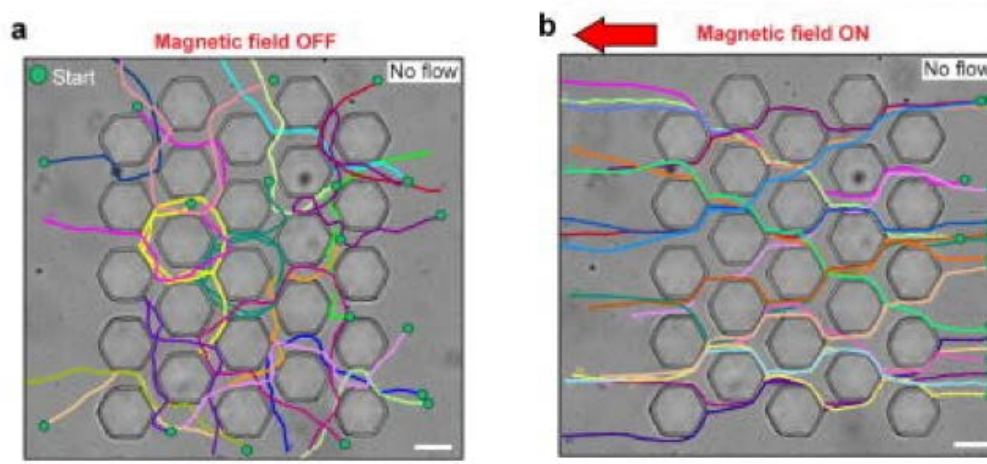


Figure H.2: Swimming trajectories of MTB through a homogeneous porous micromodel (a) in the absence and (b) in the presence of the applied magnetic field of $B=0.3$ mT. Scale bar: $300\ \mu\text{m}$. Reproduced with permission from from Rismani Yazdi *et al.* [103] RightsLink Order Number: 4398750548293.

I Appendix: Calculating the Mobility Matrix in the Center of Hydrodynamic Mobility

The mobility matrix terms depend on the chosen basis of representation. A common reference system is the so-called center of hydrodynamic mobility, where the rotational-rotational mobility matrix is diagonal and the translational-rotational part is symmetrical [30]. Following the S.I. of [30], we calculate the matrix in this center as follows through a Matlab script:

- The mobility matrix of the center of mass \mathbf{M} is calculated at time 0 in the lab reference system;
- The right eigenvectors $v_i, i = 1, 2, 3$ of the rotational-rotational matrix \mathbf{M}^{rr} are calculated, such as $\mathbf{V}^{-1}\mathbf{M}^{\text{rr}}\mathbf{V} = \mathbf{D}$, where \mathbf{V} is the matrix whose columns are the right eigenvectors and \mathbf{D} is the diagonalized matrix;
- The eigenvectors are sorted from the smallest to the highest eigenvalue; the matrix \mathbf{V} is then reordered accordingly, as well as \mathbf{D} ;
- The eigenvectors must still be a right handed triad $(v_1 \times v_2) \cdot v_3 = 1$. If this is not the case, the sign of v_3 is changed by hand, and the \mathbf{V} matrix is recalculated accordingly, as well as its inverse \mathbf{V}^{-1} ; this does not change the matrix \mathbf{D} ;
- We apply the same transformation to \mathbf{M}^{tt} , \mathbf{M}^{tr} and \mathbf{M}^{rt} : $\mathbf{V}^{-1}\mathbf{M}^{\text{--}}\mathbf{V} = \mathbf{M}_{\text{diag}}^{\text{--}}$; we obtain the matrix:

$$\begin{pmatrix} \mathbf{M}_{\text{diag}}^{\text{tt}} & \mathbf{M}_{\text{diag}}^{\text{tr}} \\ \mathbf{M}_{\text{diag}}^{\text{rt}} & \mathbf{D} \end{pmatrix};$$

- Then, we actually translate in the center of hydrodynamic mobility. To do so, we write the center of hydrodynamicity \mathbf{r}_m in the coordinate system given by \mathbf{V} . The center is

$$\mathbf{r}_m(1) = (\mathbf{M}_{\text{diag}}^{\text{tr}}(3, 2) - \mathbf{M}_{\text{diag}}^{\text{tr}}(2, 3)) / (\mathbf{D}(2, 2) + \mathbf{D}(3, 3))$$

$$\mathbf{r}_m(2) = (\mathbf{M}_{\text{diag}}^{\text{tr}}(1, 3) - \mathbf{M}_{\text{diag}}^{\text{tr}}(3, 1)) / (\mathbf{D}(1, 1) + \mathbf{D}(3, 3))$$

$$\mathbf{r}_m(3) = (\mathbf{M}_{\text{diag}}^{\text{tr}}(2, 1) - \mathbf{M}_{\text{diag}}^{\text{tr}}(1, 2)) / (\mathbf{D}(1, 1) + \mathbf{D}(2, 2))$$

- The matrix $\mathbf{X} = [\times \mathbf{r}_m]$ is calculated as follows:

$$\mathbf{X}(1,2) = -\mathbf{r}_m(3)$$

$$\mathbf{X}(1,3) = \mathbf{r}_m(2)$$

$$\mathbf{X}(2,1) = \mathbf{r}_m(3)$$

$$\mathbf{X}(2,3) = -\mathbf{r}_m(1)$$

$$\mathbf{X}(3,1) = -\mathbf{r}_m(2)$$

$$\mathbf{X}(3,2) = \mathbf{r}_m(1)$$

and zero in all the other entries;

- Finally we obtain the matrix in the center of hydrodynamic mobility through a translation in the center \mathbf{r}_m :

$$\mathbf{M}_{\text{hyd}}^{\text{tt}} = \mathbf{M}_{\text{diag}}^{\text{tt}} - \mathbf{X}\mathbf{D}\mathbf{X} - \mathbf{X}\mathbf{M}_{\text{diag}}^{\text{rt}} + \mathbf{M}_{\text{diag}}^{\text{tr}}\mathbf{X}$$

$$\mathbf{M}_{\text{hyd}}^{\text{tr}} = \mathbf{M}_{\text{diag}}^{\text{tr}} - \mathbf{X}\mathbf{D}$$

$$\mathbf{M}_{\text{hyd}}^{\text{rt}} = \mathbf{M}_{\text{diag}}^{\text{rt}} + \mathbf{D}\mathbf{X}$$

$$\mathbf{M}_{\text{hyd}}^{\text{rr}} = \mathbf{D}.$$

J Appendix: Simulation Parameters for the Helices

parameter	description	value (dimension)
η	water viscosity at 25°	8.9×10^{-4} Pas
a	bead radius	$0.1 \mu\text{m}$
n	number of beads per turn (touching)	9
m	number of turns	4
r	radius of the helix	$0.25 \mu\text{m}$
p	pitch of the helix	$4r$
h	handedness of helix	right handed
θ_m	polar magnetization angle	0°
α_m	azimuthal magnetization angle	0°
$ \mathbf{m} $	modulus of the magnetic moment \mathbf{m}	$1. \times 10^{-15}$ (Am ²)
B	magnetic field	2 mT

Table J.1: Basic set of parameters for the helix study

K Appendix: Random shaped propellers: the Center of Hydrodynamic Mobility

In this Appendix, I report the mobility matrices of the random-shaped propellers of Chapter 9 obtained through the method illustrated in the appendix I. The matrices change accordingly to the bead-discretization used.

K.1 Propeller 1, 49 beads

$$M = \left(\begin{array}{ccc|ccc} & 0 & 0 & 0 & -0.1 * 10^{11} & -1.2 * 10^{11} & -7.8 * 10^{11} \\ & 0 & 0 & 0 & -1.2 * 10^{11} & 0.5 * 10^{11} & -1.2 * 10^{11} \\ & 0 & 0 & 0 & -7.8 * 10^{11} & -1.2 * 10^{11} & -0.9 * 10^{11} \\ \hline -0.1 * 10^{11} & -1.2 * 10^{11} & -7.8 * 10^{11} & & 1.1 * 10^{19} & 0 & 0 \\ -1.2 * 10^{11} & 0.5 * 10^{11} & -1.2 * 10^{11} & & 0 & 1.2 * 10^{19} & 0 \\ -7.8 * 10^{11} & -1.2 * 10^{11} & -0.9 * 10^{11} & & 0 & 0 & 2.5 * 10^{19} \end{array} \right)$$

$$f_0 = 133.8 \text{ Hz}$$

K.2 Propeller 1, 501 beads

$$M = \left(\begin{array}{ccc|ccc} & 0 & 0 & 0 & -1.3 * 10^{11} & 0.7 * 10^{11} & 5.7 * 10^{11} \\ & 0 & 0 & 0 & 0.7 * 10^{11} & 1.8 * 10^{11} & -0.3 * 10^{11} \\ & 0 & 0 & 0 & 5.7 * 10^{11} & -0.3 * 10^{11} & -1.5 * 10^{11} \\ \hline -1.3 * 10^{11} & 0.7 * 10^{11} & 5.7 * 10^{11} & & 1.0 * 10^{19} & 0 & 0 \\ 0.7 * 10^{11} & 1.8 * 10^{11} & -0.3 * 10^{11} & & 0 & 1.0 * 10^{19} & 0 \\ 5.7 * 10^{11} & -0.3 * 10^{11} & -1.5 * 10^{11} & & 0 & 0 & 2.2 * 10^{19} \end{array} \right)$$

$$f_0 = 120.4 \text{ Hz}$$

K.3 Propeller 2, 55 beads

$$M = \left(\begin{array}{ccc|ccc} & 0 & 0 & 0 & -0.8 * 10^{11} & 1.4 * 10^{11} & 6.8 * 10^{11} \\ & 0 & 0 & 0 & 1.4 * 10^{11} & -0.2 * 10^{11} & 5.3 * 10^{11} \\ & 0 & 0 & 0 & 6.8 * 10^{11} & 5.3 * 10^{11} & 3.9 * 10^{11} \\ \hline -0.8 * 10^{11} & 1.4 * 10^{11} & 6.8 * 10^{11} & & 2.1 * 10^{19} & 0 & 0 \\ 1.4 * 10^{11} & -0.2 * 10^{11} & 5.3 * 10^{11} & & 0 & 2.2 * 10^{19} & 0 \\ 6.8 * 10^{11} & 5.3 * 10^{11} & 3.9 * 10^{11} & & 0 & 0 & 4.9 * 10^{19} \end{array} \right)$$

$$f_0 = 253.8 \text{ Hz}$$

K.4 Propeller 2, 518 beads

$$M = \left(\begin{array}{ccc|ccc} & 0 & 0 & 0 & 1.7 * 10^{11} & 1.7 * 10^{11} & -8.4 * 10^{11} \\ & 0 & 0 & 0 & 1.7 * 10^{11} & -1.5 * 10^{11} & 3.4 * 10^{11} \\ & 0 & 0 & 0 & -8.4 * 10^{11} & 3.4 * 10^{11} & -0.6 * 10^{11} \\ \hline 1.7 * 10^{11} & 1.7 * 10^{11} & -8.4 * 10^{11} & & 1.5 * 10^{19} & 0 & 0 \\ 1.7 * 10^{11} & -1.5 * 10^{11} & 3.4 * 10^{11} & & 0 & 1.5 * 10^{19} & 0 \\ -8.4 * 10^{11} & 3.4 * 10^{11} & -0.6 * 10^{11} & & 0 & 0 & 3.2 * 10^{19} \end{array} \right)$$

$$f_0 = 179.0 \text{ Hz}$$

K.5 Propeller 2, 4276 beads

$$M = \left(\begin{array}{ccc|ccc} & 0 & 0 & 0 & -0.2 * 10^{11} & -2.3 * 10^{11} & -8.4 * 10^{11} \\ & 0 & 0 & 0 & -2.3 * 10^{11} & 0.2 * 10^{11} & 5.0 * 10^{11} \\ & 0 & 0 & 0 & -8.4 * 10^{11} & 5.0 * 10^{11} & -0.4 * 10^{11} \\ \hline -0.2 * 10^{11} & -2.3 * 10^{11} & -8.4 * 10^{11} & & 1.5 * 10^{19} & 0 & 0 \\ -2.3 * 10^{11} & 0.2 * 10^{11} & 5.0 * 10^{11} & & 0 & 1.5 * 10^{19} & 0 \\ -8.4 * 10^{11} & 5.0 * 10^{11} & -0.4 * 10^{11} & & 0 & 0 & 3.1 * 10^{19} \end{array} \right)$$

$$f_0 = 175.4 \text{ Hz}$$